



HAL
open science

Experimental astrochemistry: the kinetics of neutral-neutral reactions at low temperature and their relevance to the chemistry of planetary atmospheres and interstellar clouds

Dianailys Núñez Reyes

► To cite this version:

Dianailys Núñez Reyes. Experimental astrochemistry: the kinetics of neutral-neutral reactions at low temperature and their relevance to the chemistry of planetary atmospheres and interstellar clouds. Theoretical and/or physical chemistry. Université de Bordeaux, 2019. English. NNT : 2019BORD0032 . tel-02181159

HAL Id: tel-02181159

<https://theses.hal.science/tel-02181159>

Submitted on 12 Jul 2019

HAL is a multi-disciplinary open access archive for the deposit and dissemination of scientific research documents, whether they are published or not. The documents may come from teaching and research institutions in France or abroad, or from public or private research centers.

L'archive ouverte pluridisciplinaire **HAL**, est destinée au dépôt et à la diffusion de documents scientifiques de niveau recherche, publiés ou non, émanant des établissements d'enseignement et de recherche français ou étrangers, des laboratoires publics ou privés.

THÈSE PRÉSENTÉE
POUR OBTENIR LE GRADE DE

DOCTEUR DE

L'UNIVERSITÉ DE BORDEAUX

ÉCOLE DOCTORALE DES SCIENCES CHIMIQUES
SPÉCIALITÉ: Chimie - Physique

Par Dianailys NÚÑEZ REYES

**ASTROCHIMIE EXPÉRIMENTALE: CINÉTIQUE DES RÉACTIONS NEUTRE-NEUTRE
À BASSE TEMPÉRATURE ET PERTINENCE POUR LA CHIMIE DES ATMOSPHÈRES
PLANÉTAIRES ET DES NUAGES INTERSTELLAIRES**

Sous la direction de : Jean-Christophe LOISON
co-directeur : Michel DOBRIJEVIC
co-directeur : Kevin M. HICKSON

Soutenue le 19/03/2019

Membres du jury :

M. LE PICARD, Sébastien	Professeur	Président
Mme. BATTIN-LECLERC, Frédérique	Directeur de Recherche	Rapporteur
Mme. BOYÉ-PÉRONNE, Séverine	Professeur	Rapporteur
M. HICKSON, Kevin M.	Directeur de Recherche	Examineur
M. LOISON, Jean-Christophe	Directeur de Recherche	Examineur
M. DOBRIJEVIC, Michel	Maître de Conférences	Examineur

Titre : Astrochimie expérimentale: Cinétique des réactions neutre-neutre à basse température et pertinence pour la chimie des atmosphères planétaires et des nuages interstellaires

Résumé:

Les 50 dernières années ont été caractérisées par le développement rapide de l'astrochimie. Plus de 150 réactions entre espèces neutres ont déjà été étudiées aux basses températures qui sont celles du milieu interstellaire et des atmosphères planétaires. Néanmoins, les constantes de vitesse et la nature des produits restent inconnues pour de nombreuses réactions potentiellement importantes pour caractériser ces milieux. Nous avons effectué des études cinétiques pour des processus réactifs, et non réactifs entre des atomes dans un état électronique excité [$C(^1D)$, $O(^1D)$ et $N(^2D)$] et plusieurs molécules stables afin de quantifier leur importance dans la chimie des atmosphères planétaires. Nous avons aussi étudié la réaction entre les atomes de carbone dans leur état électronique fondamental (3P) et l'eau, confirmant l'importance, pour certaines réactions avec barrière, de l'effet tunnel pour la réactivité à basse température. Les constantes de vitesse et les rapports de branchement pour ces processus ont été déterminés dans la gamme de température entre 50 et 296 K en utilisant un appareil CRESU, les atomes étudiés ont été produits par photolyse à l'aide d'un laser pulsé (PLP) et détectés par fluorescence induite par laser dans l'ultraviolet du vide (VUV LIF).

MOTS CLES: astrochimie, cinétique chimique, réactions en phase gazeuse, atomes à l'état excité, CRESU

Title : Experimental Astrochemistry: The kinetics of neutral-neutral reactions at low temperature and their relevance to the chemistry of planetary atmospheres and interstellar clouds

Abstract:

The last 50 years have been characterized by the fast development of astrochemistry as a science. To date, more than 150 gas-phase neutral-neutral reactions have been investigated at low temperatures relevant to planetary atmospheres and in cold regions of the interstellar medium. However, the rate constants and nature of the products for many potentially important gas-phase processes remain unknown. We performed kinetic studies of reactive and non-reactive removal processes between electronically excited atoms [$C(^1D)$, $O(^1D)$ and $N(^2D)$] with several molecules in order to quantify their importance in the chemistry of planetary atmospheres. Furthermore, we also investigated the reaction between carbon atoms in their ground electronic state (3P) with water, providing new evidence of a quantum mechanical tunnelling mechanism at low temperatures, which could play an important role in the chemistry of interstellar clouds. Rate constants and branching ratios for these processes were determined over the 50 - 296 K temperature range using a CRESU (Cinétique de Réaction en Ecoulement Supersonique Uniforme) apparatus coupled with pulsed laser photolysis (PLP) and vacuum ultraviolet laser induced fluorescence (VUV LIF).

KEYWORDS: astrochemistry, chemical kinetics, gas-phase reactions, excited state atoms, CRESU

Unité de recherche

Institut des Sciences Moléculaires – UMR 5255
Université de Bordeaux. 351 cours de la Libération
33405 TALENCE cedex
FRANCE

Résumé:

Pendant de nombreuses années, les scientifiques ont été sceptiques quant à la présence de molécules dans l'espace interstellaire, principalement en raison des conditions physiques difficiles y régnant (température, pression et champ de rayonnement à haute énergie). Cependant plus de 200 espèces ont déjà été détectées dans le milieu interstellaire à ce jour, ce qui a donné naissance au domaine de l'astrochimie, les astronomes cherchant à expliquer la présence de molécules dans les environnements interstellaires. L'objectif principal de l'astrochimie est donc d'étudier la nature et le comportement des espèces détectées en étudiant leurs processus de formation et de destruction dans divers environnements astronomiques et éventuellement de prévoir quelles autres espèces pourraient être présentes. Parmi ces processus, les réactions neutres-neutres en phase gazeuse jouent un rôle important. À ce jour, plus de 150 de ces réactions neutres-neutres en phase gazeuse ont été étudiées à basse température correspondantes aux atmosphères planétaires et aux régions froides du milieu interstellaire. Toutefois, les constantes de vitesse et la nature des produits pour de nombreux procédés potentiellement importants en phase gazeuse demeurent inconnues. Cette thèse résume trois années de travail doctoral à l'Institut des Sciences Moléculaires (ISM) au sein du groupe COMEX (Collisions Moléculaires en Milieux Extrêmes). Les installations expérimentales CRESU (Cinétique de Réaction en Encoulement Supersonique Uniforme) ont été utilisées pour étudier la cinétique de plusieurs réactions en phase gazeuse, d'intérêt pour la communauté astrochimique, entre 50 K et 296 K. Ce manuscrit est composé de cinq chapitres répartis comme suit.

Le chapitre 1 présente l'astrochimie, le milieu interstellaire et les atmosphères planétaires, en particulier Mars et Titan (la plus grande lune de Saturne). L'importance des données cinétiques (constantes de vitesse et rapports de branchement) pour les modèles astrochimiques est également discutée. Ce chapitre établit les fondements des questions qui ont motivé ce travail expérimental.

Le chapitre 2 présente la cinétique des réactions en phase gazeuse et leur dépendance en température. Les méthodes expérimentales employées pour étudier les réactions en phase gazeuse y sont décrites, en particulier le dispositif CRESU utilisé dans ce travail pour les mesures cinétiques à basse température (entre 50 et 296 K). Tout d'abord, un aperçu général de la technique est donné suivi de la description du mini CRESU de Bordeaux. Puis les techniques expérimentales de photolyse laser pulsée (PLP) et de fluorescence induite par laser (LIF) utilisées dans ce travail pour produire et détecter les espèces étudiées. Les espèces atomiques $C(^3P)$, $C(^1D)$ et $O(^1D)$ sont produits par PLP dans l'ultraviolet à partir de différents précurseurs (CBr_4 ou O_3). Dans le cas de la production de $N(^2D)$, nous proposons une nouvelle méthode qui implique la réaction $C(^3P) + NO$. Les espèces atomiques $C(^3P)$, $O(^3P)$ et $N(^2D)$ ont

été suivies directement par VUV-LIF. Mais dans le cas de $C(^1D)$ les transitions électroniques dans la gamme VUV accessible sont très faibles et les cinétiques ont été étudiées par la détection de H ou D. Le chapitre 2 se termine par un bref aperçu des calculs de l'équation maîtresse (Master équation) effectués dans cette thèse pour prédire les constantes de vitesse dans des conditions interstellaires.

Le chapitre 3 porte sur les réactions en phase gazeuse du carbone atomique ($C(^3P)$ et $C(^1D)$) avec plusieurs molécules. Les constantes de vitesse pour neuf réactions neutres-neutres et les rendements en atomes d'hydrogène pour cinq d'entre elles ont été déterminées. Tout d'abord, nous avons étudié la réactivité de $C(^3P) + \text{eau}$ et l'eau deutérée pour déterminer le mécanisme de cette réaction caractérisé par la formation d'un complexe de van der Waals ($C \dots H_2O$) avant la présence d'une barrière. Classiquement, seules les molécules ayant une énergie supérieure à la barrière peuvent réagir. Mais si l'on tient compte des effets de la mécanique quantique, la réaction est possible même pour les énergies inférieures à la barrière par effet tunnel. Les constantes de vitesse pour les deux systèmes augmentent en dessous de 100 K avec une augmentation plus importante dans le cas de la réaction $C(^3P) + H_2O$, un résultat attendu en raison de la plus faible efficacité de l'effet tunnel pour le deutérium. Nous avons également déterminé la production de H et D à 52 K. Ces productions en atomes H et D suggèrent qu'une grande partie du complexe est stabilisée en collision avec le gaz porteur et ne provoque pas de réaction. Des calculs statistiques en utilisant le programme MESMER (Master Equation Solver for Multi-Energy Well Reactions) ont été effectués pour expliquer le mécanisme de réaction et extrapoler nos résultats aux basses températures et pressions qui caractérisent le milieu interstellaire, la constante de vitesse réactive étant égale $2 \times 10^{-10} \text{ cm}^3 \text{ s}^{-1}$ à 10 K et à basse pression. Cette constante de vitesse élevée permet d'expliquer l'abondance de l'eau dans les nuages interstellaires denses.

Dans le chapitre 3, les réactions du carbone atomique dans son premier état excité (1D) avec CH_4 , C_2H_6 , HD, CO_2 , NO et O_2 ont aussi été étudiées. Pour $C(^1D) + CH_4$, nous avons mesuré des constantes de vitesse du second ordre qui présentent une dépendance négative à la température. Ce comportement s'explique par l'influence d'effets non-adiabatiques tels que le passage intersystème de la surface singulet à la surface triplet ouvrant une nouvelle voie de réaction et produisant une augmentation de la constante de vitesse du second ordre lorsque la température diminue. Dans le cas de $C(^1D) + C_2H_6$, nous avons déterminé des constantes de vitesse de second ordre, dans toute la plage de température, constantes de vitesse compatibles avec une réaction dominée par les forces à longue portée avec un taux donné par la théorie de capture. Pour ces deux réactions, nous avons déterminé les rendements de production de l'atome H dans le but d'expliquer les mécanismes de ces réactions. Nous avons obtenu des rendements en atomes H légèrement supérieurs à un, ce qui suggère que plus d'un atome

H est produit pour ces réactions, un résultat qui pourrait s'expliquer par la dissociation de certains produits obtenus dans ces réactions. Les constantes de vitesse du second ordre pour la réaction $C(^1D) + HD$ présentent peu ou pas de dépendance avec la température dans la plage 50 - 296 K. Nous avons également déterminé le rapport de branchement CD/CH , qui fournit des informations précieuses pour sonder la dynamique de cette réaction en encourageant de nouvelles études théoriques. La réaction de $C(^1D) + CO_2$ présente une dépendance négative à la température et le résultat le plus probable est la formation de produits $CO(^1\Sigma^+) + CO(^1\Sigma^+)$. Les réactions de $C(^1D) + NO$ et O_2 représentent un cas particulier dans ce travail car $C(^1D)$ ne peut être suivi directement et ces réactions ne produisent pas d'atomes H. Pour étudier la cinétique, nous avons utilisé une méthode de traçage chimique dans laquelle nous ajoutons une petite quantité fixe de H_2 au système pour produire des atomes H par la réaction $C(^1D) + H_2$. Comme les constantes de vitesse du deuxième ordre ont été déterminées indirectement, nous devons vérifier l'influence des réactions secondaires menant à la production d'atomes d'hydrogène qui pourraient affecter notre détermination des constantes de vitesse du deuxième ordre pour la réaction primaire. Des études expérimentales supplémentaires ont été réalisées pour vérifier l'influence de ces réactions secondaires en utilisant différentes concentrations de H_2 dans le cas de $C(^1D) + NO$. Pour $C(^1D) + O_2$, nous utilisons du CH_4 comme traceur chimique pour éliminer le radical CH hautement réactif du réacteur et aussi parce que le $O(^1D)$ formé comme produit dans cette réaction réagit avec le H_2 pour produire 100 % des atomes d'hydrogène et réagit avec le CH_4 pour ne produire que 20% des atomes d'hydrogène. Les résultats de ces expériences supplémentaires suggèrent que les réactions secondaires n'ont qu'une influence mineure sur notre détermination des constantes de vitesse de second ordre pour les processus primaires. Par ailleurs, nous avons également réalisé des simulations numériques où la contribution de toutes les réactions probables a été prise en compte. Enfin, la dépendance négative de la température observée pour les réactions $C(^1D) + NO$ a été expliquée à la lumière des états d'orbite de spin car si cette réaction se produit adiabatiquement à partir d'états d'orbite de spin spécifiques, il faut s'attendre à une dépendance marquée des constantes de vitesse du second ordre avec la température. Comme $C(^1D)$ est cinq fois plus dégénéré, seules les populations spin-orbit de NO changent avec la température et si la réaction entre $C(^1D)$ et NO dans son état électronique fondamental est l'une des voies préférées, nous devrions voir une augmentation des constantes de vitesse du second ordre lorsque la température diminue. En revanche, pour la réaction $C(^1D) + O_2$, la distribution des populations de $C(^1D)$ et O_2 ne devrait pas changer avec la température et nous ne devrions pas voir de dépendance de la température pour la constante de vitesse du second ordre. Un résultat en plein accord avec les données expérimentales obtenues.

Le chapitre 4 est consacré à la réactivité des atomes d'oxygène dans leur premier état excité (1D) avec plusieurs molécules (C_2H_6 , C_2H_2 , HD et D_2). De plus, le processus de relaxation de $O(^1D)$ par CO_2 et Kr

sont également étudiés. Dans le cas de $O(^1D) + C_2H_6$ et C_2H_2 , les constantes de vitesse du second ordre présentent peu ou pas de dépendance à la température dans la plage de température 50 - 296 K. Ces réactions sont des réactions avec plusieurs voies de sorties dont la production d'atomes d'hydrogène. Pour la réaction $O(^1D) + C_2H_6$, nous avons mesuré une production d'atomes d'hydrogène indépendante de la température et qui se comparent bien aux données expérimentales précédentes à 298 K. Cependant, notre résultat est légèrement supérieur au résultat précédent à température plus élevée. Cette différence pourrait s'expliquer par un changement dans le mécanisme de réaction où, à haute température, on s'attend à ce que le produit thermodynamiquement le plus stable ($CH_3CHOH + H$) se forme facilement tandis qu'à température ambiante et au-dessous, on s'attend à ce que la voie ayant la barrière la plus basse ($C_2H_5O + H$) soit favorisée. Pour $O(^1D) + C_2H_2$, nous n'avons pas pu déterminer les rendements des atomes H en raison de l'influence de la réaction secondaire menant à la production des atomes H. La réaction de $O(^1D) + H_2$ a été largement étudiée dans la littérature en raison de son importance en chimie atmosphérique. Dans cette thèse, nous avons étudié la réactivité des isotopologues D_2 et HD dans le but de clarifier le mécanisme de réaction et de comparer les méthodes théoriques. Les constantes de vitesse de second ordre déterminées pour $O(^1D) + D_2$ ont été comparées à quatre méthodes théoriques conçues pour traiter les réactions de formation complexes et la bonne concordance entre les données expérimentales et théoriques suggère que cette réaction implique un complexe de longue durée dans sa dynamique. Nous avons également déterminé le rapport de branchement isotopique qui relie les deux canaux de sortie pour la réaction $O(^1D) + HD$. Nous obtenons ici des rapports de branchement supérieurs à un, ce qui suggère la formation préférentielle de l'OD + H sur l'OH + D. Un résultat qui pourrait s'expliquer par le fait que l'atome H quitte le complexe formé avec une probabilité plus élevée que les atomes de deutérium étant donné sa masse plus légère et sa vitesse supérieure.

Dans le chapitre 4 nous avons également étudié la relaxation électronique du $O(^1D)$ par CO_2 qui joue un rôle important dans la chimie de Mars. Dans ce cas, la constante de vitesse du second ordre augmente lorsque la température est abaissée à 50 K en raison d'une vitesse de redissociation plus lente de l'intermédiaire 1CO_3 conduisant à une augmentation du passage intersystème vers la surface triplet. De plus, nous avons également étudié la relaxation de $O(^1D)$ par le Krypton car ce gaz rare peut être utilisé comme gaz porteur dans des expériences en laboratoire. Ici, la constante de vitesse du second ordre ne présente pas de dépendance marquée à l'égard de la température dans la plage de température de 50 à 296 K.

Enfin, au chapitre 5, nous avons étudié la réactivité de $N(^2D)$ avec 4 molécules (NO , CH_4 , C_2H_6 , C_3H_8). Malgré l'importance des données cinétiques pour les réactions de $N(^2D)$ avec les hydrocarbures dans

l'atmosphère de Titan, il y a très peu d'expériences rapportées dans la littérature car il est particulièrement difficile de produire photolytiquement $N(^2D)$. Dans cette thèse, nous proposons une nouvelle méthode de production de $N(^2D)$ qui facilitera l'étude de ces réactions à la basse température qui caractérise l'atmosphère de Titan. Cette méthode implique la production de $C(^3P)$ par PLP de CBr_4 , suivi de la réaction chimique de $C(^3P) + NO$ pour obtenir les atomes $N(^2D)$ désirés. Ici, comme le NO est ajouté au réacteur pour produire du $N(^2D)$, c'est la première réaction que nous devons étudier. La constante de vitesse de deuxième ordre pour $N(^2D) + NO$ présente une dépendance négative à la température qui pourrait s'expliquer par la contribution accrue d'autres mécanismes de réaction à basse température, comme le croisement intersystème. A température ambiante, les constantes de vitesse du second ordre pour ces réactions sont en bon accord avec les valeurs précédemment rapportées, ce qui valide notre méthode de production $N(^2D)$. Il est alors possible d'utiliser cette méthode de production pour étudier la réactivité de $N(^2D)$ avec plusieurs hydrocarbures. Pour la réaction de $N(^2D) + CH_4$, C_2H_6 et C_3H_8 , nous avons obtenu des constantes de vitesse de second ordre qui diminuent lorsque la température est abaissée, un résultat qui suggère que ces réactions sont caractérisées par une barrière dans le canal de l'entrée. Par conséquent, les constantes de vitesse du deuxième ordre pour ces trois réactions seront inférieures à ce qui avait été prévu précédemment aux basses températures qui caractérisent l'atmosphère du Titan. Ces résultats représentent une amélioration pour les modèles photochimiques actuels qui, en raison du manque de données, utilisent des constantes de vitesse indépendantes de la température pour la réaction de $N(^2D) + C_2H_6$ et C_3H_8 en extrapolant les valeurs de température ambiante recommandées aux basses températures, ce qui représente une surestimation de l'importance des processus à basse température.

Les études cinétiques réalisées dans le cadre de cette thèse contribuent à une meilleure compréhension de la chimie complexe à l'œuvre dans le milieu interstellaire et dans les atmosphères planétaires, fournissant des données importantes pour que les modèles puissent expliquer les abondances observées de plusieurs molécules. Les constantes de vitesse de la plupart des processus étudiés ici, y compris les atomes dans des états excités, présentent des comportements complexes et, par conséquent, leur influence devrait être testée sur des modèles photochimiques en incluant les canaux de formation et de perte de ces atomes à état excité. La méthode de production d'atomes d'azote dans l'état électronique excité 2D , mise au point dans le cadre de ces travaux, jette les bases d'études futures d'autres réactions clés identifiées dans des modèles photochimiques tels que $N(^2D) +$ acétylène et éthylène.

Dans le but d'identifier et de quantifier les canaux de produits des réactions étudiées, il serait intéressant de coupler l'appareil CRESU à une méthode de détection par spectrométrie de masse ou

par spectroscopie micro-onde à large bande pour détecter les produits possédant un moment dipolaire. Cette dernière méthode spectroscopique est actuellement mise en œuvre dans notre laboratoire dans le cadre du projet OSCAR (Original Submillimeter Chirped Pulsed Instrumentation for Astrochemical Reactivity) qui combinera l'appareil CRESU existant avec un nouveau spectromètre micro-onde à large bande dans le domaine submillimétrique. De plus, le schéma de génération de VUV utilisé dans cette thèse pour détecter les atomes d'hydrogène va permettre d'étudier pour la première fois à basse température plusieurs réactions entre les atomes d'hydrogène ou de soufre et des radicaux tels que NO_2 , OH , CH , NH , NH_2 , et CH_3 . Cette méthode devrait permettre également de déterminer les constantes de vitesse de plusieurs réactions qui pourraient être des mécanismes importants pour l'enrichissement en deutérium dans les atmosphères planétaires et le milieu interstellaire.

Outline of the thesis

This thesis summarizes three years of doctoral work at the Institute des Sciences Moléculaires (ISM) working in the COMEX group (Collisions Moléculaires en Milieux Extrêmes). The facilities of the CRESU (Cinétique de Reaction en Encoulement Supersonique Uniforme) apparatus were employed to study the kinetics of several gas-phase reactions of interest for the astrochemistry community over the 50 – 296 K temperature range. This manuscript is divided as follows:

Chapter 1 provides a background to astrochemistry, the interstellar medium and planetary atmospheres setting the basis of the importance for the kinetics measurements at low temperatures.

Chapter 2 introduces the kinetics of gas-phase reactions and their temperature dependence. Furthermore, the CRESU apparatus and the experimental techniques employed in this work to produce and detect the species of interest are described.

Chapter 3 focuses on the gas-phase reactions of atomic carbon, reporting rate constants for nine neutral-neutral reactions and branching ratios for five of them. In the case of $C(^3P) + \text{water}$ reaction, MESMER (Master Equation Solver for Multi-Energy Well Reactions) calculations were performed to clarify the reaction mechanism and to extrapolate our results to the low temperatures and densities that characterize the interstellar medium.

Chapter 4 is dedicated to the reactions of oxygen in its first excited electronic state (1D). In this case, we studied the kinetics of six neutral-neutral reactions and reported the branching ratios for one of them. For the reaction of $O(^1D)$ with molecular hydrogen and its isotopic variants, the kinetic isotope effect (KIE) and the intramolecular isotopic branching ratio were also analysed.

Chapter 5 is devoted to the chemistry of nitrogen in its first excited electronic state (2D). Here, a new method for the production of $N(^2D)$ atoms is proposed facilitating the study of the reactivity of $N(^2D)$ with several molecules such as hydrocarbons, which represents the basis for the formation of complex molecules in planetary atmospheres.

Contents

1. Introduction	3
1.1. Astrochemistry	3
1.2. Interstellar medium	6
1.3. Reactions at work in the interstellar medium	9
1.4. Planetary Atmospheres	11
1.4.1. The atmosphere of Titan.....	13
1.4.2. The atmosphere of Mars.....	15
1.5. Importance of rate constants and branching ratios in astrochemical models	16
1.6. References	18
2. Reaction kinetics of gas-phase processes at low temperature	23
2.1. The reaction rate	23
2.1.1. Determination of the rate constant.....	24
2.1.2. The temperature dependence of the rate constants	28
2.2. Branching ratios	30
2.2.1. Determination of the branching ratios	31
2.2.2. Correction to the branching ratios.....	33
2.3. Experimental methods to study the kinetics at low temperature	33
2.3.1. Conventional methods.....	33
2.3.2. Expansion based cooling methods.....	34
2.3.2.1. Free jet expansions.....	35
2.4. The CRESU technique	37
2.4.1. Supersonic Flow	37
2.4.2. Nozzle characterization.....	40
2.4.3. Continuous and pulsed CRESUs: The mini continuous CRESU of Bordeaux.....	43

2.4.4.	Strengths and limitations of the CRESU technique	44
2.4.5.	Determination of the concentration in the CRESU apparatus	45
2.4.5.1.	Calibration of the mass flow controllers.....	46
2.5.	Production of the reactive atoms	49
2.6.	Detection methods coupled with the CRESU technique.....	51
2.6.1.	Laser induced fluorescence technique	51
2.7.	Determination of errors	54
2.7.1.	Statistical errors and weighting	54
2.7.2.	Systematic errors	55
2.7.3.	Combination of statistic and systematic errors	56
2.8.	Master equations calculations.....	56
2.9.	References	60
3.	<i>The reactivity of carbon atoms</i>	67
3.1.	Experimental details	68
3.1.1.	Generation of atomic carbon and detection procedures	68
3.1.2.	Temperature range	69
3.1.3.	Experimental details of the ground state carbon atoms + water reaction	69
3.1.4.	Branching ratio procedure	70
3.1.5.	Gases	71
3.2.	The C(³P) + H₂O/D₂O reactions.....	72
3.2.1.	Results.....	74
3.2.1.1.	Rate constants	74
3.2.1.2.	Branching ratios.....	77
3.2.1.3.	MESMER calculations	82
3.2.2.	Discussion	84

3.2.3.	Relevance of the $C(^3P) + H_2O$ reaction in the interstellar medium	85
3.3.	The $C(^1D) + CH_4/C_2H_6$ reactions	87
3.3.1.	Results	89
3.3.1.1.	Rate constants	89
3.3.1.2.	Influence of secondary reactions.....	91
3.3.1.3.	H-atom yields.....	92
3.3.2.	Discussion	93
3.3.2.1.	The $C(^1D) + CH_4$ reaction	93
3.3.2.2.	The $C(^1D) + C_2H_6$ reaction	95
3.4.	The $C(^1D) + CO_2$ reaction	96
3.4.1.	Results.....	97
3.4.2.	Discussion	100
3.5.	The $C(^1D) + HD$ reaction.....	101
3.5.1.	Results.....	101
3.5.1.1.	Rate constants	102
3.5.1.2.	CD/CH branching ratio.....	104
3.5.2.	Discussion	105
3.6.	The $C(^1D)+NO/O_2$ reactions.....	107
3.6.1.	Results.....	108
3.6.1.1.	Rate constants	108
3.6.1.2.	Influence of secondary reactions.....	110
3.6.1.3.	Numerical simulations	112
3.6.2.	Discussion	116
3.7.	Astrochemical implications	118
3.8.	References	119

4.	<i>The Reactivity of Electronically Excited Oxygen Atoms</i>	133
4.1.	Experimental details	133
4.1.1.	Temperature range	133
4.1.2.	Production and detection of electronically excited oxygen atoms	133
4.1.3.	Experimental details of O(¹ D) + Kr reaction	134
4.1.4.	Determination of the branching ratio	135
4.1.5.	Gases	138
4.2.	The O(¹D) + D₂/HD reactions	138
4.2.1.	Results	140
4.2.1.1.	Rate constants	140
4.2.1.2.	Kinetic isotope effect	143
4.2.1.3.	Isotopic branching ratio H/D	144
4.2.2.	Discussion	144
4.2.2.1.	The O(¹ D) + D ₂ reaction	144
4.2.2.2.	The O(¹ D) + HD reaction	146
4.3.	The O(¹D) + C₂H₆/C₂H₂ reaction	146
4.3.1.	Results	148
4.3.1.1.	Rate constants	149
4.3.1.2.	Branching ratios	151
4.3.2.	Discussion	152
4.3.2.1.	The O(¹ D) + C ₂ H ₆ reaction	152
4.3.2.2.	The O(¹ D) + C ₂ H ₂ reaction	153
4.4.	The O(¹D) + CO₂ reaction	154
4.4.1.	Results	156
4.4.2.	Discussion	158
4.5.	The O(¹D) + Kr reaction	159

4.5.1.	Results	160
4.5.2.	Discussion	162
4.6.	Astrochemical implications	163
4.7.	References	164
5.	<i>A viable source of N(²D) atoms for kinetic studies at low temperature</i>	175
5.1.	Introduction	175
5.2.	Experimental details	177
5.2.1.	Temperature range	177
5.2.2.	Production and detection of N(² D) atoms	178
5.2.3.	Influence of secondary reactions	179
5.2.4.	Experimental details of the N(² D) + alkanes reactions.....	179
5.2.5.	Gases.....	180
5.3.	The N(²D) + NO reaction	180
5.3.1.	Results.....	181
5.3.2.	Discussion	184
5.4.	The N(²D) + alkanes (C_nH_{2n+2}) reactions	185
5.4.1.	Results.....	187
5.4.2.	Discussion	192
5.5.	Astrochemical implications	196
5.6.	References	197
	<i>Conclusions and perspectives</i>	203
	<i>Publications</i>	205

List of Abbreviations

CEM	Controlled Evaporation Mixing
CMB	Crossed Molecular Beams
CPM	Channel Photomultiplier
CRESU	Cinétique de Reaction en Ecoulement Supersonique Uniforme
CSEs	Chemically Significant Eigenvalues
ICSS	Integral Cross Sections
IEREs	Internal Energy Relaxation Eigenvalues
ILT	Inverse Laplace Transform
IRC	Intrinsic Reaction Coordinate
ISC	Intersystem Crossing
ISM	Interstellar medium
KIDA	Kinetic Database for Astrochemistry
KIE	Kinetic Isotope Effect
LTE	Local Thermodynamic Equilibrium
MECP	Minimum Energy Crossing Point
MESMER	Master Equation Solver for Multi-Energy Well Reactions
MPPST	Mean Potential Phase Space Theory
PES	Potential Energy Surface
PLP	Pulsed Laser Photolysis

PMT	Photomultiplier Tube
QCT	Quasi-classical Trajectory
QM WP	Quantum Mechanical Wave Packet
QM	Quantum Mechanical
QMT	Quantum Mechanical Tunneling
RPMD	Ring Polymer Molecular Dynamics
RRKM	Rice, Ramsperger, Kassel and Marcus Theory
RWP	Real Wave Packet
SQM	Statistical Quantum Mechanics
TS	Transition State
UDfA	UMIST Database for Astrochemistry
VRC TST	Variable Reaction Coordinate Transition State Theory
VUV LIF	Vacuum Ultraviolet Laser Induced Fluorescence
ZPE	Zero Point Energy

Chapter 1

Introduction

1.1	Astrochemistry	3
1.2	Interstellar medium	6
1.3	Reactions at work in the interstellar medium	9
1.4	Planetary Atmospheres.....	11
1.4.1	The atmosphere of Titan	13
1.4.2	The atmosphere of Mars	15
1.5	Importance of rate constants and branching ratios in astrochemical models	16
1.6	References	18

1. Introduction

1.1. Astrochemistry

For many years, scientists were sceptical about the idea of molecules in interstellar space mainly due to the harsh physical conditions (temperature, pressure and high-energy radiation field). Indeed, under the conditions found close to stars, molecules readily dissociate and ionize.¹ However, in 1940 two radicals, CN and CH were identified in the interstellar medium (ISM) through sharp optical absorption lines (387.46 nm and 430.03 nm) in visible spectra toward bright stars.² Subsequently, in 1941 the CH⁺ cation was detected through an electronic transition around 430 nm.³ From the 1960's onwards many more species were identified, clearly demonstrating that a wide range of molecules can exist in space. These observations effectively gave rise to the field of astrochemistry, as astronomers searched to explain the presence of molecules in interstellar environments.

Astrochemistry is devoted to the study of the chemical process at work in astrophysical environments including the interstellar medium, planetary atmospheres, comets and circumplanetary regions.⁴ This rapidly growing science overlaps three major fields: chemistry, physics and astronomy.⁵ Thus, three kinds of scientific activity are involved. First, it is necessary to identify the species that are present in the different astrochemical environments; a task that is achieved by astronomers with the help of laboratory scientists working to characterize and identify the spectral signatures of individual molecules. Secondly, it is necessary to explain the presence of the observed species through the construction and application of chemical models, which consist of large networks of elementary chemical and physical processes. Lastly, to obtain quantitative information regarding the species observed, theoretical and experimental studies of individual processes are performed to provide better constraints for the chemical models. The main objective of astrochemistry is thus to study the nature and behaviour of the detected species by investigating their formation and destruction processes in various astronomical environments and eventually to make predictions about which other species could be present.⁶

To date, more than 200 molecules have been identified in the interstellar and circumstellar medium (*Table 1.1*). Most of these molecules have been detected due to their spectroscopic signature in the millimetre wave region of the electromagnetic spectrum, where radiative transitions between rotational levels occur. A fundamental requirement for rotational spectroscopy detection is that the molecule must have a permanent electric dipole to allow strong electric-dipole-induced transitions between the rotational levels. The observations can be performed using ground based radio telescopes because the Earth's atmosphere is transparent at these wavelengths. Usually, an array of radio

telescopes is tuned to match a rotational transition (such as the $J = 1 \rightarrow J = 0$ transition at 2.6 mm) in the $^{12}\text{C}^{16}\text{O}$ molecule to find the densely populated regions. Subsequently, spectroscopic measurements are performed by scanning over a range of emission frequencies which are assigned to their respective molecules by comparison with laboratory spectra. Here the $^{12}\text{C}^{16}\text{O}$ molecule is typically used as a tracer of molecular density as it is a moderately strong mm-wave emitter and as CO is the second most abundant molecule in the ISM after H_2 . Unfortunately, this method does not allow the detection of molecules such as N_2 , CO_2 , C_2H_2 and H_2 .¹ In this regard, molecular hydrogen (the most abundant molecule in the ISM) only radiates weakly via forbidden electric quadrupole transitions. Other non-polar molecules such as CO_2 and C_2H_2 can be detected in the infrared range.^{7,8} However, to observe these transitions it is necessary to minimise the effects of IR absorption in the Earth's atmosphere either by performing measurements in situ (such as the Infrared space observatory, ISO), or from observing platforms at high altitude on Earth. Some interstellar molecules such as H_2 , HD, CO and N_2 have been observed through their electronic transitions in the UV with the requirement that these measurements are made in situ due to the opacity of the Earth's atmosphere to UV photons from space.⁹

Many chemically reactive species (free radicals and molecular ions) have been identified in the ISM. These discoveries reflect the low densities and very low temperature conditions of interstellar clouds leading to conditions of non-thermodynamic equilibrium, which allow these chemically reactive species to survive for a long time.¹⁰ Furthermore, the number of detected molecules is indicative of the very rich chemistry within these environments in which the molecules must be formed at rates sufficient to counterbalance their destruction.¹¹

Table 1.1 Molecular species identified in the interstellar and circumstellar medium

2 atoms	H ₂	AlF	AlCl	C ₂	CH	CH ⁺	CN
	CO ⁺	CP	SiC	HCl	KCl	NH	NO
	NaCl	OH	PN	SO	SO ⁺	SiN	SiO
	CS	HF	HD	FeO *	O ₂	CF ⁺	SiH *
	AlO	OH ⁺	CN ⁻	SH ⁺	SH	HCl ⁺	TiO
	CO	NS	SiS	PO	ArH ⁺	N ₂	NO ⁺ *
	NS ⁺						
3 atoms	C ₃	C ₂ H	C ₂ O	C ₂ S	CH ₂	HCN	HCO
	HCS ⁺	HOC ⁺	H ₂ O	H ₂ S	HNC	HNO	MgCN
	N ₂ H ⁺	N ₂ O	NaCN	OCS	SO ₂	c-SiC ₂	CO ₂
	H ₃ ⁺	SiCN	AlNC	SiNC	HCP	CCP	AlOH
	H ₂ Cl ⁺	KCN	FeCN	HO ₂	TiO ₂	C ₂ N	Si ₂ C
	HCO ⁺	MgNC	NH ₂	H ₂ O ⁺	HS ₂	HCS	HSC
	NCO						
4 atoms	c-C ₃ H	l-C ₃ H	C ₃ N	C ₃ O	C ₃ S	C ₂ H ₂	NH ₃
	HCNH ⁺	HNCO	HNCS	HOCO ⁺	H ₂ CO	H ₂ CN	H ₂ CS
	c-SiC ₃	CH ₃	C ₃ N ⁻	PH ₃	HCNO	HOCN	HSCN
	C ₃ H ⁺	HMgNC	HCCO	CNCN	HCCN	H ₃ O ⁺	H ₂ O ₂
5 atoms	C ₅	C ₄ H	C ₄ Si	l-C ₃ H ₂	c-C ₃ H ₂	H ₂ CCN	CH ₄
	HC ₂ NC	HCOOH	H ₂ CNH	H ₂ C ₂ O	H ₂ NCN	HNC ₃	SiH ₄
	C ₄ H ⁻	HC(O)CN	HNCNH	CH ₃ O	NH ₄ ⁺	H ₂ NCO ⁺	NCCNH ⁺
6 atoms	C ₅ H	l-H ₂ C ₄	C ₂ H ₄	CH ₃ CN	CH ₃ NC	CH ₃ OH	CH ₃ SH
	HC ₂ CHO	NH ₂ CHO	C ₅ N	l-HC ₄ H	l-HC ₄ N	c-H ₂ C ₃ O	H ₂ CCNH *
	HNCHCN	SiH ₃ CN	C ₅ S	HC ₃ N	H ₂ COH ⁺	CH ₃ Cl	HC ₃ NH ⁺
	C ₅ N ⁻						
7 atoms	C ₆ H	CH ₂ CHCN	CH ₃ C ₂ H	HC ₅ N	CH ₃ CHO	CH ₃ NH ₂	c-C ₂ H ₄ O
	C ₆ H ⁻	CH ₃ NCO	HC ₅ O	H ₂ CCHOH			
8 atoms	CH ₃ C ₃ N	HC(O)OCH ₃	CH ₃ COOH	C ₇ H	C ₆ H ₂	CH ₂ OHCHO	l-HC ₆ H
	CH ₂ CCHCN	H ₂ NCH ₂ CN	CH ₃ CHNH	CH ₃ SiH ₃	CH ₂ CHCHO		
9 atoms	CH ₃ C ₄ H	CH ₃ CH ₂ CN	(CH ₃) ₂ O	CH ₃ CH ₂ OH	HC ₇ N	C ₈ H	CH ₃ C(O)NH ₂
	C ₃ H ₆	CH ₃ CH ₂ SH	CH ₃ NHCHO *	HC ₇ O	C ₈ H ⁻		
10 atoms	CH ₃ C ₅ N	(CH ₃) ₂ CO	(CH ₂ OH) ₂	CH ₃ CH ₂ CHO	CH ₃ CHCH ₂ O	CH ₃ OCH ₂ OH	
11 atoms	HC ₉ N	CH ₃ C ₆ H	C ₂ H ₅ OCHO	CH ₃ OC(O)CH ₃			
12 atoms	c-C ₆ H ₆	n-C ₃ H ₇ CN	i-C ₃ H ₇ CN	C ₂ H ₅ OCH ₃ *			
>12 atoms	C ₆₀	C ₇₀	C ₆₀ ⁺	c-C ₆ H ₅ CN			

Source <http://www.astro.uni-koeln.de/cdms/molecules>. *Tentative detections, which have a reasonable chance to be correct.

1.2. Interstellar medium

The interstellar medium is the region in space between the stars containing a tenuous mixture of gas and dust. By mass, it is composed of approximately 99% gas and 1% of dust grains,¹² where hydrogen (around 90%) and helium (around 10%) are by far the most abundant gaseous species. Other heavier atoms such as carbon, oxygen and nitrogen are also present, although their abundances are approximately four orders of magnitude lower than that of hydrogen (*Table 1.2*).

Table 1.2 Typical abundance of the elements in the interstellar medium with respect to atomic hydrogen. Extracted from Dishoeck.¹³

Element (X)	Abundance (X/H)
H	1.0
He	0.085
C	2.7×10^{-4}
O	4.9×10^{-4}
N	6.8×10^{-5}
Mg	4×10^{-5}
Si	3.2×10^{-5}
S	1.3×10^{-5}
Fe	3.2×10^{-5}

The ISM is extremely heterogeneous and can be divided into four kinds of interstellar clouds depending on their physical and chemical properties.

- ✓ Diffuse atomic clouds are fully exposed to the interstellar radiation field and nearly all molecules are photodissociated. These clouds are composed mainly of atomic hydrogen and ionic species with a molecular fraction in the range 0.0 - 0.1 compared to the number of hydrogen nuclei. The low density ($10 - 100 \text{ cm}^{-3}$) and the average time between collisions, which is measured in decades, implies that very little chemistry occurs in these regions. Diffuse atomic clouds typically have temperatures that range from 30 – 100 K.^{11,14}
- ✓ Diffuse molecular clouds have a radiation field that is sufficiently attenuated so that the molecular populations and the molecular hydrogen fraction lies between 0.1 and 0.5. However, enough interstellar radiation is still present to photoionize atomic carbon or photodissociate CO molecules. Molecular hydrogen is abundant allowing a much richer

chemistry than in diffuse atomic clouds. Diffuse molecular clouds typically have densities about $100 - 500 \text{ cm}^{-3}$ and temperature that range from $30 - 100 \text{ K}$.

- ✓ Translucent clouds have sufficient protection from interstellar radiation. Consequently, molecular populations and the molecular hydrogen fraction increases to nearly 1. Carbon exists as the ionized or neutral atomic form with the CO fraction beginning to rise. Here, the chemistry is quite different from diffuse clouds due to the presence of the highly reactive neutral carbon atoms and the decreasing electron fraction. The densities range between $500 - 5000 \text{ cm}^{-3}$ and the temperatures between $15 - 50 \text{ K}$.
- ✓ Dense molecular clouds (*Figure 1.1*) are molecular in nature and are considered to be the birthplaces of new stars. In terms of molecular content, they are composed of H_2 followed by CO with an abundance of 10^{-4} with respect to H_2 . Other minor species such as OH, CH, CN and water typically represent only 10^{-7} of the abundance of H_2 . Molecular clouds are shielded from external UV irradiation by interstellar dust particles that efficiently absorb UV and visible radiation. However, they are still exposed to cosmic rays whose interaction with hydrogen produces secondary UV photons and electrons ionizing the cloud gas. There, the average time between collisions is reduced to a few hours. Typical densities are at least 10^4 cm^{-3} and the temperatures range between $10 - 50 \text{ K}$.¹⁴

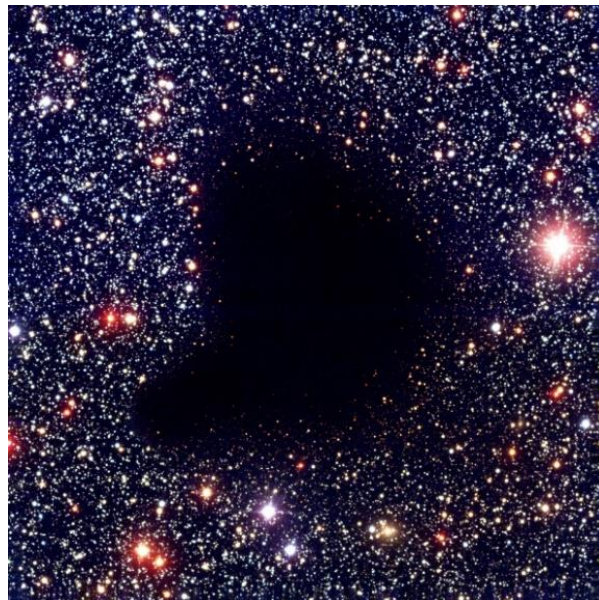


*Figure 1.1 Dense molecular cloud Barnard 68. Image credit: European Southern Observatory (ESO).
Extracted from https://en.wikipedia.org/wiki/Molecular_cloud*

The main factors that determine the physical and chemical conditions in the four types of interstellar clouds are listed in *Table 1.3*.

Table 1.3 Classification of Interstellar clouds types. Extracted from Snow and Bierbaum.¹⁴

Property	Cloud type				
	Diffuse atomic	Diffuse molecular	Translucent	Dense molecular	
				Cold cores	Hot cores
Defining characteristic	$f_{\text{H}_2}^n < 0.1$	$f_{\text{H}_2}^n > 0.1$	$f_{\text{CO}}^n < 0.9$	$f_{\text{CO}}^n < 0.9$	$f_{\text{CO}}^n > 0.9$
A_V	0 - ~0.2	~0.2 - 1	~1 - 5	~5 - >10	>50
Typical n_{H} (cm^{-3})	10 - 100	100 - 500	500 - 5000	$10^4 - 10^6$	$>10^6$
Typical T(K)	30 - 150	30 - 100	15 - 50	10 - 50	>100
Observational techniques	UV/visible absorption, H-atoms radio emission	UV/visible/IR/radio absorption	UV/visible/IR/radio absorption, radio emission	IR absorption, radio emission	IR absorption, radio emission

Abbreviations: $f_{\text{H}_2}^n$ is the fraction of hydrogen nuclei contained in the form of H_2 , i.e., $f_{\text{H}_2}^n = 2n(\text{H}_2)/[n(\text{H}) + 2n(\text{H}_2)]$, where n symbolizes the number density. $f_{\text{C}^+}^n$ and f_{CO}^n are the fractions of carbon present in these different forms. A_V is the visual extinction parameter; a logarithmic value expressed in units of stellar magnitudes, and refers to extinction of visible wavelengths. n_{H} is the number density of hydrogen nuclei.

Solid dust grains, which represent 1% of the interstellar medium composition, play an important role in controlling the physics and chemistry. Grains are thought to consist of a core of carbonaceous material and/or silicates, on top of which layers of material are added (*Figure 1.2*). The grains have diameters of 10 – 500 nm and are capable of absorbing and scattering the UV, visible and to some extent the IR radiation thereby controlling the attenuation of the light passing through interstellar clouds. The surface of the dust grains facilitates some chemical reactions such as the association of H-atoms to form H_2 , a process that is very inefficient in the gas-phase. Atoms and molecules from the gas-phase accumulate on the surface of dust grains in the form of ices.¹² These icy grain mantles are thought to be the starting point of complex organic formation in the ISM and represent the main reservoir of volatiles.

Although the ice mantle composition can vary substantially between different clouds, in general, the most abundant atoms in the gas-phase H, O, C and N accrete onto grains forming water, methane and ammonia by hydrogenation. Consequently, water ice is the most abundant ice constituent, followed by CO and CO_2 at ~ 20 – 30% each with respect to water (CO being formed in the gas-phase and then stick on grain). Additionally CH_4 , NH_3 and CH_3OH are found with typical abundances of 5%, although

methanol can be notably more abundant. The ices are not perfectly mixed, they are supposed to have at least two different phases: a water-rich phase (containing H_2O , CH_4 , NH_3 and CO_2) and a water-poor phase (rich in CO , CO_2 and CH_3OH) arising from the different stages of their formation in which atom hydrogenation initially occurs followed by subsequent reactions involving CO .

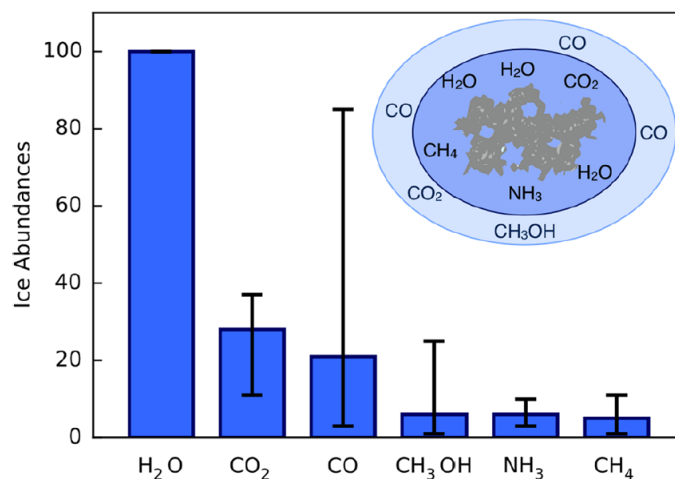


Figure 1.2 Median composition of interstellar ices grain mantles (bars) normalized to the most abundant ices species, water. Extracted from Oberg.¹²

A very rich chemistry can also be found in circumstellar envelopes where mixtures of dust and molecules are expelled from stars at high velocity. These envelopes are created by extensive mass loss in the later stages of stellar evolution, caused by thermal pulses in the star interior and radiation pressure on dust. For example, in the circumstellar envelope of the carbon-rich star IRC+10216, exotic species such as C_8H , C_3S , SiC_3 have been found. The chemistry in this envelope is dominated by molecules containing long carbon chains, silicon and metals such as magnesium, sodium and aluminium, which make it quite different to what is found in molecular clouds.¹⁵

In conclusion, the interstellar medium provides a unique environment in which chemistry occurs under extreme conditions. The study of these chemical processes by means of chemical modelling, theoretical calculations or laboratory experiments is fundamental to understand the chemical evolution of these regions and to explain the observed abundances of interstellar species.

1.3. Reactions at work in the interstellar medium

Interstellar clouds are characterized by temperatures in the range of 10 - 150 K and densities from $10 - 10^7 \text{ cm}^{-3}$. Under these conditions, chemical reactions are subject to some constraints. For example, three body reactions are almost negligible due to the low densities. Endothermic reactions do not proceed because they require an external energy input that cannot be supplied by the low

temperatures of the interstellar medium. Even for exothermic processes, many of this type of reaction do not occur at low temperature due to the presence of an activation barrier, except if tunnelling through the barrier plays a role. The main gas-phase reactions at work in the ISM are summarized in *Table 1.4*.

Table 1.4 Gas-phase reactions in the ISM

Photochemical reactions	Photodissociation	$AB + h\nu \rightarrow A + B$
	Photoionization	$A + h\nu \rightarrow A^+ + e$
Electronic Recombination	Radiative recombination	$A^+ + e \rightarrow A + h\nu$
	Dissociative recombination	$AB^+ + e \rightarrow A + B$
Ion-molecule reactions	Charge transfer	$A^+ + B \rightarrow A + B^+$
	Radiative association	$A^+ + B \rightarrow AB^+ + h\nu$
	Exchange reaction	$AB^+ + C \rightarrow A^+ + BC$
Neutral-neutral Reactions	Exchange reaction	$A + BC \rightarrow AB + C$
	Radiative association	$A + B \rightarrow AB + h\nu$
	Reactions between neutrals	$A + B \rightarrow C + D$
Other Reactions	Positive ion-negative ion reaction	$A^+ + B^- \rightarrow AB + h\nu$
	Neutral-negative ion reaction	$A^- + B \rightarrow AB + e$
	Electronic attachment	$A + e \rightarrow A^- + h\nu$
		$AB + e \rightarrow A^- + B$

Generally, bimolecular reactions between ions and molecules proceed quickly as they do not have an activation barrier to products owing to strong attractive forces.^{14,16} These reactions contribute to the formation of complex ions and molecules in the ISM and have been extensively studied because it was believed for many years that they should dominate the chemistry of the ISM. In contrast, bimolecular reactions between neutral species were mostly ignored as it was thought that these processes were almost always characterized by an activation barrier along the reaction pathway. However, studies of neutral-neutral reactions such as the $CN + O_2$ reaction¹⁷ revealed that the reactivity could be efficient at temperatures lower than 100 K, changing the previous beliefs. Neutral-neutral reactions are very important processes, sometimes dominant, in regions of the interstellar medium where the ions are

less abundant, such as dense molecular clouds. Nowadays, although a large number of neutral-neutral reactions have been studied at the low temperatures of the ISM (approximately 150 reactions¹⁸), the rate constants for many other potentially important processes remain unknown.

1.4. Planetary Atmospheres

In our solar system, all the planets share a common origin of about 4.6 billion years ago. Their formation is thought to have started in the interstellar medium with the collapse of a dense molecular cloud core. During this collapse, a disk and an outflow are formed which mediate the transport of angular momentum. Once the collapse has proceeded far enough for the core to heat up, a protostar is formed. The remaining cloud envelope accretes onto the star or disperses, leaving a pre-main sequence star with a disk which is the formation site of planets.¹² The different phases of star and planet formation are shown in *Figure 1.3*.

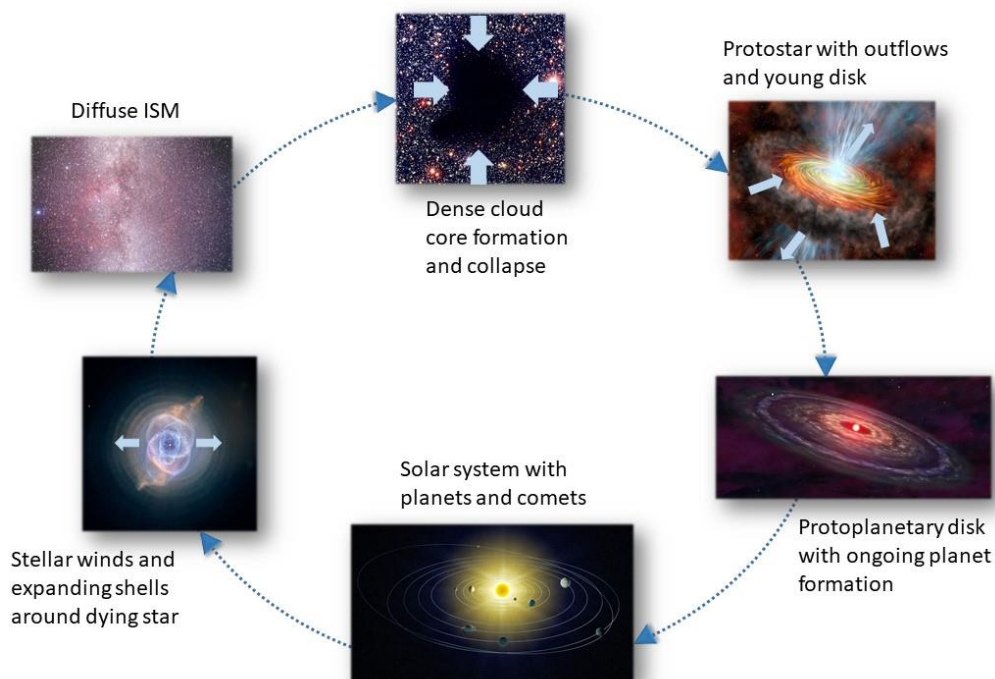


Figure 1.3 Different phases of star and planet formation for an isolated Solar-type star. Modified from Oberg.¹²

In our solar system, the planets fall in two groups, four small, rocky inner planets (Mercury, Venus, Earth and Mars) and four large gaseous outer planets (Jupiter, Saturn, Uranus and Neptune). Venus, Earth and Mars are characterized by substantial atmospheres and high photon flux conditions that create a suitable environment for the formation of reactive atoms and molecules in their ground and excited electronic states. The four giant planets Jupiter, Saturn, Uranus and Neptune have deep gaseous atmospheres because they were formed far from the Sun.¹⁹ The planets have natural satellites

(moons) that orbit around them. Among them, Titan, the largest moon of Saturn has attracted considerable attention because it is the only known satellite to have a thick atmosphere (thicker than Earth's) where the main component is nitrogen. As this is thought to be "similar" to the composition of the prebiotic Earth's atmosphere, the study of the chemistry of Titan's atmosphere could provide some important insights into the evolution of the early Earth.

Planetary atmospheres can be considered as huge photochemical reactors where very rich chemistry occurs given the abundance of the species and the bombardment by UV photons and other energetic particles. In these atmospheres, the importance of many chemical processes is dependent on altitude. For example, at high altitude, where the atmospheric species are exposed to high intensity energetic radiation, ionization readily occurs, so that the chemistry at high altitudes is largely driven by ions and electrons. At lower altitudes where the atmospheric species are shielded from the external radiation field, the chemistry is mostly driven by reactions between neutral species.

Over the years, these complex environments have attracted the attention of many scientists using Earth-based observatories, several space missions and other observational facilities (*Table 1.5* and *Table 1.6*) to measure and detect the physical conditions and species present in these atmospheres.

Table 1.5 Observational facilities

SST	Spitzer Space Telescope	mid and far-infrared wavelengths
JWST	James Webb Space Telescope	mid-infrared
HSO	Herschel Space Observatory	mid and far-infrared wavelengths
ALMA	Atacama Large Millimetre/submillimetre Array	millimetre/submillimetre wavelengths
SOFIA	Stratospheric Observatory for Infrared Astronomy	infrared wavelengths

Table 1.6 List of some space missions and their success.
https://en.wikipedia.org/wiki/Timeline_of_space_exploration

Mission name/year	Planet/Satellite	Mission Success
Venus Express (2011)	Venus	Detection of a layer of O ₃ in the upper atmosphere
Messenger (2011)	Mercury	First orbiter + water detection in the exosphere
Apollo 8 (1968)	Moon (Earth)	First piloted orbital mission
Mariner 9 (1971)	Mars	First spacecraft to orbit another planet
Pioneer 11 (1979)	Saturn/Titan	First Saturn flyby + first photograph of Titan
Galileo (1995)	Jupiter	First Jupiter orbiter
Voyager 1 & 2 (1977-present)	Outer solar system	Data and photographs of the four giant planets and their moons
Mars Express (2004)	Mars	Detection of CH ₄ , NH ₃
Maven (2014)	Mars	Confirmation that solar winds strip H-atoms from Mars's atmosphere
Cassini-Huygens (2005)	Saturn	First Saturn Orbiter
Cassini-Huygens (2005)	Titan	First landing on a moon other than our own

As the focus of this manuscript is the experimental study of the chemical reactions at work in the atmospheres of Titan and Mars, more details regarding their atmospheric composition and main conditions are given in the next section.

1.4.1. The atmosphere of Titan

Titan is the largest moon of Saturn, the sixth planet from the Sun. It was first discovered in 1655 by Christiaan Huygens²⁰ but very little was known about its atmosphere until the Voyager encounters (1977 - 1989). This satellite is the only solar system body that has a dense atmosphere mainly composed of N₂, CH₄, H₂ and other trace compounds (*Figure 1.4*). N₂ is the main constituent of the atmosphere followed by CH₄ with a fractional composition of approximately 2.0 to 5.0%.²¹

Space missions like Voyager (1977) and Cassini (1997) confirmed the presence of other larger hydrocarbons and trace species such as ethane. In this regard, it is thought that solar UV photons dissociate N₂ and CH₄ at high altitudes creating radicals such as N(⁴S), N(²D), CH₃, CH₂, C₂H giving rise to a very complex chemistry (*Figure 1.5*). In general, Titan's chemistry is driven by the interactions among hydrocarbons, nitrogen and even oxygen-containing species.

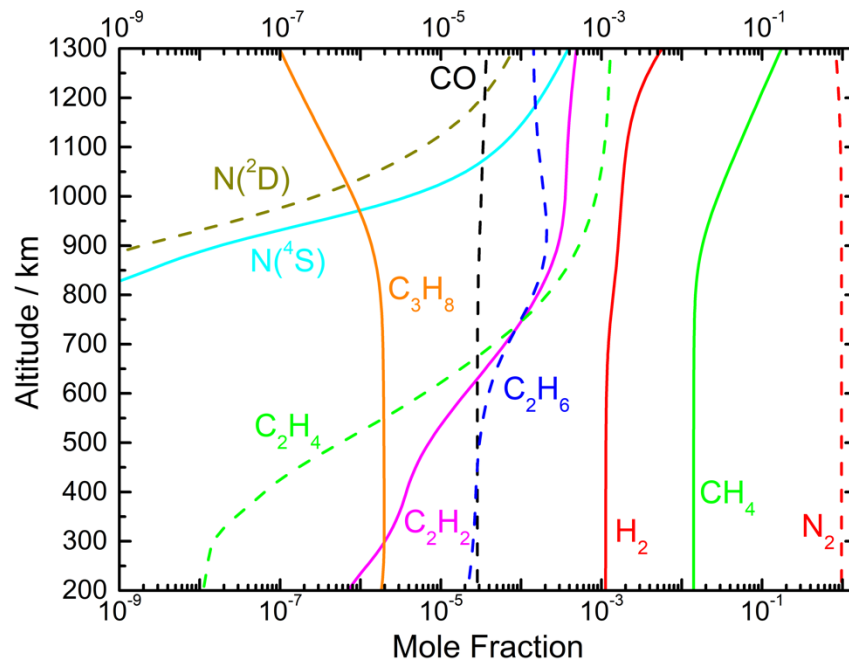


Figure 1.4 Mole fraction of the principal constituents of Titan's atmosphere. Calculated mole fractions from the model of Dobrijevic et al.²²

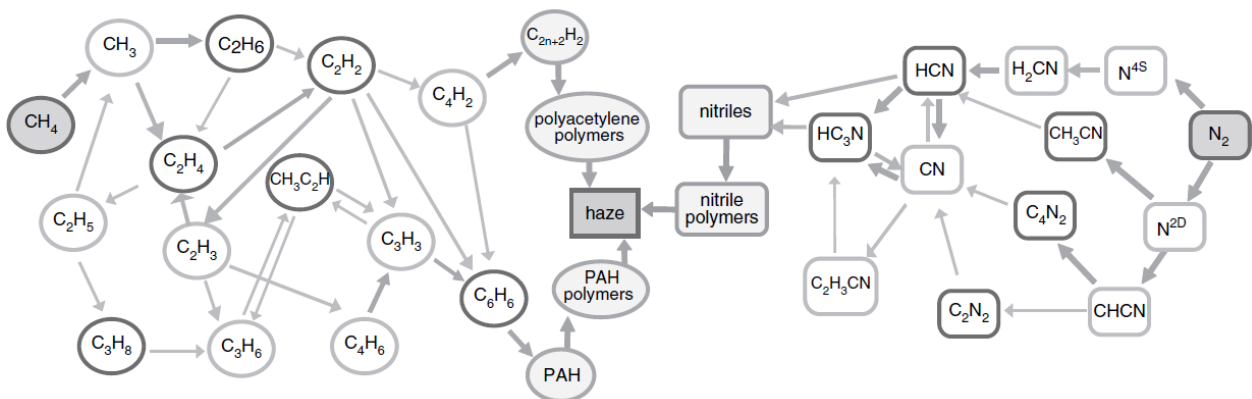


Figure 1.5 Schematic of the photochemistry of N_2 and CH_4 in Titan's atmosphere. Extracted from Strobel et al.²³

An opaque global layer of orange-coloured aerosols obscures Titan. This orange haze resides primarily between 50 and 200 km and is thought to be produced from photolytic and catalytic destruction of CH_4 and N_2 , which leads to various chemical processes at different atmospheric levels. This haze plays an important role in the atmospheric radiative balance, affecting the temperature structure and shielding the surface from harmful radiation.^{23,24}

The atmosphere of Titan exhibits temperatures from 70 K near the surface (in the tropopause) to 200 K in the mesopause. In addition to being cold, Titan's atmosphere is also dense with a surface pressure of 1.5 bar; conditions that facilitate frequent collisions. As the physical conditions present in Titan's

atmosphere are quite challenging to reproduce experimentally only a few reactions of potential importance have been characterized at the appropriate temperatures.

1.4.2. The atmosphere of Mars

Mars is the fourth planet from the Sun. Its atmosphere is thin and relatively transparent to sunlight with a total atmospheric pressure of 6 mbar. As the mean solar flux received by Mars is about half of the solar flux received by Earth, it is a colder planet with temperatures ranging between 90 and 250 K.^{19,25} The composition of the Martian atmosphere (*Table 1.7*) was determined in the mid-1970s by the Viking landers with CO₂ as the main constituent followed by nitrogen, argon, oxygen, carbon monoxide and a trace amount of water vapour.

The photodissociation of the major constituent, CO₂, below 205 nm produces CO and atomic oxygen, where the oxygen atoms are produced in the ground electronic state, O(³P), near the threshold but at shorter wavelengths the atoms are also produced in excited states O(¹D) and O(¹S). Although the primary fate of the excited states is quenching to the ground state by collisions with CO₂, a small fraction of the excited state atoms react with other constituents.

The chemical environment of Mars is sensitively controlled by trace constituents that can act as a catalyst for important chemical cycles.²⁵ For example, Mars photochemistry is regulated by the photolysis of water vapour producing odd-hydrogen radicals H, OH and HO₂, which are used as a catalyst in the recombination of CO and oxygen to form back CO₂ and in the formation of the O-O bond leading to O₂ and O₃. As the catalytic species (H, OH and HO₂) are not consumed in the previous chemical pathways their ultimate fate is to form H₂O (+ O₂) through the recombination of OH and HO₂ radicals.²⁶

Table 1.7 Chemical composition of Mars' atmosphere. Extracted from *Photochemistry of Planetary atmospheres*²⁵.

Species	Abundance
CO ₂	0.9532
N ₂	0.027
⁴⁰ Ar	0.016
O ₂	1.3 x 10 ⁻³
CO	7.0 x 10 ⁻⁴
H ₂ O	3.0 x 10 ⁻⁴
³⁶ Ar + ³⁸ Ar	5.3 x 10 ⁻⁶
Ne	2.5 x 10 ⁻⁶
Kr	3.0 x 10 ⁻⁷
Xe	8.0 x 10 ⁻⁸
O ₃	3.0 x 10 ⁻⁸

1.5. Importance of rate constants and branching ratios in astrochemical models

Astrochemical models are virtual laboratories that consist of thousands of reactions. They aim at computing the chemical evolution of astrochemical environments such as planetary atmospheres, and the interstellar medium. Their general purpose is to make predictions of the abundance for the various chemical species with the goal to reproduce the reported observational data to the best extent possible. If the latter is accomplished by the model, the proposed reaction schemes are validated and then it is possible to predict abundances for the species that have not been detected yet or cannot be directly observed.

Although in the literature there are astrochemical models with various degrees of sophistication (1D, 2D, 3D),²⁷ in general they share some common features:²⁸

- ✓ a set of starting conditions such as total density, temperature, optical depth, etc.
- ✓ a series of chemical reactions characterized by their respective temperature-dependent rate constants and their likely exit channels.

Therefore, the main differences in the predictions of the models arise from:

- ✓ the number of chemical species
- ✓ the number of reactions considered

- ✓ the estimation of the rate constant values
- ✓ the mathematical procedure to solve the system of kinetic equations.

Chemical models are continuously improved via comparisons with observations, and by incorporating the results of laboratory experiments and theoretical studies in which individual processes are investigated. Current reaction networks used in astrochemical models contain more than 4000 gas-phase reactions for more than 400 atomic and molecular species including neutral, positively and negatively charged species.²⁹ However, most of these reactions have not been studied under the conditions of the cold ISM or planetary atmospheres so that their rate coefficients can be quite uncertain if not completely wrong.³⁰ For example, in photochemical models of Titan's atmosphere, less than 10% of the rate constants have been measured in the relevant temperature range. Consequently, these models are based mostly on low temperature extrapolations, which can often be inappropriate at low temperatures.³¹

Global sensitivity analyses and uncertainty propagation studies used in conjunction with the model predictions allow to identify which reaction rate constants are the most important model parameters. Furthermore it is possible to predict which species abundances are strongly sensitive to their uncertainties.^{32,33} Then to improve the current model predictions, these *key reactions* responsible for the large uncertainties on the abundances are those that should be studied in more detail by laboratory experiments and/or theoretical methods to provide the rate constants and branching ratios with better precision.

1.6. References

- (1) Smith, I. W. M. Reactions at Very Low Temperatures: Gas Kinetics at a New Frontier. *Angew. Chemie - Int. Ed.* **2006**, *45*, 2842–2861.
- (2) Adams, W. S. Some Results with the COUDÉ Spectrograph of the Mount Wilson Observatory. *Astrophys. J.* **1941**, *93*, 11–23.
- (3) Douglas, A.; Herzberg, G. CH⁺ in Interstellar Space and in the Laboratory. *Astrophys. J.* **1941**, *94*, 381–381.
- (4) Munoz-Caro, G.; Escribano, R. *Laboratory Astrophysics*, Astrophysi.; 2018; Vol. 451.
- (5) Smith, I. W. M. Laboratory Astrochemistry: Gas-Phase Processes. *Annu. Rev. Astron. Astrophys.* **2011**, *49*, 29–66.
- (6) Woon DE. The Astrochymist <http://www.astrochymist.org/> (accessed Dec 5, 2018).
- (7) D’Hendecourt, L. B.; Jourdain de Muizon, M. The Discovery of Interstellar Carbon Dioxide. *Astron. Astrophys.* **1989**, *223*, L5–L8.
- (8) Lacy, J. H.; Evans, N. J.; Achtermann, J. M.; Bruce, D. E. Discovery of Interstellar Acetilene. *Astrophys. J.* **1989**, *342*, L43–L46.
- (9) Snow, T. P. Ultraviolet Observations of Interstellar Molecules. *Proc. Int. Astron. Union* **2005**, *231*, 175–186.
- (10) Yamamoto, S. *Introduction to Astrochemistry*; Springer Nature, 2017.
- (11) Snow, T. P.; McCall, B. J. Diffuse Atomic and Molecular Clouds. *Annu. Rev. Astron. Astrophys.* **2006**, *44*, 367–414.
- (12) Öberg, K. I. Photochemistry and Astrochemistry: Photochemical Pathways to Interstellar Complex Organic Molecules. *Chem. Rev.* **2016**, *116*, 9631–9663.
- (13) Van Dishoeck, E. F. Astrochemistry of Dust, Ice and Gas: Introduction and Overview. *Faraday Discuss.* **2014**, *168*, 9–47.
- (14) Snow, T. P.; Bierbaum, V. M. Ion Chemistry in the Interstellar Medium. *Proc. Int. Astron. Union*

- 2008**, *1*, 229–259.
- (15) Ziurys, L. M. The Chemistry in Circumstellar Envelopes of Evolved Stars: Following the Origin of the Elements to the Origin of Life. *Proc. Natl. Acad. Sci.* **2006**, *103*, 12274–12279.
- (16) Fournier, M.; Picard, S. D. L. E.; Sims, I. R. Low-temperature Chemistry in Uniform Supersonic Flows. In *Cold Chemistry Molecular Scattering and Reactivity Near Absolute Zero*; Dulieu, O., Osterwalder, A., Eds.; The Royal Society of Chemistry, 2018; pp 1–42.
- (17) Sims, I. R.; Smith, I. W. M. Rate Constants for the Radical-Radical Reactions between CN and O₂ at Temperatures down to 99 K. *Chem. Phys. Lett.* **1988**, *151*, 481–484.
- (18) Potapov, A.; Canosa, A.; Jiménez, E.; Rowe, B. Uniform Supersonic Chemical Reactors: 30 Years of Astrochemical History and Future Challenges. *Angew. Chemie - Int. Ed.* **2017**, *56*, 8618–8640.
- (19) Taylor, F. W. Review Planetary Atmospheres. *Meteorol. Appl* **2010**, *17*, 393–403.
- (20) Showman, A. P. Planetary Atmospheres/ Jupiter and the Outer Planets. *Encycl. Atmos. Sci.* **2003**, 1730–1745.
- (21) Kammer, J. A.; Shemansky, D. E.; Zhang, X.; Yung, Y. L. Composition of Titan's Upper Atmosphere from Cassini UVIS EUV Stellar Occultations. *Planet. Space Sci.* **2013**, *88*, 86–92.
- (22) Dobrijevic, M.; Hébrard, E.; Hickson, K. M. Coupling of Oxygen, Nitrogen, and Hydrocarbon Species in the Photochemistry of Titan's Atmosphere. *Icarus* **2014**, *228*, 324–346.
- (23) Strobel, D. F.; Atreya, S. K.; Bézard, B.; Ferri, F.; Flasar, F. M.; Fulchignoni, M.; Lellouch, E.; Müller-Wodarg, I. Atmospheric Structure and Composition. In *Titan from Cassini-Huygens*; Al., R. H. B. et, Ed.; 2010; pp 235–257.
- (24) *Titan from Cassini-Huygens*; Brown, R. H., Lebreton, J.-P., Waite, J.-H., Eds.; 2010.
- (25) Yung, Y. L.; DeMore, W. B. *Photochemistry of Planetary Atmospheres*, Oxford Uni.; New York, 1999.
- (26) Krasnopolsky, V. A. Photochemistry of the Martian Atmosphere : Seasonal , Latitudinal , and Diurnal Variations. *Icarus* **2006**, *185*, 153–170.
- (27) Dobrijevic, M.; Loison, J. C.; Hickson, K. M.; Gronoff, G. 1D-coupled Photochemical Model of

- Neutrals, Cations and Anions in the Atmosphere of Titan. *Icarus* **2016**, *268*, 313–339.
- (28) Carbo, R.; Ginebreda, A. Interstellar Chemistry. *J. Chem. Educ.* **1985**, *62*, 832–836.
- (29) Aikawa, Y.; Wakelam, V.; Garrod, R. T.; Herbst, E. Molecular Evolution and Star Formation: From Prestellar Cores to Protostellar Cores. *Astrophys. J.* **2008**, *674*, 984–996.
- (30) Wakelam, V.; Herbst, E.; Bourlot, J. Le; Hersant, F.; Selsis, F.; Guilloteau, S. Sensitivity Analyses of Dense Cloud Chemical Models. *Astron. Astrophys.* **2010**, *517*, A21.
- (31) Hebrard, E.; Dobrijevic, M.; Pernot, P.; Carrasco, N.; Bergeat, A.; Hickson, K. M.; Canosa, A.; Le Picard, S. D.; Sims, I. R. How Measurements of Rate Coefficients at Low Temperature Increase the Predictivity of Photochemical Models of Titan's Atmosphere. *J. Phys. Chem. A* **2009**, *113*, 11227–11237.
- (32) Dobrijevic, M.; Claeys-Bruno, M.; Sergent, M.; Phan-Tan-Luu, R. Experimental Designs for the Determination of Key Reactions in Photochemical Models: Application to the Photochemistry of Hydrocarbons in the Atmosphere of Titan. *Planet. Space Sci.* **2008**, *56*, 519–529.
- (33) Loison, J. C.; Hébrard, E.; Dobrijevic, M.; Hickson, K. M.; Caralp, F.; Hue, V.; Gronoff, G. The Neutral Photochemistry of Nitriles, Amines and Imines in the Atmosphere of Titan. *Icarus* **2015**, *247*, 218–247.

Chapter 2.

Reaction kinetics of gas-phase processes at low temperature

2.1	The reaction rate	23
2.1.1	Determination of the rate constant	24
2.1.2	The temperature dependence of the rate constants	28
2.2	Branching ratios.....	30
2.2.1	Determination of the branching ratios.....	31
2.2.2	Correction to the branching ratios	33
2.3	Experimental methods to study the kinetics at low temperature	33
2.3.1	Conventional methods	33
2.3.2	Expansion based cooling methods	34
2.3.2.1	Free jet expansions.....	35
2.4	The CRESU technique	37
2.4.1	Supersonic Flow	37
2.4.2	Nozzle characterization	40
2.4.3	Continuous and pulsed CRESUs: The mini continuous CRESU of Bordeaux.....	43
2.4.4	Strengths and limitations of the CRESU technique	44
2.4.5	Determination of the concentration in the CRESU apparatus	45
2.4.5.1	Calibration of the mass flow controllers.....	46
2.5	Production of the reactive atoms	49
2.6	Detection methods coupled with the CRESU technique.....	51
2.6.1	Laser induced fluorescence technique.....	51
2.7	Determination of errors	54
2.7.1	Statistical errors and weighting.....	54
2.7.2	Systematic errors.....	55

2.7.3	Combination of statistic and systematic errors.....	56
2.8	Master equations calculations.....	56
2.9	References	60

2. Reaction kinetics of gas-phase processes at low temperature

Studies of reactions and their dependence on certain physical parameters such as temperature and concentration are commonly known as chemical kinetics. Knowledge of the reaction rate for a process allows us to predict the evolution of reactants and products as a function of time. Over the years, a considerable experimental and theoretical effort has been devoted to the determination of reaction rates of a wide range of processes given their importance to predict the nature and abundance of chemical species in different environments.

In chemical kinetics, two types of information are crucial.¹ The first one is a quantity that describes the intrinsic rate, the rate constant symbolized by k or by $k(T)$, emphasizing the fact that rate constants generally depend on temperature (for the rest of this work the rate constants are going to be represented as k for simplicity). The second one is the nature of the reaction products.

In this work, rate constants and branching ratios are determined for several gas-phase reactions of astrochemical interest. The following sections contain detailed information regarding the determination of rate constants and branching ratios for bimolecular reactions at low temperature.

2.1. The reaction rate

Consider a bimolecular reaction in which the reactant species A and B with concentrations $[A]$ and $[B]$ react to yield the product species C and D with concentrations $[C]$ and $[D]$:



The rate of this reaction (v) can be defined as the rate of loss of reagents A and B or the rate of formation of C and D (products). Then the reaction rate can be defined as:

$$v = -\frac{d[A]}{dt} = -\frac{d[B]}{dt} = \frac{d[C]}{dt} = \frac{d[D]}{dt} \quad (2.1)$$

For a second-order or bimolecular process, the rate constant (k) is defined in terms of the change in concentration with time

$$v = -\frac{d[A]}{dt} = k[A][B] \quad (2.2)$$

The rate constant reflects the efficiency of the reaction and has units of $\text{cm}^3 \text{s}^{-1}$ (or $\text{cm}^3 \text{molecule}^{-1} \text{s}^{-1}$) as the concentrations are usually expressed in units of cm^{-3} (or $\text{cm}^{-3} \text{molecule}$).

2.1.1. Determination of the rate constant

Integration of expression (2.2) yields

$$[A] = \frac{[A]_0[B]}{[B]_0} e^{-([B]_0 - [A]_0)kt}$$

Then to determine the second-order rate constant, it is necessary to follow the concentrations of both reactants *A* and *B* simultaneously. However, as it is already challenging enough to follow the concentration of one species, the determination of the concentration of both species simultaneously makes the measurement of rate constants for bimolecular reactions very difficult without the use of certain approximations.

To simplify the problem and to be able to measure second-order rate constants, the most commonly used method in chemical kinetics is the isolation method or the pseudo-first-order approximation. Here, one of the reactants (usually the most stable one) is added with a large and known excess concentration with respect to the other reactant so that to a good approximation, its concentration is constant throughout the reaction. Then expression (2.2) can be rewritten to give expression (2.3).

In the following, the reactant in excess is denoted by *B*. Then $[B] \gg [A]$ and $[B]$ can be considered constant. Now the rate of the reaction can be expressed as

$$v = -\frac{d[A]}{dt} = k'[A] \tag{ 2.3 }$$

and the pseudo-first-order rate constant k' is defined by

$$k' = k[B] \tag{ 2.4 }$$

where k is the second-order rate constant for the process.

Simple integration of expression (2.3) yields an expression which describes $[A]$ as a function of time (expression (2.5)). *A* is the minor reagent (in the experiments described here, *A* is an unstable atom or radical as will be detailed in section 2.6.1).

$$[A] = [A]_0 e^{-k't} \tag{ 2.5 }$$

To perform kinetic measurements under pseudo-first-order conditions it is necessary to determine accurately the concentration of *B*; a procedure which will be described in section 2.4.5. However,

precise knowledge of the absolute concentration of A is not required (although it is important to estimate $[A]$ in order to quantify the influence of secondary reactions). In these experiments, the evolution of $[A]$ with time is followed by a suitable spectroscopic technique such as fluorescence or chemiluminescence, where the fluorescence signal is assumed to be proportional to the minor reactant concentration. A typical curve displaying the evolution of the intensity of a minor reactant (followed by laser induced fluorescence) with time under pseudo-first-order conditions is shown in *Figure 2.1*. This decay allows us to determine the pseudo-first-order rate constant for a target reaction with a known concentration of B for a specified temperature. Then, from expression (2.4), knowing the pseudo-first-order rate constant and $[B]$ it is possible to determine the second-order rate constant.

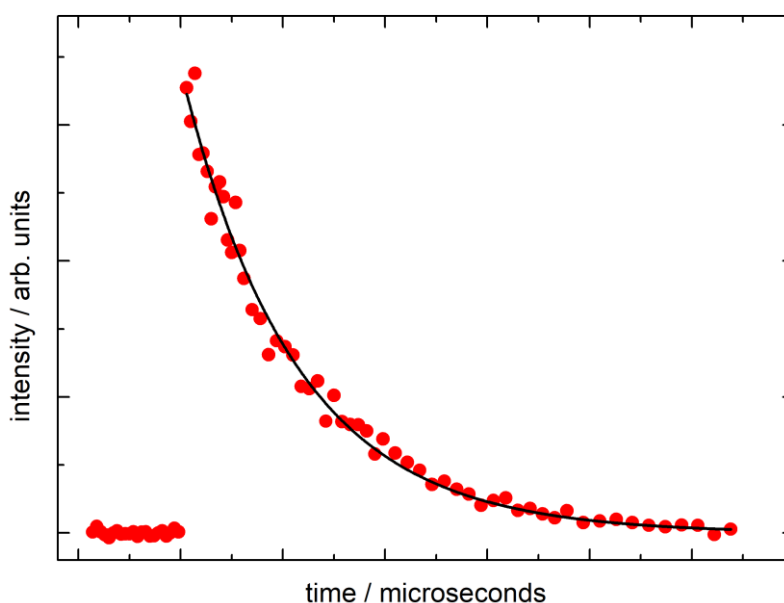


Figure 2.1 Fluorescence signal of reagent A , fitted to determine the pseudo-first-order rate constant using expression (2.5)

The discussion presented above represents the theoretical case where secondary losses of the minor reagent are negligible. However, in reality, the minor reagent can potentially react with other species present in the system such as products of the target reaction. In addition, it can be quenched by collisions (for excited state species) or diffuse out of the observation region. Consequently, the term ($k_{L(A)}$) has to be added to expression (2.4) in order to represent the secondary losses of the minor reagent A yielding expression (2.4.1). Here, it is important to notice that these secondary processes should not depend on the concentration of the reagent in excess (B).

$$k' = k_{A+B}[B] + k_{L(A)} \quad (2.4.1)$$

Under these conditions, the determination of the second-order rate constants from a single measure of k' implies the use of a very high $[B]$ in order to make the contribution of the secondary processes negligible compared to k' . To solve this problem, several values of k' are obtained for different values of $[B]$ and the second-order rate constant for a bimolecular process is extracted from the slope in a plot of k' vs. $[B]$ using a linear least squares fit to expression (2.4.1) as shown in *Figure 2.2*. The loss of the minor reagent $k_{L(A)}$ is represented here by the intercept in *Figure 2.2*.

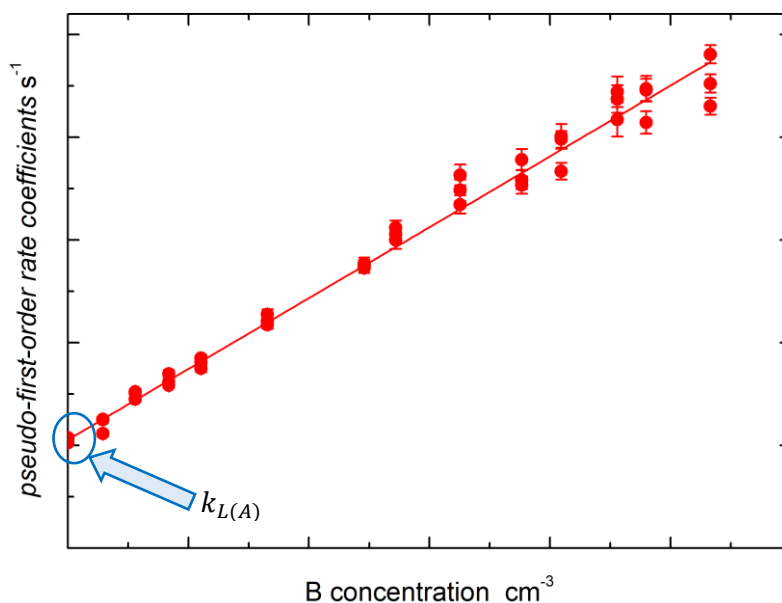


Figure 2.2 Plot of k' against $[B]$ to determine the second-order rate constant using expression (2.4.1)

The kinetics of a reaction can be also studied following the evolution in time of the concentration of a product species C or D . In the ideal case where reactants and products are not removed from the system by secondary processes, the $[C]$ can be described by the following exponential

$$[C] = X(1 - e^{-k't}) \quad (2.6)$$

where X is the preexponential factor representing the amplitude of the signal from C and $k' = k[B]$. This process is represented in *Figure 2.3* by the red dashed line. However, in reality, the products can diffuse from the reaction zone or react with other species producing secondary losses. The loss of the product is represented in reaction R 2.2 by $k_{L(C)}$.



The reaction rate for this process, written as a function of product C , can be described by the following expression

$$v = \frac{d[C]}{dt} = k[A][B] - k_{L(C)}[C] \quad (2.7)$$

Then applying pseudo-first-order conditions to the system

$$v = \frac{d[C]}{dt} = k'[A] - k_{L(C)}[C] \quad (2.8)$$

and integrating expression (2.8) we get a bi-exponential function of the form

$$[C] = X(e^{-k_{L(C)}t} - e^{-k't}) \quad (2.9)$$

where X is a pre-exponential factor, which represents the theoretical amplitude of the signal from C without secondary losses; the two terms inside the parentheses represent the formation of the product (rapid rise) and its loss (slow decay). The pseudo-first-order formation rate comprises two terms $k' = k_{A+B}[B] + k_{L(A)}$ as was explained earlier.

The bi-exponential function that describes the concentration of product C as a function of time is represented in *Figure 2.3*. Finally, the second-order rate constants are obtained from the slope when k' is plotted against $[B]$ in an identical manner to the method explained above when the reactant species is followed.

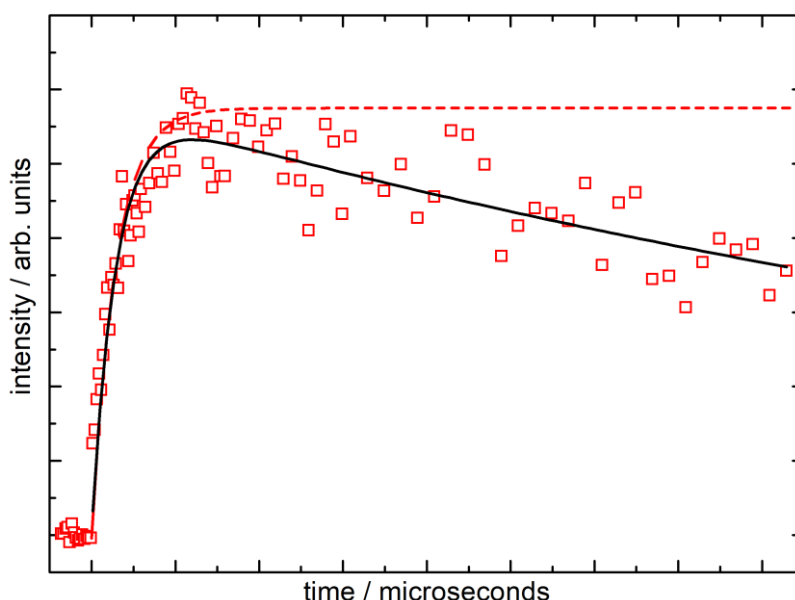


Figure 2.3 Fluorescence signal of product C (red open squares) fitted to determine the pseudo-first-order rate constant using expression (2.9) (black solid line). The red dashed line represents the theoretical fluorescence signal of product C without losses.

2.1.2. The temperature dependence of the rate constants

In 1889, Svante Arrhenius proposed expression (2.10), based on a series of experiments in which the rate constant for a reaction increased with temperature. This expression is universally known as the Arrhenius expression.

$$k = Ae^{\left(\frac{-E_{act}}{RT}\right)} \quad (2.10)$$

where A is the Arrhenius pre-exponential factor, which takes into account the collision frequency and steric factors, E_{act} is the activation energy defined as the minimum energy that the reactants must have in order to form products² (Figure 2.4 Panel A), R is the gas constant ($8.314 \text{ J mol}^{-1} \text{ K}^{-1}$) and T is the temperature.

For many years, it was thought that temperature dependent rate constants (k) could be universally described by expression (2.10) because a large number of reactions at room temperature and at higher temperatures (combustion processes for example) were well described by this expression. Arrhenius behaviour over a certain temperature range can be easily verified by displaying the results in an Arrhenius plot ($\ln k$ vs $1/T$). If the plot yields a straight line, Arrhenius behaviour is observed over that temperature range, where the intercept of the plot is the natural logarithm of the pre-exponential factor ($\ln A$) and the slope yields the activation energy of the reaction ($-E_{act}/R$). Deviations from linearity in these plots can arise for several reason such as the temperature dependence of the pre-exponential factor and the activation energy of the system or Quantum Mechanical Tunnelling (QMT) phenomena.³

The temperature dependence of the pre-exponential factor and the activation energy are included in a modification of the Arrhenius expression known as the Kooij expression

$$k = AT^m e^{\left(\frac{-E_0}{RT}\right)} \quad (2.11)$$

where E_0 and m are two adjustable factors related to the activation energy according to expression

$$E_{act} = E_0 + mRT \quad (2.12)$$

although for most applications in astrochemistry, only the temperature dependence of the pre-exponential factor is retained. For exothermic reactions where there is no activation barrier separating reactants and products (see Figure 2.4 Panel B) the expression(2.11) can be simplified to

$$k = AT^m \quad (2.13)$$

The Kooij expression is widely used by the Astrochemistry community because it allows a more precise representation of the temperature dependence for reactions of interest in astrochemical environments. In databases such as KIDA (Kinetic Database for Astrochemistry) and UDFa (UMIST Database for Astrochemistry) the parameters A , m and (E_0/R) which characterize the reaction rate are substituted by α , β and γ respectively. These parameters are found from fitting to experimental or theoretical data using expression (2.11) in a given temperature range.

The development of experimental techniques to measure rate constants over a wide range of temperatures has allowed scientists to see significant deviations from Arrhenius behaviour. Indeed, the rate constants for many ion-molecule reactions and for some reactions between neutral species do not obey the Arrhenius expression having a negative dependence on temperature; that is, rate constants that increase as the temperature is lowered.⁴ This behaviour is characteristic of reactions that do not have an activation barrier on the potential energy surface leading to products (*Figure 2.4* Panel B). These reactions, often called barrierless reactions, are usually fast at room temperature and may remain rapid or even become faster as the temperature falls to the low temperatures of astrochemical environments.

A combination of the two previous behaviours, where an initial relatively weakly bound complex is formed followed by a small barrier in the potential energy surface leading to products (*Figure 2.4* Panel C), has also been observed.⁵⁻⁷ In this case, the relationship between the formation of the initial complex and its dissociation back to reactants versus subsequent crossing of the barrier (which may or may not be above the reagent energy) has been used to explain the observed behaviour of the rate constant in a given temperature range. Many radical-molecule reactions fall into this category where the well depth and the barrier height strongly influence the rate constants for the reaction.

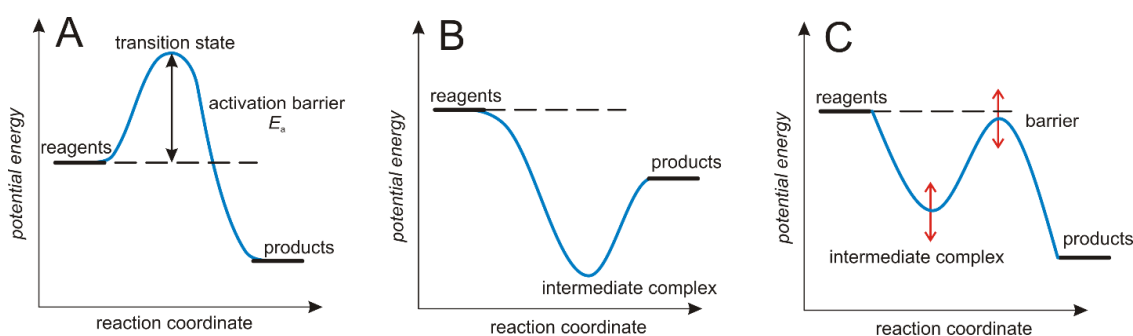


Figure 2.4 Schematic representation of the potential energy for exothermic reactions. (Panel A) reaction with a substantial barrier to products. (Panel B) reaction with no barrier to products. (Panel C) reaction with an initial weakly bound complex followed by a barrier.

The overall rate constant for exothermic bimolecular neutral-neutral reactions shows a temperature dependence that is controlled by a subtle interplay of barrier heights as well as the possible effects of QMT in the case of relatively small barriers.^{8,9} A recent article by Sims⁸ summarizes the temperature dependence for exothermic bimolecular reactions in three general cases (*Table 2.1*). These cases include the interaction of radicals with other radicals and closed-shell molecules. However, less is known about the reactivity of atoms in excited electronic states such as C(¹D), O(¹D) and N(²D) which represent the main part of this thesis.

Table 2.1 Temperature dependence of the rate constant for exothermic bimolecular reactions.

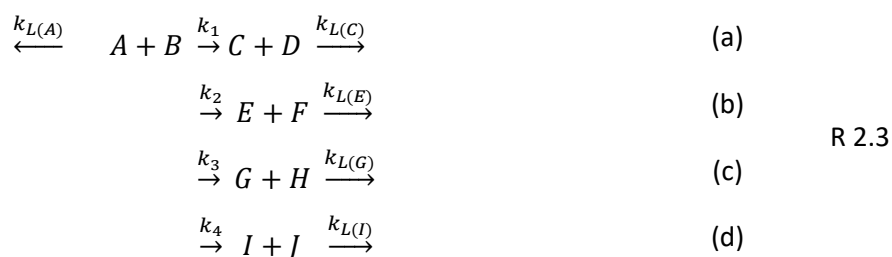
Type of reaction	Temperature dependence of the rate constants	Some examples in this thesis
Reactions with a substantial barrier to products	Arrhenius behaviour where the pre-exponential factor is dependent on temperature and QMT might play a role.	
Barrierless reactions (radical + radical; radical + closed-shell molecules)	Non-Arrhenius behaviour where the reaction rate becomes faster as the temperature drops.	C(¹ D) + CH ₄ C(¹ D) + NO N(² D) + NO
Reactions with an initial weakly bound complex followed by a small potential energy barrier to products (radical + molecule).	Arrhenius behaviour at high temperatures followed by a minimum and finally an increase of almost an order of magnitude at low temperatures.	C(³ P) + H ₂ O

2.2. Branching ratios

As was mentioned before, two types of information are crucial in chemical kinetics: the overall rate of the reaction and the product branching ratios for multichannel reactions. The branching ratios are defined for a reaction with multiple exit channels as the ratio of one channel divided by the sum of all the channels. This information allows us to quantify the importance of each reaction channel and can provide additional insight into the reaction mechanism.

2.2.1. Determination of the branching ratios

If we consider the following bimolecular multichannel reaction R 2.3.



where k_1, k_2, k_3, k_4 are the second-order rate constants for each individual exit channel (a, b, c, d). $k_{L(A)}$ is the loss of the minority reagent A through collisions with the carrier gas, by secondary reactions if there are any or by diffusion. $k_{L(C)}, k_{L(E)}, k_{L(G)}, k_{L(I)}$ represent the loss of the products by diffusion from the probe volume or loss by secondary reactions if there are any.

A branching ratio for bimolecular multichannel reactions is defined as the ratio between the rate constant for a particular exit channel, for example channel (a), and the rate constant for the total set of possible exit channels, (a) + (b) + (c) + (d) (expression (2.14)).

$$Br = \frac{k_1}{k_T} = \frac{k_1}{k_1 + k_2 + k_3 + k_4} \quad (2.14)$$

k_T represents the overall second-order rate constant for a multichannel reaction and is expressed as the sum of the second-order rate constants for each individual exit channel (a, b, c, d) (expression (2.15)).

$$k_T = k_1 + k_2 + k_3 + k_4 \quad (2.15)$$

If we detect the formation of product C , the kinetics of the reaction can be followed by applying expression (2.9) to this system.

$$[C] = X(e^{-k_{L(C)}t} - e^{-k't}) \quad (2.9)$$

No information on the product branching ratios can be extracted up to this point, even if the pseudo-first-order rate constant k' is measured because k' here represents the total rate constant for formation of product C ($k' = (k_1 + k_2 + k_3 + k_4)[B] + k_{L(A)}$) and not the rate constant corresponding to channel (a) alone.

However, if we analyse more carefully the kinetic equations, it is possible to derive an expression that allows us to extract the branching ratios for multichannel reactions. Under pseudo-first-order conditions, where $[B] \gg [A]$ and $[B]$ is considered constant throughout the reaction, the rate of formation of C product or any other product is given by

$$v = \frac{d[C]}{dt} = k_1[A][B] - k_{L(C)}[C]$$

$$v = \frac{d[C]}{dt} = k'_1[A] - k_{L(C)}[C] \quad (2.8)$$

Substituting equation (2.5) (see section 2.1.1) into (2.8)

$$\frac{d[C]}{dt} = k'_1[A]_0 e^{-(k'_T)t} - k_{L(C)}[C]$$

And solving this differential equation, we get

$$[C] = \frac{k'_1[A]_0}{k'_T - k_{L(C)}} \left(e^{-k_{L(C)}t} - e^{-(k'_T)t} \right) \quad (2.9.1)$$

where $\frac{k'_1[A]_0}{k'_T - k_{L(C)}}$ is the pre-exponential factor (X from the expression (2.9)) and contains the branching ratio for the exit channel (a) according to the expression (2.14).

$$X = \frac{k'_1[A]_0}{k'_T - k_{L(C)}} = \frac{k_1[B][A]_0}{(k_1 + k_2 + k_3 + k_4)[B] + k_{L(A)} - k_{L(C)}} \quad (2.16)$$

However, while $[B]$ is known and $k_{L(C)}$ and $k_{L(A)}$ can be obtained experimentally, $[A]_0$, the initial minor reagent concentration is not precisely known so the absolute branching ratio cannot easily be derived. Instead, one way to solve this problem is to choose a reference reaction (for example R 2.4) which shares a common reagent A with the target reaction, forming product C with a well-known yield.¹⁰



If possible, the reference reaction is chosen to be a process with a single exit channel, thereby producing product C with a 100% yield. In this specific case, $k_1 = k_T$, and $[A]_0$ is identical for the target and reference reactions so that the absolute branching ratio can be derived simply by dividing the pre-exponential factors obtained by fitting to the temporal profiles of the target and reference reactions.

During the development of this thesis, we use two procedures to obtain absolute branching ratios, measuring in both cases the formation of H- (or D-) atom products. More details of these procedures are given in chapters 3 and 4.

2.2.2. Correction to the branching ratios

The reactions take place in a chamber where the presence of residual gases might affect the determination of the branching ratios due to attenuation of the initial light. As the magnitude of this correction is likely to be different for the excess target and reference reagents, a correction is applied when necessary to the derived A factors to account for absorption of the excitation source and the emitted fluorescence using the Beer-Lambert Law (expression (2.17)).

$$I = I_0 e^{-\sigma cl} \quad (2.17)$$

Where I_0 and I are the incident and transmitted light intensities, σ is the absorption cross section in $\text{cm}^2 \text{molecule}^{-1}$, c is the concentration of the absorber in molecule cm^{-3} , l is the absorption path length in cm.

2.3. Experimental methods to study the kinetics at low temperature

Over the last 30 years, an increasing interest in the chemistry of cold environments has motivated the development of various methods that allow the investigation of reactions at low temperatures. The experimental study of gas-phase processes can be divided into conventional techniques and expansion based cooling techniques.

2.3.1. Conventional methods

Conventional experiments employ cryogenic cooling to reach temperatures below 200 K. Here, some refrigerant such as liquid nitrogen, helium, methanol, etc is circulated through an envelope surrounding the reaction vessel. The low temperatures inside the reactor are therefore attained through collisions of the gases inside the chamber with the cold reactor walls. The temperature inside the reactor is typically monitored using a thermocouple. The main drawback of these techniques is that reagents and precursors can condense on the walls of the reactor when their partial pressure exceeds their saturated vapour pressure at the temperature of the wall, leading to a large uncertainty in the concentration of the reagent remaining in the gas phase. As a result, only reactions between reagents with high saturated vapour pressures at low temperature can be studied accurately using cryogenic methods.

There are two main categories of conventional methods for studying the kinetics of gas-phase reactions. The first one, the flow tube technique, is a continuous method where the gas flow is characterized by a constant flow velocity. The reactants are injected into the flow at a known distance from the detection zone using an injector or through fixed distance injector ports. The variation of the minor reagent concentration is followed as a function of the distance between the injection point and the detection zone. As the reaction time is known due to the constant flow velocity and the known distance from the point of initial mixing of the reagents, pseudo-first-order rate constants can be determined. By changing the flow velocity and/or the concentration of the major reagent, reactions with rate constants between 10^{-10} to 10^{-15} $\text{cm}^3 \text{s}^{-1}$ can be studied using this technique. One of the main advantages of this type of experiment is that the minor reagent concentration is constant at any point along the flow tube. As a result, the time response of the detection method is unimportant and significant signal averaging can be performed due to the continuous nature of the technique. However, this method relies on the assumption of plug flow^{11,12} which limits its use to relatively low pressures. A secondary disadvantage associated with the use of low pressures is that the reactive species undergo more collisions with the walls. Consequently, the flow tube technique operates over a relatively limited range below room temperature.

The second method, the flash photolysis technique, uses a slow (or static) flow reactor and a pulsed flash to initiate the reaction by photodissociation of a suitable precursor. In this case, the reaction time is given by the time elapsed since the initial flash. A detection method with a fast time response is required for this technique in order to maintain a good temporal resolution. The carrier gas flow, containing the excess reactant and the precursor molecule, is usually slow enough to ensure that the minor reagent (radicals) have not been displaced to any great extent on the reaction timescale but it is fast enough to avoid the next photolysis pulse acting on the same volume of gas. As the minor reactive species is generated by photolysis of a suitable precursor; the variety of reactions that can be studied with this method is more limited than with flow tube experiments. However, there is no limit to the gas pressure that can be used in this technique, allowing the study of reactions at a lower temperature than in flow tube experiments.

2.3.2. Expansion based cooling methods

Many of the molecular species of potential interest for low temperature chemistry (such as hydrocarbons) have low vapour pressures. As a result, conventional cryogenic cooling methods are not well suited to the study of the gas-phase reactions of these molecules because they easily condense on the reactor walls at low temperatures. This issue can be overcome using expansion based cooling methods. In these techniques, the cooling effect is produced by an adiabatic and isentropic expansion

of a gas from a reservoir through an orifice or nozzle into a vacuum chamber to produce a cold supersonic jet.

Among the expansion based cooling methods, two techniques can be distinguished: the free molecular regime/free jet expansions and a technique that involves the use of Laval nozzles. This last method was used during this work to determine rate constants and branching ratios for reactions of interest in cold environments.

2.3.2.1. Free jet expansions

In free jet expansions, while the expansion of the gas occurs from a reservoir held at higher pressure through a small orifice into a chamber held at lower pressure, the internal energy of the molecules is transferred into directional kinetic energy within the hydrodynamic zone. Outside that zone, there are no more collisions among molecules and their internal motions, vibration and rotation are frozen. The physical conditions (pressure, temperature, density and velocity) vary in the different zones of the considered jet *Figure 2.5*. The region where the jet is supersonic is called the zone of silence. This zone is surrounded by boundary layers where the flow is subsonic (Mach number, $M < 1$) and there are large gradients of temperature and pressure.

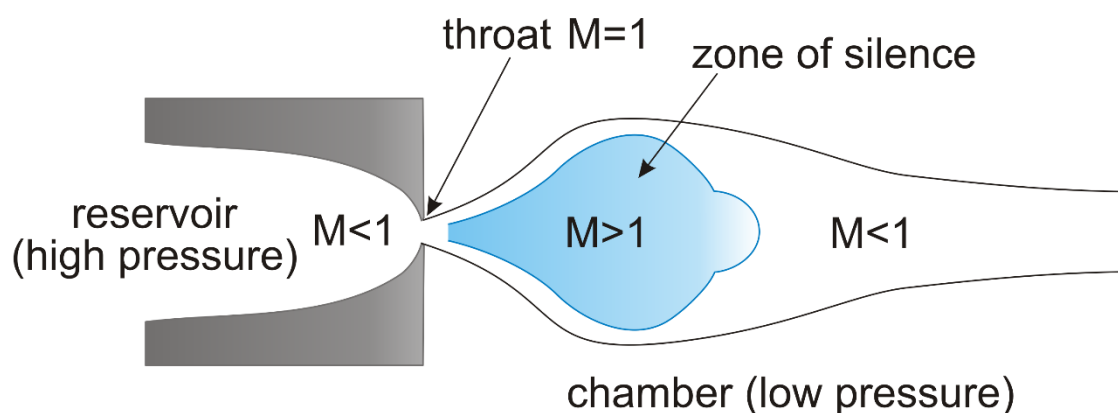


Figure 2.5 Free jet expansion from a high pressure reservoir through an orifice into a low pressure chamber.

During this expansion, as thermal equilibrium is not reached only a translational temperature and a flow velocity can be defined along the beam axis.¹³ Due to the significant temperature and velocity gradients produced during a free jet expansion, the overall rate constant is difficult to determine, but not impossible.¹⁴ Furthermore, given the extent of the zone of silence and its characteristics, only rapid reactive processes can be studied with this technique. Usually, free jet expansions are mostly used in spectroscopic studies because the rotational temperature can be frozen out to temperatures of a few kelvins or even less, which simplifies considerably the spectral analysis.

Free jet expansions are also used in Crossed Molecular Beams (CMB) where two collimated beams (atomic or molecular) are collided together to study the dynamics of certain reaction. In this technique, to produce the molecular beam, one or more skimmers are inserted into the supersonic zone of a free jet expansion as shown in *Figure 2.6*. This arrangement allows the selection of molecules with parallel or quasi-parallel trajectories to the beam axis and with a narrow velocity distribution. The result is a beam of molecules moving around the same mean velocity and few or no collisions occurring between them due to the low density of the beam. The collision energy of molecules resulting from the crossing of the two beams is given by $E_c = \frac{1}{2}\mu(v_1 + v_2 - 2v_1v_2\cos\theta)$ where μ is the reduced mass, v_1 and v_2 are the velocity of the two beams and θ is the angle of intersection of the two molecular beams. Finally, low energy collisions are generated by varying the collision angle between the two beams and/or by adjusting the velocity of the beams. Using this technique, reaction cross sections (σ) can be determined for different collision energies. Although CMB apparatuses are well suited to study the reaction dynamics, because the beam densities are not precisely known, it is difficult to convert the measured cross sections to absolute rate constants in such experiments.¹⁴

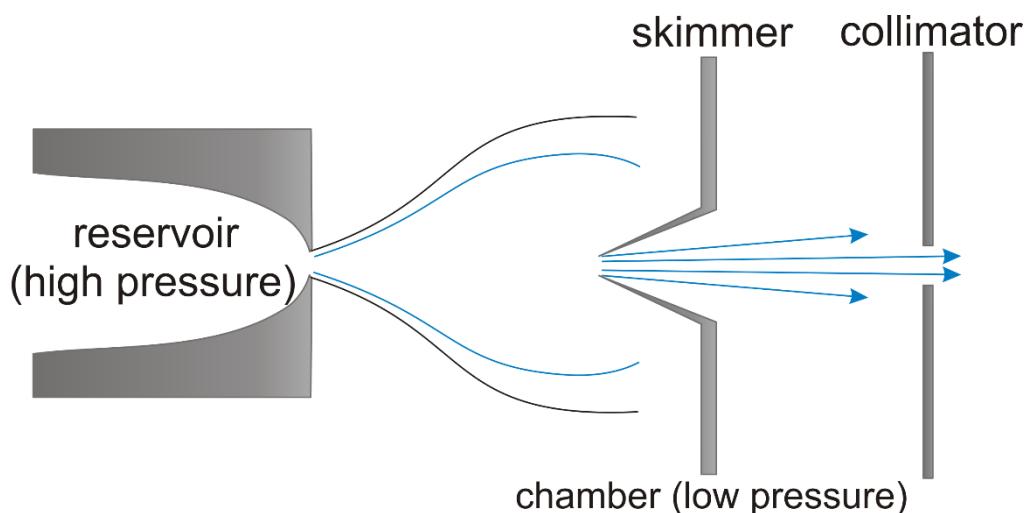


Figure 2.6 Production of a Molecular beam

2.4. The CRESU technique

While the free jet expansion technique solves the problem of condensation on the reactor walls at low temperatures, their use to study the kinetics of bimolecular reactions is limited due to the low densities in the beam and the strong velocity and temperature gradients. These factors result in the loss of local thermodynamic equilibrium (LTE), with non-Boltzmann rotational distributions in the system and few collisions during the expansion.

In contrast to free jet expansions, the CRESU technique is dominated by collisions and thermal equilibrium is maintained at all points in the flow. CRESU is a French acronym (Cinétique de Réaction en Ecoulement Supersonique Uniforme) which translates as Reaction Kinetics in a Uniform Supersonic Flow. Rowe and coworkers developed this technique in 1984 to study the kinetics of ion-molecule reactions,¹⁵ and it was adapted by Smith, Rowe and co-workers in 1992 to study the kinetics of neutral-neutral reactions.¹⁶ This latter study brought about a turnaround in the chemistry of the interstellar medium, clearly demonstrating that neutral-neutral reactions could remain rapid at low temperatures, in contrast with earlier assumptions. Since then, more than 150 reactions have been studied by the CRESU community with an emphasis on reactions involving atomic and molecular radical species in their ground state.¹⁷ However there is still much work to do given the growing number of species detected in the interstellar medium (to date more than 200 with most of them being neutral species)^{1,18} along with the necessity to provide kinetic data to improve the estimations of astrochemical models.

2.4.1. Supersonic Flow

The CRESU technique is based on the adiabatic expansion of a gas through a convergent-divergent Laval nozzle (*Figure 2.7*) producing a supersonic flow with uniform temperature, velocity and density profiles for several tens of centimetres. The principal element of this technique is the axisymmetric nozzle. The nozzle consists of two sections: first, a convergent section in which the gas is accelerated but not compressed followed by a divergent section in which the gas is further expanded. While the gas held in the reservoir is considered to be static with a Mach number ($M < 1$), at the throat of the Laval nozzle it reaches ($M = 1$) and after the divergent section it can reach higher Mach numbers ($M > 1$). The adiabatic expansion of the gas from the high-pressure reservoir to the low-pressure chamber results in its acceleration to supersonic velocities accompanied by the conversion of some of the internal energy of the gas into kinetic energy lowering its temperature.¹² Furthermore, the density of the expanded gas is quite high (typically 10^{15} to 10^{18} cm⁻³) which assures frequent collisions and LTE as was stated before.

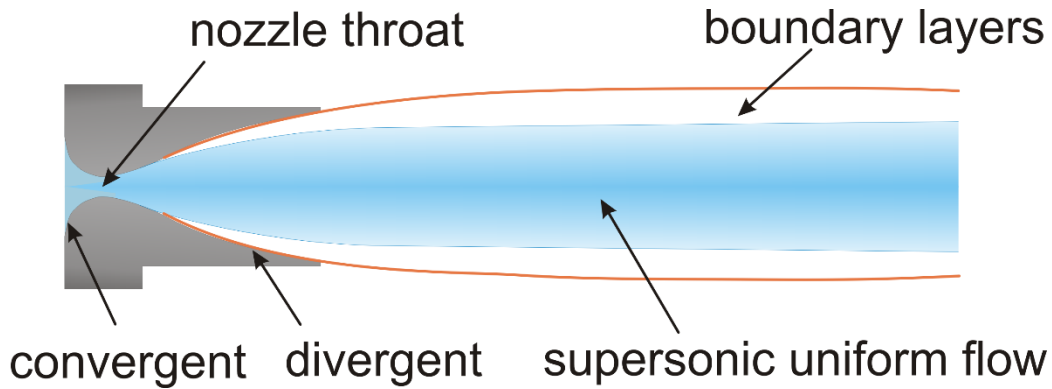


Figure 2.7 Scheme of a Laval nozzle and the uniform supersonic flow.

Around the uniform supersonic flow also known as the isentropic core, there are boundary layers. These layers result from friction between the isentropic core, the internal surface of the nozzle and the residual gases present in the chamber. Since the uniform supersonic flow is the desired part of the flow the smaller the size of the boundary layer, the better the flow quality.

The expansion of the gas through the Laval nozzle is isentropic so that the first law of thermodynamics and the conservation of energy allows us to write a variation of Bernoulli's equation (2.18); which shows that the higher velocity of the gas after the expansion results in a lower temperature.

$$C_p T_{reser} + \frac{v_{reser}^2}{2} = C_p T_{flow} + \frac{v_{flow}^2}{2} \quad (2.18)$$

where C_p is the specific heat capacity at a constant pressure, T_{reser} and T_{flow} are the temperature in the reservoir and at any point of the flow after the expansion respectively, v_{reser} and v_{flow} are the velocity of the gas in the reservoir and in the flow respectively.

The Mach number (M), which was introduced earlier in this section, is an essential parameter to describe fast flows. It is defined as the ratio of the flow speed, v , to the speed of the sound in the same fluid, a

$$M = \frac{v}{a} = v \left(\frac{\gamma R T}{M_m} \right)^{-\frac{1}{2}} \quad (2.19)$$

where γ is the ratio of specific heat capacities defined by $\gamma = C_p/C_v$ with C_v as the specific heat capacity at a constant volume, R is the gas constant ($R = 8.314 \text{ J K}^{-1}\text{mol}^{-1}$), T is the temperature of the fluid and M_m is its molar mass. If $M < 1$ the flow is subsonic, if $M = 1$ the flow is sonic and if $M > 1$ the flow is supersonic.

The value of γ has a large influence on the calculation of the physical parameters of the flow.

- ✓ For a monoatomic gas $C_p = 5/2R$ and $C_v = 3/2R$.
- ✓ For a diatomic gas $C_p = 7/2R$ and $C_v = 5/2R$.
- ✓ For a polyatomic gas $C_p = 4R$ and $C_v = 3R$.

Then if argon is used as a carrier gas the values of C_p and C_v for a monoatomic gas give $\gamma = 5/3$. However, if a mixture of gases such as Ar and N₂ is used, the γ value is calculated depending of the individual C_p and C_v taking into account the molar fraction (X) as follows:

$$\gamma = \frac{X_1 C_{p,1} + X_2 C_{p,2}}{X_1 C_{v,1} + X_2 C_{v,2}} \quad (2.20)$$

For an ideal gas, $C_p - C_v = R$, then by substituting expression (2.19) into (2.18) we obtain

$$T_{Flow} = T_{reser} \left(1 + \frac{\gamma - 1}{2} M^2 \right)^{-1} \quad (2.21)$$

As the gas expansion is adiabatic, in order to derive other physical parameters of the flow such as pressure and density, the Laplace law can be used $PV^\gamma = constant$.

$$T^\gamma P^{1-\gamma} = ctte; \frac{P_{reser}}{P_{flow}} = \left(1 + \frac{\gamma - 1}{2} M^2 \right)^{\frac{\gamma}{\gamma-1}} \quad (2.22)$$

$$T d^{1-\gamma} = ctte; \frac{d_{reser}}{d_{flow}} = \left(1 + \frac{\gamma - 1}{2} M^2 \right)^{\frac{1}{\gamma-1}} \quad (2.23)$$

where P_{reser} and d_{reser} are the pressure and density in the reservoir, P_{flow} and d_{flow} are the pressure and the density in the flow.

In reality, during the expansion of the gas through the nozzle, the fluid viscosity is never zero and a small heat exchange with the outer layer occurs. Consequently, the process is not strictly adiabatic and these phenomena need to be considered in the calculation of the Laval nozzle profiles. An inverse solution of the Navier-Stokes flow equations is not analytically possible but a numerical solution can be found using a perturbation method.¹³ First, an ideal flow is considered where there is no viscosity or heat exchange. A contour of an ideal nozzle (*Figure 2.8*) is obtained for this system when the Euler hydrodynamic equations are solved. Secondly, a flow is computed considering that the walls of the nozzle are at a fixed temperature (usually room temperature) and the gas has a zero velocity at the wall (due to the non-zero fluid viscosity). This allows the calculation of a secondary flow, non-isentropic

of thickness δ_1 where the gas velocity increases as the distance increases from the wall within the layer. After this layer the rest of the boundary layer corresponds to a zone where the isentropicity of the fluid is not always achieved.

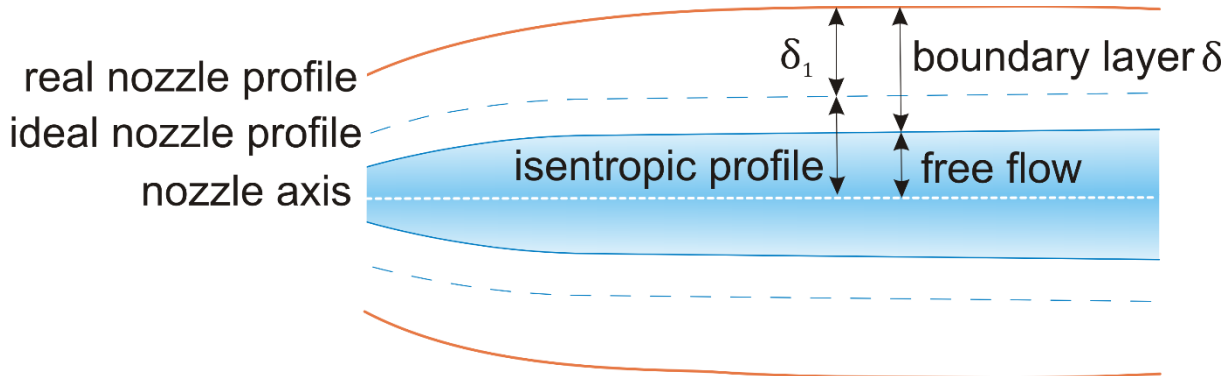


Figure 2.8 Real and ideal nozzle profiles

The flow quality is given by the thickness of this boundary layer. The Reynolds number (R_e), which is equal to the ratio of the inertial forces (given by pressure differences on the fluid) to viscous forces (given by the interactions of the nozzle walls on the flow) is a good indicator of the quality of the flow.

$$R_e = \frac{\rho v L}{\mu} \quad \text{with} \quad \frac{\delta}{L} \propto \frac{1}{\sqrt{R_e}} \quad (2.24)$$

where ρ is the fluid volumetric mass, v is the flow velocity, L is the uniform flow length and μ is the dynamic viscosity of the fluid. Then a higher R_e indicates a better flow with a smaller boundary layer.

The uniformity of the density profile of the supersonic flow can be affected by shockwaves. This phenomenon produces a larger standard deviation of the temperature, density and velocity along the flow. Shockwaves can be caused by small imperfections in the throat of the nozzle produced during the machining process, thus, once the nozzle is manufactured it must be characterized.

2.4.2. Nozzle characterization

Before a nozzle is manufactured, calculations are performed to produce a nozzle profile, which allows us to generate the desired physical conditions. However, small approximations during these calculations or slight imprecisions during the machining process can produce deviations from the desired theoretical conditions. These imperfections in the machining of the nozzle could result in different temperature and density profiles in addition to the generation of shockwaves as mentioned above. Consequently, each nozzle must be characterized to obtain the optimal conditions that guarantee a *uniform* cold supersonic flow.

The quality of the flow generated by a nozzle can be tested through measurements of the impact pressure (P_i) using a Pitot tube (Figure 2.9).

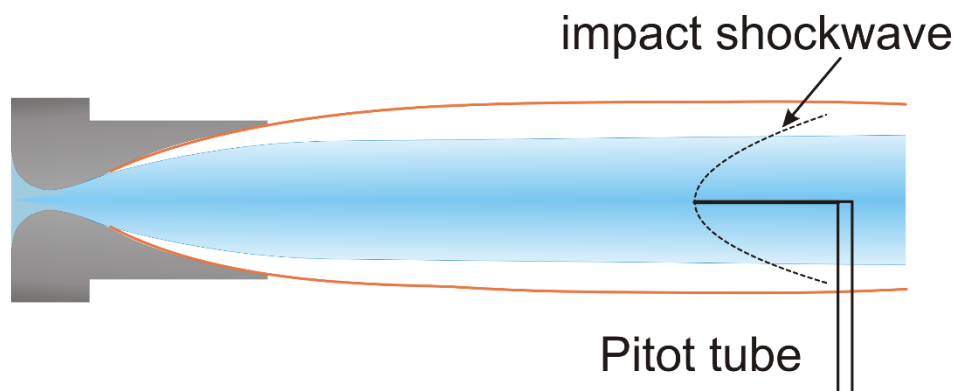


Figure 2.9 Principle of Pitot tube measurements.

A Pitot tube is a hollow tube inserted inside the flow parallel to its propagation direction. The impact of the flow at the tip of the tube creates a shockwave, which produces an impact pressure that is measured at the other end of the tube with a pressure gauge. The characterizations are performed by following the evolution of the impact pressure as a function of the distance between the Pitot tube and the exit of the nozzle. The impact pressure (P_i) and the static pressure (P_s) within the flow are related by the following equation:

$$P_i = P_s \left(\frac{\gamma + 1}{2} \right)^{\frac{\gamma + 1}{\gamma - 1}} M^{\frac{2\gamma}{\gamma - 1}} \left(\gamma M^2 - \frac{\gamma - 1}{2} \right)^{\frac{1}{1 - \gamma}} \quad (2.25)$$

Because the expansion is isentropic, the impact pressure can be expressed as a function of the reservoir pressure (P_r):

$$P_i = P_r \left(\frac{(\gamma + 1)M^2}{(\gamma - 1)M^2 + 2} \right)^{\frac{\gamma}{\gamma - 1}} \left(\frac{\gamma + 1}{2\gamma M^2 - \gamma + 1} \right)^{\frac{1}{\gamma - 1}} \quad (2.26)$$

During the measurement of the impact pressure, we must keep constant at any point the pressure in the reservoir, the mass flow and the temperature in order to obtain the flow characteristics. The objective is to obtain the longest and most uniform flow possible so that the impact pressure should be stable over the greatest distance possible. Indeed, the study of slow reactions requires the longest uniform supersonic flow possible. It is important to point out that in our case, we have calculated supersonic flow densities of around $1 \times 10^{17} \text{ cm}^{-3}$, which allows us to introduce maximum reagent concentrations of approximately $5 \times 10^{15} \text{ cm}^{-3}$ (5% of the total flow). This concentration combined with

an exploitable time of around 300 μs and considering 4 half-lives for the decay of the minor reagent in the reactive process allow us to study reactions with rate constants greater than $1 \times 10^{-12} \text{ cm}^3\text{s}^{-1}$. Although it is not strictly necessary to follow the reaction over 4 half-lives, a better determination of the pseudo-first-order rate constants can be achieved in this way.

At each distance between the Pitot tube and the end of the nozzle, the pressure in the reservoir and the impact pressure are measured, allowing the physical parameters of the flow to be calculated, and providing important information on the flow quality. As an analytical solution for expression (2.26) is not possible, a numerical solution by an iterative algorithm is the preferred method to obtain the Mach number. Once the Mach number for each point probed is obtained, the average temperature and density can be derived using expressions (2.21) and (2.23) respectively. In addition, the flow velocity (v) can be calculated through the expression

$$v = \sqrt{\frac{\gamma k_B T}{m}} \quad (2.27)$$

where k_B is the Boltzmann constant ($1.38065 \times 10^{-23} \text{ JK}^{-1}$) and m is the mass of the gas in Kg.

Each nozzle is designed to produce specific conditions of temperature, density and flow velocity. Some of the Laval nozzles used during this work are shown in *Figure 2.10* and the specific characteristics of all the nozzles used in this work are listed in *Table 2.2*.



Figure 2.10 Laval nozzles from the mini CRESU setup of Bordeaux

Table 2.2 Continuous supersonic flow characteristics

Laval nozzle	Mach2 N ₂	Mach3 N ₂	Mach2 N ₂	Mach3 Ar	Mach3 Ar	Mach4 Ar	Mach2 Ar
Mach number	1.83±0.02	3.0±0.02	2.0±0.03	3.0 ± 0.1	3.0 ± 0.1	3.9 ± 0.1	3.9 ± 0.1
Temperature (K)	177 ± 2	106 ± 1	127 ± 2	77 ± 2	75 ± 2	52 ± 1	50 ± 1
Carrier gas	N ₂	N ₂	Ar	Ar(7%)	Ar	Ar(7% N ₂)	Ar
Density (x 10 ¹⁶ cm ⁻³)	9.4 ± 0.2	10.3±0.03	12.6±0.3	14.7± 0.6	14.7±0.6	25.9± 0.9	25.9±0.9
Impact Pressure (torr)	8.2 ± 0.1	13.4±0.27	10.5±0.2	15.3± 0.5	15.3±0.5	29.6± 1.0	29.6±1.0
Stagnation Pressure (torr)	10.3	34.9	13.9	34.9	34.9	113	113
Chamber pressure (torr)	1.4	1.1	1.5	1.2	1.2	1.4	1.4
Mean flow velocity (ms ⁻¹)	496 ± 4	626 ± 2	419 ± 3	479 ± 3	479 ± 3	505 ± 1	505 ± 1

2.4.3. Continuous and pulsed CRESUs: The mini continuous CRESU of Bordeaux

The CRESU technique was initially developed for continuous gas expansions achieving temperatures as low as 8 K in the study of ion-molecule reactions.¹⁹ Later on it was adapted to the study of neutral-neutral reactions and in this case the lowest temperature achieved without gas precooling is 15 K²⁰ and 6 K when the gas is precooled with liquid nitrogen before passing through the Laval nozzle.²¹ However, one of the major practical disadvantages of continuous CRESU apparatuses is the large consumption of gases required to produce a uniform jet for several tens of centimetres. Thus, a huge pumping capacity is necessary to conduct the experiments. For example, the original continuous CRESU system (Université de Rennes) requires an average effective pumping capacity of 25 000 m³/h. To solve these problems several groups around the world have developed variations of the technique. In 1995, Atkinson and Smith²² at the University of Arizona developed a pulsed CRESU apparatus using a pulsed electromagnetic valve to admit gas into the reservoir. In this experiment, the reservoir should be as small as possible to assure that the flow rate into and out of the reservoir is the same leading to a constant pressure, which is critical to achieving the continuum flow. This technique presents the disadvantage that the gas is no longer static before being accelerated in the convergent section of the nozzle, which can cause instabilities in the flow. A solution to this problem was presented in 2014 by Oldham and coworkers²³ using a high-force fast piezoelectric stack actuator to enable very fast high-throughput valves. An alternative method is to insert the pulsing system a few millimetres downstream of the nozzle throat by interrupting the flow with a slotted rotating disk²⁴ or with a Teflon coated aerodynamic chopper.²⁵ While with the first design of pulsed apparatus²² the lowest temperatures were limited to around 50 K (given the small volume of the reservoir and the small pumping capacities), the last two pulsed alternatives employing fast piezoelectric stack actuators²⁴ and the aerodynamic chopper method²⁵ give superior performance and achieve temperatures as low as 20 K.

Another way to reduce the large consumption of gases and optimize the size of the experiment is to use a miniaturized continuous CRESU setup (*Figure 2.11*). This experiment was developed in 2005 by Daugey and co-workers²⁶ at Université de Bordeaux. It consists of a stainless steel chamber 660 mm long with a 180 mm inner diameter (Panel A). The Laval nozzle is mounted on a piston that can be moved 350 mm along the chamber axis and is equipped with a reservoir (Panel C). The chamber is pumped by a Roots blower backed by a mechanical pump (Leybold RUBAC WAU 1000-SOGEVAC SV300) which operates with a pumping capacity $< 1000 \text{ m}^3/\text{h}$. The pumping speed is adjusted by a controlled throttling valve (MKS-MEIVAC VARI-Q™ 100) (Panel B). The background pressure in the chamber and the stagnation pressure in the reservoir are measured by capacitance manometers (Edwards 0-1.33/13.33/133.32 kPa). Using this experimental setup and our home-designed Laval nozzles, temperatures as low as 50 K can be achieved.

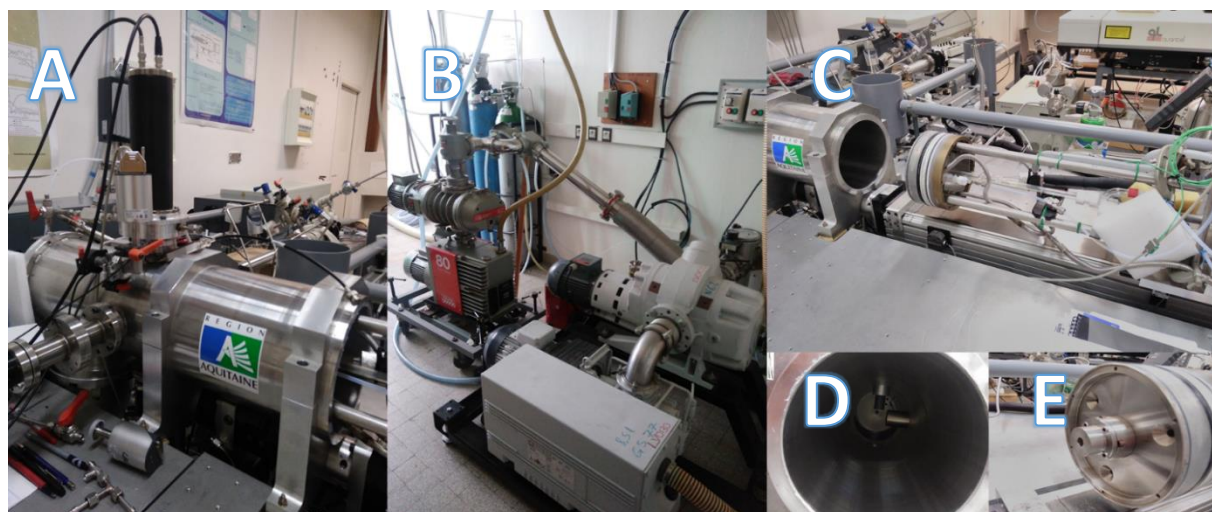


Figure 2.11 (Panel A) stainless steel chamber; (Panel B) pumps, (Panel C) movable piston and reservoir; (Panel D) interior of the chamber, (Panel E) Laval nozzle attached to the movable piston.

2.4.4. Strengths and limitations of the CRESU technique

For a long time, the production of temperatures below 100 K in the laboratory to study the kinetics of gas-phase reactions was a major challenge to the experimentalist. Nowadays, the CRESU technique has revolutionized gas-phase chemistry at low temperatures, allowing the study of a wide range of ion-molecule and neutral-neutral reactions. As briefly mentioned above, CRESU experiments present several advantages with respect to other methods used to attain low temperatures:

- ✓ Is a wall-free reactor where condensation of the reactive species is negligible
- ✓ Is essentially the only technique that allows us to measure rate constants for molecular processes involving electrically neutral species below 100 K

- ✓ The density, velocity and temperature are uniform along the flow
- ✓ Laval nozzle expansions are characterized by high density and frequent collisions which allow local thermodynamic equilibrium to be maintained
- ✓ The total number of sample molecules in the irradiated volume can be quite large given the high density and large flows, allowing greater signal levels

Among its limitations are the following:

- ✓ It is an expensive and large experiment
- ✓ It has a large consumption of gases and significant pumping capacities
- ✓ It is restricted to the measurement of relatively rapid reactions (with rate constants $> 10^{-12} \text{ cm}^3 \text{ s}^{-1}$) due to the limited time in which the supersonic flow is exploitable
- ✓ The reagents are usually restricted to a few percent of the total carrier gas flow due to the need to maintain the nominal flow conditions (temperature and density)
- ✓ The study of pressure dependent reactions at the same low temperature requires several nozzles because each nozzle is designed to work under specific conditions
- ✓ At the lowest temperatures and highest reagent concentrations, cluster formation can occur in the cold flow

During the course of this thesis, the mini continuous CRESU setup in Bordeaux has been used to study several neutral-neutral reactions of potential interest to planetary atmospheres and the interstellar medium. The kinetics and branching ratios of these reactions have been investigated using a combination of pulsed laser photolysis to create the minor reactive species in-situ and vacuum ultraviolet laser induced fluorescence has been used to follow the changes in the concentration of the target species.

2.4.5. Determination of the concentration in the CRESU apparatus

To be able to extract the second-order rate constant for any target reaction, it is important to accurately determine the major reactant's concentration. In addition, knowledge of the concentrations of the species present in the flow allows us to minimize the influence of secondary reactions. The concentration of a species X in the flow can be determined from the calculated total density of the supersonic flow and the flow rates of each of the species present in the system according to expression (2.28)

$$[X] = \frac{Q_X}{Q_T} * [nozzle] \quad (2.28)$$

where $[X]$ is the concentration of the species, Q_X is its flow rate, Q_T is the combined flow rate for all gases that comprise the supersonic flow and $[nozzle]$ is the characteristic density of the nozzle as derived by the Pitot tube measurements described above (*Table 2.2*). The concentration of the reactive species in the flow are generally limited to less than 5% of the total density in order to preserve the nominal properties of the supersonic flow.

2.4.5.1. Calibration of the mass flow controllers

As the accurate determination of the majority species' concentration depends on the performance of the mass flow controllers, it is necessary to calibrate these devices to obtain accurate results. In this work, the mass flow controllers Brooks Smart series (models 5850S) were used to provide accurate control of the gas flows. These controllers are designed to work up to a specified maximum flow, which is reported in standard units (standard cubic centimetres per minute, sccm, or standard litres per minute, slpm). The flow controllers are factory calibrated for a specific gas (typically N_2) and the use of these devices with another gas will result in a different flow rate given by the ratio of the molar specific heat of the two gases. The new gas flow rate can be calculated approximately by multiplying the nominal flow rate by the gas conversion factor associated with each gas *Table 2.3*.

Table 2.3 Gas conversion list

Gas	Gas factor
Nitrogen	1
Argon	1.395
Oxygen	0.988
Acetylene	0.615
Carbon Dioxide	0.740
Deuterium	0.995
Ethane	0.490
Ethylene	0.619
Hydrogen	1.008
Krypton	1.382
Methane	0.763
Propane	0.343
Nitric Oxide	0.995

For example, if a mass flow controller is set to its maximum flow rate of 100 sccm of N₂, this same mass-flow controller will allow a maximum of approximately 49 sccm of ethane to pass. The gas flow conversion factors are supplied by the manufacturer and although they usually allow the actual flow rate to be determined with reasonable accuracy, the flows can be more precisely controlled if they are calibrated under our actual laboratory conditions. Here, we used a pressure rise method for the calibrations. In this method, the flow controller is connected to a known volume and the pressure increase as a function of time is recorded for different percentage values of the flow controller.

The standard volumetric flow for a perfect gas is defined as:

$$Q = \frac{\Delta V}{\Delta t} = \frac{\Delta n * R * T_0}{P_0 * \Delta t} \quad (2.29)$$

where ΔV , Δt and Δn represent the variation of volume, time and number of moles respectively, T_0 and P_0 are the standard temperature (273 K) and pressure (1 atm) and R is the gas constant

In the calibration volume

$$\Delta n = \frac{\Delta P * V_{cal}}{R * T} \quad (2.30)$$

Combining expressions (2.29) and (2.30) we are able to calculate the standard volumetric flow into the calibration volume

$$Q = \frac{\Delta P * T_0 * V_{cal}}{P_0 * T * \Delta t} \quad (2.31)$$

For each percentage value of the flow controller (0 - 100%) there is a standard volumetric flow associated. Then if Q is plotted against the percentage value of the flow controller, a straight line is obtained. Finally, a linear least-squares fit using expression (2.32) is performed for each gas (or gas mixture), allowing us to precisely control the flow under our laboratory conditions.

$$Q = a * (0 - 100)\% + b \quad (2.32)$$

The calibrated values obtained for the gases used during this thesis are listed in *Table 2.4*. Then if the theoretical maximum flow of ethane for the flow controller d20 is 49 sccm we have an actual maximum flow of 47.2 sccm using the calibrations performed under our laboratory conditions.

Table 2.4 Calibration parameters for the flow controllers used during this thesis.

Flow Controller	d11 (20slpm)		d41 (10slpm)		d45 (0.1slpm)		d05 (0.020slpm)		d43 (3slpm)	
Gas	a	b	A	b	a	b	a	b	a	b
N ₂	0.211	0.013	0.095	0.042	9.75E-4	-1.9 E-4			0.029	0.025
Ar	0.268	0.373	0.120	0.221	13.7E-4	1.47E-05				
O ₂							2.02E-4	-5.13E-05		
Flow Controller	D14 (0.5slpm)		d852 (0.003slpm)		d20 (0.1slpm)		d35 (0.020slpm)		d52 (0.1slpm)	
O ₂	5.10E-3	-6.60E-06								
N ₂	50.7E-4	4.75E-4								
Ar	73.3E-4	-40.4E-4								
C ₂ H ₄			1.85E-05	4.47E-05						
CO ₂	3.78E-3	1.17E-03			7.02E-4	1.25E-4	1.49E-4	8.83E-04		
C ₂ H ₆	2.62E-3	2.11E-04			4.7E-4	1.96E-4				
D ₂	5.35E-3	-1.9E-05			9.99E-4	3.36E-4				
C ₃ H ₈	1.84E-3	5.40E-04								
H ₂	5.38E-3	7.72E-04					2.08E-4	1.17E-4	9.58E-4	-1.50E-4
C ₂ H ₂	3.24E-3	4.86E-04			5.98E-4	8.83E-04	1.23E-4	3.36E-05	5.76E-4	-1.17E-4
CH ₄	4.08E-3	7.94E-04							7.29E-4	5.64E-4
NO									9.31E-4	2.52E-4

In order to perform these calibrations, two different calibration volumes were used depending on the maximum flow capacities of the flow controllers. For the smallest flows (d05, d852, d20, d35, d52, d45 and d14) a reservoir with a volume around 1800 cm³ was used, while for the largest flows (d11, d41 and d43), the chamber of the CRESU apparatus was used which had an approximate volume of 50000 cm³.

Boyle's law was used to determine the volume of the reservoir and the chamber

$$P_1 * V_1 = P_2 * V_2 \quad (2.33)$$

The chamber/reservoir was maintained under vacuum and connected to a glass balloon that was isolated using a valve. The glass balloon was initially held at atmospheric pressure and room temperature. A pressure gauge was attached to the chamber/reservoir to monitor the changes in pressure when the valve was opened (*Figure 2.12*). Under these conditions, P_1 is the pressure in the balloon (atmospheric pressure), V_1 is its calibrated volume (10.655 L), P_2 is the final pressure in the system and V_2 is the total volume, which is equal to the volume in the chamber/reservoir plus the

volume of the balloon. Finally, the volume in the chamber/reservoir can be calculated through the following expression

$$V_{\text{chamber/reservoir}} = \left(\frac{P_{\text{balloon}} * V_{\text{balloon}}}{P_{\text{final}}} \right) - V_{\text{balloon}} \quad (2.34)$$

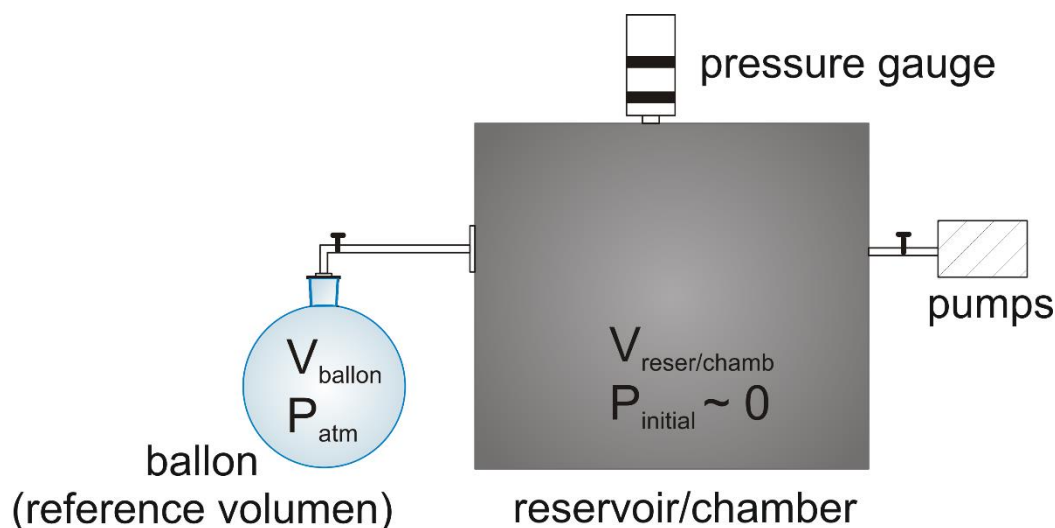


Figure 2.12 Volume calibration setup

2.5. Production of the reactive atoms

The study of neutral-neutral reactions requires the in-situ production of atoms or radicals from a suitable precursor molecule. Although these reactive species can be produced in several ways (pulsed radiolysis, chemical reactions, etc) the most common method employed in CRESU experiments is pulsed laser photolysis (PLP).

This technique employs a pulsed laser, the pump, which generates a short and intense monochromatic laser pulse capable of breaking bonds selectively. Photolysis occurs when the molecule absorbs one or more photons with an energy greater than its bond dissociation energy. Depending on the molecule and the wavelength used for photodissociation, the atoms/radicals might be formed in their ground or excited electronic states. Some advantages associated to the laser photolysis technique for the production of radicals in situ are: the monochromatic nature of the photochemical light source, which provides some control over radical generation by limiting the production of secondary radicals compared with conventional polychromatic sources. In addition, as the laser pulses are generally very short (a few ns) and very intense, radical generation is much more efficient than in experiments employing spontaneous sources.

In this work, the minor reactive species ($C(^1D) + C(^3P)$ and $O(^1D)$) were produced by PLP of precursor molecules CBr_4 and O_3 respectively, using the fourth harmonic of an Nd:YAG laser (Spectra-Physics LAB-150) at 266 nm. The pulse energies ranged from 21 to 26 mJ with a pulse repetition rate of 10 Hz in a 6 mm diameter beam. The photolysis laser was aligned along the supersonic flow to create a column of atoms of uniform density.

The CBr_4 precursor was introduced inside the reactor using a flow of carrier gas over solid CBr_4 held at a known pressure in a separate vessel. The CBr_4 concentrations in the flow were estimated using the expression (2.28):

$$[CBr_4] = \frac{F_{CBr_4}}{F_T} * [nozzle] \quad (2.28)$$

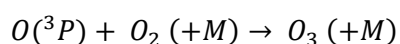
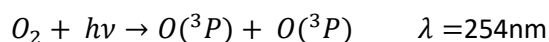
with

$$F_{CBr_4} = F_{cg} * \frac{P_{v_{CBr_4}}}{P_{vessel}} \quad (2.35)$$

where F_{CBr_4} is the flow of CBr_4 from the vessel, F_T the total supersonic flow, $[nozzle]$ the known total concentration of the nozzle (see *Table 2.2*), F_{cg} the flow of carrier gas arriving in the vessel, $P_{v_{CBr_4}}$ the saturated vapor pressure of CBr_4 at room temperature (0.72 Torr) and P_{vessel} the pressure in the vessel, which is set by a needle valve upstream.

The multiphoton dissociation of CBr_4 at 266 nm produces among other fragments $C(^3P)$ and $C(^1D)$ atoms. Previous studies²⁷ performed in the Bordeaux mini-CRESU setup under similar conditions to this work reported a $C(^1D)/C(^3P)$ ratio of (0.15 ± 0.04) and (0.10 ± 0.02) at 296 K and 127 K respectively.

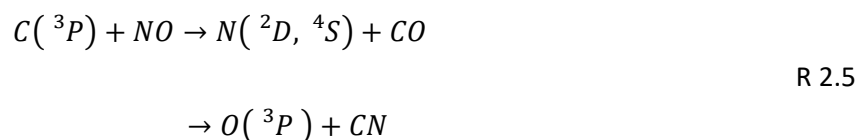
O_3 molecules were synthesized by flowing O_2 into a quartz cell continuously irradiated by a high-pressure mercury lamp (UVP Pen-Ray 3SC-9) producing $O(^3P)$ atoms from O_2 photolysis. Under these conditions, the formation of O_3 occurs through the following mechanism:



The termolecular association reaction was enhanced by using higher pressures (700 Torr). The output of the quartz cell was connected to the reservoir in which all the gases are mixed before entering the

Laval nozzle. O₃ concentrations were estimated to be in the range $(5 - 7) \times 10^{12} \text{ cm}^{-3}$ assuming that 5% of the initial O₂ was photodissociated.²⁸

In chapter 5 of this thesis, a new alternative method to produce metastable N(²D) atoms is proposed with the aim to perform kinetics studies of their reactions. Briefly, N(²D) atoms were generated through the reaction of ground state atomic carbon (product of the photolysis of CBr₄ precursor at 266 nm) with NO molecules



where the ratio $[N(^2D, ^4S)/O(^3P)]$ has been previously estimated to be 1.5 ± 0.3 at room temperature.²⁹ More details of this technique and how it can be used to study the kinetics of a wide range of N(²D) atom reactions are provided in Chapter 5 section 5.2.

2.6. Detection methods coupled with the CRESU technique

Once the atoms or radicals are produced in situ from a suitable precursor in the presence of a much larger known coreactant concentration, the changes in the concentration of the target species must be monitored by spectroscopic techniques such as absorption, laser induced fluorescence and chemiluminescence among others. During this thesis, vacuum ultraviolet laser induced fluorescence (VUV LIF) was the selected technique to determine rate constants and branching ratios given its high sensitivity and selectivity.

2.6.1. Laser induced fluorescence technique

This technique employs a tuneable laser, the probe, to excite the desired species from a lower electronic state to an excited electronic state. The species relaxes back to a lower electronic state through the emission of a photon. These photons are collected using a photomultiplier tube, which is usually positioned perpendicular to the pump and probe lasers to minimize detection of any scattered light from them. The fluorescence can be either at the same wavelength as the excitation source (resonant) or at a different wavelength (non-resonant). For molecular species, both types of fluorescence can be observed given the various vibrational and rotational levels within each of the electronic states. Once the molecules are excited, they can relax into any of the several vibrational levels in the lower electronic state emitting photons at several discrete wavelengths. However, for atomic species, only resonant fluorescence can be observed because they do not have rotational

and/or vibrational energy levels. As the frequency of a laser with a narrow spectral bandwidth is tuned to match the transition of the species to be detected, this excitation is usually very selective. The efficiency of fluorescence is given by the quantum yield, which expresses the relation between the number of emitted and absorbed photons according to the expression:

$$\Phi = \frac{N_{emitted\ photons}}{N_{absorbed\ photons}} \quad (2.36)$$

It is well known that the intensity of fluorescence in a sample is proportional to concentration according to the Beer-Lambert law. Furthermore, the intensity of fluorescence is dependent on the intensity of the incident laser under unsaturated regime conditions;³⁰ as a result, attention should be paid to small fluctuations in the intensity of the laser, which can affect the measured fluorescence intensity.

In this work, the changes in the concentration of the desired atoms were followed by on-resonance VUV LIF. The required wavelength was produced using the second harmonic of an Nd:YAG laser (Quantel YG980) to pump a narrowband dye laser (Quantel TDL 90). The resulting tuneable beam was directed into a Beta Barium Borate (BBO) crystal to double the frequency (SHG), producing UV light that was steered and focused into a cell containing a specific noble gas for frequency tripling (THG). Argon was added for phase matching purposes. (The pressures used in the tripling cell for each rare gas and the excitation wavelength are given in *Table 2.5*). The resulting tuneable VUV light was collimated at the output of the cell by a magnesium fluoride (MgF₂) lens and directed into the chamber. The tripling cell was attached perpendicular to the reactor and the supersonic flow through a 75 cm long sidearm. The sidearm was constantly flushed by Ar or N₂ to avoid attenuation of the VUV beam by reactive gases in the chamber. Furthermore, circular baffles were collocated along the length of the side arm to trap the divergent residual UV radiation.

Table 2.5 Rare gas pressures used to detect H(²S), O(¹D), C(³P) and N(²D) in addition to their transition and transition wavelengths.

Species	H(² S)	O(¹ D)	C(³ P)	N(² D)
Pressures in the tripling cell (torr)	210 Kr 540 Ar	100 Xe 230 Ar	100 Xe 360 Ar	40 Xe 560 Ar
Excitation Wavelength (nm)	121.567	115.215	127.755	116.745
Transitions	1s ² S ½-2p ² P° ½	2p ¹ D-3s ¹ D°	2s ² 2p ² ³ P-2s ² 2p3d ³ D°	2s ² 2p ³ ² D°-2s ² 2p ² (³ P)3d ² F

The fluorescence emission of the sample was collected using a solar blind photomultiplier tube (PMT) that was isolated from the flow reactor by a lithium fluoride (LiF) window. The zone between the window and the PMT was maintained under vacuum to prevent supplementary losses of light by atmospheric absorption. Moreover, a LiF lens was used to focus the fluorescence onto the photocathode of the PMT. With the aim to reduce the collection of scattered light close to the observation zone an arrangement of circular baffles was placed between the supersonic flow and the LiF window in addition to those between the LiF window and the LiF lens.

The reaction kinetics is followed by recording the fluorescence intensity from the sample as a function of delay time between the probe and pump lasers. This delay is controlled by a delay generator (Quantum Composers Model 9518+) which is coupled to a boxcar integrator (Stanford Research System SR250 with module SR280 computer interface). An oscilloscope (Lecroy WaveJet 354A) is used to optimize the fluorescence signal and to place the gate with respect to the fluorescence signal. Instrument control and signal acquisition are controlled using the platform "Laboratory Virtual Instrument Engineering Workbench (LabVIEW)".

The temporal profile of the fluorescence signal is generally composed of more than 70 points, some of them recorded with the probe laser firing before the pump laser to establish the baseline. Each of these points consists of 30 laser shots recorded at each delay time point to reduce the uncertainty in the measurements due to small fluctuations of the laser energy.

A schematic representation of the CRESU setup, including the detection and acquisition systems in our laboratory is shown in *Figure 2.13*. Specific changes in the setup due to the different experimental configurations will be detailed in each chapter.

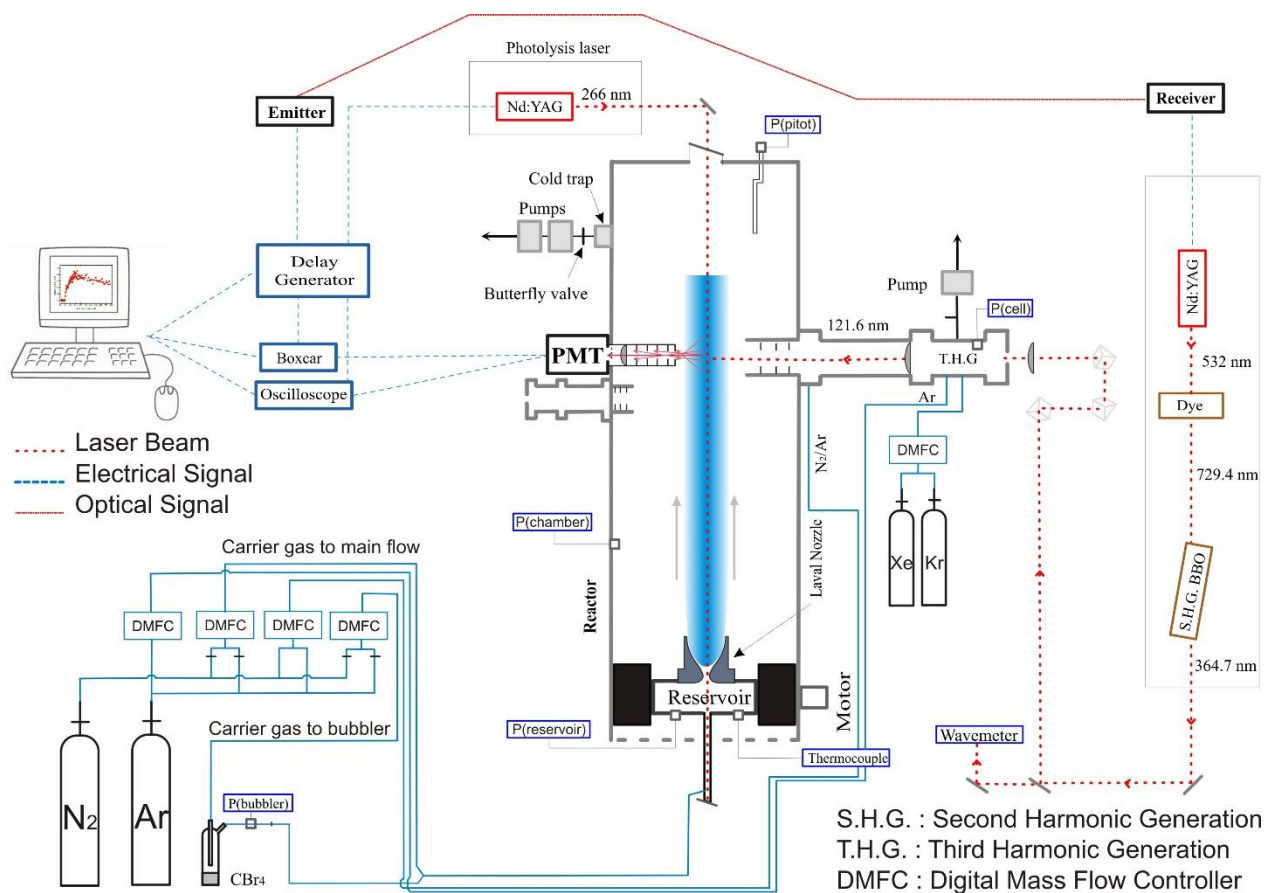


Figure 2.13 Schematic representation of the CRESU apparatus used to follow $H(^2S)$ atom formation at 121.567 nm.

2.7. Determination of errors

The uncertainties on a reported measurement generally consist of the combination of the statistical and systematic errors, which are differentiated depending on the method used to estimate their numerical values.³¹ The statistical errors are determined using statistical methods such as the standard deviation of the mean of a series of measurements, the method of least squares to fit a curve, analysis of variance etc. In contrast, the systematic errors are usually based on scientific judgment according to the available information on the system and they are difficult to determine exactly because they arise through uncontrolled changes during the experiments.

2.7.1. Statistical errors and weighting

The statistical errors on the rate constants were determined in Origin (9.0) software using a least-squares fitting method in which the best fitting curve to a given set of points is found by reducing χ^2 according to the expression:

$$\chi^2 = \sum_{i=1}^n w_i (Y_i - \hat{Y}_i)^2 \quad (2.37)$$

with w_i the weight, Y_i experimental measurements, \hat{Y}_i expected value

The pseudo-first-order rate constants were obtained from a nonlinear fit to the experimental data (section 2.1.1). No weighting was necessary for these determinations because intensity measurements are not ponderable. The second-order rate constant was obtained in a linear fit when the pseudo-first-order rate constants were plotted against the concentration of the reactant in excess (section 2.1.1). In this case, an instrumental weighting was used according to the expression:

$$w_{ji} = \frac{1}{\sigma_{ji}^2} \quad (2.38)$$

Where σ_{ji} is the standard deviation obtained from the pseudo-first-order rate constant in the nonlinear fit to the experimental data. The overall statistical error is based on two stages of analysis, first the determination of the pseudo-first-order rate constant and its associated standard deviation, followed by the use of this standard deviation as the weighting parameter for the determination of the second order rate constant.

The uncertainties on the branching ratios are reported at the 95% confidence level, employing a Student's T distribution. To obtain these uncertainties the critical value t is multiplied by the standard error of the mean. t is obtained depending on the number of degrees of freedom of the sample and the percentage of confidence (95% in this case) and the standard error of the mean is equal to the standard deviation of the sample divided by the square root of the number of measurements.

2.7.2. Systematic errors

Systematic errors in the CRESU experiments arise from a wide range of sources including uncertainties on the calibration of the mass-flow controllers and the subsequent determination of the concentration of the reactants and the total gas density in the flow and errors in other devices such as pressure gauges. Although the mass-flow controllers were calibrated to reduce these effects, there could be still slight fluctuations given by their sensitivity to small variations in the room temperature and other effects. Furthermore, as the supersonic flows are characterized in previous experiments, the establishment of the required flow conditions for each temperature are based on pressure measurements and the pressure gauges could be also sensitive to small changes in room temperature.

Systematic errors in our CRESU experiments are usually estimated to be 10%, obeying a rectangular distribution where it is equally probable that the uncertainty value lies anywhere within the interval $\pm 10\%$. For the experiments where secondary reactions might have influenced the overall rate constant, a value of 20% was used instead.

2.7.3. Combination of statistic and systematic errors

In this thesis, the reported uncertainties in the rate constants consist of a combination of the statistical and systematic errors according to the following expression

$$u(k) = \sqrt{(u_{syst})^2 + \left(\frac{u_{stat}}{k}\right)^2} \times k$$

where u_{stat} is the statistical error and u_{syst} is the systematic error.

This procedure allows us to report an uncertainty, $u(k)$, which depends on the statistical errors result of the mathematical treatment of the data and systematic changes in the measurements such as uncertainties on the estimation of the densities during the experiments.

2.8. Master equations calculations

During the course of this work, statistical calculations employing MESMER (Master Equation Solver for Multi-Energy Well Reactions) code were performed to complement the experimental results. MESMER is an open source code (C++) that uses matrix techniques to formulate and solve the Energy Grained Master Equations for unimolecular systems composed of an arbitrary number of wells, transitions states, sinks and reactants.³²

MESMER uses the energy and structures of the transition states and complexes calculated by quantum chemical calculations to obtain phenomenological rate constants $k(T, P)$ for unimolecular systems. To deduce these rate constants the phase space for all wells on the potential energy surface (PES) is divided into grains of specific width and average energy E_i . The time evolution of these grain populations are then calculated individually to obtain the time evolution for the concentration of each species. The isoenergetic reaction rates between grains of different isomers are calculated using a Rice, Ramsperger, Kassel and Marcus (RRKM) theory for processes with a barrier or using the inverse Laplace Transform (ILT) for a barrierless process. The energy transfer probabilities between different grains of the same species are obtained using an exponential down model parametrized by an energy

independent ΔE_{down} , which represents the average energy transferred in a downward direction upon collision with a bath gas molecule.³²⁻³⁴

Once both reactive and collisional transition probabilities have been obtained from RRKM theory and the exponential down model, the time-resolved change in the grain populations can be described using a set of coupled differential equations with the form given below

$$\frac{d}{dt}p = Mp \quad (2.39)$$

Where p is a vector containing the populations of the grains for each isomer, $n_i(E, t)$, M is the matrix that determines grain population evolution due to collisional energy transfer and reactive loss and gain for each grain. Expression (2.39) shows that the solution of the master equation can be reduced to a standard eigenvalue problem and diagonalization of M yields the corresponding eigenpair solutions. For many chemical systems, it is possible to observe a separation in eigenvalues, with the bulk corresponding to a very fast decay and a selected few corresponding to a slower decay. The eigenvalues for a fast decay correspond to the time scale for relaxation of activated intermediates and are often referred to as internal energy relaxation eigenvalues (IEREs). On the other hand, those for slow decay correspond to the time scale for chemical reaction and are often referred to as chemically significant eigenvalues (CSEs).

Finally, phenomenological rate constants from the master equation are obtained through a modified version of the approach used by Bartis and Widom.^{35,36} Briefly, the phenomenological rate constants for an arbitrary system may be described by a set of coupled differential equations similar to expression (2.39) but fewer in number. The primary difference is the absence of a description for collisional relaxation kinetics (all the rate constants correspond to interconversion between species). Then for a system of j species, the kinetics of the system may be described using a $j \times j$ rate constant matrix, K , representing j coupled first order differential equations, where the matrix element K_{ab} is the rate constant $k_{b \rightarrow a}(T, P)$. Diagonalization of this rate matrix yields a solution of j eigenvalues and j eigenvectors. The Bartis Widom method exploits the separation between the IEREs and the CSEs assuming that the CSEs eigenvalues obtained from the diagonalization of matrix M are identical to those that would be obtained from diagonalization of matrix K . This separation should be bigger than an order of magnitude to obtain reliable Bartis Widom rate constants.³²

MESMER code requires as input

1. The electronic + zero point energies (ZPE) for all the species. In the case of an association reaction (A + B) the ZPE is the sum of the associated species ZPEs.
2. The vibrational and rotational constants of all the species in the reaction that are not treated as sinks. The sink molecules are defined in the code as the products of an irreversible reaction.
3. The masses of the species
4. Symmetry number, spin multiplicity
5. Scaling factors (to correct for electron correlation effects)
6. The depth of the well and the barrier height
7. Leonard Jones collision parameters σ and ϵ (required to define the collision frequency)
8. ΔE_d (to calculate the rate of collisional energy transfer in a given molecule)

Parameters from 1 to 6 are extracted from the quantum chemical calculations. Number 7 (Leonard Jones parameters) are necessary inputs for bath gases and species declared as modelled (molecules that may undergo relaxation via collisions with the bath gas). These parameters are set to the default values in the code or they can be found in the literature. Number 8, the exponential down energy transfer parameter (ΔE_d) is often dependent on temperature according to expression (2.40). This parameter is adjusted depending on the experimental data.

$$\Delta E_d = \langle \Delta E \rangle_{d,ref} \left(\frac{T}{T_{ref}} \right)^n \quad (2.40)$$

where T is the temperature, T_{ref} is the reference temperature equal to 298 K, n is an exponent governing the temperature dependence and $\langle \Delta E \rangle_{d,ref}$ is usually floated with n to find a good reproducibility of the experimental data.

In this work, to calculate the density of states, the external rotations of all the species are considered to be rigid rotors whilst vibrational modes were treated as harmonic oscillators. In addition to the RRKM formalism, tunnelling corrections using the semiclassical method described by Garrett and Truhlar³⁷ (WKB) were included.

Tunnelling is a quantum mechanical phenomenon whereby reactants which do not have sufficient energy to surmount the potential energy barrier can still react as there is a non-zero probability for reaction to occur. This phenomenon plays an important role at a low temperature allowing several reactions characterized by a barrier to occur.^{21,38,39}

The probability of tunnelling is described by the transmission coefficient $k(E)$. This coefficient decreases exponentially with the height and the width of the potential energy barrier and with the square root of the particle mass.⁴⁰

In this work, to calculate the tunnelling probabilities the semiclassical WKB method is used. This method is a one-dimensional method because tunnelling is considered only along one coordinate, the mass-weighted intrinsic reaction coordinate (IRC). Then, only the change in potential energy along the IRC coordinate is required to obtain the rate constants. The WKB method requires a number of ab-initio points along the minimum energy path in order to represent the true shape of the potential energy barrier. In this method, numerical integration is performed over the exact ab initio barrier defined by the electronic structure calculations. Then the tunnelling probabilities are given by the following expression

$$k(E) = \frac{1}{1 + \exp[2\theta(E)]} \quad (2.41)$$

where

$$\theta(E) = \frac{2\pi}{h} \int_{S_1}^{S_2} \sqrt{\mu(E - V)} ds \quad (2.42)$$

h is the Planck constant, μ is the reduced mass, S_1 and S_2 are the classical turning points along the reaction coordinate S , E is the energy of the grain, V is the barrier height.

As the width and height of the potential energy barrier can vary significantly with the level of theory used to calculate them, these parameters are usually allowed to vary to find a good agreement with the experimental data. In general, master equation calculations are a valuable tool to complement experimental results because they offer a reliable way of extrapolating existing rate constants down to very low temperatures and pressures, conditions that can be difficult to achieve experimentally.

2.9. References

- (1) Smith, I. W. M. Laboratory Astrochemistry: Gas-Phase Processes. *Annu. Rev. Astron. Astrophys.* **2011**, *49*, 29–66.
- (2) Atkins, P.; de Paula, J. *Physical Chemistry*, Ninth Edit.; 2010.
- (3) Laidler, K. J. *Chemical-Kinetics*, Third Edit.; Pearson, 1987.
- (4) Smith, I. W. M. Neutral/Neutral Reactions without Barriers: Comparisons with Ion/Molecule Systems and their Possible Role in the Chemistry of Interstellar Clouds. *Int. J. Mass Spectrom. Ion Process.* **1995**, *149/150*, 231–249.
- (5) Sims, I. R.; Queffelec, J. L.; Travers, D.; Rowe, B. R.; Herbert, L. B.; Karthäuser, J.; Smith, I. W. M. Rate Constants for the Reactions of CN with Hydrocarbons at Low and Ultra-Low Temperatures. *Chem. Phys. Lett.* **1993**, No. 4–5, 461–468.
- (6) Sims, I. R.; Smith, I. W. M. Gas-Phase Reactions and Energy Transfer at Very Low Temperatures. *Annu. Rev. Phys. Chem.* **1995**, *46*, 109–138.
- (7) Georgievskii, Y.; Klippenstein, S. J. Strange Kinetics of the C₂H₆ + CN Reaction Explained. *J. Phys. Chem. A* **2007**, *111*, 3802–3811.
- (8) Sims, I. R. Tunnelling in Space. *Nat. Publ. Gr.* **2013**, *5*, 734–736.
- (9) Fournier, M.; Picard, S. D. L. E.; Sims, I. R. Low-temperature Chemistry in Uniform Supersonic Flows. In *Cold Chemistry Molecular Scattering and Reactivity Near Absolute Zero*; Dulieu, O., Osterwalder, A., Eds.; The Royal Society of Chemistry, 2018; pp 1–42.
- (10) Seakins, P. W. Product Branching Ratios in Simple Gas Phase Reactions. *Annu. Chem., Sect. C* **2007**, *103*, 173–222.
- (11) Howard, C. J. Kinetic Measurements Using Flow Tubes. *J. Phys. Chem.* **1979**, *83*, 3–9.
- (12) Hickson, K. M.; Bergeat, A. Low Temperature Kinetics of Unstable Radical Reactions. *Phys. Chem. Chem. Phys.* **2012**, *14*, 12057–12069.
- (13) Naulin, C.; Bergeat, A. Low-energy Scattering in Crossed Molecular Beams. In *Cold Chemistry Molecular Scattering and Reactivity Near Absolute Zero*; Dulieu, O., Osterwalder, A., Eds.; The

- Royal Society of Chemistry, 2018; pp 92–146.
- (14) Smith, I. W. M.; Rowe, B. R. Reaction Kinetics at Very Low Temperatures: Laboratory Studies and Interstellar Chemistry. *Accounts Chem. Res.* **2000**, *33*, 261–268.
- (15) Rowe, B. R.; Dupeyrat, G.; Marquette, J. B.; Gaucherel, P. Study of the Reactions $\text{N}_2^+ + 2\text{N}_2 \rightarrow \text{N}_4^+ + \text{N}_2$ and $\text{O}_2^+ + 2\text{O}_2 \rightarrow \text{O}_4^+ + \text{O}_2$ from 20 to 160 K by the CRESU Technique. *J Chem Phys* **1984**, *80*, 4915–4921.
- (16) Sims, I. R.; Queffelec, J. L.; Defrance, A.; Rebrionrowe, C.; Travers, D.; Rowe, B. R.; Smith, I. W. M. Ultralow Temperature Kinetics of Neutral–Neutral Reactions : The Reaction $\text{CN} + \text{O}_2$ down to 26 K. *J. Chem. Phys.* **1992**, *97*, 8798–8800.
- (17) Potapov, A.; Canosa, A.; Jiménez, E.; Rowe, B. Uniform Supersonic Chemical Reactors: 30 Years of Astrochemical History and Future Challenges. *Angew. Chemie - Int. Ed.* **2017**, *56*, 8618–8640.
- (18) Molecules in Space <https://www.astro.uni-koeln.de/cdms/molecules>.
- (19) Rowe, B.-R.; Marquette, J. B.; Dupeyrat, G. Reactions of He^+ and N^+ Ions with Several Molecules at 8 K. *Chem. Phys. Lett.* **1985**, *113*, 403–406.
- (20) Chastaing, D.; James, P. L.; Sims, I. R.; Smith, I. W. M. Neutral – Neutral Reactions at the Temperatures of Interstellar Clouds. *Faraday Discuss.* **1998**, *109* (165–181).
- (21) Tizniti, M.; Le Picard, S. D.; Lique, F.; Berteloite, C.; Alexander, M. H.; Sims, I. R. The Rate of the $\text{F} + \text{H}_2$ Reaction at Very Low Temperatures. *Nat. Chem.* **2014**, *6*, 141–145.
- (22) Atkinson, D. B.; Smith, M. A. Design and Characterization of Pulsed Uniform Supersonic Expansions for Chemical Applications. *Rev. Sci. Instrum.* **1995**, *66*, 4434–4446.
- (23) Oldham, J. M.; Abeysekera, C.; Joalland, B.; Zack, L. N.; Prozument, K.; Sims, I. R.; Park, G. B.; Field, R. W.; Suits, A. G. A chirped-pulse Fourier-transform microwave / pulsed uniform flow spectrometer . I . The low-temperature flow system. *J. Chem. Phys.* **2014**, *141*, 1–7.
- (24) Cheikh, S.; Ely, S.; Morales, B.; Guillemin, J.; Klippenstein, S. J.; Sims, I. R. Low Temperature Rate Coefficients for the Reaction $\text{CN} + \text{HC}_3\text{N}$. *J. Phys. Chem. A* **2013**, *117*, 12155–12164.
- (25) Jiménez, E.; Ballesteros, B.; Canosa, A.; Townsend, T. M.; Maigler, F. J.; Napal, V.; Rowe, B. R.

- Development of a Pulsed Uniform Supersonic Gas Expansion System Based on an Aerodynamic Chopper for Gas Phase Reaction Kinetic Studies at Ultra-low Temperatures. *Rev. Sci. Instrum.* **2015**, *86*, 045108.
- (26) Daugey, N.; Caubet, P.; Retail, B.; Costes, M.; Bergeat, A.; Dorthe, G. Kinetic Measurements on Methylidyne Radical Reactions with Several Hydrocarbons at Low Temperatures. *Phys. Chem. Chem. Phys.* **2005**, No. 7, 2921–2927.
- (27) Shannon, R. J.; Cossou, C.; Loison, J.-C.; Caubet, P.; Balucani, N.; Seakins, P. W.; Wakelam, V.; Hickson, K. M. The Fast $C(^3P) + CH_3OH$ Reaction as an Efficient Loss Process for Gas-Phase Interstellar Methanol. *RSC Adv* **2014**, *4*, 26342–26353.
- (28) Grondin, R.; Loison, J.-C.; Hickson, K. M. Low Temperature Rate Constants for the Reactions of $O(^1D)$ with N_2 , O_2 , and Ar. *J. Phys. Chem. A* **2016**, *120*, 4838–4844.
- (29) Bergeat, A.; Calvo, T.; Dorthe, G.; Loison, J.-C. Fast-Flow Study of the $C + NO$ and $C + O_2$ Reactions. *Chem. Phys. Lett.* **1999**, *308*, 7–12.
- (30) Lytle, F. E. *Lasers in Chemical Analysis*; The Humana Press; Clifton, New Jersey, 1981.
- (31) Taylor, B. N.; Kuyatt, C. E. Guidelines for Evaluating and Expressing the Uncertainty of NIST Measurement Results. *NIST Tech. Note 1297* **1994**, 1–20.
- (32) Glowacki, D. R.; Liang, C.; Morley, C.; Pilling, M. J.; Robertson, S. H. MESMER: An Open-Source Master Equation Solver for Multi-Energy Well Reactions. *J. Phys. Chem. A* **2012**, *116*, 9545–9560.
- (33) Shannon, R. J.; Caravan, R. L.; Blitz, M. A.; Heard, D. E. A Combined Experimental and Theoretical Study of Reactions Between the Hydroxyl Radical and Oxygenated Hydrocarbons Relevant to Astrochemical Environments. *Phys.Chem.Chem.Phys.*, **2014**, *16*, 3466–3478.
- (34) Shannon, R. J. Experimental and Computational Studies of Hydroxyl Radical Kinetics at Very Low Temperatures, The University of Leeds, 2012.
- (35) Bartis, J. T.; Widom, B. Stochastic Models of the Interconversion of Three or more Chemical Species. *J. Chem. Phys.* **1974**, *60*, 3474–3482.
- (36) Robertson, S. H.; Pilling, M. J.; Jitariu, L. C.; Hillier, I. H. Master Equation Methods for Multiple

-
- Well Systems: Application to the 1-,2-pentyl System. *Phys. Chem. Chem. Phys.* **2007**, *9*, 4085–4097.
- (37) Truhlar, B. C. G. and D. G. Semiclassical Tunneling Calculations. *J. Phys. Chem.* **1979**, *83*, 2921–2926.
- (38) Shannon, R. J.; Blitz, M. A.; Goddard, A.; Heard, D. E. Accelerated Chemistry in the Reaction Between the Hydroxyl Radical and Methanol at Interstellar Temperatures Facilitated by Tunnelling. *Nat. Chem.* **2013**, *5*, 745–749.
- (39) Caravan, R. L.; Shannon, R. J.; Lewis, T.; Blitz, M. A.; Heard, D. E. Measurements of Rate Coefficients for Reactions of OH with Ethanol and Propan-2-ol at Very Low Temperatures. *J. Phys. Chem. A* **2015**, *119*, 7130–7137.
- (40) Bell, R. P. *The Tunnel Effect in Chemistry*, Chapman and Hall, 1980.

Chapter 3.

The reactivity of carbon atoms

3.1	Experimental details	68
3.1.1	Generation of atomic carbon and detection procedures.....	68
3.1.2	Temperature range	69
3.1.3	Experimental details of the ground state carbon atoms + water reaction	69
3.1.4	Branching ratio procedure	70
3.1.5	Gases	71
3.2	The C(³P) + H₂O/D₂O reactions.....	72
3.2.1	Results	74
3.2.1.1	Rate constants	74
3.2.1.2	Branching ratios.....	77
3.2.1.3	MESMER calculations	82
3.2.2	Discussion	84
3.2.3	Relevance of the C(³ P) + H ₂ O reaction in the interstellar medium.....	85
3.3	The C(¹D) + CH₄/C₂H₆ reactions	87
3.3.1	Results	89
3.3.1.1	Rate constants	89
3.3.1.2	Influence of secondary reactions.....	91
3.3.1.3	H-atom yields.....	92
3.3.2	Discussion	93
3.3.2.1	The C(¹ D) + CH ₄ reaction	93
3.3.2.2	The C(¹ D) + C ₂ H ₆ reaction	95
3.4	The C(¹D) + CO₂ reaction	96
3.4.1	Results	97

3.4.2	Discussion	100
3.5	The C(¹D) + HD reaction.....	101
3.5.1	Results	101
3.5.1.1	Rate constants	102
3.5.1.2	CD/CH branching ratio	104
3.5.2	Discussion	105
3.6	The C(¹D)+NO/O₂ reactions.....	107
3.6.1	Results	108
3.6.1.1	Rate constants	108
3.6.1.2	Influence of secondary reactions.....	110
3.6.1.3	Numerical simulations	112
3.6.2	Discussion	116
3.7	Astrochemical implications	118
3.8	References	119

3. The reactivity of carbon atoms

Carbon is the fourth most abundant element in the universe after hydrogen, helium and oxygen.¹ The reactions of carbon in its ground electronic state (3P) have been extensively studied given their importance in the chemistry of planetary atmospheres,² the interstellar medium³ and in combustion processes.⁴ Conversely, reactions of the first electronic excited state, 1D , have been less well characterized mostly due to the difficulty to find a clean source to produce these atoms.⁵ Very recently, Hickson and coworkers initiated a series of measurements to investigate reactive and non-reactive processes involving $C(^1D)$.⁵⁻⁸

$C(^1D)$ reactions are unlikely to play a role in the gas-phase chemistry of the interstellar medium because its radiative lifetime (3230 s)⁹ is much shorter than the time between collisions, so that these atoms radiatively relax to the ground state before reacting. However, these atoms might play a role in the chemistry of planetary atmospheres such as Titan, the largest moon of Saturn. In planetary atmospheres, excited state carbon atoms can be created by the short-wavelength photodissociation of simple carbon-containing molecules. In this regard, modelling studies¹⁰ of Titan's atmosphere predict a high mole fraction of tricarbon, $C_3(^1\Sigma_g^+)$, reaching values as high as 10^{-5} at altitudes around 800 km. This molecule photodissociates in the VUV range to produce either $C(^3P)$ or $C(^1D)$ as spin allowed products. Additionally, in the Martian atmosphere, CO molecules arising from the photodissociation of CO_2 (the major constituent) can subsequently photodissociate below 100 nm to produce $C(^1D)$ atoms in significant quantities.¹¹ This finding suggests that these atoms might also play a small role in the gas-phase chemistry of Mars.

Atomic carbon in its 1D and 3P states reacts readily with unsaturated hydrocarbon molecules such as C_2H_2 , C_2H_4 , C_3H_6 , etc by addition to the π bonds.¹²⁻¹⁶ In contrast, $C(^3P)$ atoms are unreactive towards saturated hydrocarbon molecules such as CH_4 , whereas $C(^1D)$ atoms react with these molecules through a barrierless insertion into the C-H bonds.⁹ While some experimental studies of $C(^1D)$ atom reactions have been performed at room temperature^{15,17} there is a lack of knowledge about its reactivity at low temperatures. Moreover, though the reactivity of $C(^3P)$ atoms with open shell molecules such as NO or towards biradicals such as O_2 have been investigated previously,¹⁸ little is known about the reactivity of these molecules with $C(^1D)$ atoms. To the best of our knowledge, there are no low temperature kinetics studies involving the reaction of $C(^1D)$ with CO_2 , a process which might play a role in the gas-phase chemistry of the Martian atmosphere. Recently the reactions of $C(^1D)$ with H_2 and D_2 have been studied^{7,8} down to 50 K providing new experimental information and consequently renewing the theoretical interest in these systems. However as far as we know there is no experimental

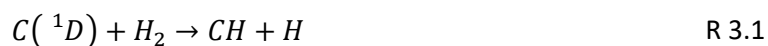
information regarding the kinetics and isotopic branching ratios for the $C(^1D) + HD$ reaction at low temperature. To address these issues in this chapter, the reactions of $C(^1D)$ with CH_4 , C_2H_6 , O_2 , NO , HD and CO_2 have been investigated over the 50 - 296 K temperature range.

In recent years there has been a growing interest in the study of reactions characterized by barriers at the low temperature of the interstellar medium. Several gas-phase processes between neutral species have been investigated to date showing the non-negligible role of these reactions at temperatures and pressures relevant to dense interstellar clouds.¹⁹⁻²⁴ $C(^3P)$ has been observed in dense interstellar clouds through its ground state fine structure line emission at 492 GHz,²⁵ indicating that it could be one of the most abundant species in these regions. Moreover, water has been observed in dark clouds such as TMC-1 and L134N typically with an upper limit of the abundance in the range 10^{-7} - 10^{-8} with respect to H_2 .^{26,27} In this chapter, the reactions of ground state carbon (3P) with water (H_2O) and deuterated water (D_2O) have been experimentally studied down to 50 K with the aim to shed light on the mechanism of this reaction at the low temperatures of the interstellar medium. Moreover, master equations calculations were performed to help our understanding of the reaction mechanism and to extrapolate the rate constants to the low temperatures and pressures that characterize the interstellar medium.

3.1. Experimental details

3.1.1. Generation of atomic carbon and detection procedures

In this chapter, the kinetics of atomic carbon in collisions with several molecules have been investigated in the mini-continuous CRESU setup of Bordeaux. The 3P and 1D states of atomic carbon were generated in situ by multiphoton dissociation of CBr_4 at 266 nm. For ground state atomic carbon, (3P), it is possible to study the reaction kinetics following directly the decay of $C(^3P)$ atoms as a function of time by VUV LIF at 127.755 nm via the $2s^22p^2\ ^3P-2s^22p3d\ ^3D^{\circ}$ transition. Consequently, the pseudo-first-order rate constants can be extracted by fitting the experimental curves to expression (2.5). However, in the case of the first excited state (1D), the identified electronic transition within the VUV wavelength ranges where tripling techniques are efficient is itself very weak, with an Einstein coefficient 10 times smaller than the one for $C(^3P)$ ($10^8\ s^{-1}$). Then to study the kinetics of these reactions two alternative methods can be employed. Firstly, if H-atoms are produced in the reaction (without H-atoms produced from $C(^3P)$ reactions) the kinetics can be studied by following H-atom formation instead and fitting the temporal profiles using expression (2.9). This is the case for the $C(^1D) + CH_4$, C_2H_6 and HD reactions. Secondly, a chemical tracer method can also be employed in which H_2 or CH_4 are added to the system in fixed quantities alongside the target excess reagent.



Processes R 3.1 and R 3.2 produce H-atom yields close to unity.^{7,28} These H-atoms are detected by VUV LIF using the Lyman α transition at 121.567 nm (121.534 nm for D(²S)) and by applying expression (2.9), the pseudo-first-order rate constant for H-atom formation can be obtained. Although C(³P) is the major atomic product of the photodissociation of CBr₄ at 266 nm, its reactions with H₂ and CH₄ under the conditions of the present experiments can be discarded because the C(³P) + H₂ reaction is endothermic by 95 kJ/mol⁷ and the C(³P) + CH₄ reaction is characterized by an activation barrier of 51 kJ/mol.²⁹ This chemical tracer method was employed to follow the kinetics of the C(¹D) + NO, O₂ and CO₂ reactions.

3.1.2. Temperature range

For the reaction of C(³P) atoms with water, four Laval nozzles (Mach2 N₂, Mach3 N₂, Mach3 Ar and Mach4 Ar) were employed using N₂ and Ar as carrier gases to generate flows with characteristic temperatures of 127 K, 106 K, 77 K, 75 K, 52 K and 50 K. In contrast, for the studies of C(¹D) atom reactions, only argon based Laval nozzles could be used given the fast quenching of C(¹D) by collisions with N₂.³⁰ Though it would be advantageous to use He as a carrier gas in these experiments given the inefficient electronic quenching of excited atoms by this rare gas,³¹ we do not possess any He based Laval nozzles in our laboratory. The characteristics of the supersonic flows produced by each Laval nozzle employed in this study can be seen in Table 2.2. Room temperature experiments were performed by removing the Laval nozzle and by reducing the flow velocity to 73 cm s⁻¹ eliminating temperature and pressure gradients within the flow. This velocity was still high enough to ensure that the gas in the probe region was always replenished between laser shots. In these room temperature experiments, the CRESU chamber was used as a conventional slow-flow flash photolysis system.

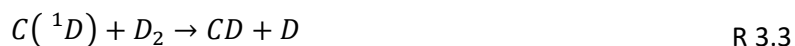
3.1.3. Experimental details of the ground state carbon atoms + water reaction

To study the C(³P) + H₂O reaction, a known flow of liquid water was passed into a controlled evaporation mixing (CEM) system held at 373 K. A small flow of Ar or N₂ was also passed to carry the water vapour into the reactor. The output of the CEM was flowed into a 10 cm absorption cell held at room temperature to determine the water vapour concentration by absorption using the 185 nm line of a mercury pen-ray lamp. The attenuation of the mercury lamp was measured with water (I) and without water (I₀) using a channel photomultiplier (CPM) operating in photon counting mode and with an interference filter centred at 185 nm to block radiation from other mercury lines. Then the

concentration was determined using the Beer-Lambert Law (expression 2.17) with the cross-section of water vapour equal to $6.87 \times 10^{-20} \text{ cm}^2$.³² The output of the absorption cell was connected to the reactor using a heating hose maintained at 353 K to avoid condensation. Furthermore, as the water vapour was diluted in the carrier gas we assume that no supplementary condensation losses occurred upstream of the Laval nozzle. In the case of the $\text{C}(^3\text{P}) + \text{D}_2\text{O}$ reaction, we could not introduce D_2O vapour in the same way as H_2O vapour because a large volume was necessary for the CEM reservoir. Furthermore, the absorption cross section of D_2O is almost an order of magnitude smaller than the one for H_2O at 185 nm, which would not allow us to determine the concentration spectroscopically. Instead, liquid D_2O was held in a bubbler at room temperature and a known pressure while a small flow of Ar or N_2 was used to carry the D_2O vapour into a cold trap held at 288 K to ensure that a saturated vapour pressure of D_2O ³³ reached the Laval nozzle reservoir. This procedure allowed us to accurately determine the D_2O concentration.

3.1.4. Branching ratio procedure

For the $\text{C}(^1\text{D}) + \text{CH}_4$, C_2H_6 , HD and $\text{C}(^3\text{P}) + \text{H}_2\text{O}/\text{D}_2\text{O}$ reactions, branching ratio studies have been performed by following H or D-atom formation and by comparing this signal intensity with the signal intensity produced by the reference reactions R 3.1,⁷ R 3.3⁸ and R 3.4³⁴ respectively. These reference reactions are known to have H/D-atom yields close to 100%.



To determine the branching ratios for these reactions, several pairs of pseudo-first-order curves for the target and reference reaction were alternately obtained under the same conditions, to avoid variations in the fluorescence intensity as a function of the experiment time. The pseudo-first-order rate constant for the target ($k'_{T_{\text{targ}}}$) and the reference ($k'_{r_{\text{ref}}}$) reactions were adjusted to the same value

$$k'_{T_{\text{targ}}} = k'_{r_{\text{ref}}} = k_{T_{\text{targ}}}[B] + k_{L(A)} = k_{r_{\text{ref}}}[L] + k_{L(A)}$$

where A is the minor reagent $\text{C}(^1\text{D})$ and $\text{C}(^3\text{P})$; B is the excess reactant from the target reaction (CH_4 , C_2H_6 , H_2O and D_2O); L is the excess reactant from the reference reaction (C_2H_4 , H_2); k_T represents the overall second-order rate constant for the target multichannel reaction; $k_{L(A)}$ represents the loss of the minor reagent.

This method relies on the assumption that A losses due to secondary reactions and diffusion from the reaction zone can be considered to be the same and small compared with the loss due to reaction with

the excess reactant, thus assuring that secondary processes do not affect the $k'_{T_{targ}}$ value. Under these conditions, when the target and reference reactions, fitted using expression (2.9.1) (see Chapter 2), are divided it is possible to simplify the equivalent terms

$$Br = \frac{\frac{k'_1[A]_0}{k'_{T_{targ}} - k_{L(H)}} \left(e^{-k_{L(H)}t} - e^{-(k'_{T_{targ}})t} \right)}{\frac{k'_{ref}[A]_0}{k'_{ref} - k_{L(H)}} \left(e^{-k_{L(H)}t} - e^{-(k'_{ref})t} \right)}$$

with k'_1 the pseudo-first-order rate constant for the exit channel that leads to H-atom production, $k_{L(H)}$ the loss of H-atoms.

Finally as $k'_{ref} = k'_{T_{targ}}$ we get the branching ratio expression

$$Br = \frac{k'_1}{k'_{T_{targ}}} = \frac{k_1 [B]}{k_{T_{targ}} [B]} = \frac{k_1}{k_1 + k_2 + k_3 + k_4}$$

Using this procedure the branching ratio can be extracted in two equivalent ways. Firstly from the ratio of the pre-exponential factors for the target and reference reaction after correction by absorption if necessary (see Chapter 2 section 2.2.2). Secondly, from the ratio of the H-atom signals for the target and reference reactions at any given delay time, performing a linear fit with the slope set to zero.

3.1.5. Gases

The gases used in the experiments were not purified prior use. The suppliers and the purities are

- ✓ Linde O₂ (99.999%), Ar (99.999%), Xe (99.998%), CO₂ (99.998%), Kr (99.99%), CH₄ (99.9995%), D₂ (99.8%), C₂H₆ (99.5%)
- ✓ Sigma-Aldrich HD (98% atom D)
- ✓ Messer C₂H₂ (99.6%)
- ✓ Air Liquide H₂ (99.9999%), N₂ (99.9999%), NO (99.9%).

3.2. The $C(^3P) + H_2O/D_2O$ reactions

Water is one of the most studied molecules on Earth and in our solar system. The first observation of interstellar water vapour was in 1969 in the Orion nebula,³⁵ and following its detection, significant efforts have been devoted to understand its formation and destruction processes.³⁶ As the gas-phase abundances of water and atomic carbon are high in dense interstellar clouds (10^{-7} - 10^{-8} and 10^{-4} - 10^{-5} ranges respectively),²⁶ the $C(^3P) + H_2O$ reaction could play an important role in the chemical evolution of these regions. The $C(^3P) + H_2O$ system has been previously studied using ab-initio calculations.^{37,38} These studies and the one performed in our group³⁹ showed that the approach of carbon to the water molecule is barrierless allowing a prereactive complex to be formed prior to a barrier to reaction (Figure 3.1).

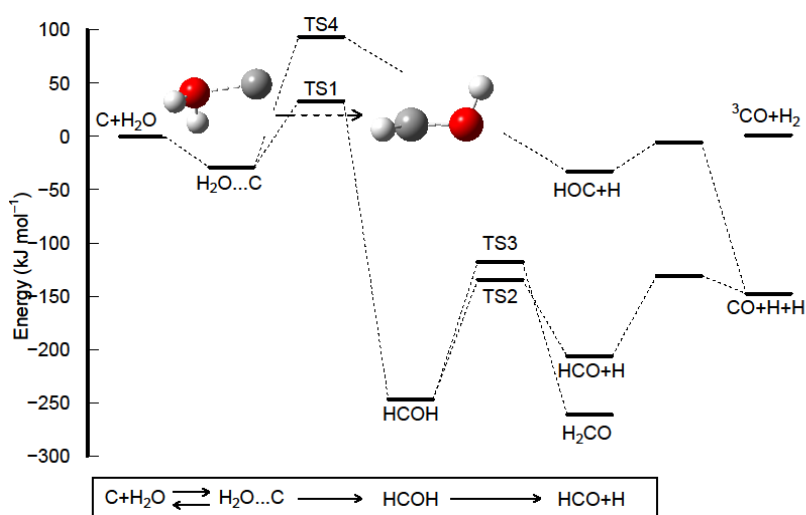


Figure 3.1 Schematic representation of the PES for the $C(^3P) + H_2O$ system extracted from Hickson et al.³⁹

For many years it was thought that reactions characterized by barriers become negligibly slow at low temperatures, obeying Arrhenius law. Nowadays it is known that certain complex forming processes involving light atoms are enhanced at low temperatures.¹⁹⁻²⁴ Classically, if there is a barrier on the PES upon which reaction occurs, the barrier acts as a bottleneck to reaction and only molecules with sufficient energy are able to surmount this barrier and proceed to products. However, when quantum effects are taken into account, species are able to penetrate through the potential barrier that is higher in energy than the reactants energy, a phenomenon that is known as quantum mechanical tunnelling (QMT). Indeed, the wave functions describing the reaction intermediates of complex-forming reactions only fall to zero for barriers of infinite height. Then as the wave functions decay exponentially with

distance there is a non-negligible probability that the species can be found on the product side if the barrier is sufficiently thin.⁴⁰

Recent studies on the reactivity of the hydroxyl radical (OH) towards several organic molecules^{19–23} (methanol, ethanol, 2-propanol, etc.) and the reaction of fluorine atoms with hydrogen²⁴ performed at very low temperatures demonstrated that the rate constants for these processes are sometimes enhanced by several orders of magnitude compared with those expected from Arrhenius fits to higher temperature data. Two features characterize these processes, firstly the formation of a weak van der Waal's prereactive complex and secondly an overall barrier to reaction. For example, in the case of the OH + CH₃OH system, ab initio calculations show that the formed prereactive complex is stabilized by 20 kJ/mol with respect to the reagent level. This system presents barriers separating reagents from products of around 4 and 15 kJ/mol with respect to the reagent energy.⁴¹ Around room temperature and above, the weakly bound complexes have generally a short lifetime due to their high internal energy. The most probable outcomes are passage over the barrier and/or redissociation to reagents. However, at low temperature, the complex lifetime increases and as passage over the barrier is inhibited because the reagents do not have sufficient energy to surmount the activation barrier, then the exothermic product channels might be accessible by QMT through the barrier.

In these previous studies there is clear evidence of the reactivity increase at low temperatures and ab initio calculations have demonstrated that the most probable reaction pathways involve H-atom transfer.^{19,21,22,41,42} However, there is still a lack of quantitative information regarding the fate of the reagents. For the systems described above there are several possible outcomes; either the prereactive complex can be stabilized through non-reactive collisions with the carrier gas, undergo chemical reaction through QMT or a combination of both effects. In this regard, product formation has only been demonstrated for two systems (OH + CH₃OH and F + H₂ reactions)^{19,24} with neither of these studies providing quantitative yields.

It is well known that the tunnelling probability decreases with the particle mass⁴⁰ leading to slower rate constants for reactions involving heavier isotopic variants and consequently noticeable Kinetic Isotope Effects (KIE). While Shannon et al.¹⁹ attempted unsuccessfully to measure the KIE in experiments using CH₃OH/CD₃OD, a noticeable KIE has been observed for the OH/OD + CO^{43,44} and C₂H + CD₄/CH₄⁴⁵ reactions. In the latter case,⁴⁵ a positive temperature dependence was observed (Arrhenius behaviour) and consequently QMT appears to be negligible over the studied temperature range (154 - 359 K). The slower measured rates for the C₂H + CD₄ reaction⁴⁵ were explained by the larger separation between the zero point energy (ZPE) of the reagents and the barrier height of the respective reaction complexes when deuterated methane was employed. Indeed, ab-initio calculations for this system⁴⁶

do not predict the formation of a prereactive complex reinforcing the idea that such intermediates could play an important role in raising the tunnelling probability.

In this work, we investigated the reactivity of ground state atomic carbon with water (H_2O) and deuterated water (D_2O) down to 50 K to see if an increase of the reactivity at low temperature could be observed due to QMT given the similarities of these systems with the above-explained ones. In addition, master equation calculations were performed to shed some light on the reaction mechanism.

3.2.1. Results

To study the $\text{C}(^3\text{P}) + \text{H}_2\text{O}$ reaction two types of experiments were performed, kinetic measurements and branching ratio determinations. To apply the pseudo-first-order approximation, the water/deuterated water concentrations were maintained in a large and known excess with respect to the $\text{C}(^3\text{P})$ concentration.

3.2.1.1. Rate constants

The kinetics of these reactions were followed directly detecting the $\text{C}(^3\text{P})$ emission at 127.755 nm as a function of time as shown in *Figure 3.2* Panels A and C. Without added $\text{H}_2\text{O}/\text{D}_2\text{O}$, carbon atoms are lost primarily through diffusion from the detection region and when an excess of $\text{H}_2\text{O}/\text{D}_2\text{O}$ is added to the flow the carbon atom losses are clearly enhanced.

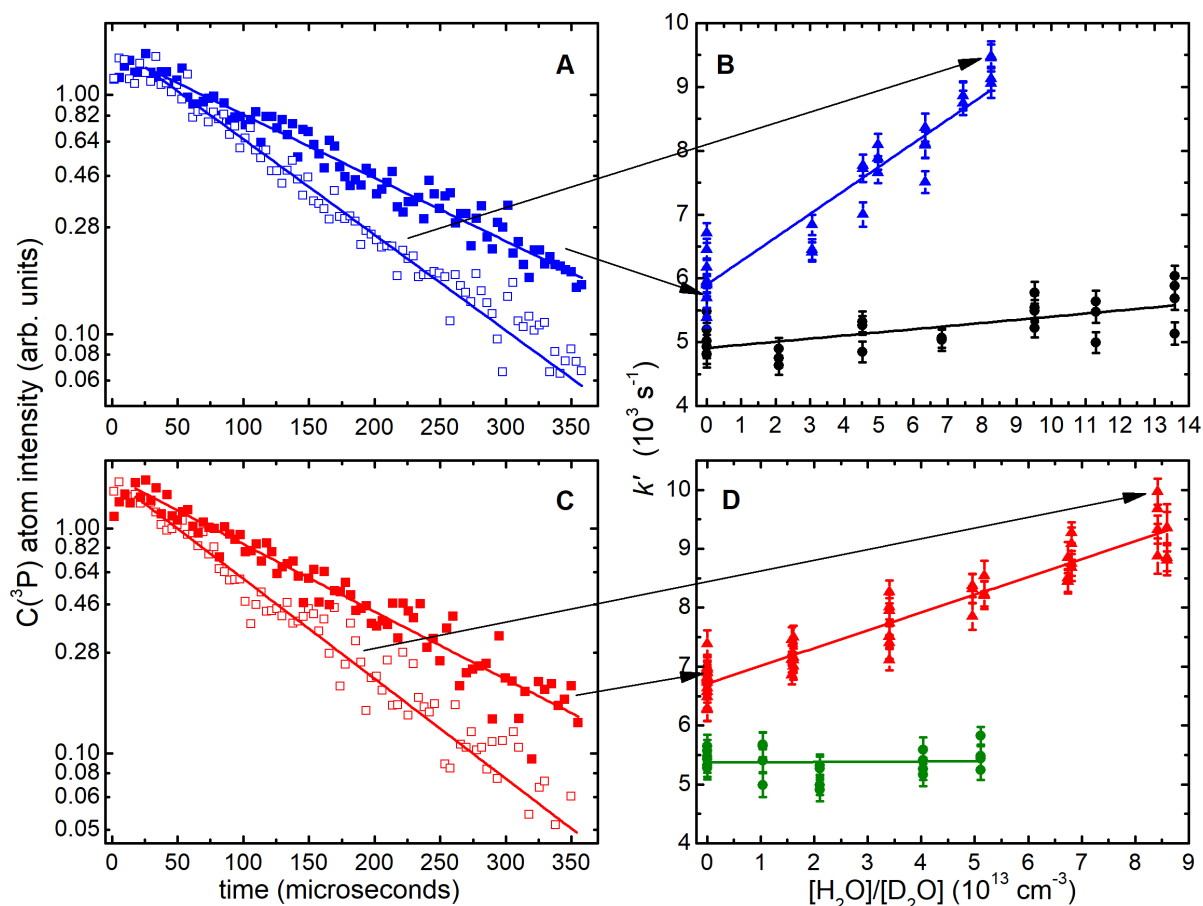


Figure 3.2 Upper panels (A and B) kinetics of the $C(^3P) + H_2O$ reaction recorded at 52 K; (blue solid squares) without H_2O ; (blue open squares) with $[H_2O] = 8.3 \times 10^{13} cm^{-3}$. Lower panels (C and D) kinetics of the $C(^3P) + D_2O$ reaction recorded at 52 K; (red solid squares) without D_2O ; (red open squares) with $[D_2O] = 8.4 \times 10^{13} cm^{-3}$. (Panel B) second-order plots of the $C(^3P) + H_2O$ reaction; (black solid circles) recorded at 106 K; (blue solid triangles) at 52 K. (Panel D) second-order plots of the $C(^3P) + D_2O$ reaction; (green solid circles) recorded at 106 K, (red solid triangles) at 52 K. Solid lines represent linear least-squares fits to the data, weighted by the statistical uncertainties of the individual datapoints in the pseudo-first-order fits.

The second-order rate constants were determined from weighted linear-least square fits of the plots of the individual k' versus the H_2O/D_2O concentration as shown in panels B and D of Figure 3.2. The second-order rate constants obtained as a function of temperature are displayed in Figure 3.3 along with theoretical determinations of the reactive and total rate of reaction (stabilization + reaction).

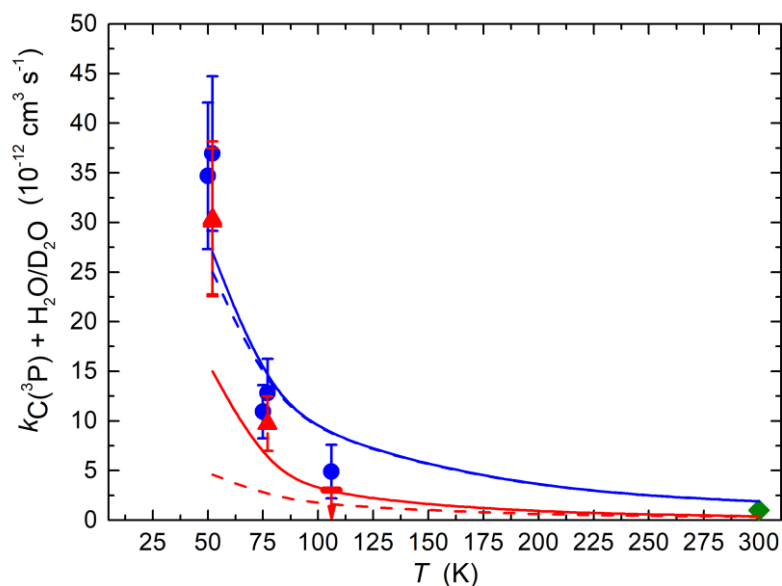


Figure 3.3 Second-order rate constants as a function of temperature. The $C(^3P) + H_2O$ reaction: (blue solid circles) this work, (green solid diamond) Husain and Kirsch;⁴⁷ (solid blue line) calculated total rate constant (stabilization + reaction); (dashed blue line) the reactive rate constant. The $C(^3P) + D_2O$ reaction: (red solid triangles) this work (solid red line) calculated total rate constant (stabilization + reaction); (dashed blue line) the reactive rate constant. Error bars represent the combined statistical and systematic uncertainties.

At 106 K, the reaction of $C(^3P)$ with deuterated water was too slow to be measured and above that temperature we were not able to identify any carbon loss for either of the systems. Table 3.1 summarizes the second-order rate constants, the concentration ranges and the number of experiments performed in each case.

Table 3.1 Temperature dependent rate constants for the $C(^3P) + H_2O/D_2O$ reactions.

T(K)	N ^b	[H ₂ O] (10 ¹³ cm ⁻³)	$k_{C(^3P)+H_2O}$ (10 ⁻¹² cm ³ s ⁻¹)	N ^b	[D ₂ O](10 ¹³ cm ⁻³)	$k_{C(^3P)+D_2O}$ (10 ⁻¹² cm ³ s ⁻¹)
106	28	0 - 13.6	(4.9 ± 2.7) ^c	23	0 - 5.1	< 3.0
77 ± 2 ^a	25	0 - 7.4	(12.8 ± 3.4)	50	0 - 8.5	(9.7 ± 2.7)
75 ± 2	30	0 - 8.3	(10.9 ± 2.7)			
52 ± 1	28	0 - 8.3	(37.0 ± 7.8)	26	0 - 8.4	(30.4 ± 7.4)
52 ± 1				26	0 - 8.6	(30.1 ± 7.8)
50 ± 1	22	0 - 8.5	(34.7 ± 7.4)			

^aUncertainties in the calculated temperatures represent the statistical (1 σ) errors obtained from Pitot tube measurements of the impact pressure. ^bNumber of individual measurements. ^cUncertainties in the measured rate constants represent the combined statistical (1 σ) and estimated systematic errors.

From *Table 3.1* it can be observed that the range of concentrations chosen to perform these experiments is quite small. The main reason to choose such small concentrations of the major reactant is to avoid the formation of water clusters in the supersonic flow. The exploitable range of concentrations used in this work was extracted from previous experiments on the kinetics of the CH + H₂O reaction performed in our laboratory.⁴⁸ The low concentrations used combined with the slow second-order rate constants for these processes lead to a small range of pseudo-first-order rate constants, potentially generating large errors in the quantitative determination of the second-order rate constants. In the kinetics experiments performed at 106 K, the second-order rate constant for the C(³P) + D₂O reaction is very small with a value of $4.0 \times 10^{-13} \text{ cm}^3 \text{ s}^{-1}$. In this case, given the small concentration range and the relatively large scatter of the measured pseudo-first-order rate constants we prefer to report an upper limiting value for the rate constant of $3.0 \times 10^{-12} \text{ cm}^3 \text{ s}^{-1}$, which is the result of the sum of the nominal rate constant and the upper bound of the statistical error. In order to account for the high scatter in the measured pseudo-first-order rate constants we estimate an additional systematic uncertainty of 50% of the nominal rate at 106 K and 20% for all the other lower temperatures.

3.2.1.2. Branching ratios

Up to this point, we have measured the rate constants for both reactions down to 50 K and observed a dramatic increase below 100 K. However, following the C(³P) decay it is impossible to determine if this reactivity increase is due to reaction through tunnelling, complex stabilization or a combination of both effects. Then to discriminate between reactive and non-reactive losses we followed the formation of the products H(²S) and D(²S) directly by VUV LIF at 121.567 nm and 121.534 nm respectively. To obtain quantitative products yields, the H-atom signals for the C(³P) + H₂O reaction were compared with the H-atom signals produced by the reference reaction C(³P) + C₂H₄ reaction. As the D and H line strength factors are identical,⁴⁹ we were able to obtain quantitative yields for the C(³P) + D₂O reaction using the same reference reaction. Typical H/D atom formation curves are shown in *Figure 3.4* for the three reactions at 52 K.

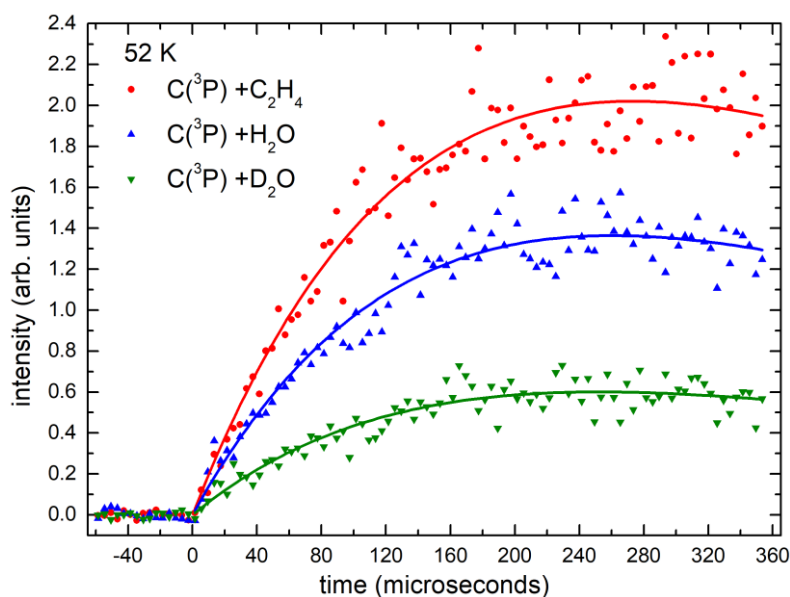


Figure 3.4 Relative yields of atomic hydrogen and atomic deuterium products. H/D atom temporal fluorescence profiles at 52 K. (Red circles) H-atoms from the $C(^3P) + C_2H_4$ reaction ($[C_2H_4] = 1.5 \times 10^{12} \text{ cm}^{-3}$); (blue triangles) H-atoms from the $C(^3P) + H_2O$ reaction ($[H_2O] = 1.8 \times 10^{13} \text{ cm}^{-3}$); (green triangles) D-atoms from the $C(^3P) + D_2O$ reaction ($[D_2O] = 2.0 \times 10^{13} \text{ cm}^{-3}$). Solid lines represent biexponential fits to the individual datapoints.

$C(^1D)$ is also produced in the supersonic flow as a product in the photolysis of CBr_4 . Thus, it was necessary to analyse the influence of $C(^1D) + H_2O/D_2O$ reactions in the kinetics and product branching ratio determinations for the $C(^3P)$ reactions. The $C(^1D) + H_2O/D_2O$ reactions are barrierless processes,⁵⁰ then at the low temperatures of the present experiments their rate constants can be several orders of magnitude larger than the $C(^3P)$ ones. As mentioned earlier, above 106 K we were not able to measure any loss of $C(^3P)$ due to its reaction with H_2O/D_2O , consequently at these temperatures H-atom formation from these reactions is negligible. Then it was possible for us to study the kinetics of the $C(^1D) + H_2O/D_2O$ reactions following the formation of H/D atoms above 106 K. For the latter experiments, to ensure a high concentration of $C(^1D)$ in the flow we used only Ar as a carrier gas due to the fast deactivation of $C(^1D)$ in the presence of N_2 .⁵ We obtained second-order rate constants of $(1.8 \pm 0.2) \times 10^{-10} \text{ cm}^3 \text{ s}^{-1}$ and $(2.1 \pm 0.2) \times 10^{-10} \text{ cm}^3 \text{ s}^{-1}$ at 296 K and 127 K respectively. These values show that the rate constants remain fast and even increase slightly as the temperature falls. To check the influence of these reactions on our target $C(^3P) + H_2O/D_2O$ reactions we performed kinetic measurements for two of our Ar based nozzles (M3Ar and M4Ar) adding a high concentration of N_2 ($[N_2] = 9 \times 10^{15} \text{ cm}^{-3}$) with the aim to relax the $C(^1D)$ atoms present in the flow. Then the result of these measurements was compared with our previous results for the same nozzles in absence of N_2 . (Figure 3.5)

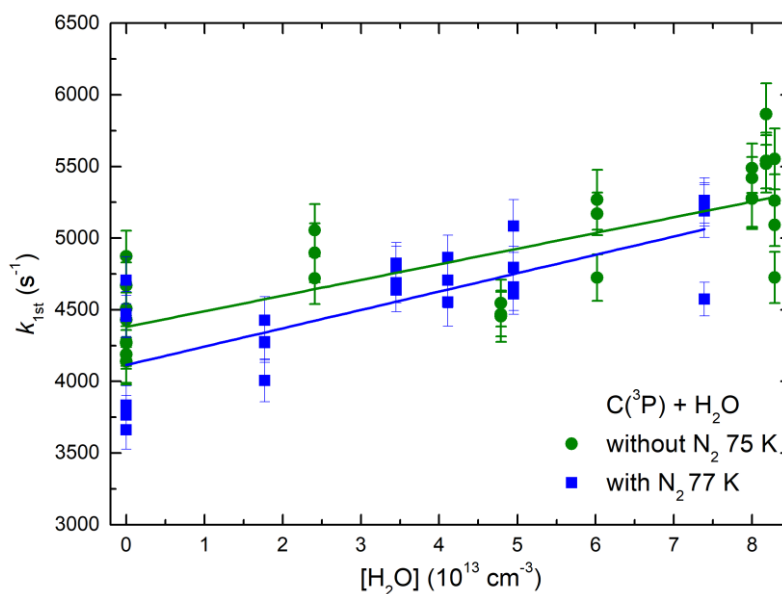


Figure 3.5 Second-order rate constants for the $C(^3P) + H_2O$ reaction obtained using the M3Ar Laval nozzle in the presence (blue solid squares, $[N_2] = 9 \times 10^{15} \text{ cm}^{-3}$) and absence of N_2 (green solid circles) at 77 K and 75 K respectively. The solid lines represent linear least squares fits to the data, weighted by the statistical uncertainties of the individual data points derived during the pseudo-first-order fits.

From Figure 3.5 and Table 3.1 it can be observed that the second-order rate constants in the presence and absence of N_2 are essentially the same, indicating that the $C(^1D) + H_2O$ reaction has little or no effect on the $C(^3P) + H_2O$ reaction. Although we do not perform the same experiments for the $C(^1D) + D_2O$ reaction, we expect a rate constant for this process similar to the one obtained for the $C(^1D) + H_2O$ reaction, given the barrierless nature of these processes.

As the $C(^1D) + H_2O/D_2O$ reactions are faster than the target $C(^3P)$ reactions, we were able to perform quantitative determinations of the H/D-atom production only when N_2 was added to the flow. With an added concentration of N_2 around $2.1 \times 10^{16} \text{ cm}^{-3}$ and the rate constant⁵ for $C(^1D) + N_2$ at 50 K equal to $14.8 \times 10^{-12} \text{ cm}^3 \text{ s}^{-1}$ we obtain a pseudo-first-order rate constant of $3.2 \times 10^5 \text{ s}^{-1}$, which means that $C(^1D)$ atoms are entirely removed from the flow within the first 10 μs . However, as can be seen from Figure 3.6 despite the high concentration of N_2 added to the flow, there remains a small instantaneous production of H-atoms from the $C(^1D) + H_2O$ reaction during the first few microseconds (exemplified by the black arrow), corresponding to 10 - 15% of the peak H-atom signal.

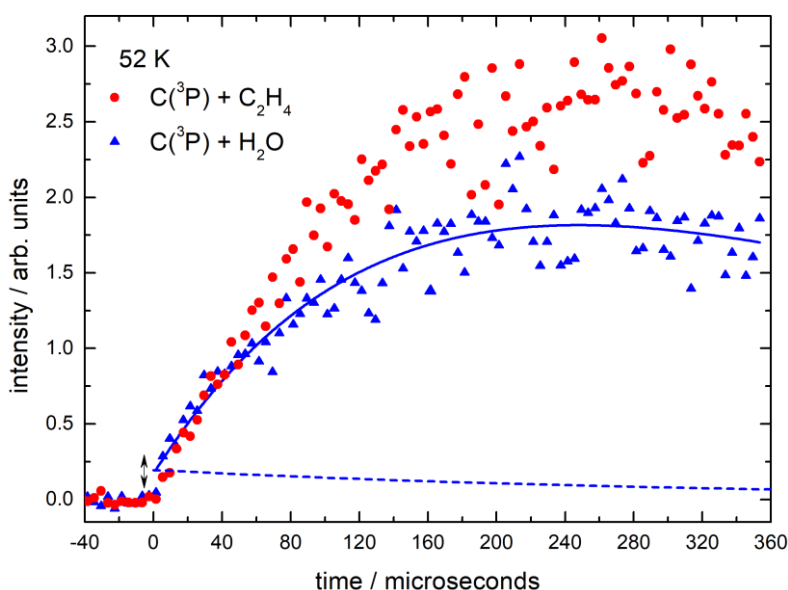


Figure 3.6 H-atom formation curves for the target $C(^3P) + H_2O$ reaction (blue solid triangles) and the reference $C(^3P) + C_2H_4$ reaction (red solid circles) recorded at 52 K with $[H_2O] = 1.8 \times 10^{13} \text{ cm}^{-3}$ and $[C_2H_4] = 1.5 \times 10^{12} \text{ cm}^{-3}$. The solid line represents biexponential fit used to determine the instantaneous H-atom signal from the $C(^3P) + H_2O$ reaction. The dashed line represents the temporal dependence of the instantaneous H-atoms signal, using a H-atom diffusional loss rate taken from earlier work in our group under similar conditions (see text for details).

Under these conditions to obtain more precise values for the relative product yields we subtract the H-atom signal from the $C(^1D) + H_2O$ reaction from the overall observable signal. To estimate the initial contribution of H-atoms from the $C(^1D) + H_2O$ reaction we perform a biexponential fit to the data including a non-zero contribution to the offset (this fit is represented by the solid blue line in Figure 3.6). Subsequently, the H-atoms are slowly lost by diffusion from the probe volume. This first-order rate of H-atom diffusion can be estimated from previous H-atom formation experiments performed under similar conditions⁷ and is represented in Figure 3.6 by the blue dashed line. This H-atom signal correction was not required for the reference reaction $C(^3P) + C_2H_4$ because the $C(^1D) + C_2H_4$ reaction is expected to occur at a similar rate¹³ making the H-atom contribution from this reaction negligibly small. Indeed, we do not observe any instantaneous H-atom formation for any of the experiments where C_2H_4 was added. Lastly, to obtain the quantitative product yields reported in this work, several pairs of H/D-atoms formation curves were recorded for the target and reference reactions using different concentrations of H_2O/D_2O and C_2H_4 reagents. These curves were divided to obtain the signal ratio as a function of time as shown in Figure 3.7 and the branching ratios were obtained from a linear fit with the slope set to zero.

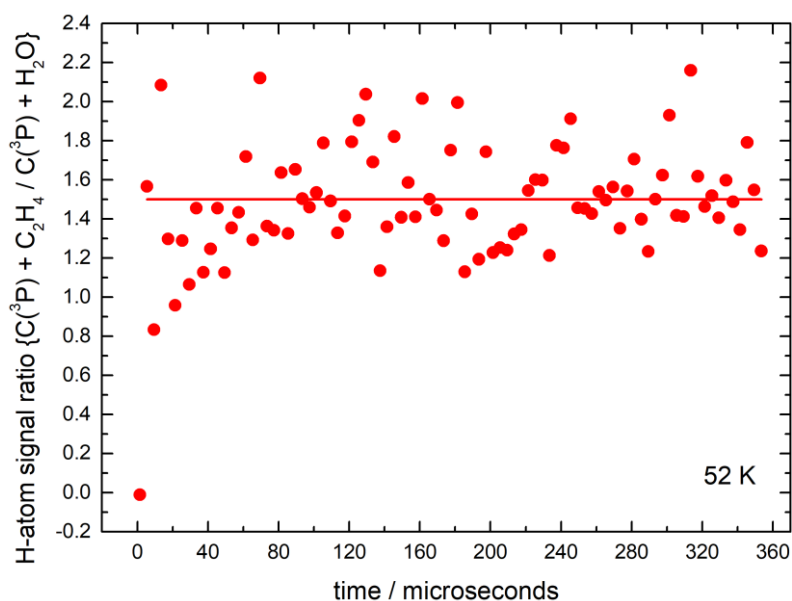


Figure 3.7 Ratio of the H-atom signal from the target $C(^3P) + H_2O$ and reference $C(^3P) + C_2H_4$ reactions as a function of time. The red solid line represents the mean product yield averaged over all time points.

The branching ratios determined in this work at 52 K are summarized in *Table 3.2* for both reactions after multiplication by 0.92 to account for the measured yield of the reference reaction.³⁴ Although we attempted to measure branching ratios at higher temperatures, we were not able to obtain conclusive results due to several issues. At 106 K where the carrier gas used is N_2 the H/D-atom signal from the target reactions were too weak leading to large branching ratio variations when comparing with the reference signal. This result was not unexpected due to the large uncertainties in the second-order rate constants for the target processes at this temperature. We tried to overcome these problems by using a much larger concentration of H_2O/D_2O , however, these measurements also failed, probably due to the influence of cluster formation in the supersonic flow. At 77 K the instantaneous production of H/D atoms from the $C(^1D) + H_2O/D_2O$ was considerably larger due to the lower rate constant for the $C(^1D) + N_2$ reaction at higher temperature,⁵ consequently we were not able to extract reliable branching ratios under these conditions.

Table 3.2 Branching ratios for the $C(^3P) + H_2O/D_2O$ reactions measured at 52 K.

$[H_2O]$ (10^{13} cm^{-3})	H-atom yield $C(^3P) + H_2O /$ H-atom yield $C(^3P) + C_2H_4$	$[D_2O]$ (10^{13} cm^{-3})	D-atom yield $C(^3P) + D_2O /$ H-atom yield $C(^3P) + C_2H_4$
	0.65 ± 0.01^a		0.31 ± 0.01
	0.54 ± 0.01		0.29 ± 0.01
	0.55 ± 0.01		0.32 ± 0.01
3.3	0.56 ± 0.01	3.8	0.29 ± 0.01
	0.52 ± 0.01		0.25 ± 0.01
	0.55 ± 0.01		
	0.58 ± 0.01		
	0.60 ± 0.01		0.32 ± 0.01
1.8	0.60 ± 0.01	2.0	0.25 ± 0.01
	0.61 ± 0.01		0.29 ± 0.01
	0.62 ± 0.01		0.28 ± 0.01
Average	0.58 ± 0.04^b		0.29 ± 0.02

^aThe uncertainties are quoted at the 1σ level. ^bFor the average branching ratios, the uncertainties are quoted at the 95% confidence level.

3.2.1.3. MESMER calculations

Statistical calculations employing the MESMER code were performed to reconcile the results of the kinetic and product studies for the $C(^3P) + H_2O/D_2O$ reactions and to provide the basis to predict rate constants under interstellar conditions. The energies and structures of the transition states and complexes were calculated using quantum chemical calculations (CCSD(T), MP2, DFT/M06-2X, CASPT2 and MRCI + Q).³⁹ For the master equations calculations we used a grain size of 20 cm^{-1} above 150 K and it was reduced to 10 cm^{-1} for the lowest temperatures to avoid numerical problems and ensure convergence of the master equation. Although the harmonic frequencies and rotational constants were taken from the CCSD(T) calculations, we varied the prereactive complex well depth and the width of the barrier connecting the prereactive complex and the HCOH adduct, given the large range of energies for the stationary points between the different methods of theory. To reproduce the experimental data, the same adjustments were applied to both systems ($C(^3P) + H_2O$ and $C(^3P) + D_2O$) to maintain a consistent description of these two reactions. The barrierless reaction step describing complex formation was treated using ILT. As the experimental branching ratios for the H/D atoms are less than unity, clearly some complex stabilization occurs and this information was used to further constrain the input parameters. To treat collisional energy transfer, ΔE_d was taken to be equal to $400 \cdot (T/300)^{0.85} \text{ cm}^{-1}$ in the initial trial model but this was found to be incompatible with the experimental results. Then we used a temperature independent ΔE_d value. The Lennard-Jones

parameters σ and ε were set to 3.47 Å and 114 cm⁻¹ for Ar, to 3.90 Å and 82 cm⁻¹ for N₂ and to 5.0 Å and 150 cm⁻¹ for the C...H₂O/D₂O prereactive complexes. The pressures used in the calculations were set to the experimental values.

When we use the CCSD(T) values of the well depth for the complex, the master equation calculations predict that some complex stabilization occurs, but bimolecular product formation is negligible. Then to increase the yields of the reactive pathway leading to products we either substantially decrease the height of the TS1 barrier or its width. Decreasing the barrier height leads to rate constants which present little temperature dependence with a significantly greater value than the upper limit measured by Husain and Young⁵¹ at room temperature. Consequently, we maintained this barrier height at the calculated value of 32.9 kJ/mol for H₂O and 35.1 kJ/mol for D₂O above the reagents level and varied the barrier width instead. To reproduce the experimental results, it was necessary to reduce the width by a factor close to 2. In addition, it was also necessary to increase either the prereactive complex well depth and/or the collisional energy transfer efficiency. Both of these adjustments lead to a longer lifetime for the prereactive complex, thereby enhancing the tunnelling processes at low temperature as well as increasing the probability of complex stabilization through three body collisions. In the absence of either of these adjustments, the major fate of the prereactive complex is dissociation back to reagents even at low temperatures. This is almost certainly due to the fact that the C(³P) + H₂O system is relatively small with a low density of rovibrational levels. Only when the complex well depth is increased from -28.9 kJ/mol (CCSD(T) level) to -60 kJ/mol is a reasonable agreement found between the calculations and the measured reaction rates/branching ratios. A good agreement could also be obtained when the well depth is set to -46 kJ/mol in addition to the use of a temperature independent ΔE_d value of 400 cm⁻¹. These latter adjustments are the ones used to obtain the calculated rates presented in *Figure 3.3*.

Using the previous parameters (well depth equal to -46 kJ/mol and ΔE_d value of 400 cm⁻¹) the calculated branching ratios between complex stabilization and reaction yielding H + HCO products, do not completely reproduce the experimental branching ratios at 52 K for the C(³P) + H₂O reaction. In this case, the calculations yield 92% of product formation (H + HCO / H + H + CO) instead of the 58% obtained experimentally. However, in the case of the C(³P) + D₂O reaction at 52 K the calculations yield 30% of product formation while the experiments yield 29%. The calculated values were predicted to decrease when the pressure increases due to an increase of the total rate constant as a result of a more efficient complex stabilization with only a weak increase of the bimolecular product formation rate.

3.2.2. Discussion

The $C(^3P) + H_2O/D_2O$ reactions occur through carbon atom addition to the oxygen atom of water forming a prereactive complex 30 - 40 kJ/mol below the reagent level. The probable exothermic products $H + HCO$ are separated from the complex by a calculated energy barrier of around 11 - 40 kJ/mol.^{37,38,50} There have been two previous experimental determinations of the rate constants for the $C(^3P) + H_2O$ reaction at room temperature^{47,51} yielding an upper limit of $1 \times 10^{-12} \text{ cm}^3 \text{ s}^{-1}$, a value that suggests a considerable barrier to products in agreement with the calculations. Then at low temperature, the reactivity of this system to yield the exothermic products $H + HCO$ should be inhibited in the absence of tunnelling effects through the barrier.

As can be seen from *Figure 3.3*, the rate constants for both reactions increase dramatically below 100 K with higher values for the $C(^3P) + H_2O$ system. Such an increase of reactivity at low temperatures might be explained due to tunnelling through the barrier yielding products, complex stabilization in collisions with the bath gas and by a combination of tunnelling and complex stabilization. In *Figure 3.4* it can be seen that H and D-atoms products are clearly observed at 52 K indicating that tunnelling is an important process for both reactions. As no H/D-atoms were observed in the experiments performed above 106 K the role of tunnelling at these higher temperatures seems to be negligible, in good agreement with the low rate constants obtained through kinetic measurements of $C(^3P)$ atom loss. The measured branching ratios for H/D formation in the $C(^3P) + H_2O/D_2O$ reactions at 52 K yield (0.58 ± 0.04) and (0.29 ± 0.02) respectively. These values assume that the energized HCO/DCO products do not fragment leading to secondary H/D-atoms, which will further decrease the measured branching ratios. Considering these low values of H/D formation branching ratios, we can state that large fractions of $C...OH_2/OD_2$ complexes do not lead to reaction, being stabilized instead.

At this point, master equation calculations can help our understanding of the $C(^3P) + H_2O/D_2O$ complex systems. Several processes characterized by the formation of a prereactive complex prior to a notable barrier in their reactive pathways have been studied using master equations.^{19,20,22,52,53} Although for all of these processes the rate constants show a similar behaviour with a strong increase at low temperatures, the reaction mechanisms are considered to be different. For the $OH + CH_3OH$ system,¹⁹ as no pressure dependence was observed at very low temperatures, the main process was thought to be tunnelling through the barrier leading to reaction. In the case of $OH + \text{acetone}$, dimethyl ether,²² ethanol and propan-2-ol²⁰ a pressure dependence of the rate constants was observed favouring complex stabilization rather than reaction. Although for these latter reactions, an extrapolation of the pressure dependent rate coefficients showed a non-zero intercept at zero pressure evidencing the small contribution of a pressure independent bimolecular channel due to tunnelling. In many of these

previous studies the RRKM calculations were generally unable to reproduce the experimental results without large adjustments. For example, Shannon et al.²² increased the well depth of the prereactive complex by approximately 50% in order to reproduce the experimental data, and in their study of OH + CH₃OH reaction¹⁹ the imaginary frequency corresponding to the transition state located at the barrier to the methyl-hydrogen atom abstraction was divided by 4.7 leading to qualitative agreement with the experimental data. Sleiman et al.⁵³ used a large value of the ΔE_d parameter (800 cm⁻¹) with the aim to stabilize efficiently the prereactive complex. If we compare our recent calculations and our variations from the initial ab-initio values with these previous works, they appear to be quite reasonable.

The C(³P) + H₂O/D₂O reactions show a large increase of reactivity below 100 K which can be reproduced theoretically by increasing the depth of the potential well for the prereactive complex and consequently its lifetime. The statistical calculations predict that while the complex stabilization step is pressure dependent, product formation is only slightly dependent on the total pressure. Indeed, three body collisions increase the complex lifetime, thereby increasing the possibility of tunnelling through the barrier. As can be seen from *Figure 3.3*, the calculations predict that the total rate constants measured at 77 and 106 K are the same as the tunnelling rate already with the contribution from complex stabilization negligible at these temperatures.

The tunnelling rate (or reaction rate) at 52 K can be calculated as the total experimental rate constant multiplied by the H-atom yield at this temperature, (approximately $21.5 \times 10^{-12} \text{ cm}^3 \text{ s}^{-1}$). The MESMER calculations have been used to extrapolate the rate constants for the C(³P) + H₂O reaction down to 30 K and pressures more representative of dense interstellar clouds. Our experimental data and the upper limit of Husain and Young⁵¹ in the 52 to 300 K temperature range can be fitted using an expression of the type $k = a * \left(\frac{T}{300}\right)^b$ with $a = 1.26 \times 10^{-12} \text{ cm}^3 \text{ s}^{-1}$ and $b = -1.59$. Then as the calculations show that the tunnelling rate has a small pressure dependence, we multiply the fitted rate constants expression by the ratio between the calculated zero pressure value and the calculated value at the pressure used in the 52 K experiment. This ratio is equal to 0.74 leading to a modified formula with $a = 9.3 \times 10^{-13} \text{ cm}^3 \text{ s}^{-1}$. Extrapolating this expression down to 10 K we obtain a rate constant of $2.0 \times 10^{-10} \text{ cm}^3 \text{ s}^{-1}$ which suggests that C(³P) + H₂O reaction should become the most efficient mechanism for H₂O loss in current models.

3.2.3. Relevance of the C(³P) + H₂O reaction in the interstellar medium

The study of the reaction between water and ground state atomic carbon provides additional evidence of the importance of QMT in the chemistry of low temperature environments such as the interstellar medium. In this work, statistical calculations have been employed to extend the measured rate

constants to temperatures and pressures more representatives of interstellar clouds yielding an estimated rate constant of $2 \times 10^{-10} \text{ cm}^3 \text{ s}^{-1}$ at 10 K in the low-pressure limit. To evaluate the importance of this reaction compared with other reactions involving water occurring in dense interstellar clouds we used the reactive flux (defined as the product $k[A][B]$ where $[A]$ and $[B]$ are the densities of the reactants A and B respectively and k is the rate constant for the process). This comparison confirms that $\text{C}(^3\text{P}) + \text{H}_2\text{O}$ reaction is the main sink for gas-phase water in dense interstellar clouds. Furthermore, the inclusion of this reaction in astrochemical models will improve the modelled water abundances which currently overestimate the observed water abundances by at least an order of magnitude (Figure 3.8).²⁶

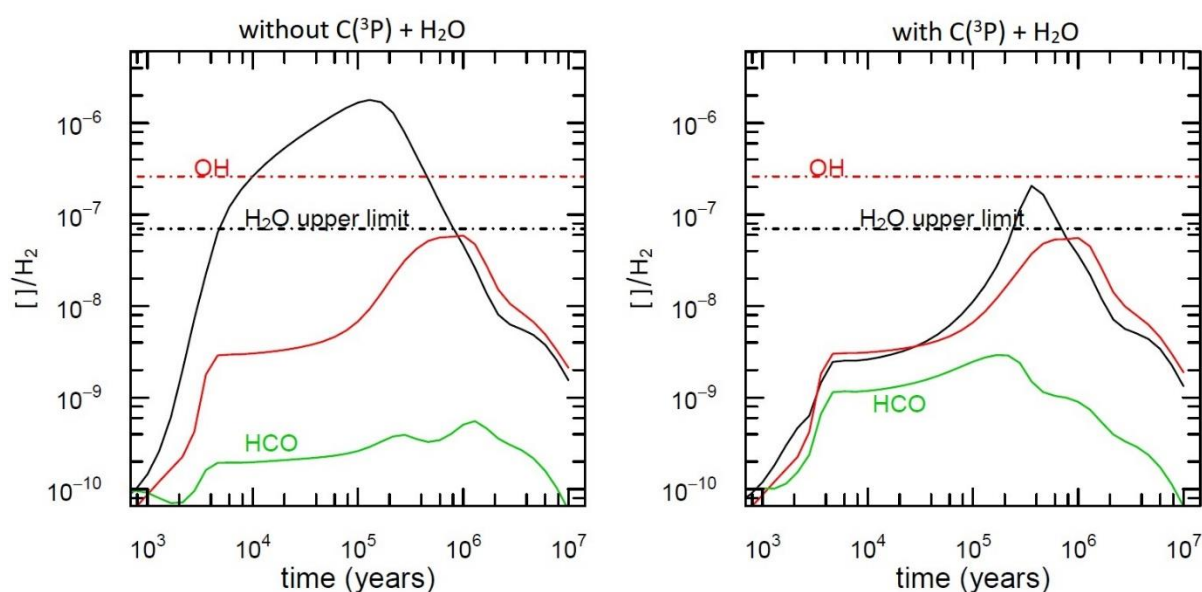


Figure 3.8 Modelled water abundances with and without the inclusion of the $\text{C}(^3\text{P}) + \text{H}_2\text{O}$ reaction.^{54,55} (Black dot-dashed line) upper limit of observed water abundances; (red dot-dashed line) upper limit of observed OH abundances; (black continuous line) modelled water abundances; (red continuous line) modelled OH abundances; (green continuous line) modelled HCO abundances.

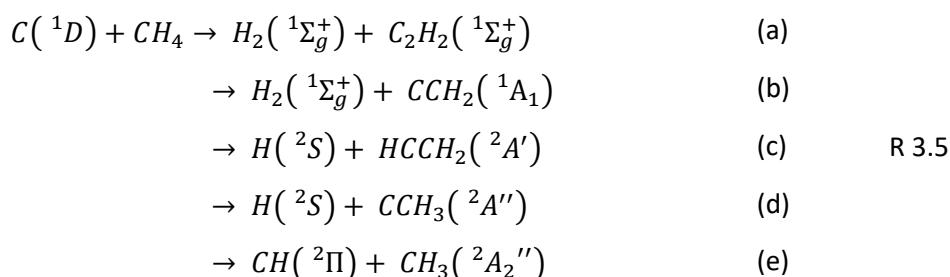
The $\text{C}(^3\text{P}) + \text{H}_2\text{O}$ reaction could also be important in interstellar dust grain chemistry. Such particles are surrounded by a water-ice mantle containing non-negligible quantities of CO_2 , CO and CH_3OH with traces of other carbon, nitrogen and sulphur containing molecules.⁵⁶ Astrochemical models predict that carbon atoms in the gas-phase deplete onto these ices reacting predominantly with H-atoms to form CH_4 .⁵⁷ If the $\text{C}(^3\text{P}) + \text{H}_2\text{O}$ reaction is introduced in the models, an alternative pathway for atomic carbon loss is opened, yielding one or both association products HCOH and H_2CO . As two hydrogenation steps of the standard CH_3OH formation mechanism ($\text{H} + \text{CO} \rightarrow \text{HCO}$ and $\text{H} + \text{H}_2\text{CO} \rightarrow \text{H}_2\text{COH}/\text{CH}_3\text{O}$) are characterized by activation barriers,⁵⁸ the $\text{C}(^3\text{P}) + \text{H}_2\text{O}$ reaction could facilitate

methanol formation through the barrierless $\text{H} + \text{HCOH}$ reaction if $\text{HCOH} \rightarrow \text{H}_2\text{CO}$ isomerization is inefficient.⁵⁹

3.3. The $\text{C}(^1\text{D}) + \text{CH}_4/\text{C}_2\text{H}_6$ reactions

Methane is the second most abundant compound in Titan's atmosphere, where also some traces of other hydrocarbons such as C_2H_6 can be found.⁶⁰ The reactivity of $\text{C}(^3\text{P})$ atoms towards saturated hydrocarbons such as CH_4 and C_2H_6 is considerably lower than for unsaturated species such as C_2H_2 , C_2H_4 and longer carbon chain species.^{12-14,61,62} Indeed the $\text{C}(^3\text{P}) + \text{CH}_4$ reaction has been studied theoretically using ab-initio calculations, where at low excess internal energies the reaction proceeds mostly through insertion of $\text{C}(^3\text{P})$ atoms into the C-H bond, a reaction path that is characterized by an activation barrier of 51 kJ/mol.²⁹ As $\text{C}(^3\text{P})$ is unreactive with saturated hydrocarbons, the production of longer chain carbon containing molecules in Titan's atmosphere might occur instead through the reactions of $\text{C}(^1\text{D})$ with CH_4 and C_2H_6 .

In the case of the $\text{C}(^1\text{D}) + \text{CH}_4$ reaction, the reaction dynamics have been previously studied experimentally and theoretically by Leonori et al.⁹ This reaction is thought to occur through $\text{C}(^1\text{D})$ insertion into a C-H bond of CH_4 to form a $^1\text{HCCH}_3$ intermediate, which lies 394.1 kJ/mol below the reagent level (*Figure 3.9*). The singlet HCCH_3 intermediate can dissociate into products directly or isomerize to the global minimum C_2H_4 through a barrier of 3.1 kJ/mol. This C_2H_4 , which lies 706.4 kJ/mol below the reagent level, can further dissociate leading to several possible exothermic exit pathways:



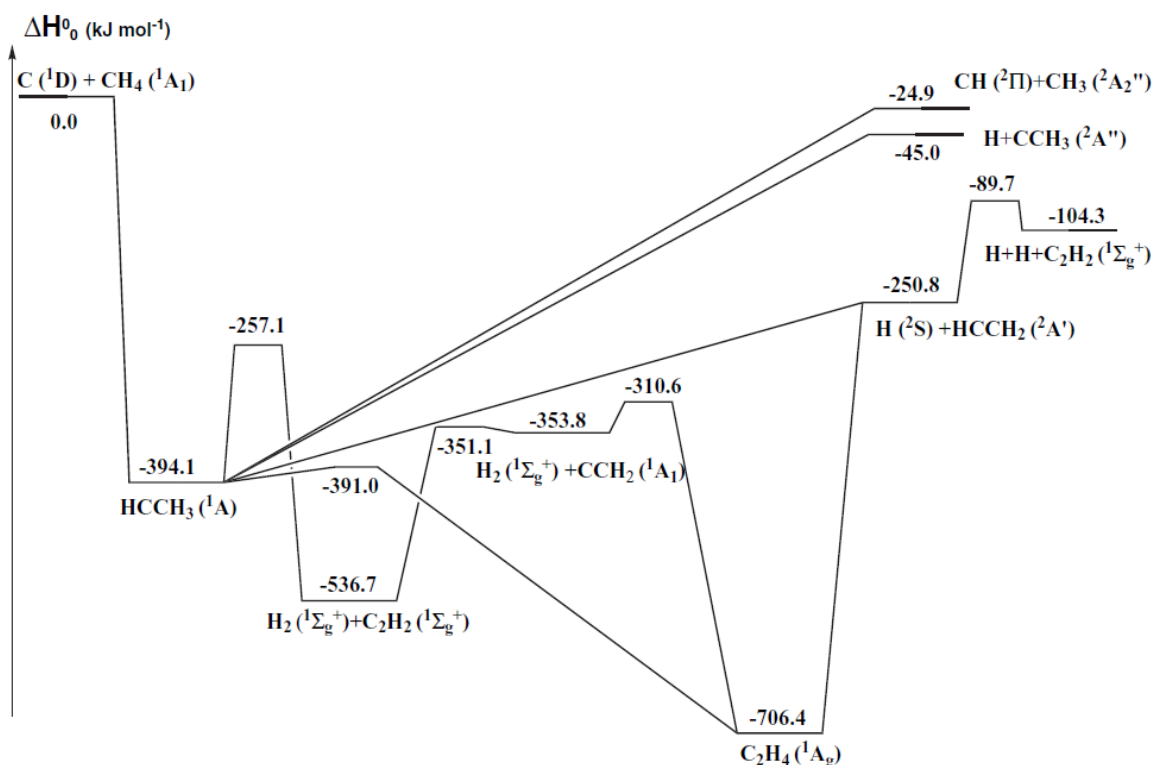


Figure 3.9 Schematic representation of the $C(^1D) + CH_4$ PES. Extracted from Leonori et al.⁹

The kinetics of the $C(^1D) + CH_4$ reaction are not well known with only two experimental determinations at room temperature. These studies^{15,17} were performed using the vacuum-ultraviolet flash photolysis of carbon suboxide (C_3O_2) to produce $C(^1D)$ and time-resolved atomic absorption spectroscopy to follow the reaction kinetics. However, the reported rate constants differ between them by almost an order of magnitude.

In the case of the $C(^1D) + C_2H_6$ reaction, to the best of our knowledge there is no dynamics or kinetic information reported in the literature. However, this reaction occurs through the formation of a C_3H_6 (propene) intermediate and some information can be taken from related studies that sample the same regions of the PES. Then previous work on the unimolecular decomposition of C_3H_6 in its singlet ground state⁶³ and other bimolecular reactions over the same PES^{64–66} allow us to extract some conclusions on the preferred exit channels for the $C(^1D) + C_2H_6$ reaction. In this work, the rate constants for both reactions have been investigated over the 50 - 296 K temperature range and H-atom yields have been determined with the aim to clarify the reaction mechanism and the preferred products for these reactions at low temperatures.

3.3.1. Results

Two types of experiments were performed to study these reactions, kinetic measurements and H-atom yields determinations. A large and known excess of the alkane concentration was maintained with respect to $C(^1D)$ concentration to achieve pseudo-first-order conditions.

3.3.1.1. Rate constants

To follow the kinetics of these reactions the H-atoms product VUV LIF signal was recorded as a function of time as shown in *Figure 3.10*.

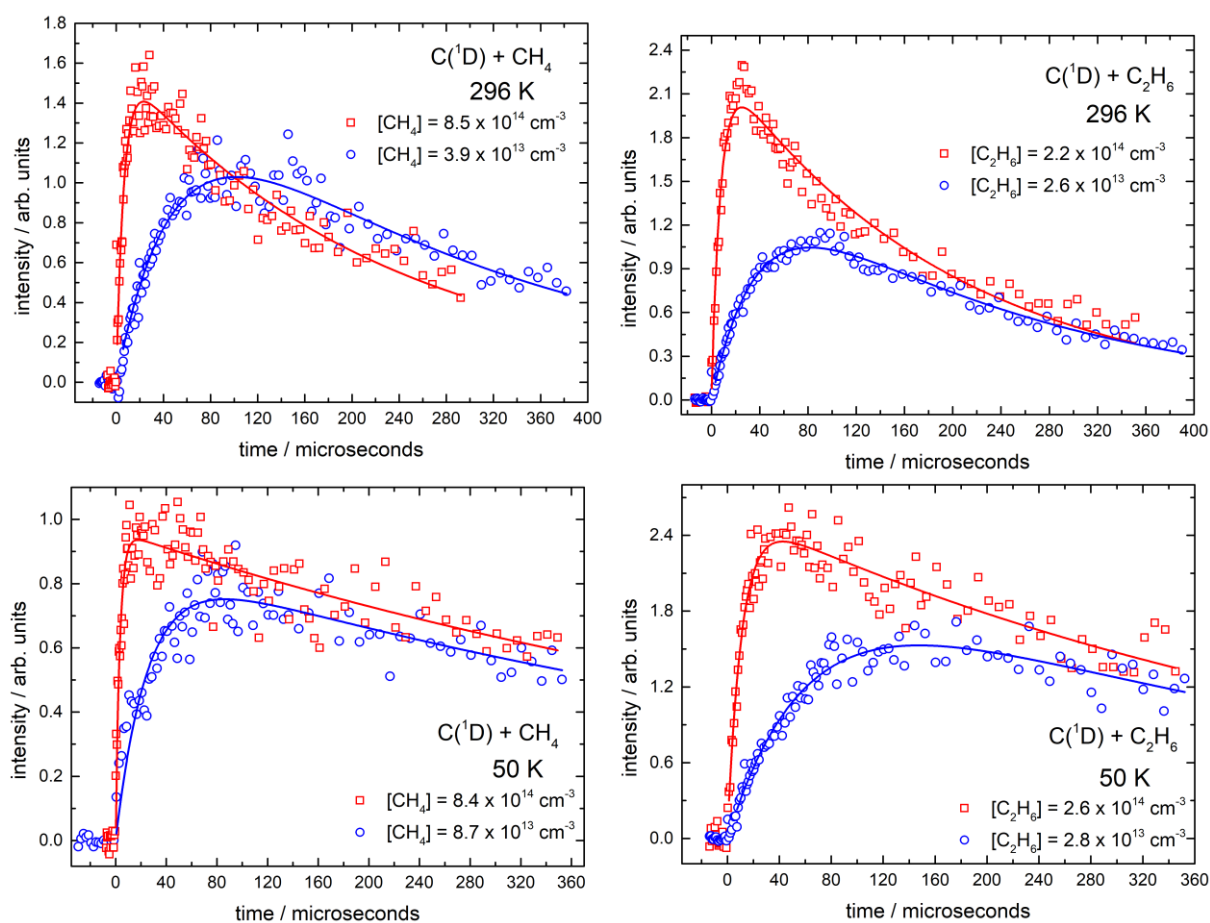


Figure 3.10 $H(^2S)$ VUV LIF signals as a function of time. (Left panels) $C(^1D) + CH_4$ reaction at 296 K and 50 K. (Right panels) $C(^1D) + C_2H_6$ reaction at 296 K and 50 K. (Red open squares) and (blue open circles) the highest and lowest concentration of alkanes respectively. (Solid blue and red lines) functional fits to the data using expression 2.9.

The measured pseudo-first-order rate constant as a function of the concentration of alkane are shown in *Figure 3.11*

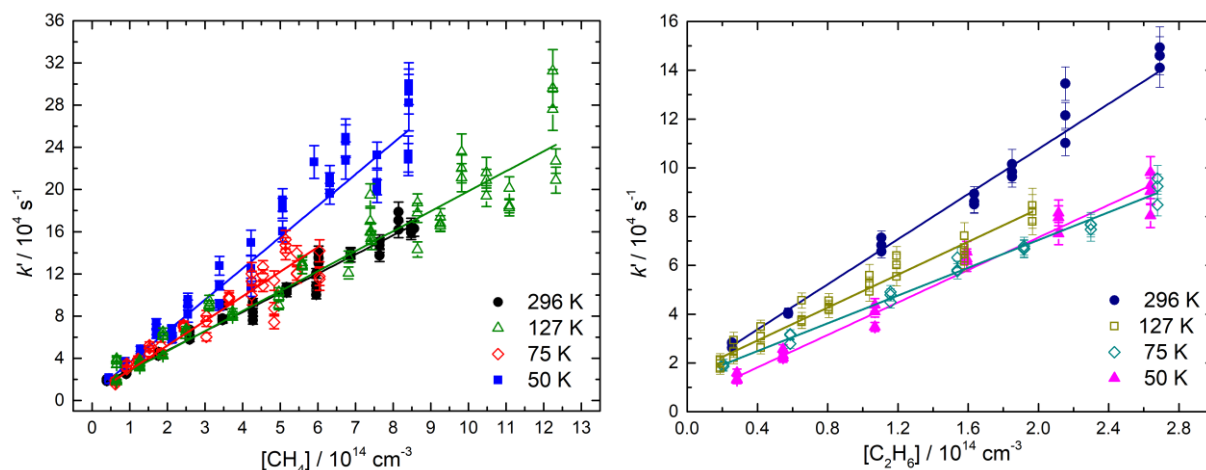


Figure 3.11 Second-order plots of $C(^1D) + CH_4/C_2H_6$ reactions. (Left panel) the $C(^1D) + CH_4$ reaction (right panel) the $C(^1D) + C_2H_6$ reaction. Solid lines represent linear least-squares fits to the data, weighted by the statistical uncertainties of the individual data points given by biexponential fits such as those shown in Figure 3.10.

The second-order rate constants obtained as a function of temperature for both reactions are displayed in Figure 3.12. In the case of the $C(^1D) + CH_4$ reaction, the rate constants are shown alongside other experimental determinations.

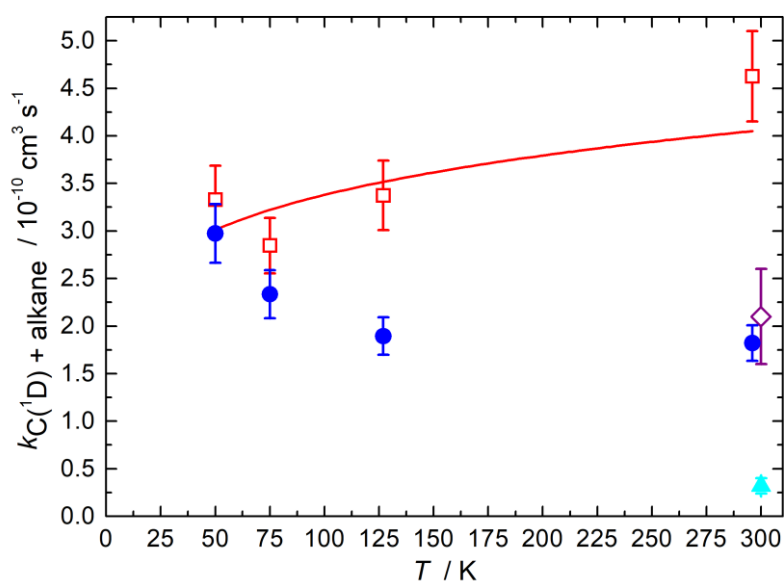


Figure 3.12 Measured rate constants as a function of temperature. $C(^1D) + CH_4$ reaction (blue solid circles) this work; (purple open diamond) Husain and Kirsch;¹⁵ (cyan solid triangle) Braun et al.¹⁷ The $C(^1D) + C_2H_6$ reaction (red open squares). The red solid line represents the fit to the $C(^1D) + C_2H_6$ rate data with a fixed $T^{1/6}$ temperature dependence (see text for details). Error bars represent the combined statistical and systematic uncertainties.

The second-order rate constants, the concentration ranges and the number of experiments performed in each case are summarized in Table 3.3.

Table 3.3 Temperature dependent rate constants for the C(¹D) + CH₄ and C(¹D) + C₂H₆ reactions.

T(K)	N ^b	[CH ₄] (10 ¹⁴ cm ⁻³)	$k_{C(^1D)+CH_4}$ (10 ⁻¹⁰ cm ³ s ⁻¹)	N	[C ₂ H ₆] (10 ¹⁴ cm ⁻³)	$k_{C(^1D)+C_2H_6}$ (10 ⁻¹⁰ cm ³ s ⁻¹)
296	42	0.9 - 8.6	(1.8 ± 0.2) ^c	21	0.3 - 2.2	(4.6 ± 0.5)
127 ± 2 ^a	60	0.7 - 12.3	(1.9 ± 0.2)	29	0.2 - 1.6	(3.4 ± 0.4)
75 ± 2	42	0.6 - 6.0	(2.3 ± 0.3)	21	0.2 - 2.7	(2.8 ± 0.3)
50 ± 1	44	0.4 - 8.4	(3.0 ± 0.3)	21	0.3 - 2.6	(3.3 ± 0.4)

^aUncertainties in the calculated temperatures represent the statistical (1σ) errors obtained from Pitot tube measurements of the impact pressure. ^bNumber of individual measurements. ^cUncertainties in the measured rate constants represent the combined statistical (1σ) and estimated systematic (10%) errors.

3.3.1.2. Influence of secondary reactions

In these experiments, given the large concentration of C(³P) produced during the photolysis of CBr₄ it was necessary to check the influence of secondary reactions leading to the formation of H-atoms. As mentioned above, the C(³P) + CH₄ reaction is characterized by a barrier and should be negligible at room temperature and below. However, as we discussed in section 3.2 despite the presence of a significant activation barrier in the way to products, reaction could still occur at low temperatures through QMT. To examine the possibility of this effect in the C(³P) + CH₄ reaction we performed a test experiment at 50 K by adding a large concentration of N₂ (3.2 × 10¹⁶ cm⁻³) to the system with the aim to quench C(¹D) atoms present in the reactor. Under these conditions, the H-atom fluorescence signal was 8 times smaller than the measured signal in the absence of N₂ (Figure 3.13 left panel). This small signal is the result of the reaction of some non-quenched C(¹D) atoms with CH₄. In the right panel of Figure 3.13, the H-atom intensity recorded in the presence of N₂ (blue solid squares) has been multiplied by a factor of eight, then it can be observed that the rise time of the curve is shorter, consistent with the rapid removal of C(¹D) atoms with N₂. In addition, the diffusional loss of H-atoms is the same with or without N₂ added to the system, which indicates that other H-atom production pathways (like those expected if tunnelling plays a role for C(³P) + CH₄ reaction) are negligible.

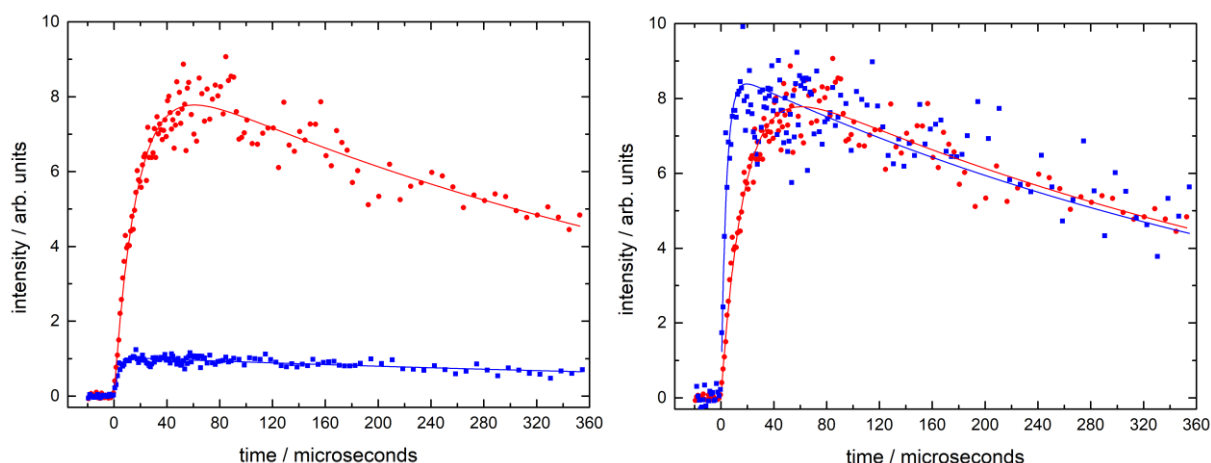


Figure 3.13 Measured H-atom VUV LIF signal for the $C(^1D) + CH_4$ reaction as a function of time recorded at 50 K. (Left panel) (red solid circles) $[CH_4] = 2.1 \times 10^{14} \text{ cm}^{-3}$; (blue solid squares) $[CH_4] = 2.1 \times 10^{14} \text{ cm}^{-3}$ and $[N_2] = 3.2 \times 10^{16} \text{ cm}^{-3}$. (Right panel) the recorded intensities in presence of the N_2 (blue solid squares) have been multiplied by a factor of eight.

3.3.1.3. H-atom yields

To determine absolute H-atom yields for these reactions, the H-atom signal intensities for the $C(^1D) + CH_4/C_2H_6$ reactions were compared with the intensity produced by the reference reaction $C(^1D) + H_2$, which is considered to produce H-atoms with a 100% yield (i.e. without relaxation of $C(^1D)$ towards $C(^3P)$). The H-atom fluorescence signals recorded sequentially for the target and reference reactions with the same pseudo-first-order rate constant are shown in Figure 3.14

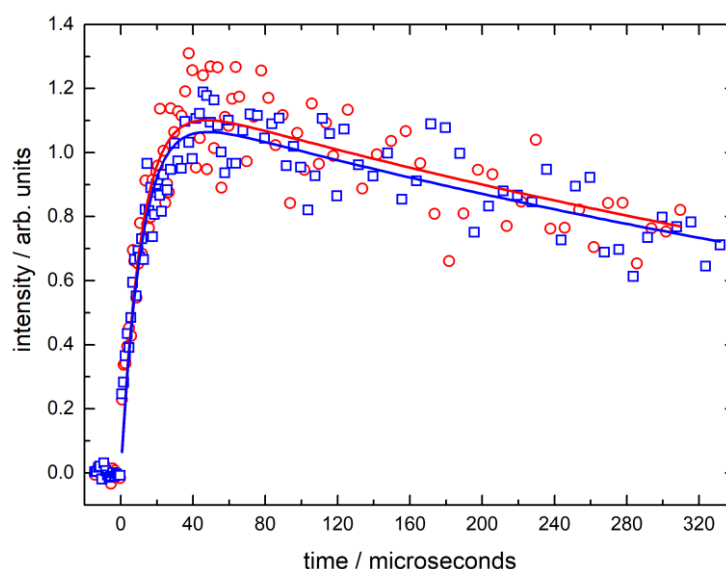


Figure 3.14 H-atom VUV LIF emission profiles recorded at 50 K. (Red open circles) H-atom signal from the $C(^1D) + CH_4$ reaction with $[CH_4] = 2.1 \times 10^{14} \text{ cm}^{-3}$; (red solid line) biexponential fit to the $C(^1D) + CH_4$ data points. (Blue open squares) H-atom signal from the $C(^1D) + H_2$ reaction with $[H_2] = 2.5 \times 10^{14} \text{ cm}^{-3}$; (blue solid line) biexponential fit to the $C(^1D) + H_2$ data points.

The pre-exponential factors used to obtain the H-atom yields were corrected to account for absorption losses of the VUV excitation and fluorescence intensities by residual gases (CH_4 and C_2H_6) in the chamber. This correction was estimated to be less than 3% for CH_4 and 7% for C_2H_6 over the entire temperature range. The temperature dependent H-atom yields for the $\text{C}(^1\text{D}) + \text{CH}_4/\text{C}_2\text{H}_6$ reactions are listed in *Table 3.4*.

Table 3.4 H-atom yields for the $\text{C}(^1\text{D}) + \text{CH}_4/\text{C}_2\text{H}_6$ reactions as a function of temperature.

T(K)	N ^b	H-atom yield $\text{C}(^1\text{D}) + \text{CH}_4$	T(K)	N	H-atom yield $\text{C}(^1\text{D}) + \text{C}_2\text{H}_6$
296	12	0.96 ± 0.06^c	296	9	1.09 ± 0.05
127 ± 2^a	8	1.08 ± 0.06	127 ± 2		
75 ± 2	8	1.10 ± 0.03	75 ± 2		
50 ± 1	9	1.05 ± 0.04	50 ± 1	2	1.05 ± 0.07

^aUncertainties in the calculated temperatures represent the statistical (1σ) errors obtained from Pitot tube measurements of the impact pressure. ^bNumber of H-atom yield determinations. ^cThe error bars represent the statistical uncertainties at the 95% of confidence level.

3.3.2. Discussion

3.3.2.1. The $\text{C}(^1\text{D}) + \text{CH}_4$ reaction

In the case of the $\text{C}(^1\text{D}) + \text{CH}_4$ reaction, it can be observed from *Figure 3.12* that our rate constant measured at room temperature is in excellent agreement with the previous value determined by Husain and Kirsch¹⁵ while the value reported by Braun et al.¹⁷ is almost an order of magnitude lower. Leonori et al.⁹ performed a CMB study of this reaction at a collision energy of 25.3 kJ/mol along with electronic structure calculations of the underlying PES (*Figure 3.9*) and RRKM theory to determine the microcanonical rate constants $k(E)$ and branching ratios.

The experimental results of Leonori et al.⁹ obtained by fitting to the laboratory angular frame and time of flight distributions of the $\text{C}(^1\text{D}) + \text{CH}_4$ reaction indicate that this reaction occurs through a bound intermediate having a relatively long lifetime comparable to its rotational period (known as an osculating complex). However, their RRKM calculations predict a very short lifetime for the insertion intermediate. To explain the differences between their experimental and theoretical findings, the authors suggested the possibility of intersystem crossing (ISC) between the singlet and triplet states of the HCCH_3 intermediate. Indeed, Kim et al.²⁹ studied the $\text{C}(^3\text{P}) + \text{CH}_4$ reaction finding a crossing seam between the two states (singlet and triplet) in the vicinity of the HCCH_3 intermediate. Then, it is possible that the increase that we observe in the rate constant at low temperature (*Figure 3.12*) originates from these non-adiabatic effects. At higher temperature, reaction over the singlet surface is expected to

dominate due to the shorter intermediate lifetimes but as the temperature is decreased, the lifetime of the $^1\text{HCCH}_3$ intermediate is expected to increase significantly, promoting ISC to the triplet surface and providing additional pathways for reaction to occur. Regarding the additional pathways on the triplet surface, Kim et al.²⁹ determined that at low excess internal energy the sole reaction products are $\text{C}_2\text{H}_3 + \text{H}$.

Leonori et al.⁹ concluded that the dissociation pathways R 3.5 (d) and R 3.5 (e) were unimportant given the high energy of these channels with respect to the initial $^1\text{HCCH}_3$ intermediate and the other possible exit channels. Using a mass spectrometric technique to identify the products through electron impact ionization, they attempted to detect the signal at $m/z = 27$ corresponding to the vinyl radical (C_2H_3) channel R 3.5 (c), however they were unable to observe any signal even at the lowest ionization energy (17 eV). This result indicates that products at this mass either fell apart before reaching the detector (which means that they lose a H-atom on a timescale shorter than the detection timescale, presumably yielding $\text{C}_2\text{H}_2/\text{H}_2\text{CC} + \text{H}$ as secondary products) or underwent complete dissociative ionization. These authors suggest that decomposition of the vinyl radical is the most probable outcome given the low energy used in that study. More evidence of the facile secondary dissociation of vinyl radicals has been provided by Lee et al.,⁶⁷ who studied C_2H_4 photolysis at a photon energy of 9.5 eV, detecting the cofragments by VUV photoionization. In this study, only 4% of the global amount of vinyl radicals at $m/z = 27$ was detected.

The signal detected at $m/z = 26$ by Leonori et al.⁹ corresponds to the contribution of two components: the H-displacement channel R 3.5 (c) and the H_2 elimination channels R 3.5 (a) and R 3.5 (b). From the contribution of these two components during the best-fit procedure, the authors determined a branching ratio of 0.8 ± 0.4 between the H_2 and H loss pathways that equates to 44% of H_2 elimination and 56% of H elimination. Then considering that all the vinyl radicals produced in the channel R 3.5 (c) (56%) decompose to form $\text{C}_2\text{H}_2/\text{H}_2\text{CC} + \text{H}$ at a collision energy of 25.3 kJ/mol we should expect a H-atom yield for the $\text{C}(^1\text{D}) + \text{CH}_4$ reaction of approximately 1.1, with two H-atoms produced due to the secondary dissociation of the vinyl radical. This result is in excellent agreement with our determined H-atom yields at much lower equivalent collision energies (from 3.7 kJ/mol to 0.6 kJ/mol) as shown in *Table 3.4*. We obtain H-atom yields that slightly increase as the temperature falls. These results are consistent with the role of ISC from the singlet to the triplet surface because if the vinyl radicals formed on the triplet surface decompose mostly to form $\text{C}_2\text{H}_2/\text{H}_2\text{CC} + \text{H}$ as a secondary products then an increase in the H-atom yield at low temperatures is expected.

3.3.2.2. The C(¹D) + C₂H₆ reaction

In the case of C(¹D) + C₂H₆ reaction, no previous studies were found in the literature. Then to help our understanding of the reaction mechanism we can refer to previous related works that sample the same regions of the C₃H₆ intermediate PES. The thermal unimolecular decomposition mechanism of propene has been experimentally and theoretically studied by Hung et al.⁶³ in the 1450 – 1712 K temperature range. The possible exit channels identified by their quantum chemical calculations are listed below:



These authors determined that the major product channels were likely to be R 3.6 (a) and R 3.6 (b). From RRKM/master equations calculations they obtained an 85% yield for channel R 3.6 (a) and a 15% yield for channel R 3.6 (b) while the other channels were considered to be negligible. Experimentally, using a shock tube apparatus and detecting H-atoms by the Atomic Resonance Absorption Spectroscopy (ARAS) technique, they found a H-atom yield of 1.7 – 2.0. The authors stated that their results were in good agreement with the theoretical branching ratios given the rapid dissociation of the vinyl (C₂H₃) and allyl (C₃H₅) products to form secondary H-atoms.

Furthermore, the ¹CH₂ + C₂H₄ reaction also occurs over the ¹C₃H₆ PES. On the experimental side, Gannon et al.^{65,66} measured H-atom yields that increase from 0.35 at 195 K to 1.08 at 498 K using a slow flow reaction cell and LIF as a detection method. On the theoretical side, Ye et al.⁶⁴ performed variable reaction coordinate transition state theory (VRC TST) calculations to determine the pressure dependent branching ratios in the 300 - 2000 K temperature range. These authors found that the major products channels were H + C₃H₅ and CH₃ + C₂H₃ in addition to C₃H₆ stabilization at 75 torr (the lowest pressure employed in the calculations). According to their calculations, the reagents ¹CH₂ and C₂H₄ are 455.2 kJ/mol above the energy level for C₃H₆, a value that can be compared to that for C(¹D) + C₂H₆ of approximately 750 kJ/mol above the energy level for C₃H₆. In our case, given the high energy of the reagents with respect to C₃H₆ and the low pressures employed during the experiments (1.1 – 5 torr), intermediate stabilization is likely to be very minor. Consequently, just the bimolecular exit channels are considered in this analysis.

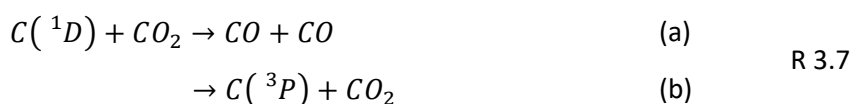
Our H-atom yields determined for the C(¹D) + C₂H₆ reaction are independent of temperature as can be seen in *Table 3.4*. These values are somewhat lower than the H-atom yields determined from the

thermal unimolecular dissociation of C_3H_6 ,⁶³ however they are in good agreement with the high temperature values reported by Gannon et al.^{65,66} a result that might be expected considering the considerable excess energy of our system compared with the $^1CH_2 + C_2H_4$ one. In common with the $C(^1D) + CH_4$ reaction, the H-atom yields are slightly greater than one which means that some of the products fall apart to give secondary H-atoms.

The measured rate constants for the $C(^1D) + C_2H_6$ reaction increase from $(3.3 \pm 0.4) \times 10^{-10} \text{ cm}^3 \text{ s}^{-1}$ at 50 K to $(4.6 \pm 0.5) \times 10^{-10} \text{ cm}^3 \text{ s}^{-1}$ at 296 K. These high values ($k > 10^{-10} \text{ cm}^3 \text{ s}^{-1}$) are consistent with a reaction being dominated by long-range forces.⁶⁸⁻⁷¹ For exothermic reactions with no barrier along the reaction path and characterized by large rate constants, classical capture theory combined with a treatment of the long-range interactions (dipole-dipole, dipole-quadrupole, dipole-induced dipole and dispersion) might be appropriate to describe the systems.^{72,73} In the case of the $C(^1D) + C_2H_6$ reaction, as neither of the reagents has a permanent dipole moment, reaction arises through dispersion interactions alone, which depend on the polarizability of the individual species. Then in the absence of other long-range interactions we would expect that the dispersion terms yield a rate constant with a slight temperature dependence proportional to $T^{1/6}$.⁷⁴ The solid red line in *Figure 3.12* illustrates this theoretical dependence of the rate constant which compares quite well with the experimental values.

3.4. The $C(^1D) + CO_2$ reaction

In the Martian atmosphere, the UV photodissociation of CO_2 (the main constituent) produces CO molecules.⁷⁵ The photodissociation of CO below 100 nm has been studied experimentally by Gao et al.¹¹ showing that $C(^1D)$ is produced in significant quantities. Consequently, the reaction of carbon atoms in its first excited state with CO_2 might play a role in the chemistry of Mars's atmosphere. This reaction has two possible exothermic outcomes: reaction to form two CO molecules or electronic quenching to produce $C(^3P) + CO_2$.



Husain and coworkers^{15,76} performed a study of all the electronic states of atomic carbon (1S , 1D and 3P) in their interactions with CO_2 molecules. The results of their work were discussed based on the symmetry of the potential energy surfaces involved in the processes according to the following correlation diagram (*Figure 3.15*). These authors stated that the $C(^1D)$ collision with CO_2 is a very reactive process that occurs adiabatically over the $^1A'$ PES to form two ground state CO molecules, a result that agrees with the rate constant determined at room temperature¹⁵ of $(3.7 \pm 1.7) \times 10^{-11} \text{ cm}^3$

s^{-1} . On the other hand, the electronic quenching involves non-adiabatic transitions to the triplet surface which correlates with $C(^3P) + CO_2$ products.

To the best of our knowledge, there are no other dynamics or kinetics studies on the $C(^1D) + CO_2$ reaction reported in the literature. However, this reaction is expected to occur through the insertion of $C(^1D)$ into one of the C=O bonds of CO_2 to form singlet ethylenedione (OCCO), which has attracted lots of theoretical and experimental attention.^{77,78} These studies can shed some light on the reaction mechanism of the $C(^1D) + CO_2$ reaction. In this thesis, the rate constants for this process are measured over the temperature range 50 - 296 K.

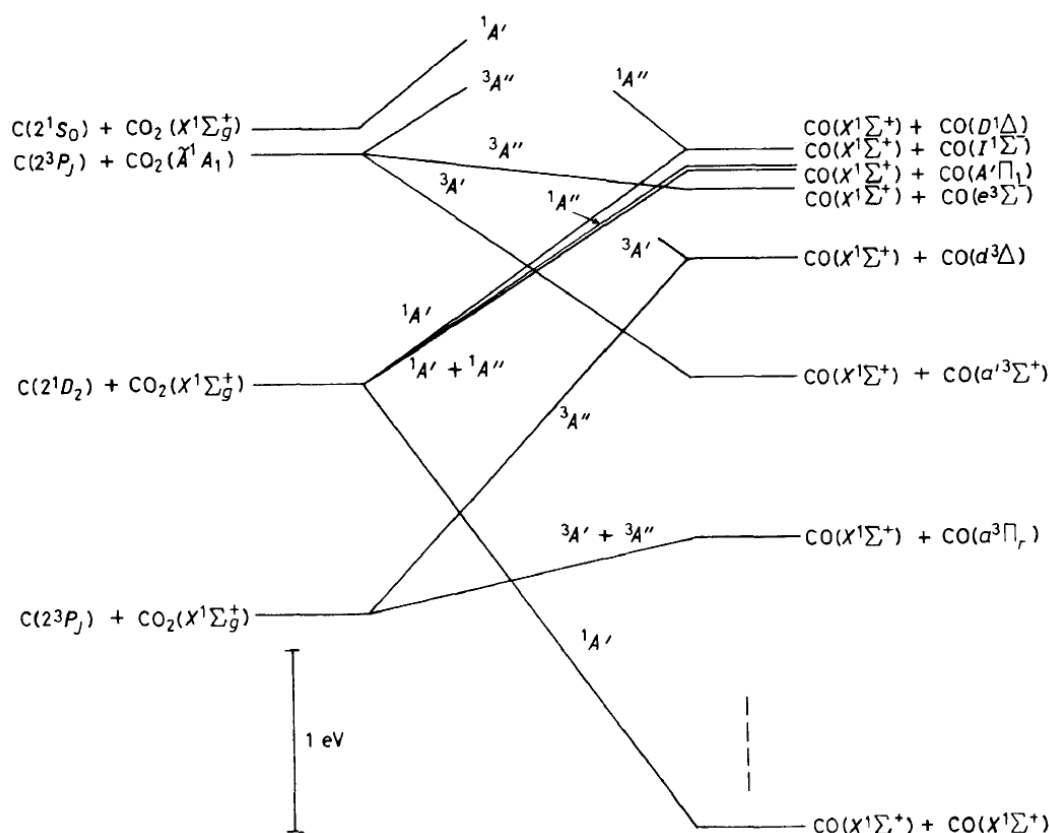


Figure 3.15 Correlation diagram for $C + CO_2$ with those of $CO + CO$ assuming C_s symmetry in the collision complex. Extracted from Husain and Newton.⁷⁶

3.4.1. Results

To apply the pseudo-first-order approximation, the CO_2 concentration was maintained in a large and known excess with respect to the $C(^1D)$ concentration. The reaction of CO_2 with $C(^3P)$ can be neglected because the formation of $CO(^1\Sigma^+) + CO(^1\Sigma^+)$ products is spin forbidden and very slow at room temperature⁷⁶ while the formation of the spin allowed products $CO(^1\Sigma^+) + CO(^3\Pi)$ is endothermic. To study the $C(^1D) + CO_2$ reaction, we used a chemical tracer method (see section 3.1). The H-atom

fluorescence signal (using the chemical tracer method to follow the progress of the reaction) as a function of time with and without CO_2 added are presented in *Figure 3.16*.

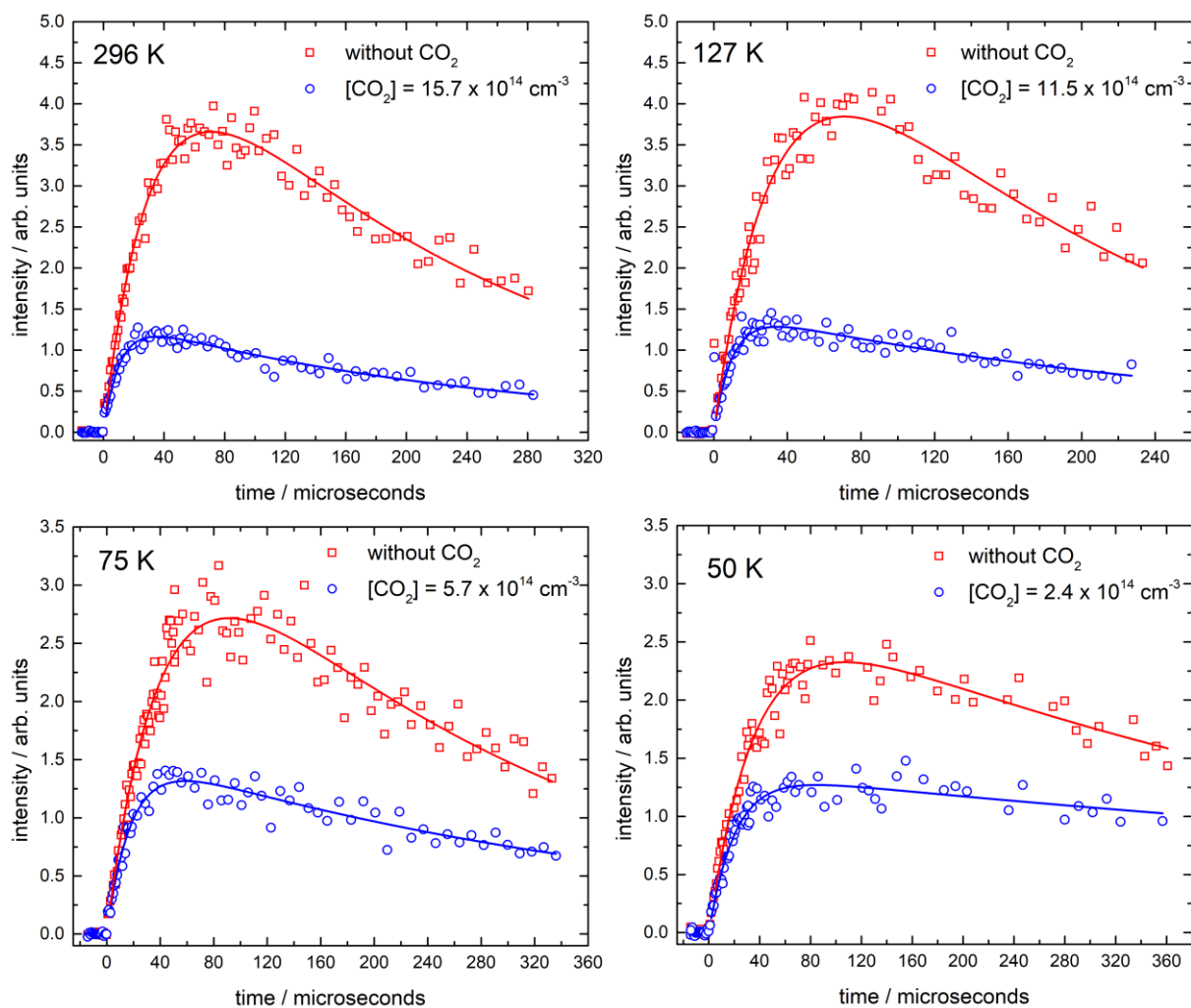


Figure 3.16 $\text{H}(^2\text{S})$ VUV LIF signals as a function of time for the $\text{C}(^1\text{D}) + \text{CO}_2$ reaction employing $\text{C}(^1\text{D}) + \text{H}_2$ as a chemical tracer. (Left panels) reaction at 296 K and 75 K. (Right panels) reaction at 127 K and 50 K. (Red open squares) H-atom temporal profiles without CO_2 added. (Blue open circles) H-atom temporal profiles with the maximum concentration of CO_2 added during the experiments. Solid blue and red lines represent functional fits to the data using expression 2.9.

The measured pseudo-first-order rate constants are plotted as a function of $[\text{CO}_2]$ in *Figure 3.17*. The y-intercept values represent the contributions from the $\text{C}(^1\text{D}) + \text{H}_2$ (the chemical tracer) and $\text{C}(^1\text{D}) + \text{CBr}_4$ (the $\text{C}(^1\text{D})$ precursor) reactions which are constant for any single series of measurements.

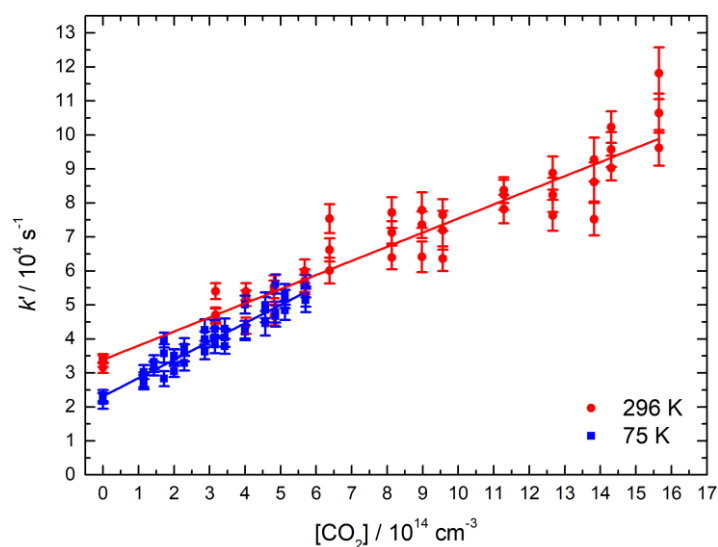


Figure 3.17 Second-order plots of the $\text{C}(^1\text{D}) + \text{CO}_2$ reaction. (Red solid circles) data recorded at 296 K; (blue solid squares) data recorded at 75 K. The solid lines represent linear least-squares fits to the data, weighted by the statistical uncertainties of the individual data points obtained from the pseudo-first-order fits.

The second-order rate constants obtained as a function of temperature are displayed in Figure 3.18 along with the only previous experimental determination.

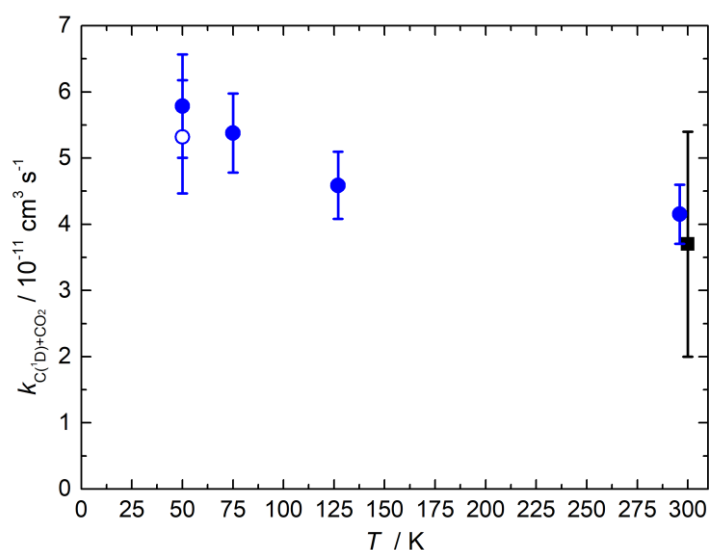


Figure 3.18 Rate constants for the $\text{C}(^1\text{D}) + \text{CO}_2$ reaction as a function of temperature. Experimental studies (blue solid circles) this work using H_2 as a chemical tracer; (blue open circle) this work using CH_4 as a chemical tracer; (black solid square) Husain and Kirsch.¹⁵ Error bars on the present result represent the combined statistical and systematic uncertainties.

The second-order rate constants, the CO_2 concentration ranges, the H_2 or CH_4 concentration used in each series of experiments and the number of experiments performed in each case are summarized in Table 3.5

Table 3.5 Temperature dependent rate constants for the $C(^1D) + CO_2$ reaction.

T(K)	N ^b	[CO ₂] (10 ¹⁴ cm ⁻³)	[H ₂] (10 ¹³ cm ⁻³)	$k_{C(^1D)+CO_2}$ (10 ⁻¹¹ cm ³ s ⁻¹)
296	42	0 - 15.7	6.2	(4.2 ± 0.4) ^c
127 ± 2 ^a	40	0 - 11.5	7.6	(4.6 ± 0.5)
75 ± 2	42	0 - 5.7	7.6	(5.4 ± 0.6)
50 ± 1	42	0 - 2.4	10.5	(5.8 ± 0.8)
T(K)	N	[CO ₂] (10 ¹⁴ cm ⁻³)	[CH ₄] (10 ¹³ cm ⁻³)	$k_{C(^1D)+CO_2}$ (10 ⁻¹¹ cm ³ s ⁻¹)
50 ± 1	20	0 - 2.4	8.7	(5.3 ± 0.9)

^aUncertainties in the calculated temperatures represent the statistical (1σ) errors obtained from Pitot tube measurements of the impact pressure. ^bNumber of individual measurements. ^cUncertainties on the measured rate constants represent the combined statistical (1σ) and estimated systematic (10%) errors.

3.4.2. Discussion

From *Figure 3.18* it can be seen that our measured rate constant at room temperature is in excellent agreement with the previous result of Husain and Kirsch¹⁵ obtained using a combination of pulsed VUV irradiation of carbon suboxide (C₃O₂) to produce C(¹D) atoms and time-resolved atomic absorption spectroscopy to follow the C(¹D) decay through collisions with CO₂. Regarding the temperature dependence of this reaction, it can be seen that when the temperature is decreased to 50 K an increase in the rate constant is observed. In order to check for a possible secondary source of H atoms (which might interfere with our measurements of the target C(¹D) + CO₂ reaction), the chemical tracer H₂ was replaced by CH₄ with the goal to eliminate the highly reactive CH radical formed as a product of the C(¹D) + H₂ reaction. As can be seen from *Figure 3.18*, both rate constants are very similar which indicates that the secondary formation of H-atoms is likely to play only a minor role in the present experiments.

As far as we know, there are no other kinetic studies of this reaction. However, insertion of C(¹D) into the C=O bond of CO₂ will produce an ethylenedione (C₂O₂) molecule. Schröder et al.⁷⁸ reported a combined experimental and theoretical study of the neutral ethylenedione molecule suggesting that the singlet state molecule is short-lived and undergoes spontaneous spin-allowed dissociation to form two CO molecules in their ground state. These authors found a minimum energy crossing point (MECP) between the singlet and triplet surface stating that the short-lived triplet state of the neutral ethylenedione molecule proceeds by efficient non-adiabatic crossing to the singlet surface followed by fast dissociation to produce ground state CO molecules. More recently, Talbi et al.⁷⁷ performed an ab initio study of the singlet (¹Δ_g) and triplet (³Σ_g⁻) states of C₂O₂. These authors found an energy gap of 38 kJ/mol between the singlet and triplet states of C₂O₂. The ground state products CO (¹Σ⁺) + CO (¹Σ⁺)

which correlate adiabatically with the singlet surface are located 283.7 kJ/mol below the singlet state and the non-adiabatic products CO ($^1\Sigma^+$) + CO ($^3\Pi$) lie almost 300 kJ/mol above the singlet state. Consequently, the formation of CO ($^1\Sigma^+$) + CO ($^3\Pi$) is not possible in this case given the high-energy gap between the singlet reactants and the non-adiabatic products. Another possible outcome for this reaction is quenching to form C(3P) + CO₂, however as these products are higher in energy than the crossing point found by Schröder et al.⁷⁸ the most likely outcome for this reaction is the formation of CO ($^1\Sigma^+$) + CO ($^1\Sigma^+$) products.

3.5. The C(1D) + HD reaction

The reactions of C(1D) with H₂ and its isotopic variants are important reactions in hydrocarbon combustion chemistry and atmospheric chemistry.⁷⁹ Furthermore these reactions have attracted considerable theoretical attention during the years given the simplicity of this tri-atomic system composed by only eight electrons, thus allowing comparison between several theoretical methods.^{80,81} Besides, reactions with different isotopic forms of hydrogen (D₂ and HD) allow us to study the mass effects on the rate constants and dynamics of the system. Specifically, for the reaction of C(1D) with HD we can determine the isotopic branching ratio between the CH + D and CD + H exit channels. Although there are several experimental studies on the dynamics^{82–85} of the C(1D) + H₂/D₂/HD reactions, kinetics studies are scarce with most of the determinations restricted to room temperature.^{17,81,86–88} Very recently, Hickson and coworkers^{7,8} have extended the kinetic measurements for the C(1D) + H₂/D₂ reactions down to 50 K, renewing the interest in these processes. In these previous studies,^{7,8} the authors also analysed the behaviour of the C(1D) + H₂/D₂ reactions over the two lowest singlet potential energy surfaces ($^1A'$ and $^1A''$) using the ring-polymer molecular dynamics method (RPMD). In this chapter, we measured rate constants and the isotopic branching ratios for the C(1D) + HD reaction over the 50 – 296 K temperature range and compared our results with the previous ones determined for the C(1D) + H₂ and D₂ reactions under similar conditions.

3.5.1. Results

For this reaction, kinetics experiments and isotopic branching ratio determinations were performed following the formation of D-atoms at 121.534 nm. The pseudo-first-order approximation was applied by maintaining the HD concentration in a large and known excess with respect to the C(1D) concentration. Although C(3P) is produced during the photolysis of CBr₄, the C(3P) + HD reaction can be neglected at room temperature and below because of its high endothermicity.⁸⁷

3.5.1.1. Rate constants

The D-atom fluorescence signals as a function of time with different HD concentrations added are presented in *Figure 3.19*.

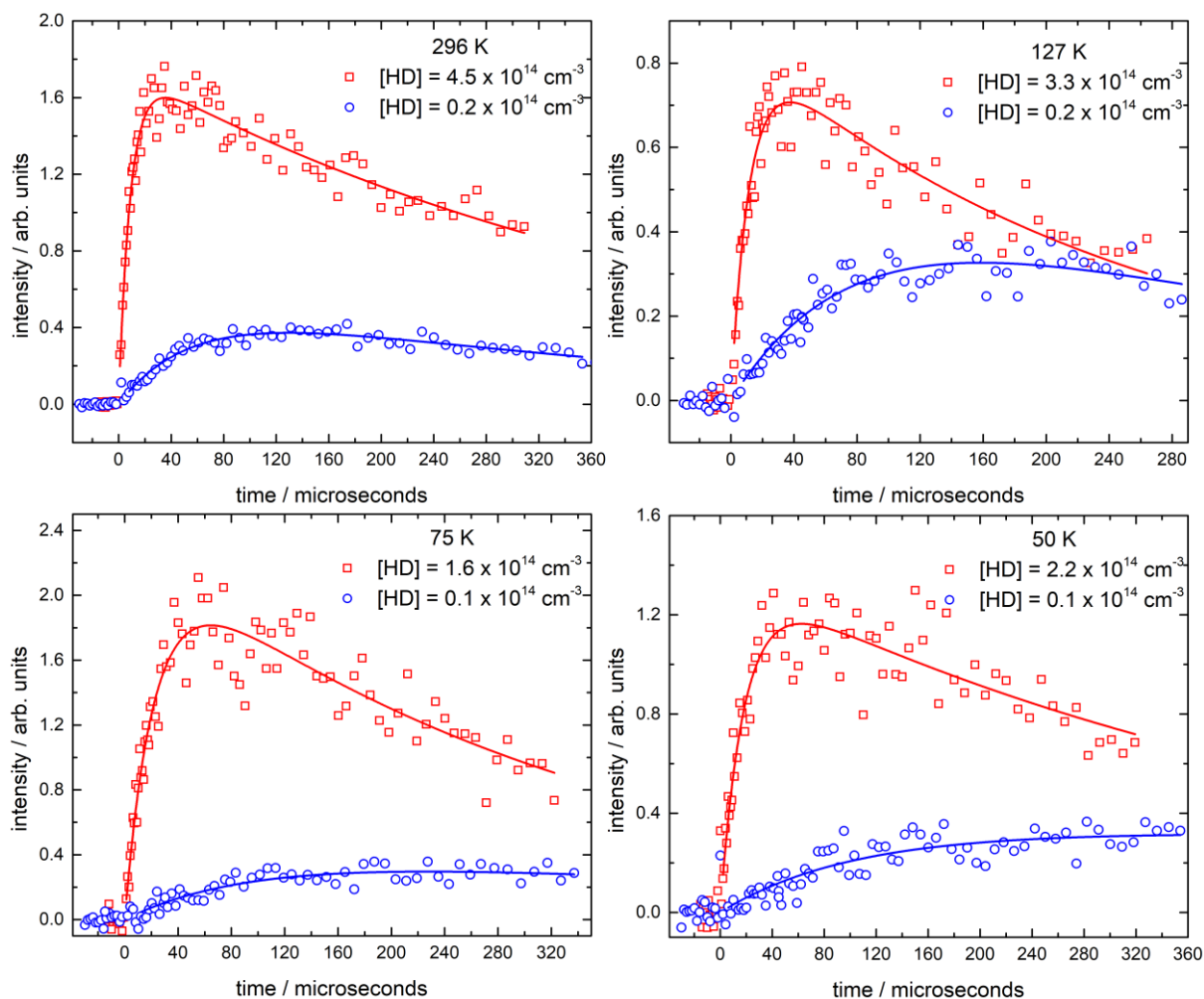


Figure 3.19 $D(^2S)$ VUV LIF signals as a function of time for the $C(^1D) + HD$ reaction. (Left panel) reaction at 296 K and 75 K. (Right panel) reaction at 127 K and 50 K. (Red open squares) D-atom temporal profiles with the maximum concentration of HD used during the experiments. (Blue open circles) D-atom temporal profiles with the minimum concentration of HD used during the experiments. Solid blue and red lines represent functional fits to the data using expression 2.9.

The measured pseudo-first-order rate constants are plotted as a function of [HD] in *Figure 3.20*.

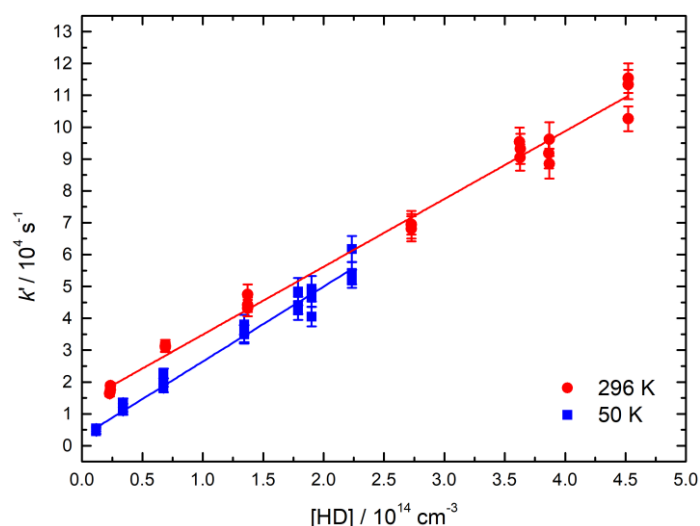


Figure 3.20 Second-order plots of the $C(^1D) + HD$ reaction. (Red solid circles) data recorded at 296 K; (blue solid squares) data recorded at 50 K. The solid lines represent linear least-squares fits to the data, weighted by the statistical uncertainties of the individual data points derived from the pseudo-first-order fits.

The second-order rate constants obtained as a function of temperature are displayed in Figure 3.21 along with previous experimental determinations of the $C(^1D) + H_2$ and D_2 reactions under similar conditions for comparison.

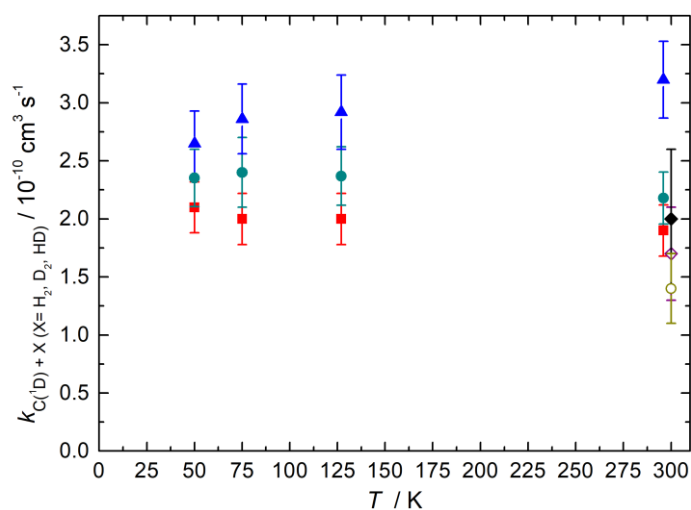


Figure 3.21 Rate constants for the $C(^1D) + X$ reactions (where $X = H_2, D_2$ or HD) as a function of temperature. $C(^1D) + HD$ reaction (green solid circles) this work; (purple open diamond) Sato et al.⁸⁶ $C(^1D) + H_2$ reaction (blue solid triangles) Hickson et al.⁷; (black solid diamond) Sato et al.⁸⁶ $C(^1D) + D_2$ reaction (red solid squares) Hickson et al.⁸⁹ (yellow open circle) Sato et al.⁸⁶ Error bars on the present result represent the combined statistical and systematic uncertainties.

The second-order rate constants, the HD concentration ranges used and the number of experiments performed in each case are summarized in Table 3.6.

Table 3.6 Temperature dependent rate constants for the $C(^1D) + HD$ reaction.

T(K)	N ^b	[HD] (10^{14} cm^{-3})	$k_{C(^1D)+HD}$ ($10^{-10} \text{ cm}^3 \text{ s}^{-1}$)
296	21	0.2-4.5	$(2.2 \pm 0.2)^c$
127 ± 2^a	21	0.2-3.3	(2.3 ± 0.2)
75 ± 2	21	0.1-1.6	(2.4 ± 0.3)
50 ± 1	21	0.1-2.2	(2.4 ± 0.3)

^aUncertainties in the calculated temperatures represent the statistical (1σ) errors obtained from Pitot tube measurements of the impact pressure. ^bNumber of individual measurements. ^cUncertainties in the measured rate constants represent the combined statistical (1σ) and estimated systematic (10%) errors.

3.5.1.2. CD/CH branching ratio

To determine D-atom yields as a function of temperature the D-atom signal intensity from the $C(^1D) + HD$ reaction was compared with the D-atom signal from the reference reaction $C(^1D) + D_2$, which is considered to produce a 100% D-atom yield. D-atom fluorescence signals recorded sequentially at 50 K for the target and reference reaction with the same pseudo-first-order time constant are shown in Figure 3.22.

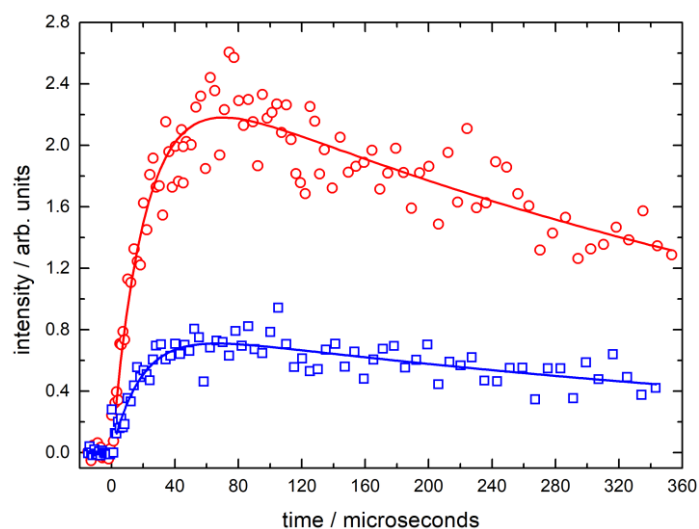


Figure 3.22 D-atom VUV LIF emission profiles recorded at 50 K. (Red open circles) D-atom signal from the $C(^1D) + D_2$ reaction with $[D_2] = 2.2 \times 10^{14} \text{ cm}^{-3}$; (red solid line) biexponential fit to the $C(^1D) + D_2$ data points. (Blue open squares) D-atom signal from the $C(^1D) + HD$ reaction with $[HD] = 1.9 \times 10^{14} \text{ cm}^{-3}$; (blue solid line) biexponential fit to the $C(^1D) + HD$ data points.

Relative D-atom yields were derived from the amplitude parameter A of biexponential fits to profiles such as those shown in Figure 3.22. The absolute D-atom yield at any given temperature was thus determined by the ratio of the A factors for the target and reference reactions. As both HD and D_2 have negligible absorption cross-sections at 121.534 nm, no additional corrections to the derived signal

amplitude values were necessary. Absolute D-atom yields were converted to the CD/CH branching ratio using the following formula:

$$\frac{CD}{CH} = \frac{1 - D \text{ atom yield}}{D \text{ atom yield}}$$

Table 3.7 CD/CH branching ratios as a function of temperature

T(K)	N ^b	CD/CH branching ratio
296	6	1.58 ± 0.17 ^c
127 ± 2 ^a	3	2.02 ± 0.23
75 ± 2	6	2.10 ± 0.34
50 ± 1	6	2.07 ± 0.22

^aUncertainties in the calculated temperatures represent the statistical (1σ) errors obtained from Pitot tube measurements of the impact pressure. ^bNumber of individual measurements. ^cThe error bars represent the statistical uncertainties at the 95% of confidence level.

3.5.2. Discussion

The C(¹D) + HD reaction is a barrierless process occurring through the insertion of the C(¹D) atom into the H-D bond generating a strongly bound HCD intermediate which dissociates to form CH + D and CD + H products. As can be seen from *Figure 3.21* the rate of reaction when comparing C(¹D) + H₂/D₂/HD reactions shows a noticeable isotope effect with the rate constants decreasing from H₂ to HD to D₂ in agreement with the previous study of Sato et al.⁸⁶ performed at room temperature. These authors attributed the reactivity differences to an increase of the reduced mass of the reactants with $\mu_{H_2} < \mu_{HD} < \mu_{D_2}$ and $k_{H_2} > k_{HD} > k_{D_2}$. However, the rate constant reported by these authors is somewhat smaller than our measured value for HD at room temperature. Sato et al.⁸⁶ produced C(¹D) through the multiphoton dissociation of carbon suboxide (C₃O₂) at 308 nm and followed the kinetics of the reaction by LIF probing the CH and CD products of the reaction. The discrepancy between their result and ours could be due to the fitting procedure used by them to extract the rate constants. In their case, if the rate constants for secondary reactions were incorrectly estimated, this could potentially lead to errors in the derived rate constant.

From *Figure 3.21* it can be seen that there is little or no temperature dependence for the C(¹D) + HD reaction with the determined values within errors in the 50 - 296 K temperature range. Interestingly, the C(¹D) + H₂/D₂ reactions show slight positive and negative temperature dependence respectively. Hickson et al.^{7,8} explained these behaviours in the light of the spin-isomer population ratio (ortho and

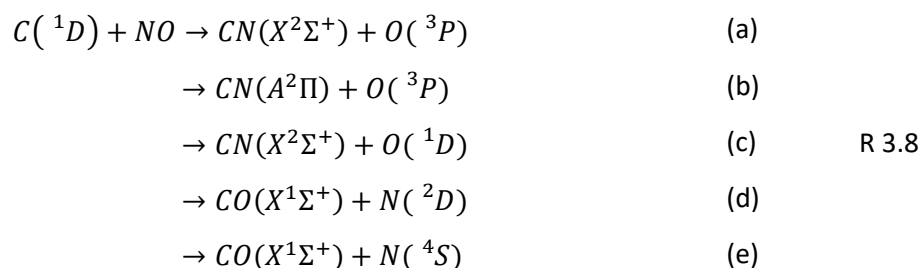
para forms) for H₂ and D₂ isotopologues. In these experiments, they have a fixed 3:1 ratio for the ortho/para forms of H₂ and a fixed 2:1 ratio for D₂ at all temperatures due to the inefficient gas-phase spin conversion. However, these values deviate from the expected equilibrium mixtures of ortho/para forms as the temperature is lowered. Consequently, if the reactivity of the ortho and para forms differ towards C(¹D) atoms, the observed effects on the temperature dependence should be largest at the lowest temperatures where deviation from the equilibrium populations are greatest. In our case, a similar effect is not expected given the absence of identical nuclei.

Regarding the CD/CH branching ratios, there are two previous experimental determinations to the best of our knowledge. Sato et al.⁸⁶ reported a value of 1.6 ± 0.1 at room temperature or equivalent energy of 3.7 kJ/mol while Fisher et al.⁸¹ measured a value of 1.7 ± 0.1 at room temperature. On the theoretical side, several calculations using different levels of theory have been performed and recently compared in Gonzalez-Lezana et al.⁸⁰ From *Table 3.7*, a slight increase in the branching ratios is observed as the temperature is lowered from 296 to 127 K. While our measured branching ratio at room temperature is in agreement with the result of Sato et al.⁸⁶ the theoretical values reported in the literature differ depending on the method used. Sun et al.⁷⁹ performed quantum mechanical wavepacket calculations over the ¹A' PES finding a branching ratio that increases from 1.3 at room temperature to 1.6 at 50 K. This result is quite low compared with our experimental result in the same temperature range probably because the calculations were performed using only the ¹A' PES while other studies on the C(¹D) + H₂/D₂/HD systems confirm the importance of the inclusion of the first excited PES ¹A''.^{7,8,90} Joseph et al.⁹¹ performed quasiclassical trajectory calculations over the ¹A' PES obtaining branching ratios of 2.1 at room temperature and 2.0 at 100 K. More recently Gonzalez-Lezana et al.⁸⁰ performed statistical quantum mechanical (SQM) and mean potential phase space theory (MPPST) calculations. They found branching ratios that remain around 1.8 in the 100 - 500 K temperature range with the SQM method while for the MPPST method, the branching ratio is 2.1 at 500 K and 2.0 at 100 K. The last three methods report isotopic branching ratios that are very close to our experimental results. In general, CD/CH branching ratios greater than unity indicate that the CD + H product channel is dominant because the elimination of a light H-atom is faster than that of the heavy D-atom. As the CD/CH branching ratio is considered to be a sensitive probe of the PES^{79,86,91} this new experimental data provides valuable information for further theoretical calculations.

3.6. The C(¹D)+NO/O₂ reactions

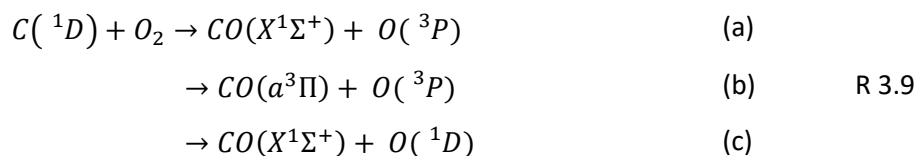
Studies of reactions involving C(¹D) with NO and O₂ have a fundamental importance because little is known about the reactivity of this excited state atom towards open shell molecules (NO) or biradicals (O₂). The equivalent reactions involving C(³P) have been studied on several occasions at room temperature^{51,92,93} and in the 15 – 295 K temperature range yielding rate constants that increase as the temperature is lowered.^{12,18,94}

In the case of C(¹D) + NO reaction there are several possible exothermic exit channels:



The R 3.8 (e) channel is spin-forbidden and highly exothermic (-567 kJ/mol⁻¹), a fact which might influence the overall reactivity of the system. Regarding the kinetics of this reaction there is only one previous determination of the rate constant at room temperature. Husain and Kirsch¹⁵ produced C(¹D) by pulsed VUV irradiation of carbon suboxide (C₂O₃) and followed the kinetics by time resolved atomic absorption spectroscopy obtaining a rate constant of $(4.7 \pm 1.3) \times 10^{-11} \text{ cm}^3 \text{ s}^{-1}$. This rate constant value indicates that the kinetics of excited state atomic carbon in reaction with NO could be significantly slower in comparison with the reaction between ground state atomic carbon and NO.

In the case of the C(¹D) + O₂ reaction, there are several exothermic exit channels with channel R 3.9 (c) being spin-forbidden:



The kinetics of this reaction has been studied by Husain and Kirsch¹⁵ at room temperature. These authors compared the reactivity of the excited and ground electronic states indicating that the C(¹D) + O₂ reaction occurs less efficiently than the C(³P) one. In this chapter, the reactivity of C(¹D) with NO and O₂ is investigated over the 50 - 296 K temperature range.

3.6.1. Results

The NO and O₂ concentrations were maintained in a large and known excess with respect to the C(¹D) concentration to apply the pseudo-first-order approximation. The kinetics of the C(¹D) + NO and O₂ reactions were studied using a chemical tracer method (see section 3.1).

3.6.1.1. Rate constants

The H-atom fluorescence signal from the chemical tracer as a function of time with different NO/O₂ concentrations added at 296 and 50 K are presented in *Figure 3.23*.

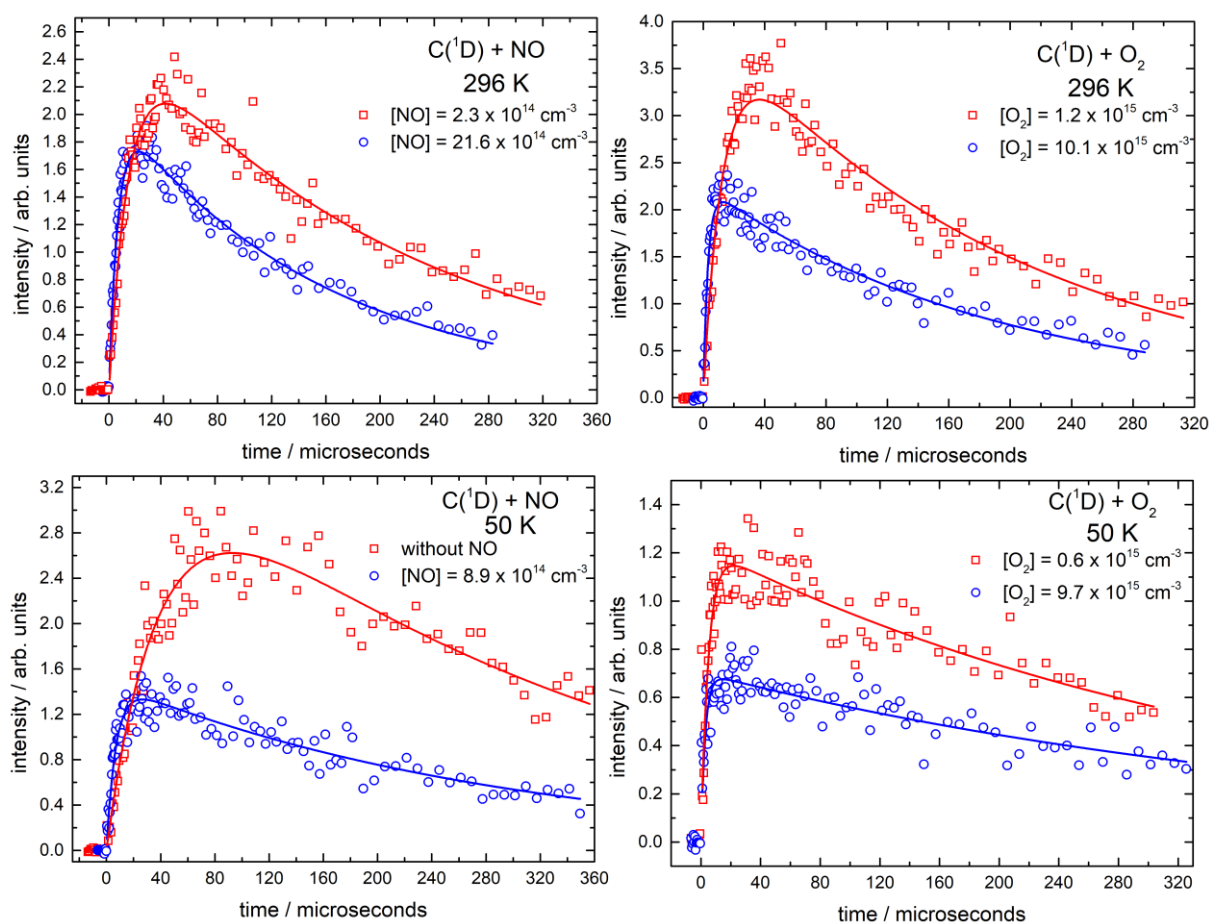


Figure 3.23 H-atom formation curves recorded as a function of time using the H₂ chemical tracer method. (Left panel) the C(¹D) + NO reaction at 296 and 50 K. (Right panel) the C(¹D) + O₂ reaction at 296 and 50 K. (red open squares) and (blue open circles) the highest and lowest coreagent concentrations respectively. Solid blue and red lines represent functional fits to the data using expression 2.9.

The second-order rate constants for the C(¹D) + NO and C(¹D) + O₂ reactions were obtained from the slopes when the derived pseudo-first-order rate constants were plotted against the concentration of NO and O₂ respectively (*Figure 3.24*).

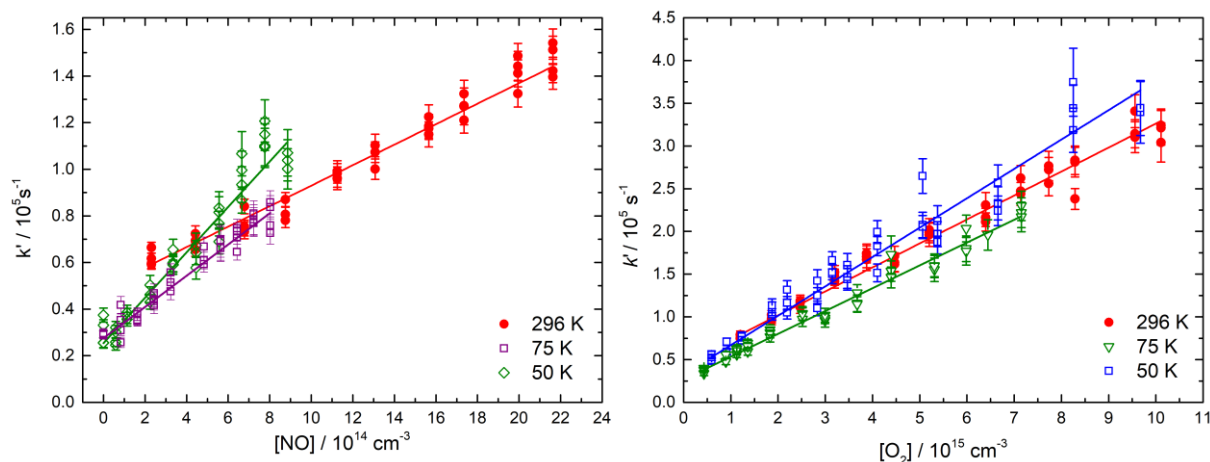


Figure 3.24 Second-order plots of the $C(^1D) + NO/O_2$ reactions. (Left panel) the $C(^1D) + NO$ reaction (right panel) the $C(^1D) + O_2$ reaction. Solid lines represent linear least-squares fits to the data, weighted by the statistical uncertainties of the individual data points given by biexponential fits such as those shown in Figure 3.23

Our second-order rate constants as a function of temperature are displayed in Figure 3.25 together with the previously reported experimental values for these reactions.

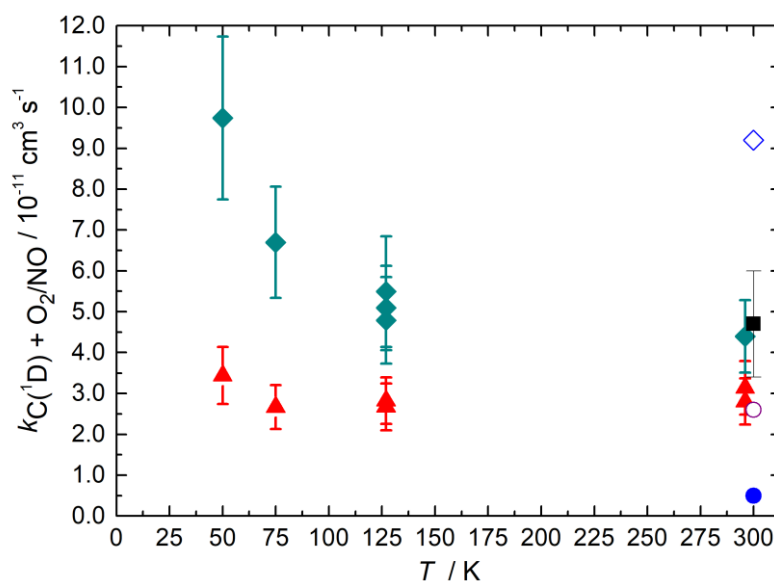


Figure 3.25 Measured rate constants as a function of temperature. The $C(^1D) + NO$ reaction (solid green diamonds) this work; (black solid square) Husain and Kirsch;¹⁵ (blue open diamond) Braun et al.¹⁷ The $C(^1D) + O_2$ reaction (red solid triangles) this work; (purple open circle) Husain and Kirsch;¹⁵ (blue solid circle) Braun et al.¹⁷ Error bars on the present values represent the combined statistical and systematic uncertainties.

The second-order rate constants, the number of experiments performed in each case, the concentration ranges for the reagents and the chemical tracer employed are summarized in Table 3.8.

Table 3.8 Temperature dependent rate constants for the C(¹D) + NO and C(¹D) + O₂ reactions.

T(K)	N ^b	[NO] (10 ¹⁴ cm ⁻³)	[H ₂] (10 ¹⁴ cm ⁻³)	k _{C(¹D)+NO} (10 ⁻¹¹ cm ³ s ⁻¹)	N	[O ₂] (10 ¹⁵ cm ⁻³)	[H ₂] (10 ¹⁴ cm ⁻³)	k _{C(¹D)+O₂} (10 ⁻¹¹ cm ³ s ⁻¹)
296	37	2.3-21.6	1.4	(4.4 ± 0.9) ^c	39	1.2-10.1	1.4	(2.8 ± 0.6)
127 ± 2 ^a	11	0-13.1	0.7	(4.8 ± 1.1)	41	0.9-9.8	1.7	(2.8 ± 0.6)
127 ± 2	35	0-16.3	1.7	(5.1 ± 1.0)				
127 ± 2	12	3.3-16.4	3.5	(5.5 ± 1.4)				
75 ± 2	37	0-8.0	0.8	(6.7 ± 1.4)	36	0.4-7.2	0.9	(2.7 ± 0.5)
50 ± 1	36	0-8.9	1.2	(9.7 ± 2.0)	41	0.6-9.7	1.2	(3.4 ± 0.7)

T(K)	N	[NO] (10 ¹⁴ cm ⁻³)	[CH ₄] (10 ¹⁴ cm ⁻³)	k _{C(¹D)+NO} (10 ⁻¹¹ cm ³ s ⁻¹)	N	[O ₂] (10 ¹⁵ cm ⁻³)	[CH ₄] (10 ¹⁴ cm ⁻³)	k _{C(¹D)+O₂} (10 ⁻¹¹ cm ³ s ⁻¹)
296					35	1.2-10.1	0.7	(3.1 ± 0.7)
127 ± 2					18	0.9-9.8	0.5	(2.7 ± 0.6)

^aUncertainties in the calculated temperatures represent the statistical (1σ) errors obtained from Pitot tube measurements of the impact pressure. ^bNumber of individual measurements. ^cUncertainties in the measured rate constants taking into account a systematic error of 20% of the nominal rate constant value due to the influence of secondary reactions in the overall chemistry of the system (see section 3.6.1.2).

3.6.1.2. Influence of secondary reactions

In these experiments, as the kinetics of the C(¹D) + NO/O₂ reactions was followed indirectly using a chemical tracer method, it is possible that secondary reactions could have an influence on the formation of H-atoms, interfering with our study of the primary processes. For example, C(³P) is also formed in the reactor as a product in the photolysis of CBr₄. Then it is important to evaluate the influence of the C(³P) + NO/O₂ reaction products on the overall chemistry inside the reactor.

In the case of the C(¹D)/C(³P) + NO system, the C(³P) + NO reaction leads to the production of 60% of atomic nitrogen (N(⁴S) + N(²D)) and 40% of O(³P) at room temperature.⁹² Subsequently, N(²D) can react with H₂, leading to the formation of secondary H-atom products. In addition, the C(¹D) + NO reaction could lead to O(¹D) and N(²D) formation which could also react with H₂ to produce secondary H-atoms. To test for the possible influence of these reactions in the rate constant measurements, we perform additional experiments at 127 K. In these experiments, three different fixed H₂ concentrations ([H₂] = 0.7, 1.7 and 3.5 × 10¹⁴ cm⁻³) were used to record the H-atom formation profiles as a function of time using different NO concentrations. The measured pseudo-first-order rate constants as a function of NO concentration are shown in *Figure 3.26* and the second-order rate constants are listed in Table 3.8. The y-intercept values represent the contribution from the C(¹D) + H₂ reaction which increases with

increasing $[H_2]$ due to the increased rate of H-atom formation. As can be seen from Table 3.8, the second-order rate constants obtained from the slopes of these plots at 127 K are essentially the same within experimental errors.

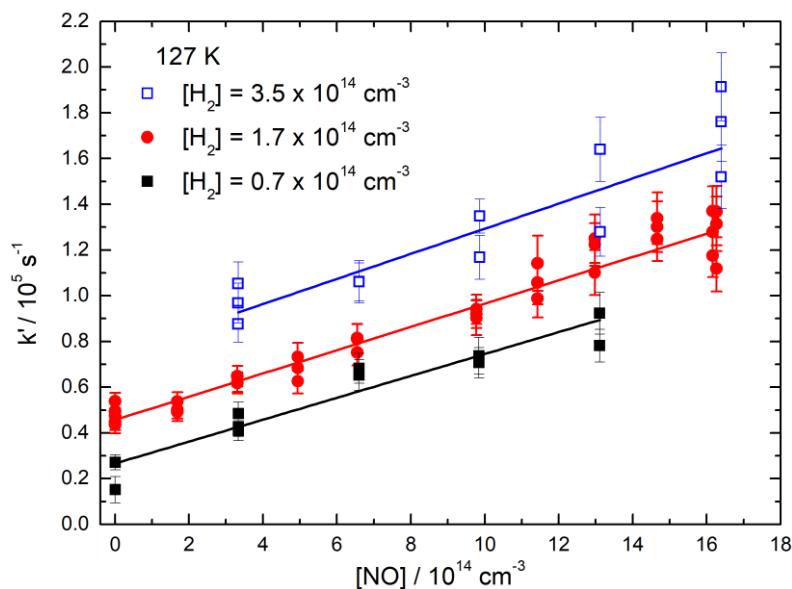


Figure 3.26 Second-order plots of the $C(^1D) + NO$ reaction at 127 K. (Blue open squares) $[H_2] = 3.5 \times 10^{14} \text{ cm}^{-3}$; (red solid circles) $[H_2] = 1.7 \times 10^{14} \text{ cm}^{-3}$; (black solid squares) $[H_2] = 0.7 \times 10^{14} \text{ cm}^{-3}$. The solid lines represent linear least squares fits to the data, weighted by the statistical uncertainties of the individual data points obtained from the pseudo-first-order fits.

In the case of the $C(^1D)/C(^3P) + O_2$ system, $O(^1D)$ is likely to be a major product for at least one of these reactions,^{94,95} consequently the $O(^1D) + H_2$ reaction will produce secondary H-atoms in the reactor which might affect the determination of the rate constants. To check for the possible influence of these secondary reactions in the chemistry of the system we employed CH_4 as a chemical tracer instead of H_2 in experiments performed at 127 K and 296 K. In this case, the corresponding $O(^1D) + CH_4$ reaction leads to only a 20% yield of secondary H-atom products⁹⁶ in contrast with $O(^1D) + H_2$ with a 100% atom yield.⁸⁹ Then if H-atom formation through secondary reactions of $O(^1D)$ is important in the overall chemistry, a noticeable difference between the experiments performed with H_2 or CH_4 as chemical tracers is expected. However, from Figure 3.27 it can be observed that the two set of experiments yield the same second-order rate constant ($(2.8 \pm 0.6) \times 10^{-10} \text{ cm}^3 \text{ s}^{-1}$ for H_2 and $(2.7 \pm 0.6) \times 10^{-10} \text{ cm}^3 \text{ s}^{-1}$ for CH_4 at 127 K) indicating that H-atom formation from this source is negligibly small compared with the primary process.

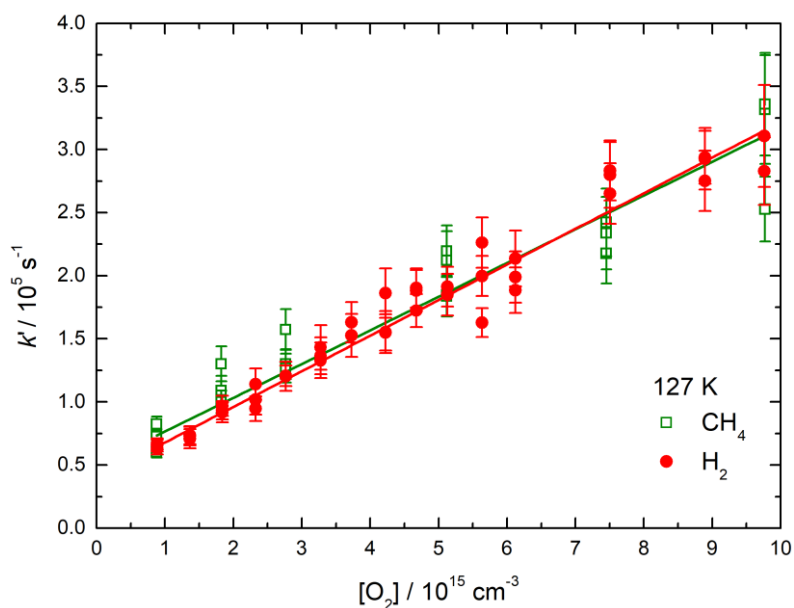


Figure 3.27 Second-order plots of the $\text{C}(^1\text{D}) + \text{O}_2$ reaction at 127 K. (Green open squares) data recorded with CH_4 as a chemical tracer $[\text{CH}_4] = 0.5 \times 10^{14} \text{ cm}^{-3}$; (red solid circles) data recorded with H_2 as a chemical tracer $[\text{H}_2] = 1.7 \times 10^{14} \text{ cm}^{-3}$. The solid lines represent linear least squares fits to the data, weighted by the statistical uncertainties of the individual data points derived from the pseudo-first-order fits.

3.6.1.3. Numerical simulations

A secondary check was performed by running numerical simulations of the reactions potentially involved in the overall chemistry for $\text{C}(^1\text{D}) + \text{NO}/\text{O}_2$ systems using the differential integrator FACSIMILE. Table 3.9 and Table 3.10 list the reactions used in the simulations, the rate constants for each channel and the references for each reaction when available.

Table 3.9 Reactions used in numerical simulations of the $C(^1D) + NO$ reaction.

R#	Reaction	$k(\text{cm}^3\text{s}^{-1})$				Reference	
		296 K	127 K	75 K	50 K		
1	a	$C(^1D) + NO \rightarrow CO + N(^2D)$	4.4×10^{-12}	5.1×10^{-12}	6.7×10^{-12}	9.7×10^{-12}	This work
	b	$C(^1D) + NO \rightarrow CN + O(^1D)$	4.4×10^{-12}	5.1×10^{-12}	6.7×10^{-12}	9.7×10^{-12}	
	c	$C(^1D) + NO \rightarrow CN + O(^3P)$	3.5×10^{-11}	4.1×10^{-11}	5.4×10^{-11}	7.8×10^{-11}	
	k_T	$C(^1D) + NO \rightarrow \text{Products}$	4.4×10^{-11}	5.1×10^{-11}	6.7×10^{-11}	9.7×10^{-11}	
2		$C(^1D) + H_2 \rightarrow CH + H$	3.2×10^{-10}	2.9×10^{-10}	2.9×10^{-10}	2.7×10^{-10}	7
3	a	$C(^3P) + NO \rightarrow CO + N(^4S)$	4.5×10^{-11}	5.2×10^{-11}	5.6×10^{-11}	6.0×10^{-11}	92,94
	b	$C(^3P) + NO \rightarrow CO + N(^2D)$	4.5×10^{-11}	5.2×10^{-11}	5.6×10^{-11}	6.0×10^{-11}	
	c	$C(^3P) + NO \rightarrow CN + O(^3P)$	6.0×10^{-11}	6.9×10^{-11}	7.5×10^{-11}	8.0×10^{-11}	
	k_T	$C(^3P) + NO \rightarrow \text{Products}$	1.5×10^{-10}	1.7×10^{-10}	1.9×10^{-10}	2.0×10^{-10}	
4		$O(^1D) + Ar \rightarrow O(^3P) + Ar$	5.3×10^{-13}	6.0×10^{-13}	6.4×10^{-13}	6.7×10^{-13}	30
5		$N(^2D) + Ar \rightarrow N(^4S) + Ar$	1.0×10^{-16}	1.0×10^{-16}	1.0×10^{-16}	1.0×10^{-16}	97
6		$O(^1D) + H_2 \rightarrow OH + H$	1.4×10^{-10}	1.4×10^{-10}	1.4×10^{-10}	1.4×10^{-10}	89
7	a	$CH + NO \rightarrow O(^1D) + HCN$	6.1×10^{-11}	6.8×10^{-11}	7.2×10^{-11}	7.5×10^{-11}	98,99
	b	$CH + NO \rightarrow O(^3P) + HCN$	6.1×10^{-11}	6.8×10^{-11}	7.2×10^{-11}	7.5×10^{-11}	
	c	$CH + NO \rightarrow H + NCO$	3.6×10^{-11}	4.0×10^{-11}	4.2×10^{-11}	4.4×10^{-11}	
	d	$CH + NO \rightarrow N(^4S) + HCO$	1.2×10^{-11}	1.3×10^{-11}	1.4×10^{-11}	1.5×10^{-11}	
	k_T	$CH + NO \rightarrow \text{Products}$	1.7×10^{-10}	1.9×10^{-10}	2.0×10^{-10}	2.1×10^{-10}	
8	a	$CH + H_2 \rightarrow H + CH_2$	1.2×10^{-12}	7.1×10^{-16}	8.6×10^{-20}	1.4×10^{-24}	100
	b	$CH + H_2 \rightarrow CH_3$	8.4×10^{-13}	2.7×10^{-12}	7.1×10^{-12}	2.4×10^{-11}	
	k_T	$CH + H_2 \rightarrow \text{Products}$	2.0×10^{-12}	2.7×10^{-12}	7.1×10^{-12}	2.4×10^{-11}	
9		$N(^2D) + H_2 \rightarrow NH + H$	2.2×10^{-12}	2.0×10^{-13}	2.0×10^{-13}	1.0×10^{-13}	101
10	a	$N(^2D) + NO \rightarrow N_2 + O(^1D)$	2.1×10^{-11}	2.1×10^{-11}	2.1×10^{-11}	2.1×10^{-11}	101,102
	b	$N(^2D) + NO \rightarrow N_2 + O(^3P, ^1S)$	3.9×10^{-11}	3.9×10^{-11}	3.9×10^{-11}	3.9×10^{-11}	
	k_T	$N(^2D) + NO \rightarrow \text{Products}$	6.0×10^{-11}	6.0×10^{-11}	6.0×10^{-11}	6.0×10^{-11}	
11		$O(^1D) + NO \rightarrow O(^3P) + NO$	1.5×10^{-10}	1.5×10^{-10}	1.5×10^{-10}	1.5×10^{-10}	87
12		$CH + CBr_4 \rightarrow \text{Products}$	1.0×10^{-10}	1.0×10^{-10}	1.0×10^{-10}	1.0×10^{-10}	Estimated
		$K_{SIM} (\text{cm}^3\text{s}^{-1})$	4.2×10^{-11}	4.6×10^{-11}	5.4×10^{-11}	7.3×10^{-11}	

k_T Denotes the overall rate constant for the process.

Table 3.10 Reactions used in numerical simulations of the $C(^1D) + O_2$ reaction.

R#	Reaction	k(cm ³ s ⁻¹)				Reference
		296 K	127 K	75 K	50 K	
13	$C(^1D) + O_2 \rightarrow CO + O(^3P)$ *●	2.8×10^{-11}	2.8×10^{-11}	2.7×10^{-11}	3.4×10^{-11}	This work
2	$C(^1D) + H_2 \rightarrow CH + H$ *	3.2×10^{-10}	2.9×10^{-10}	2.9×10^{-10}	2.7×10^{-10}	7
14	a $C(^3P) + O_2 \rightarrow CO + O(^1D)$ *●	4.9×10^{-11}	6.4×10^{-11}	7.6×10^{-11}	8.7×10^{-11}	94
	b $C(^3P) + O_2 \rightarrow CO + O(^3P)$ *●	0	0	0	0	
	k _T $C(^3P) + O_2 \rightarrow$ Products	4.9×10^{-11}	6.4×10^{-11}	7.6×10^{-11}	8.7×10^{-11}	
15	$O(^1D) + O_2 \rightarrow O(^3P) + O_2$ *●	4.0×10^{-11}	5.4×10^{-11}	5.9×10^{-11}	6.6×10^{-11}	30
4	$O(^1D) + Ar \rightarrow O(^3P) + Ar$ *●	5.3×10^{-13}	6.0×10^{-13}	6.4×10^{-13}	6.7×10^{-13}	
6	$O(^1D) + H_2 \rightarrow OH + H$ *	1.4×10^{-10}	1.4×10^{-10}	1.4×10^{-10}	1.4×10^{-10}	89
16	a $CH + O_2 \rightarrow H + CO_2$ *	1.1×10^{-11}	1.7×10^{-11}	2.2×10^{-11}	2.7×10^{-11}	99,103
	b $CH + O_2 \rightarrow OH + CO$ *	7.6×10^{-12}	1.2×10^{-11}	1.5×10^{-11}	1.8×10^{-11}	
	c $CH + O_2 \rightarrow O + H + CO$ *	1.9×10^{-11}	2.9×10^{-11}	3.7×10^{-11}	4.5×10^{-11}	
	k _T $CH + O_2 \rightarrow$ Products	3.8×10^{-11}	5.7×10^{-11}	7.4×10^{-11}	9.0×10^{-11}	
8	a $CH + H_2 \rightarrow H + CH_2$ *	1.2×10^{-12}	7.1×10^{-16}	8.6×10^{-20}	1.4×10^{-24}	100
	b $CH + H_2 \rightarrow CH_3$ *	8.4×10^{-13}	2.7×10^{-12}	7.1×10^{-12}	2.4×10^{-11}	
	k _T $CH + H_2 \rightarrow$ Products	2.0×10^{-12}	2.7×10^{-12}	7.1×10^{-12}	2.4×10^{-11}	
12	$CH + CBr_4 \rightarrow$ Products *	1.0×10^{-10}	1.0×10^{-10}	1.0×10^{-10}	1.0×10^{-10}	Estimated
17	a $C(^1D) + CH_4 \rightarrow C_2H_2 + H_2$ *●	9.0×10^{-11}	9.5×10^{-11}	1.2×10^{-10}	1.5×10^{-10}	104
	b $C(^1D) + CH_4 \rightarrow C_2H_2 + H + H$ *●	9.0×10^{-11}	9.5×10^{-11}	1.2×10^{-10}	1.5×10^{-10}	
	k _T $C(^1D) + CH_4 \rightarrow$ Products	1.8×10^{-10}	1.9×10^{-10}	2.3×10^{-10}	3.0×10^{-10}	
18	a $O(^1D) + CH_4 \rightarrow OH + CH_3$ *●	1.4×10^{-10}	1.1×10^{-10}	1.1×10^{-10}	1.1×10^{-10}	96
	b $O(^1D) + CH_4 \rightarrow H + CH_3O$ *●	3.4×10^{-11}	2.8×10^{-11}	2.8×10^{-11}	2.8×10^{-11}	
	k _T $O(^1D) + CH_4 \rightarrow$ Products	1.7×10^{-10}	1.4×10^{-10}	1.4×10^{-10}	1.4×10^{-10}	
	k _{SIM_H2} (cm ³ s ⁻¹)	2.2×10^{-11}	2.7×10^{-11}	2.8×10^{-11}	3.5×10^{-11}	
	k _{SIM_CH4} (cm ³ s ⁻¹)	2.7×10^{-11}	2.9×10^{-11}			

k_T Denotes the overall rate constant for the process. (*) Simulations with H₂. (●) Simulations with CH₄.

To perform these simulations, it was necessary to evaluate the rate constants for each individual exit channel. However, as the branching ratio and temperature dependence for some of the reactions listed above are unknown, some estimations were made in order to run the simulations and compare with the experimental data. Other parameters needed as inputs are the concentrations of the excess reagents (which were obtained from their partial pressures) and the concentrations of C(¹D) and C(³P) (which were estimated depending on the gas-phase concentration of CBr₄ and its absorption cross-section along with the photolysis laser fluence). In the simulations, H-atom profiles were generated over the same range of reagent concentrations as the experiments and fitted using expression 2.9. Then the simulated second-order rate constants were obtained from the slopes of the simulated second-order plots. Finally, the simulated second-order rate constants were compared with the input

values for the $C(^1D) + NO/O_2$ reactions to check for any significant deviation as a result of secondary chemistry leading to H-atom formation.

We estimated an uncertainty of at least 20% for the simulated rate constants given the large uncertainties in the temperature dependences and branching ratios for several important reactions used in the simulations. This value was obtained from a sensitivity analysis where the rate constants of the more important secondary reactions were varied.

In the case of the $C(^1D) + NO$ reaction, from *Table 3.9* it can be seen that the differences between the simulated rate constants and the input values increase as the temperature decreases from 5% at 296 to 25% at 50 K. The reactions that have the most influence on this system are those leading to $O(^1D)$ formation because these atoms react rapidly with H_2 to form atomic hydrogen (reaction 6). Indeed, if this reaction is removed from the simulations the differences between the input and output values at 50 K decreases to 10%. The major source of $O(^1D)$ in this simulation is the reaction of $N(^2D) + NO$ (reaction 10a) with $N(^2D)$ atoms being mostly produced by $C(^3P) + NO$ (reaction 3b). As previous branching ratio measurements⁹² for this reaction only give information about the sum of the N-atom production channels (3a + 3b), we set the rate constants for each of these channels to 30% of the total reaction rate. Consequently, it is possible that $N(^2D)$ production is overestimated in these simulations. Moreover, the branching ratios for the individual channels of the $N(^2D) + NO$ (reaction 10) have never been measured.¹⁰¹ The effect of varying the H_2 concentrations was also tested in the simulations at 127 K. For the $[H_2] = 0.7$ and $1.7 \times 10^{14} \text{ cm}^{-3}$, the simulated second-order rate constants are identical with a value of $4.6 \times 10^{-11} \text{ cm}^3 \text{ s}^{-1}$ and for $[H_2] = 3.5 \times 10^{14} \text{ cm}^{-3}$ the simulated second-order rate constant increases to $5.2 \times 10^{-11} \text{ cm}^3 \text{ s}^{-1}$ using an input value of $5.1 \times 10^{-11} \text{ cm}^3 \text{ s}^{-1}$ for the $C(^1D) + NO$ reaction with all three concentrations.

In the case of the $C(^1D) + O_2$ reaction, the simulations were performed with both H_2 and CH_4 in a similar manner to the experiments. From *Table 3.10* it can be observed that the simulated second-order rate constants are within 4% of the input value at 127, 75 and 50 K when H_2 is used as a chemical tracer. At room temperature, a difference of 21% was obtained between the input and output second-order rate constants indicating that secondary H-atom formation could lead to an error in the measured rate constant at this temperature. These larger differences arise mostly from the reaction of CH with O_2 (reactions 16a and c) which lead to atomic hydrogen as a major product. $O(^1D)$ atoms produced in reaction 14a were thought to be an important source of hydrogen atoms in a similar manner to the case of $C(^1D) + NO$ through reaction 6. However, when the branching ratio of this channel is set to zero the differences between the input and output rate constants increase slightly at all temperatures indicating the influence of non-linear effects in this complex system of coupled reactions. When the

simulations are performed with CH₄ as a chemical tracer, the differences at room temperature are reduced to 13% and at 127 K the difference is within 4% of the input value. In this case, the only secondary process leading to atomic hydrogen formation is the O(¹D) + CH₄ reaction (reaction 18b) with a much smaller yield than the O(¹D) + H₂ reaction.⁹⁶ Nevertheless, as our experimental room temperature measurements employing both H₂ and CH₄ as the chemical tracers result in very similar second-order rate constants, this might indicate that the branching ratios employed during the simulations for the CH + O₂ reaction (reaction 16) overestimate the real ones.

3.6.2. Discussion

From *Figure 3.25* it can be seen that while our measured rate constants at room temperature for both reactions (C(¹D) + NO/O₂) are in excellent agreement with the previous measurements of Husain and Kirsch¹⁵ the agreement with the results of Braun et al.¹⁷ is quite poor. In the case of the C(¹D) + NO reaction, a rapid increase of the rate constant is observed below 100 K reaching a value of $(9.7 \pm 1.1) \times 10^{-11} \text{ cm}^3 \text{ s}^{-1}$ at 50 K, this value is two times larger than the measured rate constant at room temperature. However, in the case of C(¹D) + O₂, the second order rate constants displays only small variations as a function of temperature.

To analyse these two reactions, it is interesting to compare our results with previous work on the equivalent ground state atomic carbon reactions. The kinetics of the C(³P) + NO/O₂ reactions have been studied in a CRESU apparatus over the 15 – 295 K temperature range by Smith and coworkers.^{12,18,94} These authors measured rate constants that increase as the temperature is lowered for both reactions and explain their results in the light of the spin and orbital correlation rules, which connect reactants to products via adiabatic potential surfaces. In the case of the C(³P) + NO reaction, Chastaing et al.¹⁸ found a rate constant that increases from $(1.2 \pm 0.1) \times 10^{-10} \text{ cm}^3 \text{ s}^{-1}$ at 295 K to $(2.3 \pm 0.2) \times 10^{-10} \text{ cm}^3 \text{ s}^{-1}$ at 15 K in a similar manner to our results for the C(¹D) + NO system which display a twofold increase in the 50 – 296 K temperature range. These authors state that the rapid rate at room temperature combined with a mild temperature dependence is characteristic of atom-radical reactions occurring on attractive potential energy surfaces. As for these reactions, some collisions may occur over surfaces that do not lead to thermodynamically accessible products, the increase in the rate constants as the temperature falls may result from an increase of the proportion of collisions over the surfaces that do lead to exothermically available products. In the C(³P_J) + NO(²Π_Ω) reaction, 36 different states correlate with the reagents, where 18 of those states correlate with the exothermic products CN(X ²Σ⁺) + O(³P_J) and the other 18 correlate with the weakly exothermic products CN(A ²Π) + O(³P_J).⁹⁴ The ³P₀, ³P₁ and ³P₂ spin-orbit states of C(³P) lie at 0, 16.4 and 43.4 cm⁻¹ respectively, then the changes in populations of the spin-orbit states of both C(³P_J) and NO(²Π_Ω) as the temperature falls could result in a wide range

of temperatures dependences. In our case as the fine structure of $C(^1D_2)$ is fivefold degenerate only the population distribution of the spin-orbit states of $NO(^2\Pi_{1/2})$ changes as a function of temperature. As a result, we might expect a negative temperature dependence for the process if the reaction between $C(^1D_2)$ and ground electronic state $NO(^2\Pi_{1/2})$ is one of the preferred pathways.

In the case of the $C(^3P) + O_2$ reaction, Chastaing et al.¹² found a rate constant that increases from $(4.1 \pm 0.2) \times 10^{-11} \text{ cm}^3 \text{ s}^{-1}$ at 295 K to $(11.2 \pm 0.7) \times 10^{-11} \text{ cm}^3 \text{ s}^{-1}$ at 15 K in contrast with our results that do not display a marked temperature dependence. Chastaing et al.¹² suggested that if the reactions occur only from specific spin-orbit states of $C(^3P)$, it would lead to large changes in the overall reaction rate as a function of temperature due to the marked change in the populations of the $C(^3P)$ spin-orbit levels over the temperature range studied by them. In our case, as the population distribution of $C(^1D_2)$ is unaffected by temperature, we do not expect a marked negative temperature dependence for the $C(^1D) + O_2$ reaction.

Finally, we notice that the reaction of $C(^1D) +$ open shell molecules display rate constants that are smaller than those of the reactions of $C(^1D) +$ closed-shell molecules.¹⁵ This effect might be related to the large number of electronic states correlating adiabatically with both reagents leading to small electronic degeneracy factors and a lower corresponding reactivity.

3.7. Astrochemical implications

The studies performed in this chapter contribute to broaden the knowledge on the reactivity of atomic carbon in its first excited electronic state towards several molecules, complementing the previous investigations performed in our group. In order to evaluate the relative importance of $C(^1D)$ chemistry in Titan's atmosphere, it is crucial to compare the reactive and non-reactive losses depending on the reactive fluxes. $C(^1D)$ atoms will be mainly quenched to $C(^3P)$ in collision with N_2 , the major constituent of Titan's atmosphere. If we consider 150 K as a representative temperature for Titan's atmosphere, the rate constant for non-reactive quenching with N_2 determined by Hickson et al.⁵ is approximately $8 \times 10^{-12} \text{ cm}^3 \text{ s}^{-1}$. Now, considering the mole fractions of CH_4 and C_2H_6 and the rate constants for these processes, we can compare the effectiveness of each process. Methane is the second most abundant compound in Titan's atmosphere with a mole fraction upper limit of 5% of the total density.¹⁰⁵ Then if we take a rate constant at 150 K of $1.9 \times 10^{-10} \text{ cm}^3 \text{ s}^{-1}$ for the $C(^1D) + CH_4$ reaction, the reactive loss is a factor of 1.2 larger than the non-reactive loss through collisions with N_2 indicating that the $C(^1D) + CH_4$ reaction might represent an important loss process for $C(^1D)$ in Titan atmosphere. On the other hand, the mole fraction upper limit for C_2H_6 is 0.001%¹⁰⁶ and the rate constant for the $C(^1D) + C_2H_6$ reaction at 150 K is approximately $3.4 \times 10^{-10} \text{ cm}^3 \text{ s}^{-1}$ indicating that this reaction will probably not play a significant role in the chemistry of Titan's atmosphere.

In the Martian atmosphere, as CO_2 is the main constituent, all the processes involved in its formation and depletion play fundamental roles. In this chapter, the kinetic data for the $C(^1D) + CO_2$ reaction was extended down to 50 K showing that the rate constants remain fast below room temperature. Consequently, the effect of this reaction should be tested on Martian atmospheric models by including the corresponding $C(^1D)$ production channels from the VUV photolysis of CO .

3.8. References

- (1) Anders, E.; Grevesse, N. Abundances of the Elements: Meteoritic and Solar. *Geochim. Cosmochim. Acta* **1989**, *53*, 197–214.
- (2) Dobrijevic, M.; Hébrard, E.; Hickson, K. M. Coupling of Oxygen, Nitrogen, and Hydrocarbon Species in the Photochemistry of Titan's Atmosphere. *Icarus* **2014**, *228*, 324–346.
- (3) Loison, J. C.; Wakelam, V.; Hickson, K. M.; Bergeat, A.; Mereau, R. The Gas-Phase Chemistry of Carbon Chains in Dark Cloud Chemical Models. *Mon. Not. R. Astron. Soc.* **2014**, *437*, 930–945.
- (4) Baulch, D. L.; Bowman, C. T.; Cobos, C. J.; Cox, R. A.; Just, T.; Kerr, J. A.; Pilling, M. J.; Stocker, D.; Troe, J.; Tsang, W.; et al. Evaluated Kinetic Data for Combustion Modeling : Supplement II. *J Phys Chem Ref Data* **2005**, *34*, 757–1397.
- (5) Hickson, K. M.; Loison, J.; Lique, F.; Jacek, K. An Experimental and Theoretical Investigation of the $C(^1D) + N_2 \rightarrow C(^3P) + N_2$ Quenching Reaction at Low Temperature. *J. Phys. Chem. A* **2016**, *120*, 2504–2513.
- (6) Shannon, R. J.; Cossou, C.; Loison, J.-C.; Caubet, P.; Balucani, N.; Seakins, P. W.; Wakelam, V.; Hickson, K. M. The Fast $C(^3P) + CH_3OH$ Reaction as an Efficient Loss Process for Gas-Phase Interstellar Methanol. *RSC Adv* **2014**, *4*, 26342–26353.
- (7) Hickson, K. M.; Loison, J.; Guo, H.; Suleimanov, Y. V. Ring-Polymer Molecular Dynamics for the Prediction of Low- Temperature Rates: An Investigation of the $C(^1D) + H_2$ Reaction. *J. Phys. Chem. Lett.* **2015**, *6*, 4194–4199.
- (8) Hickson, K. M.; Suleimanov, Y. V. An Experimental and Theoretical Investigation of the $C(^1D) + D_2$ Reaction. *Phys.Chem.Chem.Phys.* **2017**, *19*, 480–486.
- (9) Leonori, F.; Skouteris, D.; Petrucci, R.; Casavecchia, P.; Rosi, M.; Balucani, N. Combined Crossed Beam and Theoretical Studies of the $C(^1D) + CH_4$ Reaction. *J. Chem. Phys.* **2013**, *138*, 024311.
- (10) Hébrard, E.; Dobrijevic, M.; Loison, J. C.; Bergeat, A.; Hickson, K. M.; Caralp, F. Photochemistry of C_3H_p Hydrocarbons in Titan's Stratosphere. *A&A* **2013**, *552*, 1–21.
- (11) Gao, H.; Song, Y.; Chang, Y. C.; Shi, X.; Yin, Q. Z.; Wiens, R. C.; Jackson, W. M.; Ng, C. Y. Branching Ratio Measurements for Vacuum Ultraviolet Photodissociation of $^{12}C^{16}O$. *J. Phys. Chem. A* **2013**,

117, 6185–6195.

- (12) Chastaing, D.; James, P. L.; Sims, I. R.; Smith, I. W. M. Neutral-Neutral Reactions at the Temperatures of Interstellar Clouds: Rate Coefficients for Reactions of Atomic Carbon, $C(^3P)$, with O_2 , C_2H_2 , C_2H_4 and C_3H_6 down to 15 K. *Phys. Chem. Chem. Phys.* **1999**, *1*, 2247–2256.
- (13) Chastaing, D.; Picard, S. D. Le; Sims, I. R.; Smith, I. W. M. Rate Coefficients for the Reactions of $C(^3P_1)$ Atoms with C_2H_2 , C_2H_4 , $CH_3C \equiv CH$ and $H_2C = C = CH_2$ at Temperatures down to 15 K. *Astron. Astrophys.* **2001**, *365*, 241–274.
- (14) Leonori, F.; Petrucci, R.; Segoloni, E.; Bergeat, A.; Hickson, K. M.; Balucani, N.; Casavecchia, P. Unraveling the Dynamics of the $C(^3P, ^1D) + C_2H_2$ Reactions by the Crossed Molecular Beam Scattering Technique. *J. Phys. Chem. A* **2008**, *112*, 1363–1379.
- (15) Husain, D.; Kirsch, L. J. Study of Electronically Excited Carbon Atoms, $C(2^1D_2)$, by Time-Resolved Atomic Absorption at 193.1 nm, ($3^1P_1 \leftarrow 2^1D_2$) Part 2 reactions of $C(2^1D_2)$ with Molecules. *Trans. Faraday Soc.* **1971**, *67*, 3166–3175.
- (16) Kaiser, R. I.; Nguyen, T. L.; Mebel, A. M.; Lee, Y. T. Stripping Dynamics in the Reactions of Electronically Excited Carbon Atoms, $C(^1D)$, with Ethylene and Propylene-Production of Propargyl and Methylpropargyl Radicals. *J. Chem. Phys.* **2002**, *116*, 1318–1324.
- (17) Braun, W.; Bass, A. M.; Davis, D. D.; Simmons, J. D. Flash Photolysis of Carbon Suboxide: Absolute Rate Constants for Reaction of $C(^3P)$ and $C(^1D)$ with H_2 , N_2 , CO , NO , O_2 , and CH_4 . *Proc. R. Soc.* **1969**, *A312*, 417.
- (18) Chastaing, D.; Le Picard, S. D.; Sims, I. R. Direct Kinetic Measurements on Reactions of Atomic Carbon, $C(^3P)$, with O_2 and NO at Temperatures down to 15 K. *J. Chem. Phys.* **2000**, *112*, 8466–8469.
- (19) Shannon, R. J.; Blitz, M. A.; Goddard, A.; Heard, D. E. Accelerated Chemistry in the Reaction Between the Hydroxyl Radical and Methanol at Interstellar Temperatures Facilitated by Tunnelling. *Nat. Chem.* **2013**, *5*, 745–749.
- (20) Caravan, R. L.; Shannon, R. J.; Lewis, T.; Blitz, M. A.; Heard, D. E. Measurements of Rate Coefficients for Reactions of OH with Ethanol and Propan-2-ol at Very Low Temperatures. *J. Phys. Chem. A* **2015**, *119*, 7130–7137.

- (21) Shannon, R. J.; Taylor, S.; Goddard, A.; Blitz, M. A.; Heard, D. E. Observation of a Large Negative Temperature Dependence for Rate Coefficients of Reactions of OH with Oxygenated Volatile Organic Compounds Studied at 86–112 K. *Phys. Chem. Chem. Phys.* **2010**, *12*, 13511–13514.
- (22) Shannon, R. J.; Caravan, R. L.; Blitz, M. A.; Heard, D. E. A Combined Experimental and Theoretical Study of Reactions Between the Hydroxyl Radical and Oxygenated Hydrocarbons Relevant to Astrochemical Environments. *Phys. Chem. Chem. Phys.*, **2014**, *16*, 3466–3478.
- (23) Jiménez, E.; Antiñolo, M.; Ballesteros, B.; Canosa, A.; Albaladejo, J. First Evidence of the Dramatic Enhancement of the Reactivity of Methyl Formate (HC(O)OCH₃) with OH at Temperatures of the Interstellar Medium: A Gas-Phase Kinetic Study Between 22 K and 64 K. *Phys. Chem. Chem. Phys.* **2016**, *18*, 2183–2191.
- (24) Tizniti, M.; Le Picard, S. D.; Lique, F.; Berteloite, C.; Alexander, M. H.; Sims, I. R. The Rate of the F+H₂ Reaction at Very Low Temperatures. *Nat. Chem.* **2014**, *6*, 141–145.
- (25) Schilke, P.; Keene, J.; Le Bourlot, J.; Pineau des F, G.; Roueff, E. Atomic Carbon in a Dark Cloud: TMC-1. *Astron. Astrophys.* **1995**, *294*, L17–L20.
- (26) Agúndez, M.; Wakelam, V. Chemistry of Dark Clouds: Databases, Networks, and Models. *Chem. Rev.* **2013**, *113*, 8710–8737.
- (27) Snell, R. L.; Howe, J. E.; Ashby, M. L. N.; Bergin, E. A.; Chin, G.; Erickson, N. R.; Goldsmith, P. F.; Harwit, M.; Kleiner, S. C.; Koch, D. G.; et al. Water Abundance in Molecular Clouds Cores. *Astrophys. J.* **2000**, *539*, L101–L105.
- (28) Nuñez-Reyes, D.; Hickson, K. M. A Kinetic and Product Study of the Reactions of C(¹D) with CH₄ and C₂H₆ at Low Temperature. *J. Phys. Chem. A* **2017**, *121*, 3851–3857.
- (29) Kim, G. S.; Nguyen, T. L.; Mebel, A. M.; Lin, S. H.; Nguyen, M. T. Ab Initio/RRKM Study of the Potential Energy Surface of Triplet Ethylene and Product Branching Ratios of the C(³P) + CH₄ reaction. *J. Phys. Chem. A* **2003**, *107*, 1788–1796.
- (30) Grondin, R.; Loison, J.-C.; Hickson, K. M. Low Temperature Rate Constants for the Reactions of O(¹D) with N₂, O₂, and Ar. *J. Phys. Chem. A* **2016**, *120*, 4838–4844.
- (31) Heidner, R. F.; Husain, D. A Study of the Collisional Quenching of O(2¹D₂) by the Noble Gases Employing Time-Resolved Attenuation of Atomic Resonance Radiation in the Vacuum

- Ultraviolet. *Int. J. Chem. Kinet.* **1974**, *6*, 77–87.
- (32) Sander, S. P.; Friedl, R. R.; Barker, J. R.; Golden, D. M.; Kurylo, M. J.; Sciences, G. E.; Wine, P. H.; Abbatt, J. P. D.; Burkholder, J. B.; Kolb, C. E.; et al. Chemical Kinetics and Photochemical Data for Use in Atmospheric Studies Evaluation Number 17. *JPL Publ.* 10-6 **2011**.
- (33) Harvey, A. H.; Lemmon, E. W. Correlation for the Vapor Pressure of Heavy Water From the Triple Point to the Critical Point. *J. Phys. Chem. Ref. Data* **2002**, *31*, 173–181.
- (34) Bergeat, A.; Loison, J.-C. Reaction of Carbon Atoms, C ($2p^2$, 3P) with C_2H_2 , C_2H_4 C_6H_6 : Overall Rate Constant and Relative Atomic Hydrogen Production. *Phys. Chem. Chem. Phys* **2001**, *3*, 2038–2042.
- (35) Cheung, A. C.; Rank, D. M.; Townes, C. H.; Thornton, D. D.; Welch, W. J. Detection of Water in Interstellar Regions by its Microwave Radiation. *Nature* **1969**, *221*, 626–628.
- (36) Van Dishoeck, E. F.; Herbst, E.; Neufeld, D. A. Interstellar Water Chemistry: From Laboratory to Observations. *Chem. Rev.* **2013**, *113*, 9043–9085.
- (37) Ilker, O.; Dede Yavuz. Reactions of 1S , 1D , and 3P Carbon Atoms with Water. Oxygen Abstraction and Intermolecular Formaldehyde Generation Mechanisms; An MCSCF Study. *Int. J. Quantum Chem.* **2012**, *112*, 1165–1184.
- (38) Hwang, D. Y.; Mebel, A. M.; Wang, B. C. Ab Initio Study of the Addition of Atomic Carbon with Water. *Chem. Phys.* **1999**, *244*, 143–149.
- (39) Hickson, K. M.; Loison, J.-C.; Nuñez-Reyes, D.; Méreau, R. Quantum Tunneling Enhancement of the C + H_2O and C + D_2O Reactions at Low Temperature. *J. Phys. Chem. Lett.* **2016**, *7*, 3641–3646.
- (40) Bell, R. P. *The Tunnel Effect in Chemistry*, Chapman and Hall, 1980.
- (41) Xu, S.; Lin, M. C. Theoretical Study on the Kinetics for OH Reactions with CH_3OH and C_2H_5OH . *Proc. Combust. Inst.* **2007**, *31*, 159–166.
- (42) Stark, K.; Werner, H. J. An Accurate Multireference Configuration Interaction Calculation of the Potential Energy Surface for the $F+H_2 \rightarrow HF+H$ Reaction. *J. Chem. Phys.* **1996**, *104*, 6515–6530.

- (43) Frost, M. J.; Sharkey, P.; Smith, I. W. M. Reaction between OH (OD) Radicals and CO at Temperatures down to 80 K: Experiment and Theory. *J. Phys. Chem.* **1993**, *97*, 12254–12259.
- (44) Weston, R. E.; Nguyen, T. L.; Stanton, J. F.; Barker, J. R. HO + CO Reaction Rates and H/D Kinetic Isotope Effects: Master Equation Models with ab Initio SCTST Rate Constants. *J. Phys. Chem. A* **2013**, *117*, 821–835.
- (45) Opansky, B. J.; Leone, S. R. Low-Temperature Rate Coefficients of C₂H with CH₄ and CD₄ from 154 to 359 K. *J. Phys. Chem.* **1996**, *100*, 4888–4892.
- (46) Dash, M. R.; Rajakumar, B. Abstraction and Addition Kinetics of C₂H Radicals with CH₄, C₂H₆, C₃H₈, C₂H₄, and C₃H₆: CVT/SCT/ISPE and Hybrid Meta-DFT Methods. *Phys. Chem. Chem. Phys.* **2015**, *17*, 3142–3156.
- (47) Husain, D.; Kirsch, L. J. Reactions of Atomic Carbon C(2³P_J) by Kinetic Absorption Spectroscopy in the Vacuum Ultraviolet. *Trans. Faraday Soc.* **1971**, *67*, 2025–2035.
- (48) Hickson, K. M.; Caubet, P.; Loison, J. C. Unusual Low-Temperature Reactivity of Water: The CH + H₂O Reaction as a Source of Interstellar Formaldehyde? *J. Phys. Chem. Lett.* **2013**, *4*, 2843–2846.
- (49) Wiese, W. L.; Fuhr, J. R. Accurate Atomic Transition Probabilities for Hydrogen, Helium, and Lithium. *J. Phys. Chem. Ref. Data* **2009**, *38*, 565–719.
- (50) Schreiner, P. R.; Reisenauer, H. P. The “Non-Reaction” of Ground-State Triplet Carbon Atoms with Water Revisited. *ChemPhysChem* **2006**, *7*, 880–885.
- (51) Husain, D.; Young, A. N. Kinetic Investigation of Ground State Carbon Atoms, C(2³P_J). *J. Chem. Soc. Faraday Trans. 2 Mol. Chem. Phys.* **1975**, *71*, 525–531.
- (52) Antinolo, M.; Agundez, M.; Jimenez, E.; Ballesteros, B.; Canosa, A.; Dib, G. El; Albaladejo, J.; Cernicharo, J. Reactivity of OH and CH₃OH between 22 and 64 K: Modelling the Gas Phase Production of CH₃O in Barnard 1b. *Astrophys J* **2016**, *823*, 25.
- (53) Sleiman, C.; González, S.; Klippenstein, S. J.; Talbi, D.; El Dib, G.; Canosa, A. Pressure Dependent Low Temperature Kinetics for CN + CH₃CN: Competition between Chemical Reaction and van der Waals Complex Formation. *Phys. Chem. Chem. Phys.* **2016**, *18*, 15118–15132.

- (54) Wakelam, V.; Herbst, E.; Loison, J. C.; Smith, I. W. M.; Chandrasekaran, V.; Pavone, B.; Adams, N. G.; Bacchus-Montabonel, M. C.; Bergeat, A.; Béroff, K.; et al. A Kinetic Database for Astrochemistry (KIDA). *Astrophys. Journal, Suppl. Ser.* **2012**, *199*, 10pp.
- (55) Wakelam, V.; Loison, J. C.; Herbst, E.; Pavone, B.; Bergeat, A.; Béroff, K.; Chabot, M.; Faure, A.; Galli, D.; Geppert, W. D.; et al. The 2014 Kida Network for Interstellar Chemistry. *Astrophys. Journal, Suppl. Ser.* **2015**, *217* (20), 7pp.
- (56) Dartois, E. The Ice Survey Opportunity of ISO. *Sp. Sci Rev* **2005**, *119*, 293–310.
- (57) Garrod, R. T.; Wakelam, V.; Herbst, E. Non-Thermal Desorption from Interstellar Dust Grains via Exothermic Surface Reactions. *Astron. Astrophys.* **2007**, *467*, 1103–1115.
- (58) Peters, P. S.; Duflot, D.; Wiesenfeld, L.; Toubin, C. The $\text{H} + \text{CO} \rightleftharpoons \text{HCO}$ Reaction Studied by ab Initio Benchmark Calculations. *J. Chem. Phys.* **2013**, *139*, 164310.
- (59) Peters, P. S.; Duflot, D.; Faure, A.; Kahane, C.; Ceccarelli, C.; Wiesenfeld, L.; Toubin, C. Theoretical Investigation of the Isomerization of Trans -HCOH to H_2CO : An Example of a Water-Catalyzed Reaction. *J. Phys. Chem. A* **2011**, *115*, 8983–8989.
- (60) Maltagliatia., L.; Bézarda., B.; Vinatiera., S.; Lelloucha., M. M. H. E.; Nicholsonc., P. D.; Sotind., C.; Koke., R. J. de; Sicardy., B. Titan's Atmosphere as Observed by Cassini/VIMS Solar Occultations: CH_4 , CO and Evidence for C_2H_6 Absorption. *Icarus* **2001**, *248*, 1–24.
- (61) Hickson, K. M.; Loison, J. C.; Wakelam, V. Temperature Dependent Product Yields for the Spin Forbidden Singlet Channel of the $\text{C}(^3\text{P}) + \text{C}_2\text{H}_2$ Reaction. *Chem. Phys. Lett.* **2016**, *659*, 70–75.
- (62) Costes, M.; Halvick, P.; Hickson, K. M.; Daugey, N.; Naulin, C. Non-threshold, Threshold, and Nonadiabatic Behavior of the Key Interstellar $\text{C} + \text{C}_2\text{H}_2$ Reaction. *Astrophys. J.* **2009**, *703*, 1179–1187.
- (63) Hung, W.-C.; Tsai, C.-Y.; Matsui, H.; Wang, N.-S.; Miyoshi, A. Experimental and Theoretical Study on the Thermal Decomposition of C_3H_6 (Propene). *J. Phys. Chem. A* **2015**, *119*, 1229–1237.
- (64) Ye, L.; Georgievskii, Y.; Klippenstein, S. J. Pressure-Dependent Branching in the Reaction of $^1\text{CH}_2$ with C_2H_4 and other Reactions on the C_3H_6 Potential Energy Surface. *Proc. Combust. Inst.* **2015**, *35*, 223–230.

- (65) Gannon, K. L.; Blitz, M. A.; Liang, C. H.; Pilling, M. J.; Seakins, P. W.; Glowacki, D. R. Temperature Dependent Kinetics (195 - 798 K) and H Atom Yields (298 - 498 K) from Reactions of $^1\text{CH}_2$ with Acetylene, Ethene, and Propene. *J. Phys. Chem A* **2010**, *114*, 9413–9424.
- (66) Gannon, K. L.; Blitz, M. A.; Liang, C.; Pilling, M. J.; Seakins, P. W.; Glowacki, R.; Harvey, J. N. An Experimental and Theoretical Investigation of the Competition Between Chemical Reaction and Relaxation for the Reactions of $^1\text{CH}_2$ with Acetylene and Ethene : Implications for the Chemistry of the Giant Planets. *Faraday Discuss.* **2010**, *147*, 1–16.
- (67) Lee, S. H.; Lee, Y. T.; Yang, X. Dynamics of Photodissociation of Ethylene and its Isotopomers at 157 nm: Branching Ratios and Kinetic-Energy Distributions. *J. Chem. Phys.* **2004**, *120*, 10983–10991.
- (68) Clary, D. C.; Haider, N.; Husain, D.; Kabir, M. Interstellar Carbon Chemistry: Reaction Rates of Neutral Atomic Carbon with Organic Molecules. *Astrophys. J.* **1994**, *422*, 416–422.
- (69) Stoecklin, T.; Clary, C. Fast Reactions Between a Linear Molecule and a Polar Symmetric Top. *J. Mol. Struct.* **1995**, *341*, 53–61.
- (70) Stoecklin, T.; Dateo, C. E.; Clary, D. C. Rate Constant Calculations on Fast Diatom-Diatom Reactions. *J. Chem. Soc. Faraday Trans.* **1991**, *87*, 1667–1679.
- (71) Clary, D. C.; Buonomo, E.; Sims, I. R.; Smith, I. W. M.; Geppert, W. D.; Naulin, C.; Costes, M.; Cartechini, L.; Casavecchia, P. C + C₂H₂: A Key Reaction in Interstellar Chemistry. *J. Phys. Chem. A* **2002**, *106*, 5541–5552.
- (72) Clary, D. C. Rates of Chemical Reactions Dominated by Long-Range Intermolecular Forces. *Mol. Phys.* **1984**, *53*, 3–21.
- (73) Clary, D. Fast Chemical Reactions: Theory Challenges Experiment. *Annu. Rev. Phys. Chem.* **1990**, *41*, 61–90.
- (74) Georgievskii, Y.; Klippenstein, S. J. Long-range transition state theory. *J. Chem. Phys.* **2005**, *122*, 194103.
- (75) Stock, J. W.; Boxe, C. S.; Lehmann, R.; Grenfell, J. L.; Patzer, B. A. C.; Rauer, H.; Yung, Y. L. Chemical Pathway Analysis of the Martian Atmosphere: CO₂-Formation Pathways. *Icarus* **2012**, *219*, 13–24.

- (76) Husain, D.; Newton, D. P. Collisional Quenching of Electronically Excited Carbon Atoms $C[2p^2(^1S_0)]$. *J. Chem. Soc., Faraday Trans. 2*, **1982**, *78*, 51–71.
- (77) Talbi, D.; Chandler, G. S. Extensive Ab Initio Study of the C_2O_2 , C_2S_2 , and C_2OS Systems: Stabilities and Singlet-Triplet Energy Gaps. *J. Phys. Chem. A* **2000**, *104*, 5872–5881.
- (78) Schröder, D.; Heinemann, C.; Schwarz, H.; Harvey, J. N.; Dua, S.; Blanksby, S. J.; Bowie, J. H. Ethylenedione: An Intrinsically Short-Lived Molecule. *Chem. Eur. J.* **1998**, *4*, 2550–2557.
- (79) Sun, Z. P.; Zhao, W. K.; Yang, C. L. Quantum Reaction Dynamics of $C(^1D) + HD \rightarrow CH(CD) + D(H)$ on the Ground State Potential Energy Surface. *Int. J. Quantum Chem.* **2017**, *117*:e25431, 1–7.
- (80) González-Lezana, T.; Larrégaray, P.; Bonnet, L.; Wu, Y.; Bian, W. The Dynamics of the $C(^1D)+H_2/D_2/HD$ Reactions at Low Temperature. *J. Chem. Phys.* **2018**, *148*, 234305.
- (81) Fisher, W. H.; Carrington, T.; Sadowski, C. M.; Dugan, C. H. The Reactions of $C(^1D)$ with H_2 , D_2 and HD : Product Rotational Energies, Isotope Effects and the CD/CH Branching Ratio. *Chem. Phys.* **1985**, *97*, 433–448.
- (82) Scott, D. C.; de Juan, J.; Robie, D. C.; Schwartz-Lavi, D.; Reisler, H. Reactions of $C(^1D)$ with H_2 , and HCl : Product State Excitations, A-Doublet Propensities, and Branching Ratios. *J. Phys. Chem* **1992**, *96*, 2509–2518.
- (83) Balucani, N.; Capozza, G.; Cartechini, L.; Bergeat, A.; Casavecchia, P.; Aoiz, F. J.; Ban, L.; Launay, J.; Beaulieu, C. De. Dynamics of the Insertion Reaction $C(^1D) + H_2$: A Comparison of Crossed Molecular Beam Experiments with Quasiclassical Trajectory and Quantum Mechanical Scattering Calculations. *Phys. Chem. Chem. Phys* **2004**, *6*, 4957–4967.
- (84) Bergeat, A.; Cartechini, L.; Balucani, N.; Capozza, G. .; Phillips, L. .; Casavecchia, P.; Volpi, G. G.; Bonnet, L.; Rayez, J.-C. A Crossed-Beam Study of the Reaction $C(^1D) + H_2 \rightarrow CH + H$. *Chem. Phys. Lett.* **2000**, *327*, 197–202.
- (85) Jursich, G.; Wiesenfeld, J. R. Product Energetics of the Reaction $C(^1D) + H_2 \rightarrow CH + H$. *Chem. Phys. Lett.* **1984**, *110*, 14–19.
- (86) Sato, K.; Ishida, N.; Kurakata, T.; Iwasaki, A.; Tsunashima, S. Reactions of $C(^1D)$ with H_2 , HD and D_2 : Kinetic isotope effect and the CD/CH branching ratio. *Chem. Phys.* **1998**, *237*, 195–204.

- (87) Donovan, R. J.; Husain, D. Recent Advances in the Chemistry of Electronically Excited Atoms. *Chem. Rev.* **1970**, *70*, 489–516.
- (88) Husain, D.; Kirsch, L. J. The Study of Electronically Excited Carbon Atoms $C(2^1D_2)$, by Photoelectric Measurement of Time-Resolved Atomic Absorption. *Chem. Phys. Lett.* **1971**, *9* (5), 412–415.
- (89) Hickson, K. M.; Suleimanov, Y. V. Low-Temperature Experimental and Theoretical Rate Constants for the $O(^1D) + H_2$ Reaction. *J. Phys. Chem. A* **2017**, *121*, 1916–1923.
- (90) Defazio, P.; Gamallo, P.; González, M.; Akpınar, S.; Bussery-Honvault, B.; Honvault, P.; Petrongolo, C. Quantum Dynamics of the $C(^1D) + HD$ and $C(^1D) + D_2$ Reactions on the \tilde{a}^1A' and \tilde{b}^1A'' Surfaces. *J. Chem. Phys.* **2010**, *132*, 104306.
- (91) Joseph, S.; Caridade, P. J. S. B.; Varandas, A. J. C. Quasiclassical Trajectory Study of the $C(^1D) + H_2$ Reaction and Isotopomeric Variants: Kinetic Isotope Effect and CD/CH Branching Ratio. *J. Phys. Chem. A* **2011**, *115*, 7882–7890.
- (92) Bergeat, A.; Calvo, T.; Dorthe, G.; Loison, J.-C. Fast-Flow Study of the $C + NO$ and $C + O_2$ Reactions. *Chem. Phys. Lett.* **1999**, *308*, 7–12.
- (93) Dorthe, G.; Caubet, P.; Vias, T.; Barrère, B.; Marchais, J. Fast Flow Studies of Atomic Carbon Kinetics at Room Temperature. *J. Phys. Chem.* **1991**, No. 13, 5109–5116.
- (94) Geppert, W. D.; Reignier, D.; Stoecklin, T.; Naulin, C.; Costes, M.; Chastaing, D.; Le Picard, S. D.; Sims, I. R.; Smith, I. W. M. Comparison of the Cross-Sections and Thermal Rate Constants for the Reactions of $C(^3P_1)$ Atoms with O_2 and NO . *Phys. Chem. Chem. Phys.* **2000**, *2*, 2873–2881.
- (95) Geppert, W. D.; Naulin, C.; Costes, M. Integral cross-section of the $C(^3P_1) + O_2(X^3\Sigma_g^-) \rightarrow CO(X^1\Sigma^+) + O(^1D_2)$ reaction between 0.41 and 12.0 kJ/mol. *Chem. Phys. Lett.* **2002**, *364*, 121–126.
- (96) Meng, Q.; Hickson, K. M.; Shao, K.; Loison, J.-C.; Zhang, D. H. Theoretical and Experimental Investigations of Rate Coefficients of $O(^1D) + CH_4$ at Low Temperature. *Phys. Chem. Chem. Phys.* **2016**, *18*, 29286–29292.
- (97) Lin, C.-L.; Kaufman, F. Reactions of Metastable Nitrogen Atoms. *J. Chem. Phys.* **1971**, *55*, 3760–3770.

- (98) Bergeat, A.; Calvo, T.; Daugey, N.; Loison, J.-C.; Dorthe, G. Product Branching Ratios of the CH + NO Reaction. *J. Phys. Chem. A* **1998**, *102* (42), 8124–8130.
- (99) Bocherel, P.; Herbert, L. B.; Rowe, B. R.; Sims, I. R.; Smith, I. W. M.; Travers, D. Ultralow-Temperature Kinetics of CH($X^2\Pi$) Reactions: Rate Coefficients for Reactions with O₂ and NO (T = 13–708 K), and with NH₃ (T = 23–295 K). *J. Phys. Chem.* **1996**, *100*, 3063–3069.
- (100) Brownsword, R. A.; Canosa, A.; Rowe, B. R.; Sims, I. R.; Smith, I. W. M.; Stewart, D. W. A.; Symonds, A. C.; Travers, D. Kinetics Over a Wide Range of Temperature (13–744 K): Rate Constants for the Reactions of CH ($v=0$) with H₂ and D₂ and for the Removal of CH($v=1$) by H₂ and D₂. *J. Chem. Phys.* **1997**, *106*, 7662–7677.
- (101) Herron, J. Evaluated Chemical Kinetics Data for Reactions of N(2D), N(2P), and N($A^3\Sigma^+_u$) in the Gas Phase. *J. Phys. Chem. Ref. Data* **1999**, *28*, 1453–1483.
- (102) Li, J.; Caridade, P. J. S. B.; Varandas, A. J. C. Quasiclassical Trajectory Study of the Atmospheric Reaction N(2D) + NO($X^2\Pi$) \rightarrow O(1D) + N₂($X^1\Sigma_g^+$). *J. Phys. Chem A* **2014**, *118*, 1277–1286.
- (103) Bergeat, A.; Calvo, T.; Caralp, F.; Fillion, J.-H.; Dorthe, G.; Loison, J.-C. Determination of the CH + O₂ product channels. *Faraday Discuss.* **2001**, *119*, 67–77.
- (104) Nunez-Reyes, D.; Hickson, K. M. A Kinetic and Product Study of the Reactions of C(1D) with CH₄ and C₂H₆ at Low Temperature. *J. Phys. Chem. A* **2017**, *121*, 3851–3857.
- (105) Niemann, H. B.; Atreya, S. K.; Bauer, S. J.; Carignan, G. R.; Demick, J. E.; Frost, R. L.; Gautier, D.; Haberman, J. A.; Harpold, D. N.; Hunten, D. M.; et al. The Abundances of Constituents of Titan's Atmosphere from the GCMS Instrument on the Huygens Probe. *Nature* **2005**, *438*, 779–784.
- (106) Niemann, H. B.; Atreya, S. K.; Demick, J. E.; Gautier, D.; Haberman, J. A.; Harpold, D. N.; Kasprzak, W. T.; Lunine, J. I.; Owen, T. C.; Raulin, F. Composition of Titan's Lower Atmosphere and Simple Surface Volatiles as Measured by the Cassini-Huygens Probe Gas Chromatograph Mass Spectrometer Experiment. *J. Geophys. Res. E Planets* **2010**, *115*, E12006.

Chapter 4.

The Reactivity of Electronically Excited Oxygen Atoms

4.1. Experimental details	133
4.1.1. Temperature range	133
4.1.2. Production and detection of electronically excited oxygen atoms.....	133
4.1.3. Experimental details of O(¹ D) + Kr reaction	134
4.1.4. Determination of the branching ratio	135
4.1.5. Gases.....	138
4.2. The O(¹D) + D₂/HD reactions.....	138
4.2.1. Results.....	140
4.2.1.1. Rate constants	140
4.2.1.2. Kinetic isotope effect	143
4.2.1.3. Isotopic branching ratio H/D	144
4.2.2. Discussion	144
4.2.2.1. The O(¹ D) + D ₂ reaction	144
4.2.2.2. The O(¹ D) + HD reaction	146
4.3. The O(¹D)+ C₂H₆/C₂H₂ reaction	146
4.3.1. Results.....	148
4.3.1.1. Rate constants	149
4.3.1.2. Branching ratios.....	151
4.3.2. Discussion	152
4.3.2.1. The O(¹ D) + C ₂ H ₆ reaction	152
4.3.2.2. The O(¹ D) + C ₂ H ₂ reaction	153
4.4. The O(¹D) + CO₂ reaction	154

4.4.1.	Results	156
4.4.2.	Discussion	158
4.5.	The O(¹D) + Kr reaction	159
4.5.1.	Results	160
4.5.2.	Discussion	162
4.6.	Astrochemical implications	163
4.7.	References	164

4. The Reactivity of Electronically Excited Oxygen Atoms

Oxygen atoms in their first electronically excited state (1D) are very reactive and have been recognized as important initiators of free radical chemistry in the Earth's atmosphere.¹ Similarly to $C(^1D)$ atoms, it is unlikely that $O(^1D)$ atoms play a role in the gas-phase chemistry of the interstellar medium because the time between collisions in the ISM is considerably longer than the $O(^1D)$ radiative lifetime (110 s).² Although the gas-phase chemistry of excited state atoms is unimportant in the interstellar medium, the reactions of $O(^1D)$ atoms with hydrocarbons have been identified as a possible pathway for the formation of complex organic molecules on dust grains in star forming regions.^{3,4} The reactions of $O(^1D)$ atoms might be important for the chemistry of planetary atmospheres however. CO_2 is the main constituent of the Martian atmosphere (95%) and its photodissociation represents the basis for the gas-phase chemistry. Excited state $O(^1D)$ atoms are produced with high quantum yields by the photodissociation of CO_2 below 170 nm.⁵ Likewise $O(^1D)$ atoms can be produced by the short wavelength photodissociation of other oxygen-bearing molecules present in Mars's atmosphere. These atoms will react with trace species present in the Martian atmosphere or be removed by non-reactive collisions with CO_2 . In this chapter, the results of our kinetic measurements of $O(^1D)$ atoms reactions with D_2 , HD, C_2H_6 , C_2H_2 and their deactivation by collisions with CO_2 and Kr are presented, allowing us to quantify the importance of these processes to the chemistry in low temperature environments.

4.1. Experimental details

4.1.1. Temperature range

The kinetics of $O(^1D)$ atom reactions have been studied in the mini-CRESU setup of Bordeaux over the temperature range 50 - 296 K. Three Laval nozzles (Mach2 N_2 , Mach3 Ar and Mach4 Ar) have been used to generate flows with characteristic temperatures of 50 K, 75 K and 127 K. The characteristics of the supersonic flows produced by each of these nozzles are listed in Table 2.2. Similarly to the experiments with $C(^1D)$ atoms described in Chapter 3, only Laval nozzles employing Ar as a carrier gas were used in these studies given the fast electronic quenching of $O(^1D)$ atoms in presence of N_2 .⁶ Experiments at room temperature were performed by removing the Laval nozzle and lowering the velocity of the flow, using the CRESU chamber as a slow flow reactor.

4.1.2. Production and detection of electronically excited oxygen atoms

$O(^1D)$ atoms were generated by PLP of O_3 as detailed in Chapter 2 section 2.5 and detected directly by VUV LIF at 115.215 nm corresponding to the $2p\ ^1D-3s\ ^1D^\circ$ transition. For the reactions of $O(^1D)$ with

D₂/HD, C₂H₆/C₂H₂ and CO₂ the procedure to generate tuneable light is the same as explained in section 2.5. However, a change in the composition of the rare gas mixture used in the tripling cell (75 torr of Xe and 155 torr of Ar instead of the previous 100 torr Xe and 230 torr of Ar) was found to yield approximately 30% higher fluorescence signals compared to the ones used during our study of the O(¹D) + Kr quenching reaction.

4.1.3. Experimental details of O(¹D) + Kr reaction

As the second-order rate constant for the O(¹D) + Kr reaction is quite slow ($<10^{-11} \text{ cm}^3 \text{ s}^{-1}$) it was necessary to add a large concentration of Kr to the flow to obtain a significant range of values for the pseudo-first-order rate constants. The excess reactant concentration in the CRESU experiment is typically kept at values less than 5% of the total flow in order to maintain the nominal flow properties of the Laval nozzle (such as temperature, density and velocity). However for the reaction of O(¹D) with Kr, the highest amount of added Kr represented 11% of the flow, consequently, it was necessary to check for any deviations of the supersonic flow properties induced by the addition of large quantities of Kr. Thus we performed additional measurements of the impact pressure as a function of distance with added Kr using a Pitot tube. This procedure has been detailed in chapter 2 section 2.4.2. These calibrations showed that the velocity and density profiles of the 127 K Laval nozzle (where the fraction of added Kr was the greatest) were within 2% of the values obtained with Ar alone, with a difference in the calculated temperature of 1 K. Furthermore, the exploitable distance of the supersonic flow was unaffected by the presence of Kr.

Additionally, as large Kr flows were required to perform the experiments, it was necessary to reduce the Ar flow rate to maintain a constant reservoir pressure, which is an established parameter for each nozzle (see table 2.2). Then as [Ar] decreases as [Kr] increases, it was necessary to correct the pseudo-first-order rates to compensate for the reduced relaxation by Ar. This relaxation or loss of O(¹D) in collision with Ar is represented by the y-axis intercept on the second-order plots. The correction applied to the pseudo-first-order rate constants is given by the following formula

$$([Ar]_0 - [Ar]_{Kr})k_{O(^1D)+Ar} \quad (4.1)$$

where $[Ar]_0$ is the nominal Ar density for the specific nozzle, $[Ar]_{Kr}$ is the Ar density with added Kr, and $k_{O(^1D)+Ar}$ is the measured second-order rate constant for O(¹D) removal by Ar.⁶ Adding this correction to the measured pseudo-first-order rate constant, we obtain an increase of less than 10% of the second-order rate constant.

4.1.4. Determination of the branching ratio

For the reactions of $O(^1D)$ with C_2H_6 and HD, in addition to measurements of the rate constants, a branching ratio study has also been performed following the formation of $H(^2S)$ atoms by VUV LIF at 121.567 nm. The VUV LIF signal of the target reaction was compared with the signal produced by the reference reaction R 4.1 which is known to have a H-atom yield of 100%.⁷



In this case, given the fast electronic quenching of $O(^1D)$ in collision with the carrier gas Ar^6 we were not able to use the same procedure employed in Chapter 3, which relies on the assumption that loss of the minor reagent through collisions with the carrier gas can be considered as negligibly small compared with the loss due to reaction with the reactant in excess. Then as typical temporal profiles obtained following a product (*Figure 4.1*) are characterized by a maximum intensity (I_{max}), which corresponds to a maximum time (t_{max}), some information can be extracted from the system by employing these quantities.

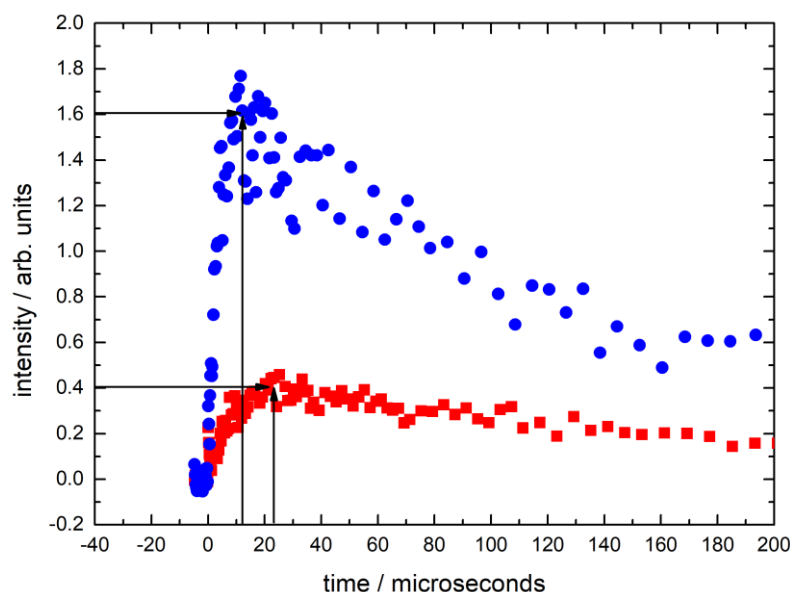


Figure 4.1 $H(^2S)$ VUV LIF signal intensity as a function of time recorded at 127 K. (Blue solid circles) $[C_2H_6] = 7.8 \times 10^{14} \text{ cm}^{-3}$; (red solid squares) $[C_2H_6] = 8.3 \times 10^{13} \text{ cm}^{-3}$. Black arrows indicate the maximum time and the maximum intensity in each case.

In Chapter 2 we derived the expression (2.9.1), which describes the kinetics of the system following a product of the reaction. Applying expression (2.9.1) to the $O(^1D) + C_2H_6$ reaction, which yields H-atoms as a product, we get the following expression:

$$[H] = \frac{k'_1[O(^1D)]_0}{k'_T - k_{L(H)}} \left(e^{-k_{L(H)}t} - e^{-(k'_T)t} \right)$$

with k'_1 the pseudo-first-order rate constant for the exit channel that leads to H-atom production, k'_T the overall pseudo-first-order rate constant for the multichannel reaction and $k_{L(H)}$ the loss of H-atoms.

Finding t_{max} from the upper expression implies

$$\frac{d[H]}{dt} = 0$$

$$\frac{d[H]}{dt} = \frac{k'_1[O(^1D)]_0}{k'_T - k_{L(H)}} \left\{ -k_{L(H)}e^{-k_{L(H)}t} + k'_Te^{-k'_Tt} \right\}$$

$$t_{max} = \frac{1}{k_{L(H)} - k'_T} \ln \left(\frac{k_{L(H)}}{k'_T} \right) \quad (4.2)$$

I_{max} can be found by substituting t_{max} in expression (2.9.1)

$$I_{max} = \frac{k'_1[O(^1D)]_0}{k'_T} e^{-k_{L(H)}t_{max}}$$

$$I_{max} = \frac{k_1[C_2H_6][O(^1D)]_0}{(k_1 + k_2 + k_3 + k_4)[C_2H_6] + k_{L(O(^1D))}} e^{-k_{L(H)}t_{max}} \quad (4.3)$$

t_{max} for the target and reference reaction needs to be calculated prior to the experiments for a range of coreagent concentrations (C_2H_6 and H_2). The values of k'_T were obtained from kinetic determinations performed before the branching ratio experiments. The values of $k_{L(H)}$ were obtained from previous H-atom detection experiments performed under similar conditions in our laboratory. Expression (4.3) links the maximum intensity with the maximum time through an exponential function. However, when there are no secondary reactions removing H-atoms it is well known from previous experiments under similar conditions that the loss of the H-atom product is small, with $k_{L(H)}$ values in the range of 2000 to 5000 s^{-1} . In addition, the calculated t_{max} values range between 12 and 33 μs for all the concentrations and temperatures studied. Consequently, the product $k_{L(H)}t_{max}$ can be considered small and the exponential can be approximated to a straight line using the Taylor series expansion ($e^{-x} \approx 1 - x$). Thus we obtain the linear relation

$$I_{max} = \frac{k_1[C_2H_6][O(^1D)]_0}{(k_1 + k_2 + k_3 + k_4)[C_2H_6] + k_{L(O(^1D))}} (1 - k_{L(H)}t_{max})$$

So if several values of I_{max} are recorded for their respective t_{max} , the plots of I_{max} against t_{max} for the target and reference reactions will yield straight lines as shown in *Figure 4.2*. Finally, the branching ratios can be extracted from the ratio of the slopes as $k'_1 = k'_T$ for the reference reaction R 4.1.

Experimentally, the delay time between the photolysis and probe lasers was set to t_{max} , and I_{max} was recorded for a given coreagent concentration. This process was repeated up to 200 times for each concentration and for 6 different coreagent concentrations. Lastly, due to the presence of residual gases in the chamber, I_{max} was corrected to account for absorption losses of the VUV excitation laser and fluorescence intensities. This correction was estimated to be less than 25% for C_2H_6 over the entire temperature range. For the $O(^1D) + HD$ reaction the same procedure was applied to find the absolute branching ratios. However, in this case given the negligible absorption cross-section of H_2 at 121.534 nm and assuming similar values for D_2 and HD isotopologues, it was unnecessary to correct for absorption losses.

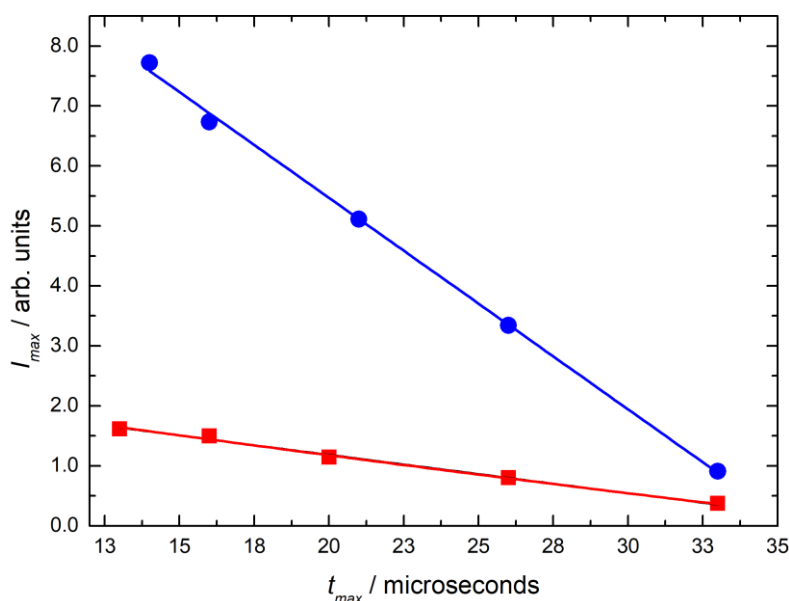


Figure 4.2 Maximum intensity as a function of the maximum time at 127 K. (Blue circles) reference $O(^1D) + H_2$ reaction. (Red squares) target $O(^1D) + C_2H_6$ reaction. (Solid lines) represent weighted fits to the individual data.

4.1.5. Gases

The gases used in the experiments were not purified prior use. The suppliers and the purities are

- ✓ Linde: O₂ (99.999%), Ar (99.999%), Xe (99.998%), CO₂ (99.998%), Kr (99.99%), D₂ (99.8%), C₂H₆ (99.5%)
- ✓ Sigma-Aldrich HD (98% atom D)
- ✓ Messer C₂H₂ (99.6%),
- ✓ Air Liquide: H₂ (99.9999%)

4.2. The O(¹D) + D₂/HD reactions

The reactions of atomic oxygen in its first excited state with H₂ and its isotopologues (D₂ and HD) are among the simplest chemical reactions involving the O(¹D) atom.



These reactions have been extensively studied given their importance for the chemistry of planetary atmospheres and due to the interest in their reaction dynamics. O(¹D) + H₂ is considered one of the sources of OH radicals in the Earth's upper atmosphere.⁸ Moreover, this reaction might play an important role in Mars' atmosphere because it is thought that OH (formed by O(¹D) + H₂) can react with CO to form CO₂, maintaining the levels of carbon dioxide in the atmosphere.⁷ Furthermore on the theoretical side, O(¹D) + H₂ offers an excellent example of a simple atom-diatom insertion type mechanism considered to involve deep potential wells.^{9,10}

Over the years, although the reactions of O(¹D) + H₂ and its isotopic variants have been considered as insertion like benchmark reactions, there has been a significant debate regarding the precise nature of the mechanism that dominates the dynamics.¹¹ In the early 1980s, the debate was centred on the insertion vs the abstraction mechanism over the same ground state potential energy surface (1¹A'). On the experimental side, Smith and Butler¹² proposed both, a simple H-atom abstraction and insertion into the H-H bond to form a short-lived vibrationally excited adduct, with the insertion channel dominating OH formation. Aker and Sloan¹³ proposed an insertion mechanism in which the lifetime of the HOH intermediate complex was very short. On the theoretical side, the first trajectory

calculations^{14,15} and statistical approaches¹² also dealt with the same issue regarding the identification of the mechanism that determines the dynamics of the process.

Until the 1990s, little attention was given to the possible contributions of excited PESs to the dynamics of the reaction. The quasi-classical trajectory (QCT) calculations by Berg et al.¹⁶ found that the trajectories that sample the excited PES yield different dynamics from those that remain on the ground PES. In 1999, the development of the ab initio PESs for the lowest excited state ($1^1A''$) of water¹⁷ allowed a more complete characterization of the dynamics mechanism for this process. Then it was generally accepted that the reaction on the ground $1^1A'$ PES proceeds via an insertion mechanism^{18,19} while the dynamics on excited PESs ($1^1A''$, $2^1A'$, ...) is the result of an abstraction reaction pathway.^{20–22}

Nowadays, it is well known that different energy regimes are dominated by different reaction mechanisms.^{20,21,23} Liu et al.²⁴ performed an investigation of R 4.2 using a crossed molecular beam technique to study the reaction in the energy range 8.37 - 13.39 kJ/mol. These authors found a transition between complex forming dynamics at lower energy to an abstraction process at higher energy. The QCT calculation of Aoiz et al.²⁵ over the same energy range found similar results for increasing collision energies with the appearance of an abstraction mechanism and a larger contribution from the $1^1A''$ PES.

More recently, Hickson and Suleimanov⁷ performed a combined experimental and theoretical investigation of R 4.1. These authors studied the temperature dependence of the rate constant over the 50 - 296 K temperature range (or at equivalent low collision energies) using the mini CRESU setup of Bordeaux. Furthermore, ring polymer molecular dynamics (RPMD) calculations were used to derive the rate constants over the ground state PES ($1^1A'$) and the excited PES ($1^1A''$). They found a major contribution for the surface $1^1A'$ to the rate constant while the contribution of $1^1A''$ surface decreases dramatically as the temperature or energy falls. The agreement between the experimental and theoretical results in their work was good with the difference between the measured and calculated rate constants less than 25%. These differences were hypothesized to be due to non-adiabatic coupling between the $1^1A''$ and $2^1A'$ surfaces.

In general, at low collision energies, the reactions of $O(^1D)$ with H_2 and its isotopologues (D_2 and HD) are thought to occur predominantly on the ground state PES. This PES correlates adiabatically with the ground state products $H(^2S) + OH(X^2\Pi)$ through the ground 1A_1 state of the water molecule by $O(^1D)$ insertion into the H-H bond to form an H_2O intermediate with no barrier in the entrance channel. This intermediate lies 703 kJ/mol below the reagent level.^{7,26,35,27–34} Surprisingly, the kinetics for these

reactions has not been well characterized. While the rate constants for the $O(^1D) + H_2$ reaction have been studied in the combined 50 - 420 K temperature range,^{7,36-38} there are only room temperature measurements for the other isotopologues.^{8,39-41} The rate constants at room temperature for the three systems show that the reactions are fast with $k_{O(^1D)+H_2,D_2,HD} \geq 10^{-10} \text{ cm}^3 \text{ s}^{-1}$.

In this section, we report the rate constants measurements for reactions R 4.2 and R 4.3 over the 50 - 296 K temperature range, where quantum effects are likely to be more pronounced. Our experimental results are compared with four theoretical methods designed to treat complex-forming reactions: Mean Potential Phase Space Theory (MPPST), Statistical Quantum Mechanical method (SQM), Ring Polymer Molecular Dynamics (RPMD) and Quantum Mechanical (QM).⁴² Furthermore, it is known that studies of the H_2 isotopologue reactions help to clarify the nature of the mechanism that dominates the $O(^1D) + H_2$ reaction. To probe the dynamics of the isotopologue reactions, important information can be obtained in two different ways. Firstly, the isotopic branching ratio, which relates the H and D yields for the two exit channels of the $O(^1D) + HD$ reaction (R 4.3 (a) and R 4.3 (b)). Secondly, the kinetic isotope effect (KIE) defined as the ratio of the rate constants of the two isotopic systems R 4.2 and R 4.1 ($k(D)/k(H)$). We performed both studies and compared our results with other experimental and theoretical studies^{8,20,34,35,43} reported in the literature.

4.2.1. Results

To apply the pseudo-first-order approximation, the D_2 and HD concentrations were maintained in a large and known excess with respect to the $O(^1D)$ concentration. Although $O(^3P)$ is also produced during the photolysis of O_3 at 266 nm, the reactions of $O(^3P)$ with hydrogen and its isotopologues are endothermic,⁴⁴ then they can be neglected at room temperature and below.

4.2.1.1. Rate constants

Pseudo-first-order decays of $O(^1D)$ with and without D_2/HD added are presented in *Figure 4.3*. In the absence of D_2/HD , the $O(^1D)$ VUV LIF signal decays to zero through non-reactive quenching collisions with the carrier gas Ar. The measured pseudo-first-order rate constants as a function of the concentration of D_2 and HD are shown in *Figure 4.4*. The large y-intercept values represent the quenching contribution of the carrier gas Ar.

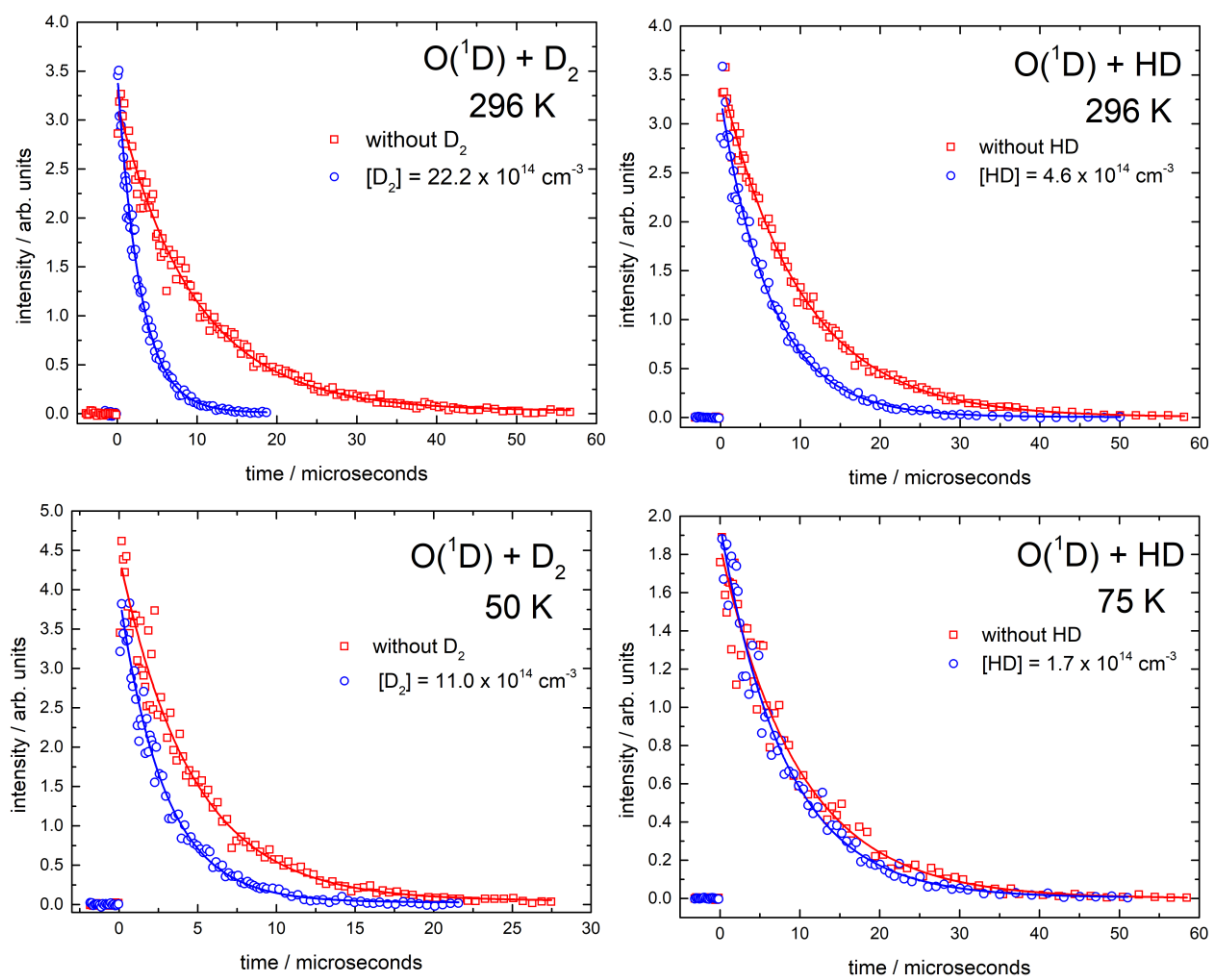


Figure 4.3 $O(^1D)$ VUV LIF signals as a function of time. (Left panels) $O(^1D) + D_2$ reaction at 296 K and 50 K. (Right panels) $O(^1D) + HD$ reaction at 296 K and 75 K. (Red open squares) $O(^1D)$ decay without D_2 or HD added. (Blue open circles) the maximum concentration of D_2 or HD used during the experiments. (Solid blue and red lines) functional fits to the data using expression 2.5.

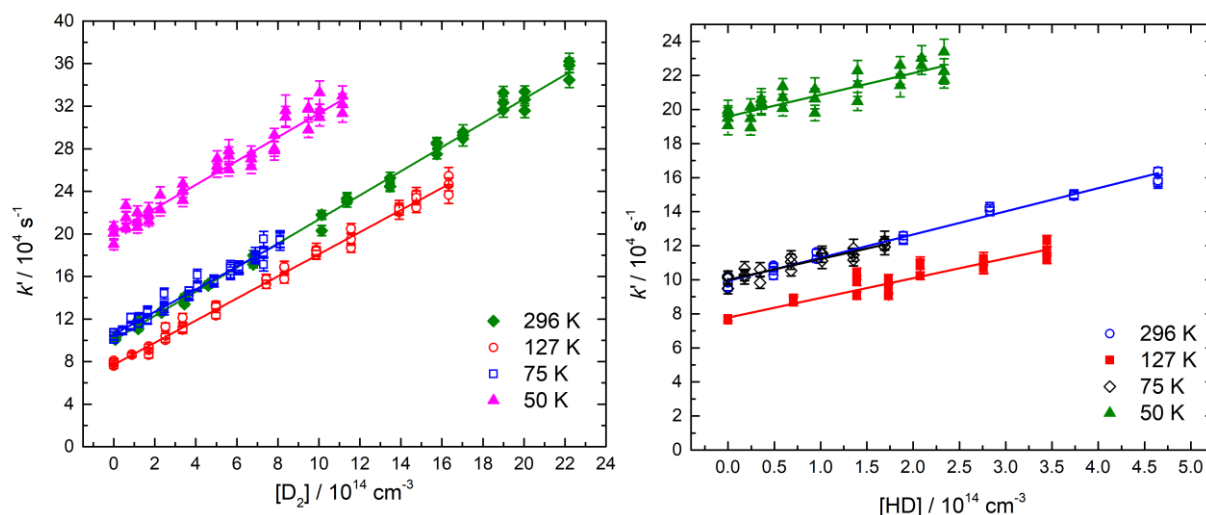


Figure 4.4 Second-order plots of the $O(^1D) + D_2/HD$ reactions. (Left panel) the $O(^1D) + D_2$ reaction. (Right panel) the $O(^1D) + HD$ reaction. The solid lines represent linear least-squares fits to the data, weighted by the statistical uncertainties of the individual data points derived during the pseudo-first-order fits.

The second-order rate constants obtained as a function of temperature are displayed in Figure 4.5 together with other reported values. In the case of the $O(^1D) + HD$ reaction, our experimental values are shown along with the rate constants determined for the $O(^1D) + D_2$ (this work) and H_2 (Hickson and Suleimanov)⁷ reactions obtained under similar conditions in the mini CRESU setup of Bordeaux for comparison.

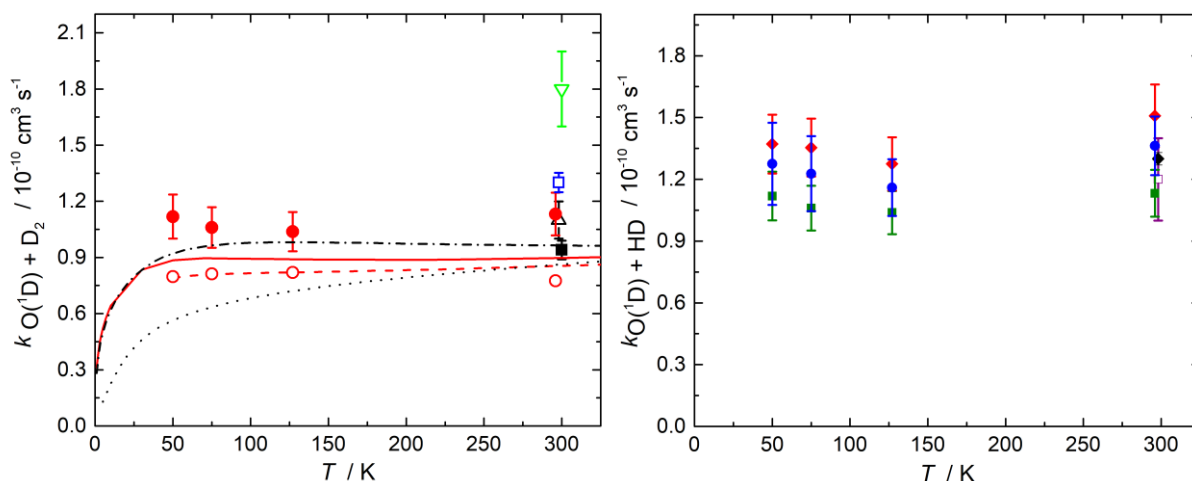


Figure 4.5 Measured rate constants as a function of temperature. (Left panel) the $O(^1D) + D_2$ reaction; Experimental values: (red solid circles) this work; (green open triangle) Heidner and Husain,³⁹ (blue open square) Davidson et al.,³⁶ (black solid square) Matsumi et al.,⁹ (black open triangle) Talukdar and Ravishankara.⁸ Theoretical values: (dashed-dotted black line) QM results of Pradham et al.,³⁴ (dotted black line) QM results of Sun et al.,³⁵ (solid red line) MPPST result, (dashed red line) SQM result, (red open circles) RPMD result of Nunez-Reyes et al.,¹⁰. (Right panel): the $O(^1D) + HD$ reaction; (blue solid circles) this work; (black solid diamond) Laurent et al.,⁴¹ (purple open square) Talukdar and Ravishankara,⁸ (green solid squares) the $O(^1D) + D_2$ reaction, this work; (red solid diamonds) the $O(^1D)$

+ H₂ reaction Hickson and Suleimanov.⁷ Error bars represent the combined statistical and systematic uncertainties.

The second-order rate constants, the concentration ranges and the number of experiments performed in each case are summarized in Table 4.1.

Table 4.1 Temperature dependent rate constants for the O(¹D) + D₂ and O(¹D) + HD reactions.

T(K)	N ^b	[D ₂] (10 ¹⁴ cm ⁻³)	$k_{O(^1D)+D_2}$ (10 ⁻¹⁰ cm ³ s ⁻¹)	N	[HD] (10 ¹⁴ cm ⁻³)	$k_{O(^1D)+HD}$ (10 ⁻¹⁰ cm ³ s ⁻¹)
296	42	0 - 22.2	(1.1 ± 0.1) ^c	21	0 - 4.6	(1.4 ± 0.1)
127 ± 2 ^a	40	0 - 16.3	(1.0 ± 0.1)	21	0 - 3.4	(1.2 ± 0.1)
75 ± 2	42	0 - 8.1	(1.1 ± 0.1)	20	0 - 1.7	(1.2 ± 0.2)
50 ± 1	40	0 - 11.1	(1.1 ± 0.1)	27	0 - 2.3	(1.3 ± 0.2)

^aUncertainties in the calculated temperatures represent the statistical (1σ) errors obtained from Pitot tube measurements of the impact pressure. ^bNumber of individual measurements. ^cUncertainties in the measured rate constants represent the combined statistical (1σ) and estimated systematic (10%) errors.

4.2.1.2. Kinetic isotope effect

As the rate constants for the O(¹D) + D₂ and O(¹D) + H₂ reactions have been measured over the same temperature range and the same type of calculations have been performed for each case, it is possible to calculate the temperature dependence of the KIE for the O(¹D) + H₂/D₂ systems.

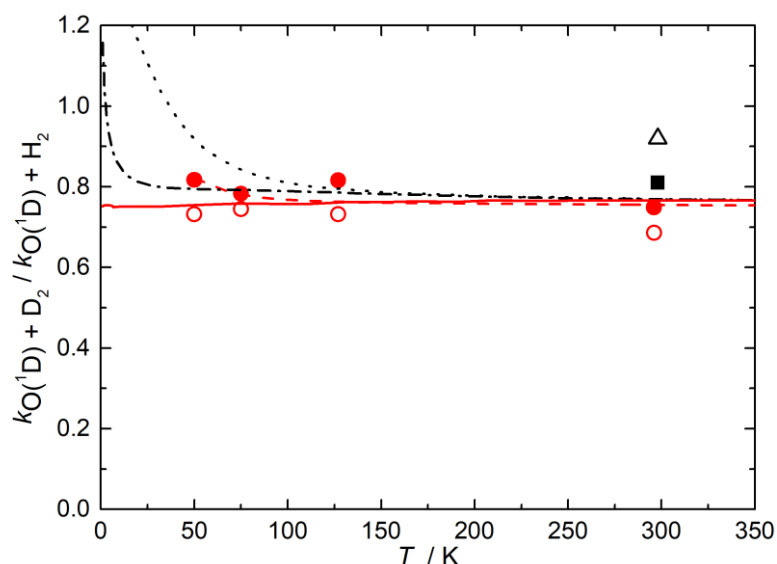


Figure 4.6 Kinetic Isotope Effect, $k_{O(^1D)+D_2}/k_{O(^1D)+H_2}$, as a function of temperature. Experimental values: (red solid circles) this work; (black solid square) Hsu et al.;²⁰ (black open triangle) Talukdar and Ravishankara.⁸ Theoretical values: (dashed dotted black line) QM results of Pradhan et al.;^{34,45} (dotted black line) QM WP results of Sun et al.³⁵/QM WP results of Lin and Guo;²⁸ (solid red line) MPPST method; (dashed red line) SQM method; (red open circles) RPMD method results of Nuñez-Reyes et al.¹⁰

4.2.1.3. Isotopic branching ratio H/D

In the case of the $O(^1D) + HD$ reaction, the absolute H-atom yields as a function of temperature were found by comparing the H-atom signal of the target reaction with the H-atom signal of $O(^1D) + H_2$ reference reaction, which is considered to have a H-atom yield of unity.⁷ Absolute H-atom yields were converted to an H/D branching ratio using the formula

$$\frac{OD + H}{OH + D} = \frac{H \text{ atom yield}}{1 - H \text{ atom yield}}$$

Our results are shown in *Figure 4.7* alongside other experimental determinations. As a secondary check, the H/D branching ratio was also obtained by following D-atom formation at 127 K and by comparing with the $O(^1D) + D_2$ reaction as a reference. Each reported branching ratio corresponds to the mean value of at least 5 individual determinations and the uncertainties were estimated at the 95% of confidence level to the mean.

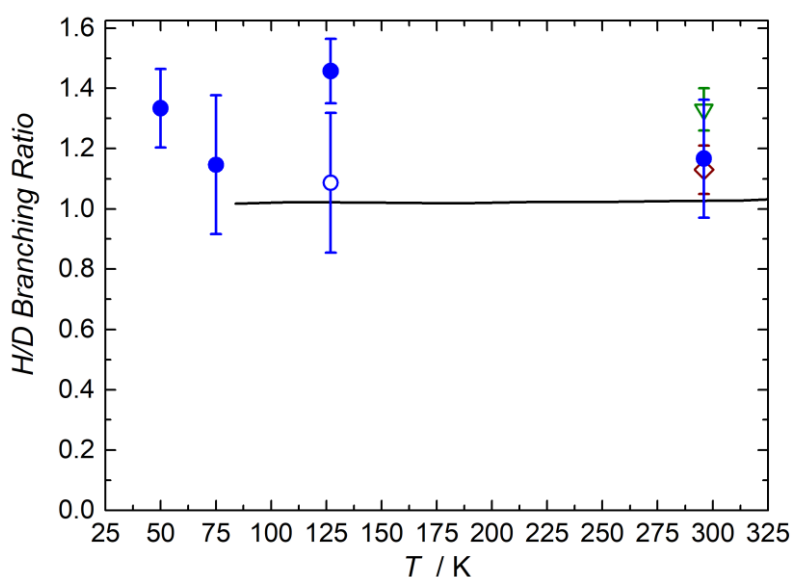


Figure 4.7 Isotopic H/D branching ratios for the $O(^1D) + HD$ reaction as a function of temperature. Experimental values: (Solid blue circles) this work detecting H-atoms; (open blue circles) this work detecting D-atoms; (open red diamond) Tsukiyama et al.;⁴³ (open green triangle) Talukdar and Ravishankara;⁸ (solid black line) Hsu et al.²⁰

4.2.2. Discussion

4.2.2.1. The $O(^1D) + D_2$ reaction

From *Figure 4.5* (left panel) it can be seen that our determined rate constant at room temperature is in excellent agreement with the experimental values reported in the literature,^{8,9,36} except for the value of Heidner and Husain.³⁹ These authors used atomic absorption spectroscopy in the VUV to follow the

O(¹D) decay obtaining one of the earliest direct measurements of the rate constant for this reaction. However, their rate constant determined at room temperature of $(1.8 \pm 0.2) \times 10^{-10} \text{ cm}^3 \text{ s}^{-1}$ is almost twice as large as the more recently reported values including ours. No temperature dependence of the rate constant is observed as the temperature falls to 50 K within the error bars of the individual measurements, a result that is in good qualitative agreement with the previous rate constants determined for O(¹D) + H₂ reaction⁷ under the same conditions and over the same temperature range. Our experimental results were compared with QM methods^{34,35} and the approximate theoretical approaches MPPST, SQM and RPMD.¹⁰ At low temperature, the theoretical calculations slightly underestimate the experimental rate constants. These discrepancies could be due to inaccuracies in the PES used, divergence problems, approximations applied during the calculations and non-adiabatic couplings. In general, a good agreement was found among these calculations and our experimental results over the temperature range 50 - 296 K, a result that strongly supports the involvement of a long-lived intermediate complex in the dynamics of the reaction at low temperature.

The KIE for the reactions O(¹D) + H₂/D₂ has been evaluated experimentally and theoretically in *Figure 4.6*. Our derived KIE at room temperature agrees very well with the experimental value of Hsu et al.²⁰ but it is slightly higher than the value reported by Talukdar and Ravishankara⁸. In general, all the experimental values over the studied temperature range confirm the dominance of the H₂ system. Regarding the derived theoretical KIE, it can be seen from *Figure 4.6* that our result agrees well above 100 K with the ratio of the rate constants obtained by Sun et al.³⁵ and Lin and Guo²⁸ for the O(¹D) + D₂ and O(¹D) + H₂ reactions respectively. These authors performed accurate QM wavepacket calculations using the three lowest PESs, the ground 1¹A' and excited 1¹A'' and 2¹A' states, where reaction over the 1¹A' PES was found to dominate over the other two PESs in the low energy regime. Below 100 K their theoretical KIE increases dramatically, giving rise to a dominance of the D₂ reaction while our experimental KIE remains constant. Sun et al.³⁵ stated that at high energies as the ICSs for both reactions are similar, the magnitude of the rate constants for both systems will be determined by the ratio of the reduced masses, however, at low energies the ICSs for the D₂ system are much larger giving rise to the dominance of the D₂ system. An alternative possibility for this difference could be due to convergence issues in one or both QM WP studies at low collision energies. In contrast, the theoretical KIE from Pradhan et al.^{34,45} and those obtained by the approximate theoretical approaches MPPST, SQM and RPMD¹⁰ are in excellent agreement with our experimental values over the entire temperature range.

4.2.2.2. The O(¹D) + HD reaction

Our rate constant determined at room temperature for the O(¹D) + HD reaction is in excellent agreement with the previous experimental values.^{8,41} Laurent et al.⁴¹ used a pump-probe technique similar to the one used in the present work, but O(¹D) atoms were produced through photodissociation of N₂O at 193 nm, and the kinetics of the reaction was followed by VUV LIF of the H/D-atom products. Talukdar and Ravishankara⁸ employed the photodissociation of O₃ at 248 nm to produce O(¹D) atoms and the reaction kinetics was also followed by H-atom detection. In our experiments, as the temperature is lowered to 50 K, no temperature dependence is observed for the rate constants. This result is in good agreement with the previously determined rate constants for the O(¹D) + H₂ (Hickson and Suleimanov)⁷ and O(¹D) + D₂ (this work) reactions.

The dynamical features of the O(¹D) + HD reaction are considered to be similar to the other isotopologue reactions with the main difference being the ratio between the two possible exit channels (OH + D and OD + H).^{32,46} From *Figure 4.7* it can be seen that our determined isotopic H/D branching ratio is greater than unity in all the temperature range studied and agrees well with the previous experimental determinations at room temperature or equivalent energies.^{8,20,43} On the theoretical side, several efforts have been devoted to the study of this reaction reporting isotopic H/D branching ratios which depend on the PES employed.^{47,48} In general, the isotopic H/D ratio determinations have been found in experimental^{8,9,18,41,43} and theoretical studies^{46,48,49} to be greater than one indicating the preferential formation of OD + H products. Then at low temperature where the insertion mechanism is dominant, it is thought that the hydrogen atom leaves the formed complex with higher probability than the deuterium atom due to its lighter mass and greater velocity.⁴⁹

4.3. The O(¹D) + C₂H₆/C₂H₂ reaction

The reactions of O(¹D) with hydrocarbons have been extensively studied given their importance in atmospheric and combustion chemistry.^{37,50,59–65,51–58} In addition, recent studies performed in astrophysical ice analogues suggest the importance of O(¹D) insertion into hydrocarbons as a possible mechanism for the formation of complex organic molecules in interstellar ices.^{3,4} While the O(¹D) + CH₄ reaction has been the subject of numerous kinetics and dynamic studies given its importance in the formation of OH radicals in the chemistry of Earth's ozone layer,⁶³ the reactions with larger saturated and unsaturated hydrocarbons such as ethane and acetylene are less well understood.

In the case of the O(¹D) + C₂H₆ reaction, there are numerous possible exothermic exit pathways (*Figure 4.8*).^{56,66} However, only four have been identified experimentally by CMB measurements.^{55,56}

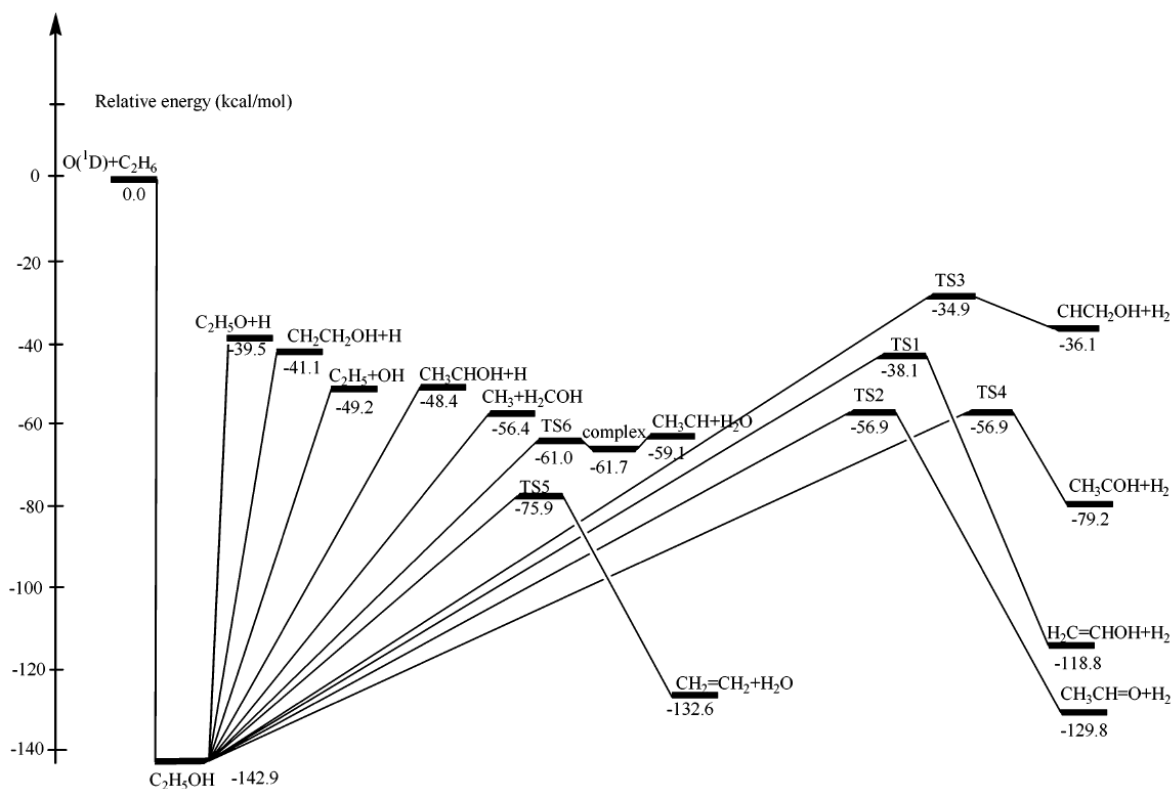
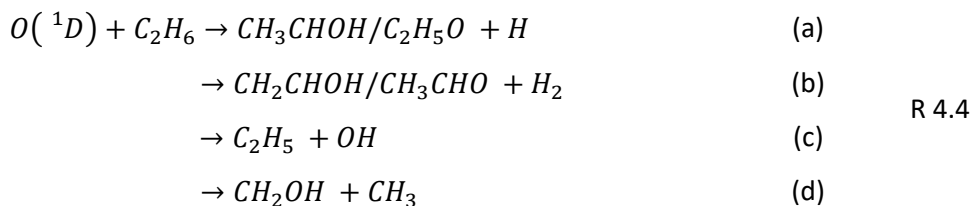


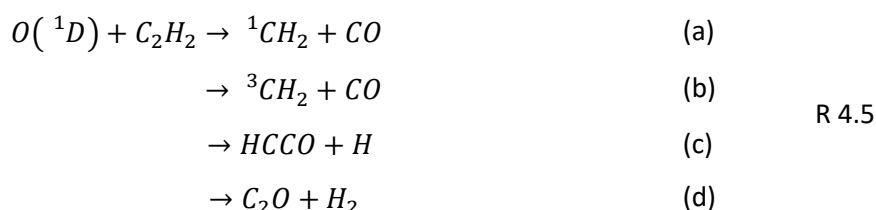
Figure 4.8 Schematic potential energy surface of $\text{O}(^1\text{D}) + \text{C}_2\text{H}_6$ reaction extracted from Sun et al.⁶⁶

Several experimental and theoretical dynamics studies^{52,56,64,67,68} suggest that the reaction mechanism is dominated by oxygen insertion into one of the C-H bonds forming a strongly bound ethanol intermediate complex that falls apart through several reactions pathways. Oxygen insertion into the C-C bond is thought not to occur as the lowest five singlet potential energy surfaces are all seen to be repulsive in the entrance region.⁶⁴ In addition, a direct H-atom abstraction mechanism^{54-56,66} has been proposed for channel R 4.4 (c) leading to OH formation.

In contrast, the kinetics of the $\text{O}(^1\text{D}) + \text{C}_2\text{H}_6$ reaction have not been well studied with just a few determinations of the rate constant at room temperature, with values differing among them by a factor of 2. Schofield⁶⁹ recommended a value of $3.2 \times 10^{-10} \text{ cm}^3 \text{ s}^{-1}$ at room temperature from a critical evaluation of the reported relative rate constants and Matsumi et al.⁷⁰ measured a rate constant of $(6.3 \pm 0.3) \times 10^{-10} \text{ cm}^3 \text{ s}^{-1}$ at room temperature. More recently, Dillon et al.⁵¹ studied the reaction over the 220 - 300 K temperature range finding a temperature independent rate constant of $(3.4 \pm 0.7) \times$

$10^{-10} \text{ cm}^3 \text{ s}^{-1}$. Regarding the branching ratio determinations for this reaction, there are several experimental and theoretical studies reported in the literature with some disagreement among them.
55,56,66,67,70

In the case of $O(^1D) + C_2H_2$ reaction, there are four exothermic exit pathways with two of these channels R 4.5 (a) and R 4.5 (c) leading to spin-allowed products:



There are very few previous studies in the literature concerning the $O(^1D) + C_2H_2$ reaction. Girard and Chaquin⁷¹ performed a theoretical investigation of the various H_2C_2O addition products providing basic information on the nature and stability of the likely primary products. However, no further simulations were performed to determine the unimolecular dissociation products, which are expected in the gas-phase at low pressure. To the best of our knowledge, there are no other theoretical or experimental studies on the dynamics of this reaction. However, conclusions can be drawn from other related works^{72,73} that treat some parts of the potential energy surface involved in this reaction. Furthermore, studies of the reaction of ground state atomic oxygen with C_2H_2 can also offer a valuable insight.^{74,75}

The kinetics of $O(^1D) + C_2H_2$ reaction has only been measured once⁷⁶ and as far as we know, there are no determinations of the branching ratios for the different exit channels. In this chapter, the rate constants and the branching ratios for the $O(^1D) + C_2H_6$ reaction and the rate constants for the $O(^1D) + C_2H_2$ reaction have been measured over the 50 - 296 K temperature range and our results are compared with previous experimental studies.

4.3.1. Results

In this case, two types of experiments were performed. Firstly, the second-order rate constants were determined by following reagent $O(^1D)$ atoms by VUV LIF. Secondly, the temperature dependent branching ratios were determined by following H-atom formation. To apply the pseudo-first-order approximation, the hydrocarbon concentrations were maintained in large and known excess with respect to the $O(^1D)$ concentration. Although $O(^3P)$ atoms were also present in the flow due to the photolysis of O_3 at 266 nm with a quantum yield of approximately 10%, these atoms are unreactive with C_2H_6 and C_2H_2 at room temperature and below.⁷⁷

4.3.1.1. Rate constants

Pseudo-first-order decays of $O(^1D)$ with and without hydrocarbon added are presented in *Figure 4.9*. Even with no hydrocarbon added, $O(^1D)$ atoms are removed rapidly due to non-reactive collisions with the carrier gas Ar. Other losses such as deactivation with residual O_2 in the reactor and diffusional loss from the probe volume are expected to be negligible in comparison.

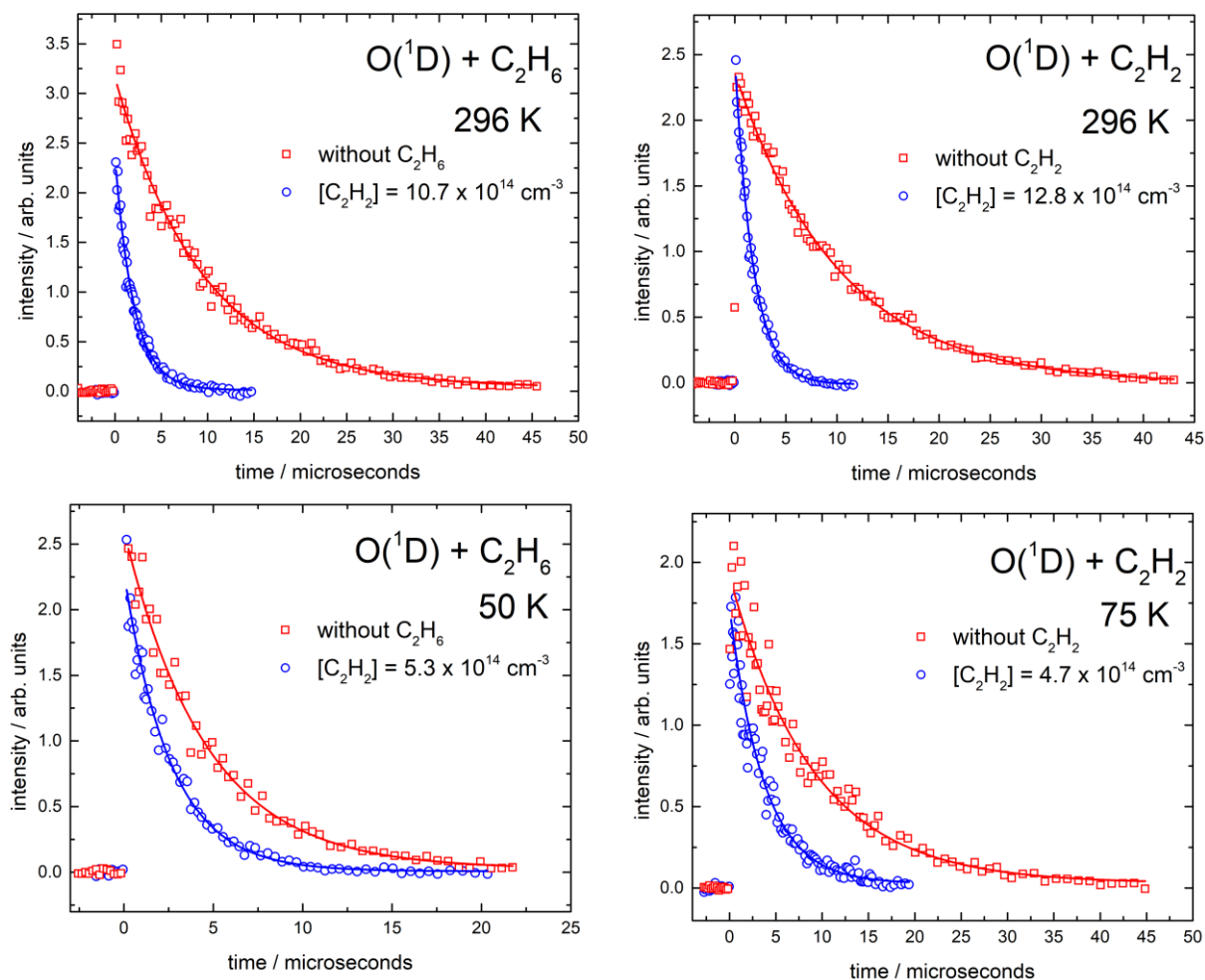


Figure 4.9 $O(^1D)$ VUV LIF signals as a function of time. (Left panel) $O(^1D) + C_2H_6$ reaction at 296 K and 50 K. (Right panel) $O(^1D) + C_2H_2$ reaction at 296 K and 75 K. (Red open squares) represent the $O(^1D)$ decay without hydrocarbon added. (Blue open circles) represent the maximum concentration of hydrocarbon used during the experiments. (Solid blue and red lines) represent functional fits to the data using expression 2.5.

Plots of the measured pseudo-first-order rate constant as a function of hydrocarbon concentration are shown in *Figure 4.10*. The y-axis intercept represents the pseudo-first-order loss of $O(^1D)$ by collisions with the carrier gas Ar.

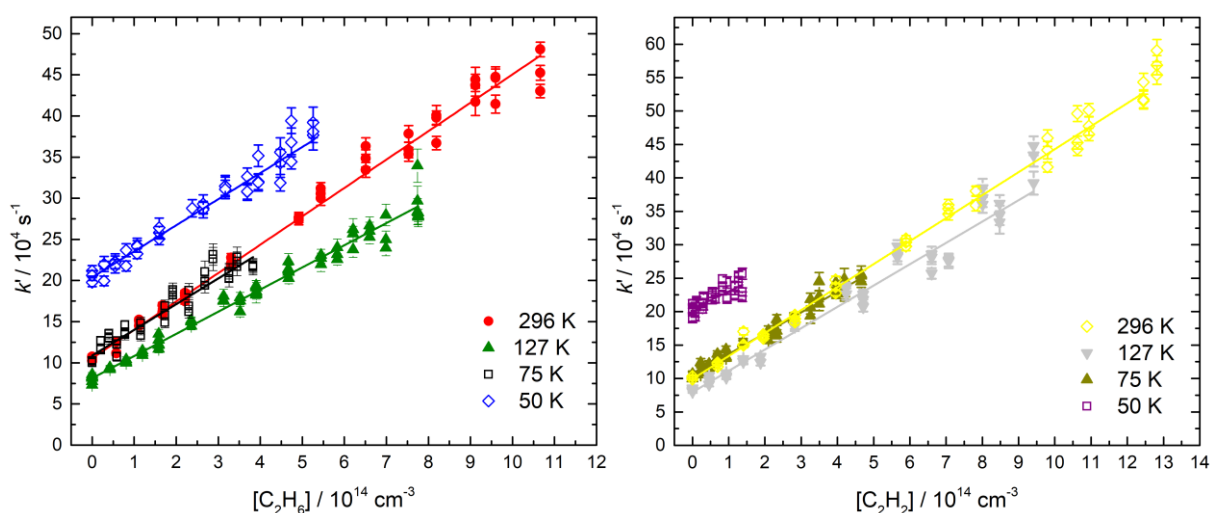


Figure 4.10 Second-order plots of the $O(^1D)$ + hydrocarbon reactions. (Left panel) the $O(^1D)$ + C_2H_6 reaction. (Right panel) the $O(^1D)$ + C_2H_2 reaction. The solid lines represent linear least-squares fits to the data, weighted by the statistical uncertainties of the individual data points given by the pseudo-first-order fits.

The second-order rate constants obtained as a function of temperature are displayed in Figure 4.11 alongside other experimental and theoretical determinations.

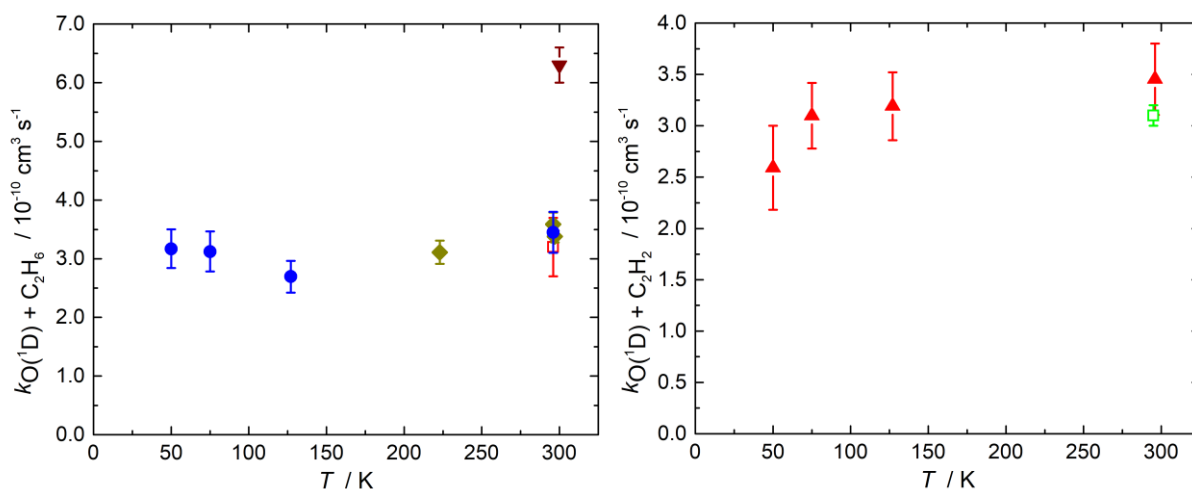


Figure 4.11 Measured rate constants as a function of temperature. (Left panel) the $O(^1D)$ + C_2H_6 reaction; (blue solid circles) this work; (dark red triangle) Matsumi et al.,⁷⁰ (dark yellow diamond) Dillon et al.,⁵¹ (red open square) Schofield.⁶⁹ (Right panel): the $O(^1D)$ + C_2H_2 reaction; (red solid triangles) this work; (green open square) Carl.⁷⁶ Error bars represent the combined statistical and systematic uncertainties.

The second-order rate constants, the concentration ranges and the number of experiments performed in each case are summarized in Table 4.2.

Table 4.2 Temperature dependent rate constants for the $O(^1D) + C_2H_6$ and $O(^1D) + C_2H_2$ reactions.

T(K)	N ^b	$[C_2H_6]$ (10^{14} cm^{-3})	$k_{O(^1D)+C_2H_6}$ ($10^{-10} \text{ cm}^3 \text{ s}^{-1}$)	N	$[C_2H_2]$ (10^{14} cm^{-3})	$k_{O(^1D)+C_2H_2}$ ($10^{-10} \text{ cm}^3 \text{ s}^{-1}$)
296	42	0 – 10.7	$(3.5 \pm 0.3)^c$	42	0 – 12.8	(3.5 ± 0.3)
127 ± 2^a	63	0 – 7.8	(2.7 ± 0.3)	42	0 – 9.4	(3.2 ± 0.3)
75 ± 2	41	0 – 3.8	(3.1 ± 0.3)	41	0 – 4.7	(3.1 ± 0.3)
50 ± 1	40	0 – 5.3	(3.2 ± 0.3)	39	0 – 1.4	(2.6 ± 0.4)

^aUncertainties in the calculated temperatures represent the statistical (1σ) errors obtained from Pitot tube measurements of the impact pressure. ^bNumber of individual measurements. ^cUncertainties in the measured rate constants represent the combined statistical (1σ) and estimated systematic (10%) errors.

4.3.1.2. Branching ratios

The absolute H-atom yields for the $O(^1D) + C_2H_6$ reaction are reported as a function of temperature in Table 4.3. Unfortunately, no H-atom yields could be determined for the $O(^1D) + C_2H_2$ reaction due to the influence of secondary reactions leading to the production of H-atoms. For this reaction, one of the major products, 1CH_2 , is known to react rapidly with C_2H_2 to form H-atoms and C_3H_3 as products with a yield that increases from 0.28 at 195 K to 0.88 at 298 K.^{78,79}

Table 4.3 H-atom yields for the $O(^1D) + C_2H_6$ reaction as a function of temperature.

T(K)	N ^b	H-atom yield $O(^1D) + C_2H_6$
296	4	0.18 ± 0.01^c
127 ± 2^a	6	0.18 ± 0.02
75 ± 2	4	0.18 ± 0.03
50 ± 1	4	0.18 ± 0.01

^aUncertainties in the calculated temperatures represent the statistical (1σ) errors obtained from Pitot tube measurements of the impact pressure. ^bNumber of H-atom determinations. ^cError bars represent the statistical uncertainties at the 95% confidence level.

As a secondary check of the H-atom branching ratio determinations, additional measurements were performed at 127 K using the method described in Chapter 3 section 3.1.4. In this case, three pairs of H-atom formation curves with the same value of k' for the reference and target reaction were recorded and fitted using expression (2.9.1). Finally, the branching ratio was obtained from the ratio of the pre-exponential factors after correction of the signal amplitudes due to absorption losses of the VUV light. With this method, a H-atom yield of 0.19 ± 0.03 was obtained which is in excellent agreement with the values reported in Table 4.3.

4.3.2. Discussion

4.3.2.1. The O(¹D) + C₂H₆ reaction

While our measured rate constant for the reaction of O(¹D) + C₂H₆ at room temperature is in good agreement with the recommended value of Schofield⁶⁹ and the determination of Dillon et al.,⁵¹ the experimental value reported by Matsumi et al.⁷⁰ is 2 times larger (*Figure 4.11* left panel). This difference has been attributed⁵¹ to possible errors in the determination of the C₂H₆ concentration by Matsumi et al. Furthermore, no temperature dependence is observed in our rate constants as the temperature falls to 50 K, in agreement with the previous results from Dillon et al.⁵¹ in the 220 – 300 K temperature range.

Dynamics studies^{52,56,64,67,68} suggest that O(¹D) atoms insert into the C-H bonds of C₂H₆ forming an energized ethanol intermediate complex. Then as the lifetime of this intermediate is expected to be only a few picoseconds due to rapid unimolecular dissociation,⁶⁶ complex stabilization will not occur under our experimental conditions. Regarding the branching ratios for the O(¹D) + C₂H₆ reaction, there are several previous determinations. On the experimental side, Shu et al.^{55,56} studied the reaction using a CMB technique at collision energies of 33.5 kJ/mol. These authors reported relative product branching ratios of 70, 25, 3 and 2% for channels R 4.4 (d), R 4.4 (c), R 4.4 (a) and R 4.4 (b) respectively. On the theoretical side, Sun et al.⁶⁶ determined branching ratios at 33.5 kJ/mol using the combined quantum chemistry calculation and RRKM approach. They found contributions of 60, 8, 4, and 1% for the channels R 4.4 (d), R 4.4 (c), R 4.4 (a) and R 4.4 (b) respectively and predicted a 27% yield for an additional exit channel leading to H₂O formation, which was not detected in the CMB experiment. These theoretical branching ratios underestimate the experimental ones, a result that was attributed to the fact that the abstraction channel was not considered. Gonzalez et al.⁵⁴ performed an experimental characterization of the OH state distribution produced by the O(¹D) + C₂H₆ reaction at an average collision energy of 50 kJ/mol. Although these experimental results were not fully conclusive regarding the influence of the direct abstraction mechanism, their complementary theoretical analysis using QCT calculations predicted 1-2% of abstraction like reactive trajectories. These authors also analysed the influence of the collision energy in the dynamics of the reaction, comparing their results with the results of Park and Wiesenfeld⁶⁷ performed at 26 kJ/mol, concluding that insertion followed by unimolecular dissociation should be the most important reaction mechanism at low and intermediate temperature.⁵⁴

On the other hand, the experimental study of Park and Wiesenfeld⁶⁷ predicted an absolute yield of 3% for the channel leading to OH formation (R 4.4 (c)) at thermal collision energies (300 K equivalent to

3.7 kJ/mol). In addition, Matsumi et al.⁷⁰ determined a H-atom yield (R 4.4 (a)) of 10% at room temperature and stated that the H-atom product is mostly formed from rupture of the O-H bond ($C_2H_5O + H$ channel) in contrast with the findings at high collision energies which suggest that H-atom formation is more likely from the rupture of a C-H bond ($CH_3CHOH + H$ channel).^{55,56}

The H-atom product yields measured in this work (*Table 4.3*) are independent of temperature from 50 - 296 K. Our results are in reasonable agreement with the value reported by Matsumi et al.⁷⁰ at room temperature, but they are somewhat higher than the theoretical and experimental branching ratios of Shu et al.^{55,56} and Sun et al.⁶⁶ This difference could be explained due to a change in the reaction mechanism where the most thermodynamically favourable channel ($CH_3CHOH + H$) is thought to dominate at higher collision energies whereas the kinetically favourable channel ($CH_3CH_2O + H$) is likely to dominate at room temperature and below.

4.3.2.2. The $O(^1D) + C_2H_2$ reaction

The rate constants determined for the $O(^1D) + C_2H_2$ reaction present little or no temperature dependence as the temperature is lowered, with the differences well within the combined error bars. Furthermore, our determined rate constant at room temperature is in excellent agreement with the only previous determination of Carl⁷⁶ performed at 295 K with a reported rate constant of $(3.1 \pm 0.2) \times 10^{-10} \text{ cm}^3 \text{ s}^{-1}$.

There is very little information regarding the dynamics of $O(^1D) + C_2H_2$ reaction. The theoretical study of Girard and Chaquin⁷¹ predicts several minima in the PES due to the formation of a C=O bond from $O(^1D)$ addition to the $C\equiv C$ bond leading to formylcarbene (HCCHO) and/or oxirene (C_2H_2O) structures, and due to the insertion of $O(^1D)$ into the C-H bond resulting in ethynol (CHCOH). From stability calculations, these authors predict that at low temperature both formylcarbene and/or oxirene could be produced with the formylcarbene being more stable by 4.18 kJ/mol, while at room temperature a further step is expected involving the interconversion of formylcarbene and/or oxirene into ketene ($CH_2=C=O$). As this study was focused on the generation of a PES for the simulation of the addition products in matrix type experiments, no further calculations were performed to determine the unimolecular dissociation products that are expected in the gas-phase.

Further information of the dynamics of $O(^1D) + C_2H_2$ reaction can be derived from theoretical studies of the $O(^3P) + C_2H_2$ reaction, where intersystem crossing (ISC) to the singlet state could play an important role. Rajak and Maiti^{74,75} performed non-adiabatic dynamics studies of the $O(^3P) + C_2H_2$ reaction at three different collision energies (34.3, 39.7, and 54.8 kJ/mol) to investigate their effect on

the extent of ISC. These authors found branching ratios of 80% for the channel leading to H + HCCO and 20% for the production of $^{1,3}\text{CH}_2 + \text{CO}$ for all collisional energies. However, the product yield for $^1\text{CH}_2$ was found to decrease with an increase of the collision energy due to a lower probability of ISC. In addition, these authors show the PES for the $\text{O}(^1\text{D}) + \text{C}_2\text{H}_2$ reaction predicting an adiabatic pathway leading to $^1\text{CH}_2 + \text{CO}$.

The PES for the $\text{O}(^1\text{D}) + \text{C}_2\text{H}_2$ reaction involves the formation of ketene as an intermediate. The dynamics of ketene photodissociation have been extensively studied theoretically and experimentally. Xiao et al.⁷² predict that once the ketene is in its ground state S_0 , which corresponds to the PES involved in the $\text{O}(^1\text{D}) + \text{C}_2\text{H}_2$ reaction, unimolecular dissociation occurs to yield H + HCCO and $^1\text{CH}_2 + \text{CO}$ as adiabatic products and $^3\text{CH}_2 + \text{CO}$ as non-adiabatic products through ISC. These authors stated that the relative branching ratios between the different exit channels will depend on the photon energy. Then if the energy is much larger than the corresponding dissociation barrier, adiabatic product channels will be favoured so that H + HCCO and $^1\text{CH}_2 + \text{CO}$ are the major products with $^3\text{CH}_2 + \text{CO}$ as minor products. This hypothesis is corroborated by the experiments of Fockenberg⁷³ who studied the product distribution of ketene photolysis at 300 K measuring the following products yields $^1\text{CH}_2 + \text{CO}$ ($66 \pm 8\%$), H + HCCO ($17 \pm 7\%$) and $^3\text{CH}_2 + \text{CO}$ ($6 \pm 9\%$).

Unfortunately, in this work, we were not able to determine H-atom branching ratios to clarify the reaction mechanism. However, the $\text{O}(^1\text{D}) + \text{C}_2\text{H}_2$ reagents are 266.9 kJ/mol above the $\text{O}(^3\text{P}) + \text{C}_2\text{H}_2$ reagents. Consequently, the intermediate $^1\text{C}_2\text{H}_2\text{O}$ complex is highly energetic and therefore expected to have a short lifetime reducing considerably the probability of ISC to the triplet surface. Thus, the spin allowed products R 4.5 (a) and R 4.5 (c) should be the major exit channels. Indeed, our observation of significant quantities of secondary H-atoms indicates that $^1\text{CH}_2 + \text{CO}$ formation represents one of the major channels of the $\text{O}(^1\text{D}) + \text{C}_2\text{H}_2$ reaction.

4.4. The $\text{O}(^1\text{D}) + \text{CO}_2$ reaction

The reaction of $\text{O}(^1\text{D})$ with CO_2 has two exothermically accessible channels, electronic quenching to the ground state R 4.6 (a) and reaction to form products R 4.6 (b).



The quenching of $\text{O}(^1\text{D})$ by carbon dioxide has been extensively studied given its importance in the atmospheric chemistry of the Earth and Mars.^{1,36,37,53,80-84} Atomic oxygen in its first excited state is produced in the Earth's atmosphere by UV photolysis of ozone (O_3) at wavelengths shorter than 320

nm.⁸¹ These atoms are deactivated to the ground state (3P) through nonreactive collisions with N_2 and O_2 ³⁶, removed by reaction with N_2O (producing NO) and with H_2O or CH_4 (producing OH radicals).³⁷ Thus the production rates of NO and OH in the Earth's atmosphere depend on the competition between collisional deactivation and reactive removal. In the Martian atmosphere, $O(^1D)$ atoms are produced by CO_2 photolysis and removed by reaction with minor constituents or by deactivation to the ground state mostly through collisions with major atmospheric component CO_2 . This quenching process is thought to occur through the formation of a long-lived CO_3 complex that subsequently fragments to form $O(^3P) + CO_2$.^{80,82}

On the other hand, chemical reaction to form $CO + O_2$ products has been experimentally studied by Shortridge and Lin⁸⁵ who were not able to observe appreciable CO production concluding that less than 1% of the collisions result in products. More recently Sedlacek et al.⁸⁶ determined a quantum yield for this reaction of $(2.1 \pm 0.3) \times 10^{-3}$ molecules/photon absorbed monitoring the formation of CO as a function of the number of laser pulses. These authors conclude that the very low quantum efficiency suggested a significant potential energy barrier on the reaction coordinate that prevents the vast majority of collisions from fragmenting into products distinguishable from the reactants. Furthermore, they determined indirectly a rate constant for the process of $(2.4 \pm 0.5) \times 10^{-13} \text{ cm}^3 \text{ s}^{-1}$ through comparisons with the rate for the quenching process. The kinetics of the $O(^1D) + CO_2$ quenching reaction have been studied experimentally over the temperature range 139 - 673 K.^{1,36,37,53,81-84} The rate constants at room temperature are in the range of $(1.0 - 1.4) \times 10^{-10} \text{ cm}^3 \text{ s}^{-1}$, which indicate that CO_2 is an efficient deactivator of $O(^1D)$ atoms and suggest that the quenching reaction has no or only a small activation energy, likely proceeding through a reaction intermediate. On the theoretical side, Mebel et al.⁸⁰ have investigated the reaction dynamics using ab initio multireference configuration interaction calculations. In addition, these authors calculated the rate constants in the 200 - 300 K temperature range using standard RRKM theory. In this work, the kinetic data for the electronic quenching of $O(^1D)$ atoms with CO_2 is extended down to 50 K.

4.4.1. Results

To apply the pseudo-first-order approximation, the CO_2 concentration was maintained in a large and known excess with respect to the $\text{O}(^1\text{D})$ concentration. Pseudo-first-order decays of $\text{O}(^1\text{D})$ with and without CO_2 added are presented in *Figure 4.12*.

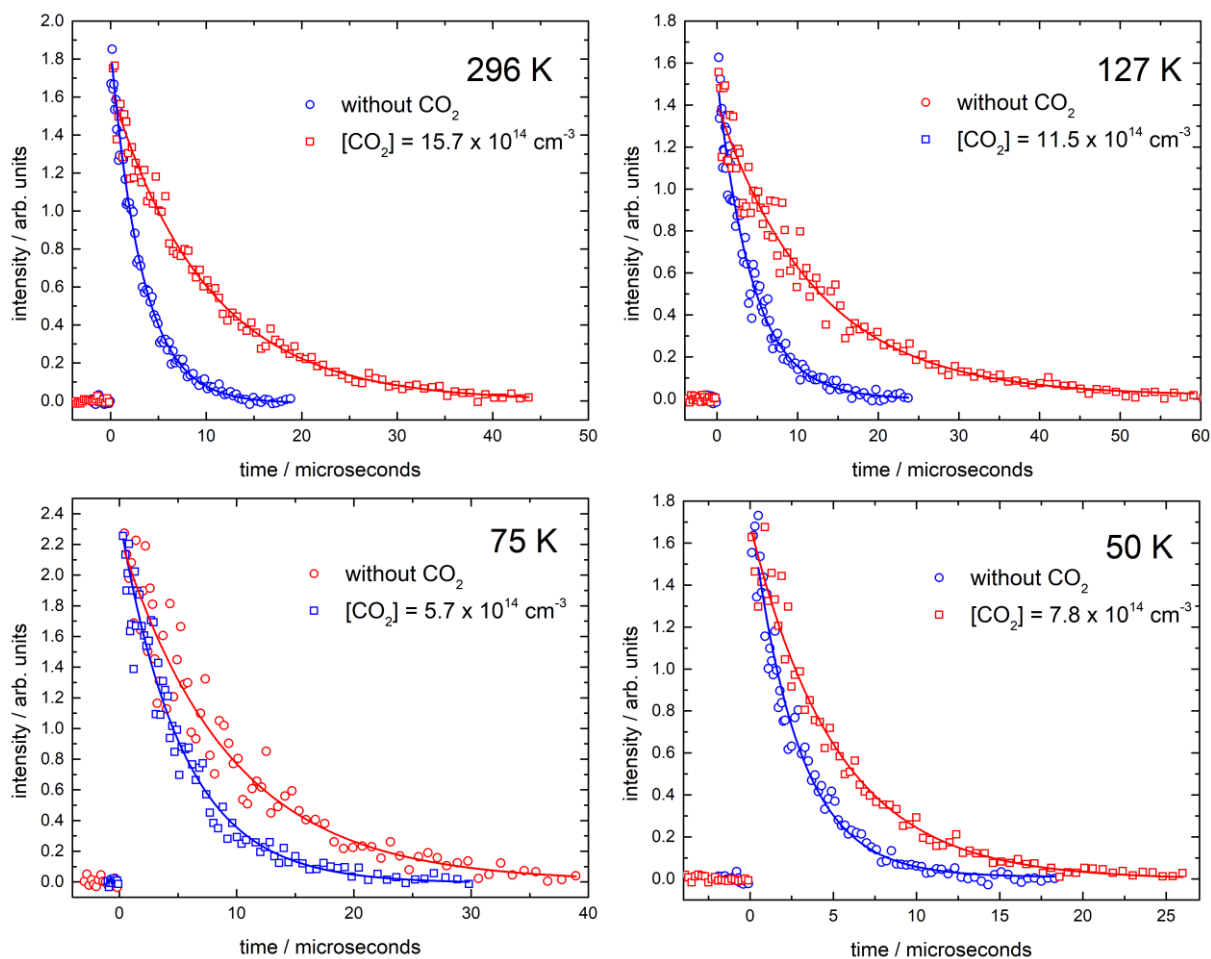


Figure 4.12 $\text{O}(^1\text{D})$ VUV LIF signals as a function of time for the $\text{O}(^1\text{D}) + \text{CO}_2$ reaction. (Left panel) recorded at 296 K and 75 K. (Right panel) recorded at 127 K and 50 K. (Red open squares) $\text{O}(^1\text{D})$ decay without CO_2 added. (Blue open circles) maximum concentration of CO_2 used during the experiments. Solid blue and red lines represent functional fits to the data using expression 2.5.

The measured pseudo-first-order rate constants as a function of $[\text{CO}_2]$ are shown in *Figure 4.13*.

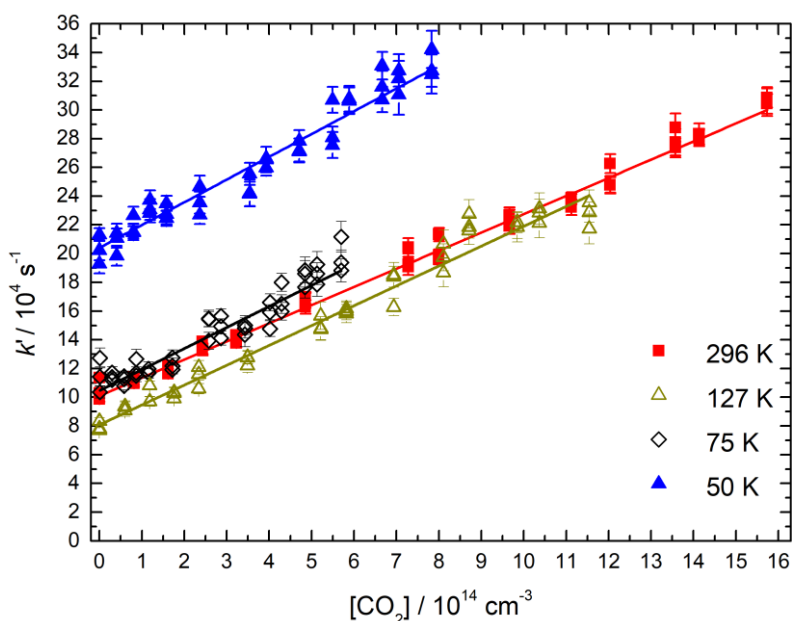


Figure 4.13 Second-order plots for the $O(^1D) + CO_2$ reaction. (Blue solid triangles) data recorded at 50 K; (black open diamonds) data recorded at 75 K; (red solid squares) data recorded at 296 K; (yellow open triangles) data recorded at 127 K. The solid lines represent linear least-squares fits to the data, weighted by the statistical uncertainties of the individual data points obtained from pseudo-first-order fits.

The second-order rate constants, the concentration ranges and the number of experiments performed in each case are summarized in Table 4.4.

Table 4.4 Temperature dependent rate constants for the $O(^1D) + CO_2$ reaction.

T(K)	N ^b	[CO ₂] (10 ¹⁴ cm ⁻³)	$k_{O(^1D)+CO_2}$ (10 ⁻¹⁰ cm ³ s ⁻¹)
296	42	0 - 15.7	(1.3 ± 0.1) ^c
127 ± 2 ^a	42	0 - 11.5	(1.4 ± 0.1)
75 ± 2	42	0 - 5.7	(1.5 ± 0.2)
50 ± 1	42	0 - 7.8	(1.6 ± 0.2)

^aUncertainties in the calculated temperatures represent the statistical (1σ) errors obtained from Pitot tube measurements of the impact pressure. ^bNumber of individual measurements. ^cUncertainties in the measured rate constants represent the combined statistical (1σ) and estimated systematic (10%) errors.

The second-order rate constants obtained as a function of temperature are displayed alongside other experimental and theoretical determinations in Figure 4.14.

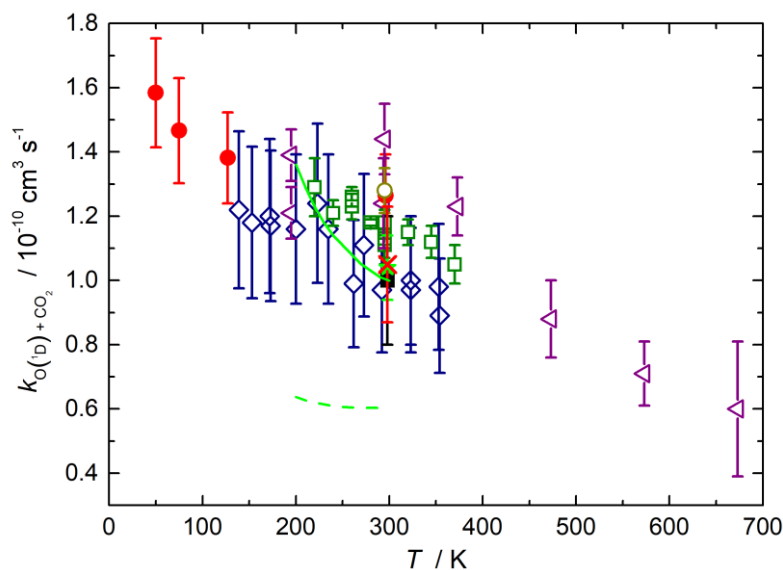


Figure 4.14 Measured rate constants as a function of temperature for the $O(^1D) + CO_2$ reaction. Experimental values: (solid red circles) this work; (open blue diamonds) Streit et al.;¹ (open purple triangles) Blitz et al.;³⁷ (open green squares) Dunlea and Ravishankara;⁵³ (open yellow circle) Amimoto et al.;⁸⁴ (solid black square) Davidson et al.;³⁶ (solid green star) Wine and Ravishankara⁸¹ and (red cross) Shi and Barker.⁸³ Theoretical studies (dashed green line) Mebel et al.⁸⁰ using a TS energy of -1.26 kJ/mol; (solid green line) Mebel et al.⁸⁰ using a TS energy of -2.51 kJ/mol. Error bars represent the combined statistical and systematic uncertainties.

4.4.2. Discussion

From Figure 4.14 it can be seen that our rate constant for the $O(^1D) + CO_2$ reaction at room temperature is in excellent agreement with the earlier determinations of the rate constant for this quenching process.^{1,36,37,53,81,83,84} When the temperature falls to 50 K, a slight increase in the rate constant is observed. This result is entirely consistent with the previous determinations of Streit et al.,¹ Blitz et al.³⁷ and Dunlea et al.⁵³ in the combined temperature range 139 - 673 K where similar temperature dependences have been measured.

Details on the reaction mechanism for the $O(^1D) + CO_2$ reaction have been provided by the theoretical work of Mebel et al.⁸⁰ These authors calculated the geometries and energies of the various intermediates and transition states of the lowest singlet and triplet CO_3 PESs using ab initio multireference configuration interaction calculations. They concluded that reaction occurs through the formation of an $O-CO_2$ complex, which then isomerizes to form a strongly bound cyclic 1CO_3 intermediate over a barrier located at 1.26 kJ/mol below the reagents as a best estimate. Mebel et al.⁸⁰ predict that as the 1CO_3 intermediate is formed with high internal energy, it can decompose into the initial reactants or undergo singlet-triplet ISC to form 3CO_3 . Indeed, experimental studies on the $O(^1D) + CO_2$ reaction leading to the products ($O_2 + CO$) predict a low occurrence for the reactive collisions

concluding that this exit channel is characterized by a significant barrier.^{85,86} Consequently, the loss of $^1\text{CO}_3$ is dominated by quenching through ISC to the $^3\text{CO}_3$ PES followed by dissociation to form $\text{O}(^3\text{P}) + \text{CO}_2$.

Mebel et al.⁸⁰ derived the total rate constant for the $\text{O}(^1\text{D}) + \text{CO}_2$ reaction as a function of temperature from the contributions of the various isomerization and dissociation steps on the singlet and triplet CO_3 PES in addition to ISC rate constants and radiationless transitions between the triplet and singlet surfaces. These rate constants are shown in *Figure 4.14* for two energies of the submerged barrier (-1.26 kJ/mol and -2.51 kJ/mol) on the singlet CO_3 surface. Using a barrier of -1.26 kJ/mol, the calculated rate constants are half as large as the experimental ones. However, when a barrier of -2.51 kJ/mol is used, the agreement with the experimental values is significantly improved. With respect to the temperature dependence, these authors found that the reaction rate was mostly dependent on the energy dependence of the unimolecular dissociation rate for the cyclic $^1\text{CO}_3$ intermediate because the $\text{O}(^3\text{P}) + \text{CO}_2$ products are mostly formed by a radiationless transition from $^1\text{CO}_3$ to $^3\text{CO}_3$ with only a weak dependence on the initial energy. Then as the collision energy or temperature decreases, a slower redissociation rate for the cyclic $^1\text{CO}_3$ intermediate leads to an increase of ISC to the triplet surface and consequently an enhancement of the rate of formation of $\text{O}(^3\text{P}) + \text{CO}_2$ occurs.

4.5. The $\text{O}(^1\text{D}) + \text{Kr}$ reaction

The electronic quenching of $\text{O}(^1\text{D})$ atoms by noble gases is a relatively simple collisional process that has attracted lots of attention.^{6,37,83,87,88} Whereas this quenching reaction has no direct significance for the chemistry of planetary atmospheres, the study of this process is of considerable fundamental interest as well as being important in the evaluation of the laboratory investigations as noble gases are used as carrier gases in many experiments leading to excited atom loss by electronic quenching.

In general, it is well established that the deactivation rates of $\text{O}(^1\text{D})$ by noble gases decrease markedly for the lighter ones ($\text{He} < \text{Ne} < \text{Ar} < \text{Kr} < \text{Xe}$). While He and Ne have very low efficiencies in the deactivation of $\text{O}(^1\text{D})$,⁸⁷ Xe is a very efficient deactivator showing a small positive temperature dependence in the 110 – 300 K temperature range.⁸⁸ In addition, the rate constants for the $\text{O}(^1\text{D}) + \text{Ar}$ quenching reaction have been determined in the temperature range 50 - 673 K showing a weak temperature dependence.^{6,37} In the case of $\text{O}(^1\text{D}) + \text{Kr}$, the quenching rate has been studied experimentally in the 113 - 673 K temperature range with a very small positive temperature dependence according to the results of Blitz et al.³⁷ In this work, the kinetic data for the $\text{O}(^1\text{D}) + \text{Kr}$ quenching reaction are extended down to 50 K and our results are compared with a quantum close-

coupling treatment of the quenching transition from the 1D state to the 3P_j fine-structure levels in collisions with Kr.⁸⁹

4.5.1. Results

To apply the pseudo-first-order approximation, the Kr concentration was maintained in a large and known excess with respect to the $O(^1D)$ concentration. To study this reaction, it was necessary to add large quantities of Kr to the flow, so that the carrier gas Ar concentration was reduced to maintain a constant flow density. Consequently, the pseudo-first-order rate constants were corrected to account for the slower relaxation by Ar in the system (for details see section 4.1.3). Pseudo-first-order decays of $O(^1D)$ with and without Kr added are presented in *Figure 4.15*

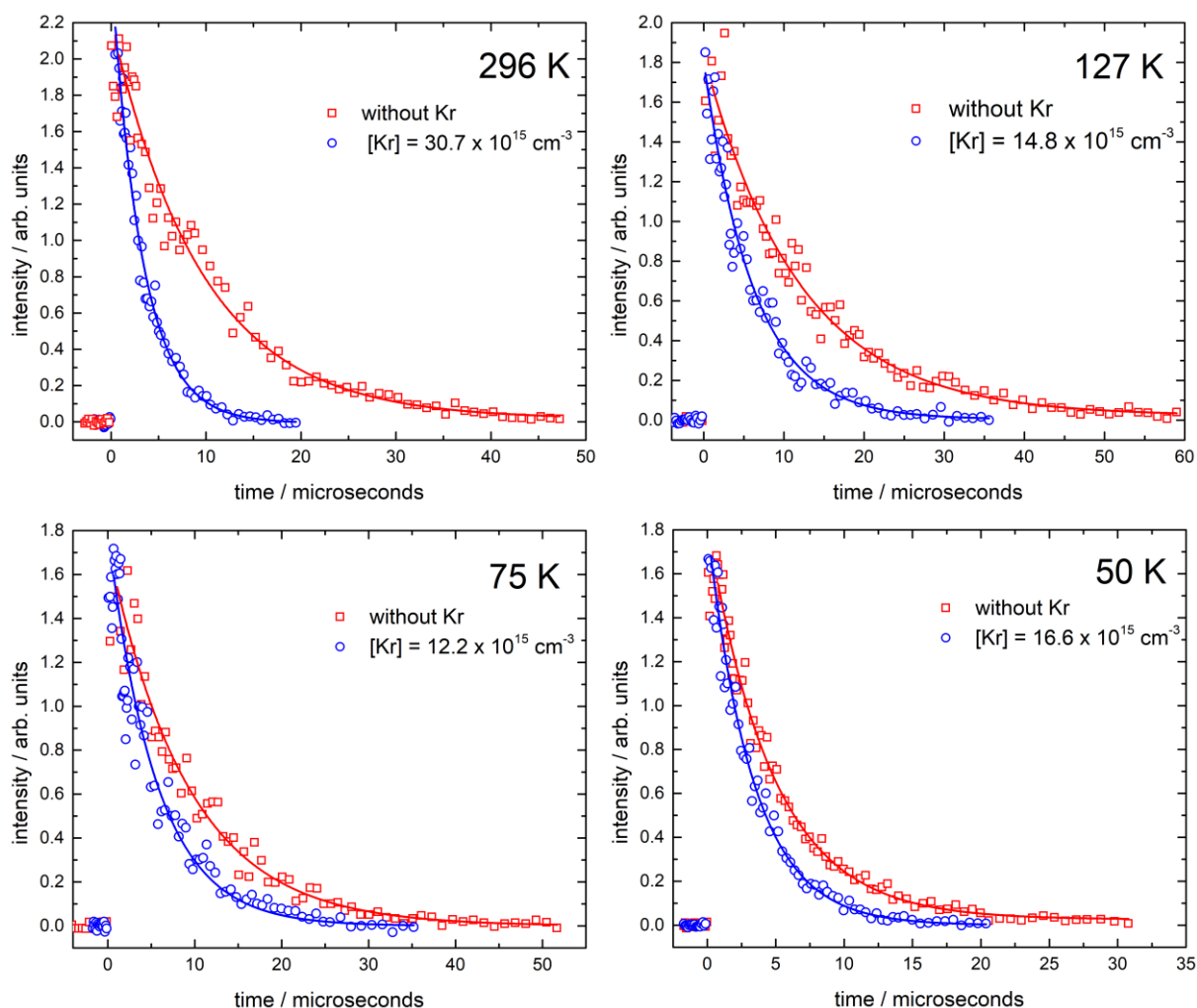


Figure 4.15 $O(^1D)$ VUV LIF signals as a function of time for the $O(^1D) + Kr$ quenching reaction. (Left panel) recorded at 296 K and 75 K. (Right panel) recorded at 127 K and 50 K. (Red open squares) $O(^1D)$ decay without Kr added. (Blue open circles) the maximum concentration of Kr used during the experiments. Solid blue and red lines represent functional fits to the data using expression 2.5.

The measured pseudo-first-order rate constants (corrected for the lower flow of Ar as described in section 4.1.3) as a function of the Kr concentration are shown in *Figure 4.16*. The second-order rate constants obtained as a function of temperature are displayed in *Figure 4.17* in conjunction with other experimental and theoretical determinations.

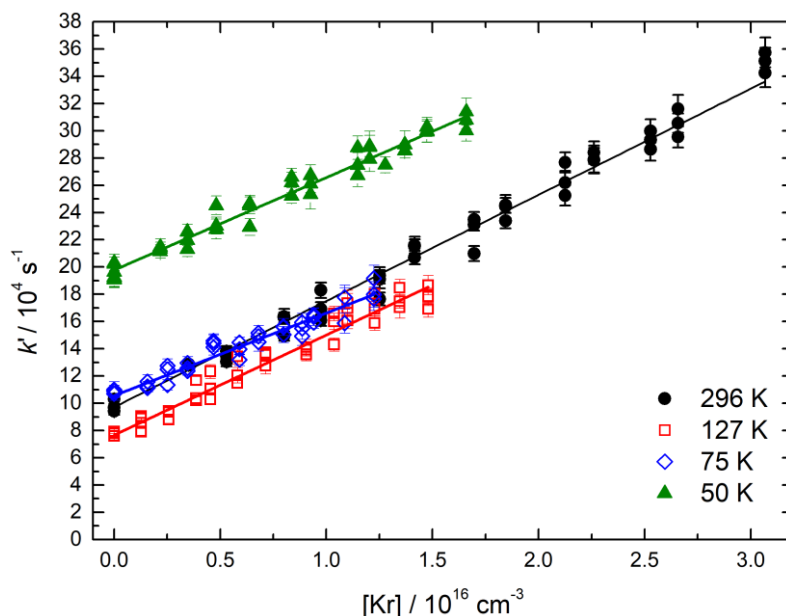


Figure 4.16 Second-order plots for the $\text{O}(^1\text{D}) + \text{Kr}$ reaction. (Green solid triangles) data recorded at 50 K; (black solid circles) data recorded at 296 K; (blue open diamonds) data recorded at 75 K; (red open squares) data recorded at 127 K. The solid lines represent linear least-squares fits to the data, weighted by the statistical uncertainties of the individual data points obtained during pseudo-first-order fits.

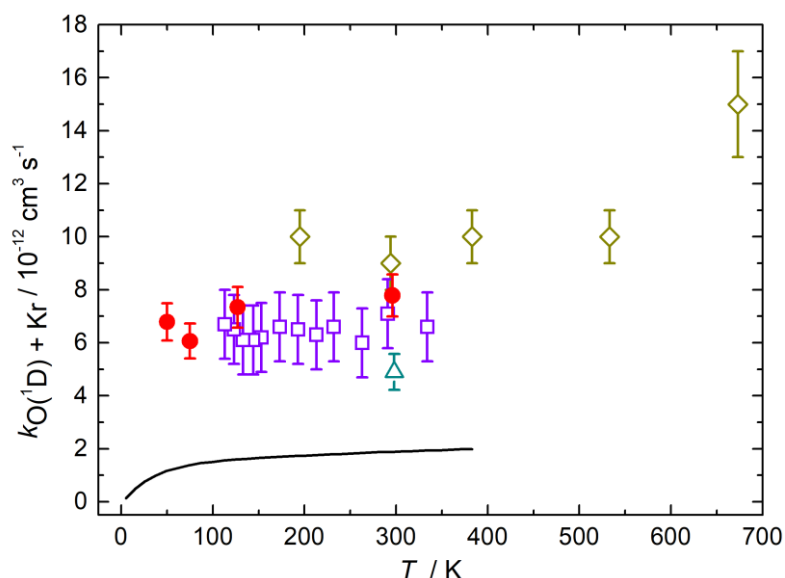


Figure 4.17 Measured rate constants as a function of temperature for the $\text{O}(^1\text{D}) + \text{Kr}$ quenching reaction. Experimental values: (solid red circles) this work; (open purple squares) Davidson et al.;⁸⁸ (open yellow diamonds) Blitz et al.;³⁷ (open green triangle) Shi and Barker.⁸³ Theoretical values: (solid black line) quantum close-coupling result of Nuñez-Reyes et al.⁸⁹

The second-order rate constants, the concentration ranges and the number of experiments performed in each case are summarized in *Table 4.5*

Table 4.5 Temperature dependent rate constants for the $O(^1D) + Kr$ quenching reaction.

T(K)	N ^b	[Kr] (10^{15} cm^{-3})	$k_{O(^1D)+Kr}$ ($10^{-12} \text{ cm}^3 \text{ s}^{-1}$)
296	42	0 - 30.7	(7.8 ± 0.8) ^c
127 ± 2^a	40	0 - 14.8	(7.3 ± 0.8)
75 ± 2	36	0 - 12.2	(6.1 ± 0.7)
50 ± 1	39	0 - 16.6	(6.8 ± 0.7)

^aUncertainties in the calculated temperatures represent the statistical (1σ) errors obtained from Pitot tube measurements of the impact pressure. ^bNumber of individual measurements. ^cUncertainties in the measured rate constants represent the combined statistical (1σ) and estimated systematic (10%) errors.

4.5.2. Discussion

As can be seen from *Figure 4.17*, our experimental rate constants are in excellent agreement with the previous experimental determinations of Davidson et al.⁸⁸ in the 113 - 296 K temperature range and with the result of Blitz et al.³⁷ at room temperature. But these latter authors,³⁷ using a chemical tracer method to follow the kinetics of the quenching process, reported a rate constant at 195 K that is approximately 40% larger than our values. Furthermore, their rate constants over the 195 - 673 K temperature range display a small positive temperature dependence. Lastly, the value reported at room temperature by Shi and Barker⁸³ using the relative rate method is lower than the rest of the data sets and lies outside of the combined error bars. The differences observed in the rate constants of Blitz et al.³⁷ and Shi and Barker⁸³ with respect to the other data including ours might be due to the influence of secondary processes affecting the system during the indirect determination of the quenching rate for $O(^1D) + Kr$. Moreover, Shi and Barker⁸³ used a value for their $O(^1D) + O_2$ reference reaction larger than the currently recommended one which led to an underestimation of the absolute rate constant for $O(^1D) + Kr$. The sets of experimental values were compared with the theoretical result obtained from a quantum close-coupling treatment of the quenching transition from the 1D state to the 3P_j fine-structure levels, where a modest quantitative agreement was reached but the temperature dependence of the rate constants was well described.⁸⁹

Regarding the experimental temperature dependence for the quenching process, we observe only a small variation of the rate constant in the 50 - 296 K temperature range with the values well within the error bars of the experiments. Then the rate constants for this quenching process are effectively temperature independent in the 50 - 296 K temperature range.

4.6. Astrochemical implications

While the reactions of oxygen atoms in their ground electronic state (^3P) have been extensively studied due to their importance in the chemistry of planetary atmospheres⁹⁰ and the interstellar medium,⁹¹ the reactions of oxygen atoms in their first excited electronic state (^1D) have received less attention over the years with most of the measurements performed at room temperature. In this chapter, reactive and non-reactive processes involving $\text{O}(^1\text{D})$ atoms have been studied to shed some light on the kinetics of these reactions at low temperature. The available kinetic data for all processes have been extended down to 50 K providing new experimental data for the improvement of astrochemical models. New data for the benchmark insertion reaction ($\text{O}(^1\text{D}) + \text{hydrogen isotopologues}$) have been obtained, opening a new chapter to further theoretical investigation of these reactions. Temperature dependent branching ratios for the formation of H-atoms have been provided for the reaction of $\text{O}(^1\text{D}) + \text{C}_2\text{H}_6$ with the aim to clarify the reaction mechanism and the nature of the products. The measured rate constants for the $\text{O}(^1\text{D}) + \text{CO}_2$ are seen to increase with decreasing temperature, which suggests that this quenching process is likely to be efficient in Mars's atmosphere. In all the cases, a careful analysis of the reaction mechanisms has been performed to characterize the most probable outcomes of these processes at low temperatures.

4.7. References

- (1) Streit, G. E.; Howard, C. J.; Schmeltekopf, A. L.; Davidson, J. A.; Schiff, H. I. Temperature dependence of O(¹D) rate constants for reactions with O₂, N₂, CO₂, O₃, and H₂O. *J. Chem. Phys.* **1976**, *65*, 4761–4764.
- (2) Bhardwaj, A.; Haider, S. A. Chemistry of O(¹D) Atoms in the Coma: Implications for Cometary Missions. *Adv. Sp. Res.* **2002**, *29*, 745–750.
- (3) Bergner, J.; Öberg, K. I.; Rajappan, M. Methanol Formation via Oxygen Insertion Chemistry in Ices. *Astrophys. J.* **2017**, *845*, 1–13.
- (4) Hays, B. M.; Wehres, N.; DePrince, B. A.; Roy, A. A. M.; Laas, J. C.; Weaver, S. L. W. Rotational Spectral Studies of O(¹D) Insertion Reactions with Methane and Ethylene : Methanol and Vinyl Alcohol in a Supersonic Expansion. *Chem. Phys. Lett.* **2015**, *630*, 18–26.
- (5) Schmidt, J. A.; Johnson, M. S.; Schinke, R. Carbon Dioxide Photolysis from 150 to 210 nm: Singlet and Triplet Channel Dynamics, UV-Spectrum, and Isotope Effects. *Proc. Natl. Acad. Sci.* **2013**, *110*, 17691–17696.
- (6) Grondin, R.; Loison, J.-C.; Hickson, K. M. Low Temperature Rate Constants for the Reactions of O(¹D) with N₂, O₂, and Ar. *J. Phys. Chem. A* **2016**, *120*, 4838–4844.
- (7) Hickson, K. M.; Suleimanov, Y. V. Low Temperature Experimental and Theoretical Rate Constants for the O(¹D) + H₂ Reaction. *J. Phys. Chem. A* **2017**, *121*, 1916–1923.
- (8) Talukdar, R. K.; Ravishankara, A. R. Rate Coefficients for O(¹D) + H₂, D₂, HD Reactions and H Atom Yield in O(¹D) + HD reaction. *Chem. Phys. Lett.* **1996**, *253*, 177–183.
- (9) Matsumi, Y.; Tonokura, K.; Kawasaki, M. Dynamics of the Reaction O(¹D) + HD, H₂, and D₂: Isotopic Branching Ratios and Translational Energy Release. *J. Phys. Chem* **1992**, *96*, 10622–10626.
- (10) Nuñez-Reyes, D.; Hickson, K. M.; Larrégaray, P.; Bonnet, L.; González-Lezana, T.; Suleimanov, Y. V. A Combined Theoretical and Experimental Investigation of the Kinetics and Dynamics of the O(¹D) + D₂ Reaction at Low Temperature. *Phys. Chem. Chem. Phys.* **2018**, *20*, 4404–4414.
- (11) González-Lezana, T. Statistical Quantum Studies on Insertion Atom-Diatom Reactions. *Int. Rev.*

- Phys. Chem.* **2007**, *26*, 29–91.
- (12) Smith, G. K.; Butler, J. E. OH ($X^2\Pi_i$) product internal energy distribution formed in the reaction of O(1D_2) with H₂. *J. Chem. Phys.* **1980**, *73*, 2243–2253.
- (13) Aker, P. M.; Sloan, J. J. The Initial Product Vibrational Energy Distribution in the Reaction Between O(1D_2) and H₂. *J. Chem. Phys.* **1986**, *85*, 1412–1417.
- (14) Schinke, R.; Lester, W. A. Trajectory Studies of O+H₂ Reactions on Fitted Ab Initio Surfaces. II. Singlet Case. *J. Chem. Phys.* **1980**, *72*, 3754–3766.
- (15) Whitlock, P. A.; Muckerman, J. T.; Fisher, E. R. Quasiclassical Trajectory Investigation of the Reaction O(1D)+H₂. *J. Chem. Phys.* **1982**, *76*, 4468–4489.
- (16) Berg, P. A.; Sloan, J. J.; Kuntz, P. J. The Effect of Reagent Excitation on the Dynamics of the Reaction O(1D_2)+H₂→OH($X^2\Pi$)+H. *J. Chem. Phys.* **1991**, *95*, 8038–8047.
- (17) Schatz, G. C.; Papaioannou, A.; Pederson, L. A.; Harding, L. B.; Hollebeek, T.; Ho, T. S.; Rabitz, H. A Global A-State Potential Surface for H₂O: Influence of Excited States on the O(1D)+H₂ Reaction. *J. Chem. Phys.* **1997**, *107*, 2340–2350.
- (18) Hsu, Y. T.; Liu, K.; Pederson, L. A.; Schatz, G. C. Reaction Dynamics of O(1D)+HD. I. The Insertion Pathway. *J. Chem. Phys.* **1999**, *111*, 7921–7929.
- (19) Alagia, M.; Balucani, N.; Cartechini, L.; Casavecchia, P.; Van Kleef, E. H.; Volpi, G. G.; Kuntz, P. J.; Sloan, J. J. Crossed Molecular Beams and Quasiclassical Trajectory Studies of the Reaction O(1D)+H₂(D₂). *J. Chem. Phys.* **1998**, *108*, 6698–6708.
- (20) Hsu, Y. T.; Wang, J. H.; Liu, K. Reaction Dynamics of O(1D)+ H₂, D₂, and HD: Direct Evidence for the Elusive Abstraction Pathway and the Estimation of its Branching. *J. Chem. Phys.* **1997**, *107*, 2351–2356.
- (21) Hermine, P.; Hsu, Y. T.; Liu, K.; Iams, M. S.; Sinica, A.; Box, P. O. A Crossed-Beam Study of the Reaction O(1D) + D₂: Collisional Energy Dependence of Differential Cross-Section. *Phys. Chem. Chem. Phys.* **2000**, *2*, 581–587.
- (22) Takayanagi, T. Nonadiabatic Quantum Reactive Scattering Calculations for the O(1D) + H₂, D₂, and HD Reactions on the Lowest Three Potential Energy Surfaces. *J. Chem. Phys.* **2002**, *116*,

2439–2446.

- (23) Aoiz, F. J.; Bañares, L.; Castillo, J. F.; Brouard, M.; Denzer, W.; Vallance, C.; Honvault, P.; Launay, J. M.; Dobbyn, A. J.; Knowles, P. J. Insertion and Abstraction Pathways in the Reaction $O(^1D_2) + H_2 \rightarrow OH + H$. *Phys. Rev. Lett.* **2001**, *86*, 1729–1732.
- (24) Liu, X.; Lin, J. J.; Harich, S. A.; Yang, X. State-to-State Dynamics for $O(^1D) + D_2 \rightarrow OD + D$: Evidence for a Collinear Abstraction Mechanism. *Phys. Rev. Lett.* **2001**, *86*, 408–411.
- (25) Aoiz, F. J.; Bañares, L.; Castillo, J. F.; Herrero, V. J.; Martínez-Haya, B. A Quasiclassical Trajectory and Quantum Mechanical Study of the $O(^1D)+D_2$ Reaction Dynamics. Comparison with High Resolution Molecular Beam Experiments. *Phys. Chem. Chem. Phys.* **2002**, *4*, 4379–4385.
- (26) Aoiz, F. J.; Bañares, L.; Castillo, J. F.; Herrero, V. J.; Martínez-Haya, B.; Honvault, P.; Launay, J. M.; Liu, X.; Lin, J. J.; Harich, S. A.; et al. The $O(^1D)+H_2$ Reaction at 56 meV Collision Energy: A comparison Between Quantum Mechanical, Quasiclassical Trajectory, and Crossed Beam Results. *J. Chem. Phys.* **2002**, *116*, 10692–10703.
- (27) Alexander, M. H.; Rackham, E. J.; Manolopoulos, D. E. Product Multiplet Branching in the $O(^1D) + H_2 \rightarrow OH(^2\Pi) + H$ reaction. *J. Chem. Phys.* **2004**, *121*, 5221–5235.
- (28) Lin, S. Y.; Guo, H. Adiabatic and Nonadiabatic State-to-State Quantum Dynamics for $O(^1D) + H_2(X^1\Sigma_g^+, v_i = j_i = 0) \rightarrow OH(X^2\Pi, v_f, j_f) + H(^2S)$ Reaction. *J. Phys. Chem. A* **2009**, *113*, 4285–4293.
- (29) Rivero-Santamaría, A.; González-Martínez, M. L.; González-Lezana, T.; Rubayo-Soneira, J.; Bonnet, L.; Larrégaray, P. The $O(^1D) + H_2(X^1\Sigma^+, v, j) \rightarrow OH(X^2\Pi, v', j') + H(^1S)$ Reaction at Low Collision Energy: when a Simple Statistical Description of the Dynamics Works. *Phys. Chem. Chem. Phys.* **2011**, *13*, 8136–8139.
- (30) Kauczok, S.; Maul, C.; Chichinin, A. I.; Gericke, K. H. Measurement of the Differential Cross Section of the Photoinitiated Reactive Collision of $O(^1D) + D_2$ using only one Molecular Beam: A Study by Three Dimensional Velocity mapping. *J. Chem. Phys.* **2010**, *132*, 244308.
- (31) Kuang, D.; Chen, T.; Zhang, W.; Zhao, N.; Wang, D. Effects of Reagent Rotation on Stereodynamics Information of the Reaction $O(^1D) + H_2(v=0, j=0-5) \rightarrow OH + H$: A Theoretical Study. *Bull. Korean Chem. Soc.* **2010**, *31*, 2841–2848.
- (32) Rio, C. M. A.; Brandao, J. Dynamical Studies and Product Analysis of $O(^1D) + H_2/D_2$ Reactions.

Mol. Phys. **2007**, *105*, 359–373.

- (33) Che, D. C.; Liu, K. Reactive Scattering of $O(^1D)+HD$: Product Speed and Angle Distributions. *J. Chem. Phys.* **1995**, *103*, 5164–5167.
- (34) Pradhan, G. B.; Balakrishnan, N.; Kendrick, B. K. Quantum Dynamics of $O(^1D)+D_2$ Reaction: Isotope and Vibrational Excitation Effects. *J. Phys. B At. Mol. Opt. Phys.* **2014**, *47*, 135202.
- (35) Sun, Z.; Lin, S. Y.; Zheng, Y. Adiabatic and Non-Adiabatic Quantum Dynamics Calculation of $O(^1D) + D_2 \rightarrow OD + D$ reaction. *J. Chem. Phys.* **2011**, *135*, 234301.
- (36) Davidson, J. A.; Schiff, H. I.; Streit, G. E.; McAfee, J. R.; Schmeltekopf, A. L.; Howard, C. J. Temperature dependence of $O(^1D)$ rate constants for reactions with N_2O , H_2 , CH_4 , HCl , and NH_3 . *J. Chem. Phys.* **1977**, *67*, 5021–5025.
- (37) Blitz, M. A.; Dillon, T. J.; Heard, D. E.; Pilling, M. J.; Trought, I. D. Laser Induced Fluorescence Studies of the Reactions of $O(^1D_2)$ with N_2 , O_2 , N_2O , CH_4 , H_2 , CO_2 , Ar , Kr , and $n-C_4H_{10}$. *Phys. Chem. Chem. Phys.* **2004**, *6*, 2162–2171.
- (38) Vranckx, S.; Peeters, J.; Carl, S. Kinetics of $O(^1D) + H_2O$ and $O(^1D) + H_2$: Absolute Rate Coefficients and $O(^3P)$ Yields Between 227 and 453 K. *Phys. Chem. Chem. Phys.* **2010**, *12*, 9213–9221.
- (39) Heidner, R. F.; Husain, D. Electronically Excited Oxygen Atoms, $O(^2D_2)$. A Time-Resolved Study of the Collisional Quenching by the Gases H_2 , D_2 , NO , N_2O , NO_2 , CH_4 and C_3O_2 Using At. *Int. J. Chem. Kinet.* **1973**, *5*, 819–831.
- (40) Koppe, S.; Laurent, T.; Naik, P. D.; Volpp, H. R.; Wolfrum, J.; Arusi-Parpar, T.; Bar, I.; Rosenwaks, S. Absolute Rate Constants and Reactive Cross Sections for the Reactions of $O(^1D)$ with Molecular Hydrogen and Deuterium. *Chem. Phys. Lett.* **1993**, *214*, 546–552.
- (41) Laurent, T.; Naik, P. D.; Volpp, H. R.; Wolfrum, J.; Arusi-Parpar, T.; Bar, I.; Rosenwaks, S. Absolute Rate Constants, Reactive Cross-Sections and Isotopic Branching Ratio for the Reaction of $O(^1D)$ with HD . *Chem. Phys. Lett.* **1995**, *236*, 343–349.
- (42) Nuñez-Reyes, D.; Hickson, K. M.; Larrégaray, P.; Bonnet, L.; González-Lezana, T.; Suleimanov, Y. V. A Combined Theoretical and Experimental Investigation of the Kinetics and Dynamics of the $O(^1D) + D_2$ Reaction at Low Temperature. *Phys. Chem. Chem. Phys.* **2018**, *20*, 4404–4414.

- (43) Tsukiyama, K.; Katz, B.; Bersohn, R. Isotopic Branching Ratio for the Reaction $A+HD\rightarrow AD(H)+H(D)$. *J. Chem. Phys.* **1985**, *83*, 2889–2893.
- (44) Nguyen, T. L.; Stanton, J. F. Accurate Ab Initio Thermal Rate Constants for Reaction of $O(^3P)$ with H_2 and Isotopic Analogues. *J. Phys. Chem. A* **2014**, *118*, 4918–4928.
- (45) Pradhan, G. B.; Balakrishnan, N.; Kendrick, B. K. Ultracold Collisions of $O(^1D)$ and H_2 : The Effects of H_2 Vibrational Excitation on the Production of Vibrationally and Rotationally Excited OH. *J. Chem. Phys.* **2013**, *138*, 164310.
- (46) Cui-Xia, Y.; Guang-Jiu, Z. Quasiclassical Trajectory Theoretical Study on the Chemical Stereodynamics of the $O(^1D)+H_2\rightarrow OH+H$ Reaction and its Isotopic Variants (HD, D_2). *Chin. Phys. B* **2013**, *22*, 083403.
- (47) Rio, C. M. A.; Brandão, J. The Branching Ratio of the $O(^1D) + HD$ Reaction: A Dynamical Study. *Chem. Phys. Lett.* **2007**, *433*, 268–274.
- (48) Fitzcharles, M. S.; Schatz, G. C. A Theoretical Study of Complex Formation, Isotope Effects, and Energy Partitioning in the $O(^1D) + H_2, (D_2, HD)$ Reaction. *J Phys Chem* **1986**, No. 9, 3634–3644.
- (49) Hankel, M.; Balint-Kurti, G. G.; Gray, S. K. Quantum Mechanical Calculation of Reaction Probabilities and Branching Ratios for $O(^1D)+HD \rightarrow OH(OD)+D(H)$ Reaction on the X^1A' and $1^1A''$ Adiabatic Potential Energy Surface. *J. Phys. Chem. A* **2001**, *105*, 2330–2339.
- (50) Yamazaki, H.; Cvetanovic, R. J. Collisional Deactivation of the Excited Singlet Oxygen Atoms and Their Insertion into the CH Bonds of Propane. *J. Chem. Phys.* **1964**, *41*, 3703–3710.
- (51) Dillon, T. J.; Horowitz, A.; Crowley, J. N. Absolute Rate Coefficients for the Reactions of $O(^1D)$ with a Series of n-alkanes. *Chem. Phys. Lett.* **2007**, *443*, 12–16.
- (52) Wiesenfeld, R. Atmospheric Chemistry Involving Electronically Excited Oxygen Atoms. *Acc. Chem. Res.* **1982**, *15*, 110–116.
- (53) Dunlea, E. J.; Ravishankara, A. R. Kinetic Studies of the Reactions of $O(^1D)$ with Several Atmospheric Molecules. *Phys. Chem. Chem. Phys.* **2004**, *6*, 2152–2161.
- (54) Gonzalez, M.; Puyuelo, P.; Hernando, J.; Sayo, R.; Enrı, P. A.; Guallar, J. Influence of Collision Energy on the Nascent OH ($X^2 \Pi, v'' = 0-4$) Product Energetics for the Reaction of $O(^1D)$ with

- Ethane . A Laser-Induced Fluorescence and Quasiclassical Trajectory Study. *J. Phys. Chem A* **2001**, *105*, 9834–9844.
- (55) Shu, J.; Lin, J. J.; Lee, Y. T.; Yang, X. A Complete Look at a Multiple Pathway Reaction : The Reaction of O(¹D) with Ethane. *J. Chem. Phys.* **2001**, *114*, 4–7.
- (56) Shu, J.; Lin, J. J.; Lee, Y. T.; Yang, X. Multiple Pathway Dynamics of the O(¹D) + C₂H₆ Reaction : A Crossed Beam Study. *J. Chem. Phys.* **2001**, *115*, 849–857.
- (57) Shu, J.; Lin, J. J.; Lee, Y. T.; Yang, X. A Crossed Molecular Beam Study of the O(¹D) + C₃H₈ Reaction : Multiple Reaction Pathways. *J. Am. Chem.Soc* **2001**, *127*, 322–330.
- (58) Lin, J. J.; Shu, J.; Lee, Y. T.; Yang, X. Multiple Dynamical Pathways in the O(¹D) + CH₄ Reaction : A Comprehensive Crossed Beam Study. *J. Chem. Phys.* **2000**, *113*, 5287–5301.
- (59) Lin, J. J.; Harich, S.; Lee, Y. T.; Yang, X. Dynamics of the O(¹D) + CH₄ Reaction : Atomic Hydrogen Channel vs Molecular Hydrogen Channel. *J. Chem. Phys.* **1999**, *110*, 10821–10829.
- (60) Lin, J. J.; Lee, Y. T.; Yang, X. Crossed Molecular Beam Studies of the O(¹D) + CH₄ Reaction: Evidences for the CH₂OH + H Channel. *J. Chem. Phys.* **1998**, *109*, 2975–2978.
- (61) Meng, Q.; Hickson, K. M.; Shao, K.; Loison, J.-C.; Zhang, D. H. Theoretical and Experimental Investigations of Rate Coefficients of O(¹D) + CH₄ at Low Temperature. *Phys. Chem. Chem. Phys.* **2016**, *18*, 29286–29292.
- (62) Schott, R.; Schlütter, J.; Olzmann, M.; Kleinermanns, K. CH₃ State Distributions Form the Reactions of O(¹D) with Saturated and Chlorinated Hydrocarbons. *J. Chem. Phys.* **1995**, *102*, 8371–8377.
- (63) Brownsword, R. A.; Hillenkamp, M.; Schmiechen, P.; Volpp, H. Absolute Reactive Cross Section for H Atom Formation in the Reaction of Translationally Energetic O(¹D) Atoms with Methane. *J. Phys. Chem A* **1998**, *102*, 4438–4443.
- (64) Kurosaki, Y.; Takayanagi, T. Ab Initio Molecular Orbital Study of the O(¹D) Insertion into the C – C Bond in Cyclopropane and Ethane. *Chem. Phys. Lett.* **2002**, *355*, 424–430.
- (65) Hack, W.; Thiesemann, H. Absolute Determination of the Decomposition Pathways of Electronic Chemically Activated Methanol. *J. Phys. Chem* **1995**, *99*, 17364–17371.

- (66) Sun, Y.; Wang, I.; Nguyen, T. L.; Lu, H.; Yang, X.; Mebel, A. M. A Combined Quantum Chemistry and RRKM Calculation Predicts the $O(^1D) + C_2H_6$ Reaction can Produce Water Molecule in a Collision-Free Crossed Molecular Beam Environment. *J. Phys. Chem A* **2003**, *107*, 6986–6994.
- (67) Park, C. R.; Wiesenfeld, J. R. Full Characterization of OH Product Energetics in the Reaction of $O(^1D_2)$ with Hydrocarbons. *J. Chem. Phys.* **1991**, *95*, 8166–8177.
- (68) Yang, X. Multiple Channel Dynamics in the $O(^1D)$ Reaction with Alkanes. *Phys. Chem. Chem. Phys.* **2006**, *8*, 205–215.
- (69) Schofield, K. Rate Constants for the Gaseous Interactions of $O(^1D)$ and $O(^1S)$. A Critical Evaluation. *J. Photochem.* **1978**, *9*, 55–68.
- (70) Matsumi, Y.; Tonokura, K.; Inagaki, Y.; Kawasaki, M. Isotopic Branching Ratios and Translational Energy Release of H and D Atoms in Reaction of $O(^1D)$ Atoms with Alkanes and Alkyl Chlorides. *J. Phys. Chem* **1993**, *97*, 6816–6821.
- (71) Girard, Y.; Chaquin, P. Addition Reactions of 1D and 3P Atomic Oxygen with Acetylene . Potential Energy Surfaces and Stability of the Primary Products . Is Oxirene Only a Triplet Molecule ? A Theoretical Study. *J. Phys. Chem A* **2003**, *107*, 10462–10470.
- (72) Xiao, H.; Maeda, S.; Morokuma, K. CASPT2 Study of Photodissociation Pathways of Ketene. *J. Phys. Chem. A* **2013**, *117*, 7001–7008.
- (73) Fockenberg, C. Product Study of the Photolysis of Ketene and Ethyl Ethynyl Ether at 193 . 3 nm. *J. Phys. Chem. A* **2005**, *109*, 7140–7150.
- (74) Rajak, K.; Maiti, B. Communications : Direct Dynamics Study of the $O(^3P) + C_2H_2$ Reaction: Contribution from Spin Nonconserving Route. *J. Chem. Phys.* **2010**, *113*, 1–4.
- (75) Rajak, K.; Maiti, B. Trajectory Surface Hopping Study of the $O(^3P) + C_2H_2$ Reaction Dynamics : Effect of Collision Energy on the Extent of Intersystem Crossing. *J. Chem. Phys.* **2014**, *140*, 1–8.
- (76) Carl, S. A. A Highly Sensitive Method for Time-Resolved Detection of $O(^1D)$ Applied to Precise Determination of Absolute $O(^1D)$ Reaction Rate Constants and $O(^3P)$ Yields. *Phys. Chem. Chem. Phys.* **2005**, *7*, 4051–4053.
- (77) Baulch, D. L.; Bowman, C. T.; Cobos, C. J.; Cox, R. A.; Just, T.; Kerr, J. A.; Pilling, M. J.; Stocker, D.;

- Troe, J.; Tsang, W.; et al. Evaluated Kinetic Data for Combustion Modeling : Supplement II. *J Phys Chem Ref Data* **2005**, *34*, 757–1397.
- (78) Gannon, K. L.; Blitz, M. A.; Liang, C. H.; Pilling, M. J.; Seakins, P. W.; Glowacki, D. R. Temperature Dependent Kinetics (195 - 798 K) and H Atom Yields (298 - 498 K) from Reactions of $^1\text{CH}_2$ with Acetylene, Ethene, and Propene. *J. Phys. Chem A* **2010**, *114*, 9413–9424.
- (79) Gannon, K. L.; Blitz, M. A.; Liang, C.; Pilling, M. J.; Seakins, P. W.; Glowacki, R.; Harvey, J. N. An Experimental and Theoretical Investigation of the Competition Between Chemical Reaction and Relaxation for the Reactions of $^1\text{CH}_2$ with Acetylene and Ethene : Implications for the Chemistry of the Giant Planets. *Faraday Discuss.* **2010**, *147*, 1–16.
- (80) Mebel, A. M.; Hayashi, M.; Kislov, V. V.; Lin, S. H. Theoretical Study of Oxygen Isotope Exchange and Quenching in the $\text{O}(^1\text{D}) + \text{CO}_2$ Reaction. *J. Phys. Chem. A* **2004**, *108*, 7983–7994.
- (81) Wine, P. H.; Ravishankara, A. R. Kinetics of $\text{O}(^1\text{D})$ interactions with the atmospheric gases N_2 , N_2O , H_2O , H_2 , CO_2 , and O_3 . *Chem. Phys. Lett.* **1981**, *77*, 103–109.
- (82) Young, R. A.; Black, G.; Slinger, T. G. Reaction and Deactivation of $\text{O}(^1\text{D})$. *J. Chem. Phys.* **1968**, *49*, 4758–4768.
- (83) Shi, J.; Barker, J. R. Kinetic studies of the deactivation of $\text{O}_2(^1\Sigma_g^+)$ and $\text{O}(^1\text{D})$. *Int. J. Chem. Kinet.* **1990**, *22*, 1283–1301.
- (84) Amimoto, S. T.; Force, A. P.; Gulotty, R. G.; Wiesenfeld, J. R. Collisional Deactivation of $\text{O}(2^1\text{D}_2)$ by the Atmospheric Gases. *J. Chem. Phys.* **1979**, *71*, 3640–3647.
- (85) Shortridge, R. G.; Lin, M. C. Co Vibrational Population Distribution in the Reactions of COS with $\text{O}(^3\text{P}_j)$ and $\text{O}(^1\text{D}_2)$ Atoms. *Chem. Phys. Lett.* **1975**, *35*, 146–150.
- (86) Sedlacek, A. J.; Harding, D. R.; Weston, R. E.; Kreutz, T. G.; Flynn, G. W. Probing the $\text{O}(^1\text{D})+\text{CO}_2$ Reaction with Second-Derivative Modulated Diode Laser Spectroscopy. *J. Chem. Phys.* **1989**, *91*, 7550–7556.
- (87) Heidner, R. F.; Husain, D. A Study of the Collisional Quenching of $\text{O}(2^1\text{D}_2)$ by the Noble Gases Employing Time-Resolved Attenuation of Atomic Resonance Radiation in the Vacuum Ultraviolet. *Int. J. Chem. Kinet.* **1974**, *6*, 77–87.

- (88) Davidson, J. A.; Schiff, H. I.; Brown, T. J.; Streit, G. E.; Howard, C. J. Rate Constants for the Deactivation of O(¹D) by Xe, Kr, and Ar over the Range 110-330 K. *J. Chem. Phys.* **1978**, *69*, 1213–1215.
- (89) Nuñez-Reyes, D.; Kłos, J.; Alexander, M. H.; Dagdigan, P. J.; Hickson, K. M. Experimental and Theoretical Investigation of the Temperature Dependent Electronic Quenching of O(¹D) Atoms in Collisions with Kr. *J. Chem. Phys.* **2018**, *148*, 124311.
- (90) Stock, J. W.; Boxe, C. S.; Lehmann, R.; Grenfell, J. L.; Patzer, B. A. C.; Rauer, H.; Yung, Y. L. Chemical Pathway Analysis of the Martian Atmosphere: CO₂-Formation Pathways. *Icarus* **2012**, *219*, 13–24.
- (91) Agúndez, M.; Wakelam, V. Chemistry of Dark Clouds: Databases, Networks, and Models. *Chem. Rev.* **2013**, *113*, 8710–8737.

Chapter 5.

A viable source of $N(^2D)$ atoms for kinetic studies at low temperature

5.1	Introduction	175
5.2	Experimental details	177
5.2.1	Temperature range	177
5.2.2	Production and detection of $N(^2D)$ atoms	178
5.2.3	Influence of secondary reactions	179
5.2.4	Experimental details of the $N(^2D)$ + alkanes reactions	179
5.2.5	Gases	180
5.3	The $N(^2D)$ + NO reaction	180
5.3.1	Results	181
5.3.2	Discussion	184
5.4	The $N(^2D)$ + alkanes (C_nH_{2n+2}) reactions	185
5.4.1	Results	187
5.4.2	Discussion	192
5.5	Astrochemical implications	196
5.6	References	197

5. A viable source of $N(^2D)$ atoms for kinetic studies at low temperature

There are several studies of the kinetics of $N(^2D)$ atom reactions at room temperature given to its role in the production of NO in the Earth's atmosphere. However, there is a lack of kinetic information at temperatures of astrochemical interest given the difficulty to find a clean source for producing $N(^2D)$ atoms. In this chapter, $N(^2D)$ atoms were produced by a combination of PLP and chemical reaction opening up a new pathway to study the kinetics of metastable $N(^2D)$ atom reactions at low temperature.

5.1. Introduction

The reactions of electronically excited nitrogen atoms play important roles in plasmas, in Earth's atmospheric chemistry and in astrochemistry.¹ $N(^2D)$ is produced in the terrestrial upper atmosphere by a variety of photochemical and ionospheric process.² The reaction of $N(^2D)$ with O_2 is considered to be the major source of NO and $O(^1D)$ atoms in Earth's lower thermosphere.³ N_2 is the main constituent of Titan's atmosphere⁴ and the second most abundant species in the Martian atmosphere,⁵ consequently, the reactions of N-atoms are expected to be important processes in the photochemistry of these planets.

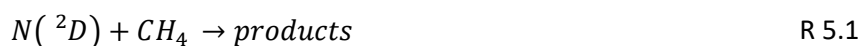
As N_2 is characterized by a strong triple bond with an associated dissociation energy of 941.7 kJ/mol neutral-neutral chemical reactions involving N-N cleavage are rare.⁶ Then the main source of atomic nitrogen in Earth and Titan's atmospheres is N_2 dissociation induced by vacuum ultraviolet photolysis, electron impact, dissociative photoionization and N_2^+ dissociative recombination.⁷ The photodissociation of N_2 molecules produces $N(^4S)$, $N(^2D)$ and $N(^2P)$ with a 50% yield of the ground state atoms and a 50% yield of $N(^2D) + N(^2P)$.⁴

In the Martian atmosphere, $N(^4S)$ atoms are lost mainly through reaction with NO to produce N_2 and atomic oxygen while the $N(^2P)$ atoms are lost by quenching to produce $N(^2D)$. The major losses of the metastable $N(^2D)$ atoms are reaction with CO_2 to form $NO + CO$ ⁷ and quenching to the ground state by collisions with atomic oxygen.⁸

In Titan's atmosphere the excited states ($N(^2D)$ and $N(^2P)$) have lifetimes much longer than the time between collisions (~ 1 s at 1000 km).⁴ Furthermore, while the excited metastable atoms are reactive with stable molecules such as saturated and unsaturated hydrocarbons, the ground state $N(^4S)$ is mostly unreactive, with the main loss channels being reactions with hydrocarbon radicals such as CH_3 ,

CH₂, C₂H₃ and C₂H₅. The N(²P) state is much less reactive with stable molecules than the N(²D) state displaying rate constants lower by several orders of magnitude.⁴ In addition, N(²P) collisions with some of the major constituents N₂, H₂ and hydrocarbons result in quenching to produce the N(²D) state.⁶ Then taking into account the N(²D) atom radiative lifetime (13.6 and 36.7 hours for the two substates ²D_{3/2} and ²D_{5/2} respectively) and its slow collisional deactivation with N₂ (1.7 x 10⁻¹⁴ cm³ s⁻¹ at room temperature⁴) the main fate of these metastable atoms is chemical reaction with other constituents of Titan's atmosphere. Actually, the reactions of N(²D) with various saturated and unsaturated hydrocarbons are considered to be among the major production sources of N-bearing molecules in Titan's atmosphere.^{9,10}

The abundance and distribution of nitrogen atoms in astrochemical environments are predicted by photochemical models. Recently, Loison and coworkers⁶ have made a careful investigation of the neutral nitrogen photochemistry in Titan's atmosphere to improve the current chemical schemes used in photochemical models. For this investigation, they included the most abundant species and the most efficient reactions. In their 1D photochemical model, they studied the propagation of uncertainties on the rate constants and determined the key reactions from a global sensitivity analysis. These authors promote the necessity of experimental or theoretical studies to provide a better estimation of the reaction rates and the branching ratios for several reactions like R 5.1, R 5.2, R 5.3 among others.



On the experimental side, while studies of the N(²D) atoms kinetics at room temperature are quite abundant due to its atmospheric importance,¹¹⁻¹⁶ studies where the metastable N(²D) atoms are obtained photolytically are scarce due to :

- ✓ Convenient photolytic sources of N(²D) are very rare.
- ✓ A high energy radiation source is necessary to cleave the multiple bonds in which nitrogen atoms are bound to other atoms.
- ✓ The production of electronically excited nitrogen atoms without other interfering states or species present a great difficulty.

On the detection side

- ✓ The high reactivity of the resulting nitrogen atoms produced in low concentrations makes its detection difficult.
- ✓ The radiative transition from the 2D state to the ground 4S state is too weak to be detected in the visible region.

In 1969, Black et al.¹¹ produced $N(^2D)$ and $N(^2P)$ from the VUV-photolysis of N_2O at 147 nm using pulsed Ar and Xe resonance lamps. These authors followed the reaction kinetics of $N(^2D)$ with several molecules at room temperature, measuring the attenuation of NO chemiluminescence emission ($B^2\Pi > X^2\Pi$) produced by the reaction between $N(^2D) + N_2O$ as a chemical tracer. In the 1970s, Husain et al.^{13,14} studied the collisional quenching of $N(^2D)$ with several molecules at room temperature, producing the $N(^2D)$ and $N(^2P)$ by flash photolysis of N_2O at wavelengths greater than 105 nm and detecting them by time-resolved atomic absorption spectroscopy in the vacuum ultraviolet. More recently, in 1998, Umemoto et al.¹⁶ studied $N(^2D)$ deactivation with hydride and deuteride molecules at room temperature. These authors produced $N(^2D)$ by multiphoton dissociation of NO by focusing a tuneable laser at 275.3 nm into their reactor and detected them by VUV fluorescence at 149 nm.

In general, the chemistry of nitrogen species is very rich in planetary atmospheres although it is only poorly understood at the present time because very few data are available under physical conditions relevant to planetary atmospheres. To solve this issue, in this chapter, we report a new source of $N(^2D)$ atom production that will allow the experimental study of several key reactions to improve the photochemical models and their prediction of the abundance and distribution of molecules in low temperature environments. In addition, the kinetics of the $N(^2D) + NO$, CH_4 , C_2H_6 and C_3H_8 reactions have been studied for the first time over the 50 - 296 K, temperature range setting the basis for the future study of other key $N(^2D)$ atom reactions.

5.2. Experimental details

5.2.1. Temperature range

In this chapter, the kinetics of the $N(^2D)$ atoms reactions with several molecules in the gas-phase have been studied in the mini-CRESU setup of Bordeaux. Three Laval nozzles (Mach2 N_2 , Mach3 Ar and Mach4 Ar) have been used to study the reactions in the temperature range 50 - 177 K. The characteristics of the supersonic flows produced by each of these Laval nozzles are listed in Table 2.2. In this study, it was possible to use both Ar and N_2 as a carrier gases given the slow rate constants for the quenching reactions $N(^2D) + N_2$ and $N(^2D) + Ar$.¹² Experiments at room temperature were performed

by removing the Laval nozzle and lowering the velocity of the flow, using the CRESU chamber as a slow flow reactor.

5.2.2. Production and detection of N(²D) atoms

During this thesis, the experiments involving C(¹D), C(³P) and O(¹D) have been performed by producing the minor reagent in situ via photolysis of a suitable precursor. However, in the case of N(²D) atoms there are no known suitable precursor molecules that can be photolysed in the UV wavelength range, except through multiphoton processes such as photodissociation of NO at 275.3 nm.¹⁶ Unfortunately, we cannot use this multiphoton dissociation as a production method due to the necessity to produce a uniform density of radicals along the length of the supersonic flow.

Instead, N(²D) atoms were generated through the reaction of ground state atomic carbon with NO molecules:



The dynamics and kinetics of reaction R 5.4 have been extensively studied experimentally and theoretically. The Birmingham continuous CRESU apparatus operated by Sims and coworkers¹⁷ was used to determine the rate constant for this reaction over the temperature range 15 - 295 K. These authors found rate constants that increase as the temperature is lowered from $(1.2 \pm 0.1) \times 10^{-10} \text{ cm}^3 \text{ s}^{-1}$ at 295 K to $(2.3 \pm 0.2) \times 10^{-10} \text{ cm}^3 \text{ s}^{-1}$ at 15 K. The ratio for the two exit channels $[N(^2D) + N(^4S)]/[O(^3P)]$ was estimated to be 1.5 ± 0.3 at room temperature using a low pressure fast flow reactor.¹⁸ The theoretical work of Andersson et al.¹⁹ using quasiclassical trajectory calculations in the temperature range 5 - 5000 K predicts that the importance of channel R 5.4 (a) should decrease as the temperature falls.

Ground state atomic carbon, C(³P), was generated by the 10 Hz pulsed sequential multiphoton dissociation of CBr₄ precursor at 266 nm with pulse energies around 24 mJ. The photolysis laser was aligned along the axis of the flow to produce a column of C(³P) atoms with uniform density. CBr₄ was introduced in the flow by flowing a small fraction of the carrier gas over solid CBr₄ contained in a flask at 296 K. The concentration of CBr₄ was calculated using expressions 2.28 and 2.35 yielding concentrations in the supersonic flow lower than $3.2 \times 10^{13} \text{ cm}^{-3}$ for all the temperatures studied. The photolysis of CBr₄ produces C(³P) and C(¹D) as well as other fragments: CBr₃, CBr₂, CBr, Br₂, Br, etc.^{20,21} Previous studies²² under similar conditions in our laboratory have determined that C(³P) is the major product between the two electronic states of atomic carbon. Although the production of C(¹D) is non

negligible, the rate constants for the reaction of $C(^1D) + NO$ are smaller than those of the equivalent ground state carbon reaction²³ and the products are likely to be similar to those of the $C(^3P) + NO$ reaction with the added possibility of $O(^1D)$ formation as a spin-allowed product. The secondary reactions of the fragments CBr_3 , CBr_2 , CBr , Br_2 and Br are unlikely to produce $N(^2D)$ atoms, consequently they are not thought to interfere with the measurements as $N(^2D)$ atoms were detected directly as described below.

The kinetics of $N(^2D)$ atoms reactions was followed by on-resonance VUV LIF through the $2s^22p^3\ 2D^\circ - 2s^22p^2(^3P)\ 3d\ ^2F$ transition at 116.745 nm. To obtain tuneable light at this wavelength, the 700.5 nm output of a pulsed tuneable dye laser was first injected into a BBO crystal to generate the second harmonic at a wavelength around 350.24 nm with a pulse energy of approximately 8 mJ. Subsequently, the UV beam was separated from the fundamental radiation and focused into a cell containing 40 torr of xenon and 560 torr of Ar, the latter added for phase matching, generating VUV light through frequency tripling. As the VUV emission from the excited $N(^2D)$ atoms is small compared with our previous studies of $O(^1D)$, $C(^3P)$ and $H(^2S)$ atoms, the PMT output was fed into a fast preamplifier, which was connected to a boxcar module for signal processing and integration.

5.2.3. Influence of secondary reactions

The presence of several atoms or molecules in the reactor such as the photolysis products or the secondary products of reaction R 5.4 made it necessary to perform an analysis of potential secondary reactions that might affect the kinetics determination. As $N(^2D)$ atoms are followed directly during these experiments, we need to specifically consider secondary processes which could form or remove $N(^2D)$ atoms. For example, $O(^1D)$ atoms and CN radicals are potentially formed from the $C(^1D) + NO$ reaction (with $C(^1D)$ produced during the photolysis of CBr_4) and these products could potentially interfere with our kinetic determinations. However, the reaction of $O(^1D) + NO$ has only one exothermically available channel ($N(^4S) + O_2$) which is only accessible by non-adiabatic transitions.²⁴ Furthermore, the reaction of CN radicals with NO has been studied in the temperature range 294 - 761 K showing results consistent with an association reaction while removing the possibility of the non-associative exit channel yielding $CO + N_2$ products.²⁵ In addition, $O(^3P)$ is a product from R 5.4, while its association reaction with NO is expected to be slow.²⁶ Then neither of the above mentioned secondary processes should influence the $N(^2D)$ measurements.

5.2.4. Experimental details of the $N(^2D)$ + alkanes reactions

The production of $N(^2D)$ atoms is a coupled process including the reaction of $C(^3P)$ atoms with NO to produce $N(^2D)$ (R 5.4) and the subsequent depletion of $N(^2D)$ through its reaction with NO. However, it

is possible to use this production method to study the reactions of N(²D) with molecules of astrochemical interest, particularly when these molecules do not react with C(³P) which is our source of N(²D) atoms. In this case, the yield of N(²D) atoms will remain relatively unaffected by the addition of these molecules to the supersonic flow. Then if the NO concentration is maintained at a constant and small value, it is possible to extract pseudo-first-order rate constants for the specific molecule reaction by varying its excess concentration.

Here the pseudo-first-order rate constant can be expressed as

$$k' = k_{N(^2D)+NO}[NO] + k_{N(^2D)+X}[X] + k_{L(N(^2D))} \quad (5.1)$$

where $k_{N(^2D)+NO}[NO]$ represents the pseudo-first-order loss rate of N(²D) through reaction with NO, $k_{N(^2D)+X}[X]$ is the pseudo-first-order loss rate of N(²D) through reaction with the molecule of astrochemical interest (CH₄, C₂H₆ and C₃H₈ in this instance) and $k_{L(N(^2D))}$ represents the first-order losses of N(²D) (mostly by diffusion from the probe volume).

Then from a plot of k' (obtained at different concentrations of the alkane and at a fixed NO concentration) against the concentration of the alkane, the second-order rate constants for the N(²D) + alkane process can be obtained from the slope as explained in Chapter 2. The intercept of this plot corresponds to the term $k_{N(^2D)+NO}[NO]$ assuming that the diffusional losses are small in comparison.

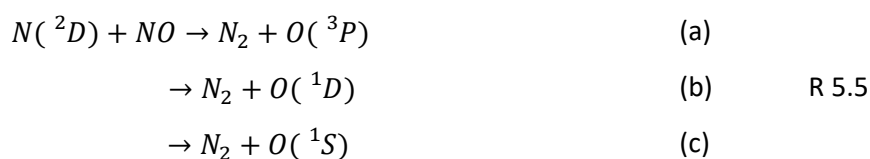
5.2.5. Gases

The gases were flowed directly from cylinders with no further purification prior use. The suppliers and purities are:

- ✓ Linde Ar (99.999%), Xe (99.999%), CH₄ (99.9995%), C₂H₆ (99.5%), C₃H₈ (99.5%)
- ✓ Air Liquide N₂ (99.999%), NO (99.9%)

5.3. The N(²D) + NO reaction

One of the reactions that has attracted significant experimental and theoretical attention in the past given its importance for atmospheric chemistry is the reaction between N(²D) and NO.



On the experimental side, there are several previous kinetics measurements¹¹⁻¹⁶ at room temperature with the rate constants in the range $(0.4 - 1.8) \times 10^{-10} \text{ cm}^3 \text{ s}^{-1}$ and a recommended value of $6.0 \times 10^{-11} \text{ cm}^3 \text{ s}^{-1}$.¹ As far as we know, there are no previous studies of this reaction at lower temperatures. Regarding the equivalent reactions for other electronic states: the $\text{N}(^2\text{P}) + \text{NO}$ reaction has a recommended rate constant value¹ at room temperature of $2.9 \times 10^{-11} \text{ cm}^3 \text{ s}^{-1}$ and no exothermic adiabatic pathways to products.²⁴ Thus physical quenching leading to $\text{N}(^2\text{D})$ is likely to be the only important process at low temperatures. The reaction of ground state $\text{N}(^4\text{S})$ atoms with NO has already been studied in the mini-CRESU setup of Bordeaux displaying a small negative temperature dependence with a rate constant decreasing from $(5.8 \pm 0.3) \times 10^{-11} \text{ cm}^3 \text{ s}^{-1}$ at 48 K to $(3.3 \pm 0.2) \times 10^{-11} \text{ cm}^3 \text{ s}^{-1}$ at 211 K.²⁷

On the theoretical side, Gonzalez et al.²⁸ performed ab initio CASSCF/CASPT2 electronic structure calculations of the ground $^1\text{A}'$ potential energy surface coupled with quasiclassical trajectory (QCT) calculations to obtain the rate constants for the exit channel R 5.5 (b) in the temperature range 300 - 1500 K. These authors found rate constants that decrease as the temperature is lowered down to 300 K. More recently, Li et al.²⁹ have performed quasiclassical trajectory calculations using a double many-body expansion potential energy surface for ground state N_2O ($^1\text{A}'$) with an accurate description of the long-range interactions to determine the rate constants for the channel R 5.5 (b) over the temperature range 5 - 3000 K. However, they determined rate constants that decrease slightly with temperature, in contrast with the previous work by Gonzalez et al.²⁸

5.3.1. Results

To apply the pseudo-first-order approximation, NO was maintained in excess with respect to $\text{C}(^3\text{P})$ atoms. Under these conditions, $\text{N}(^2\text{D})$ atoms are formed by R 5.4 (a) and consumed by R 5.5. Then the $\text{N}(^2\text{D})$ VUV LIF signal should take the form of a biexponential function according to expression (2.9). However, the $\text{N}(^2\text{D})$ VUV LIF signal levels were small compared with our previous studies of $\text{C}(^3\text{P})$, $\text{H}(^2\text{S})$ and $\text{O}(^1\text{D})$ reaction kinetics. As a result, it was necessary to amplify the PMT output signal using a fast preamplifier as stated previously. Although the PMT should have been insensitive to radiation in the UV range, with an expected cutoff around 200 nm, scattered light and/or window fluorescence generated by the photolysis laser lead to a saturation of the PMT for the first 15 microseconds after the photolysis laser pulse. Consequently, the $\text{N}(^2\text{D})$ signal could not be recorded near zero making it impossible to record the rising part of the biexponential curve (pseudo-first-order decays for the highest and the lowest concentration of NO at 50 K and 296 K are presented in *Figure 5.1*). In this case, to obtain the pseudo-first-order rate constants, the curves were fitted according to a single exponential (expression 2.5). To perform the fits, the starting point was chosen carefully to avoid fitting to the rising

part of the temporal profiles. In practice, this was achieved by displaying the signals on a logarithmic scale and by carefully selecting only the linear part of the decay curves as shown in the bottom panels of *Figure 5.1*.

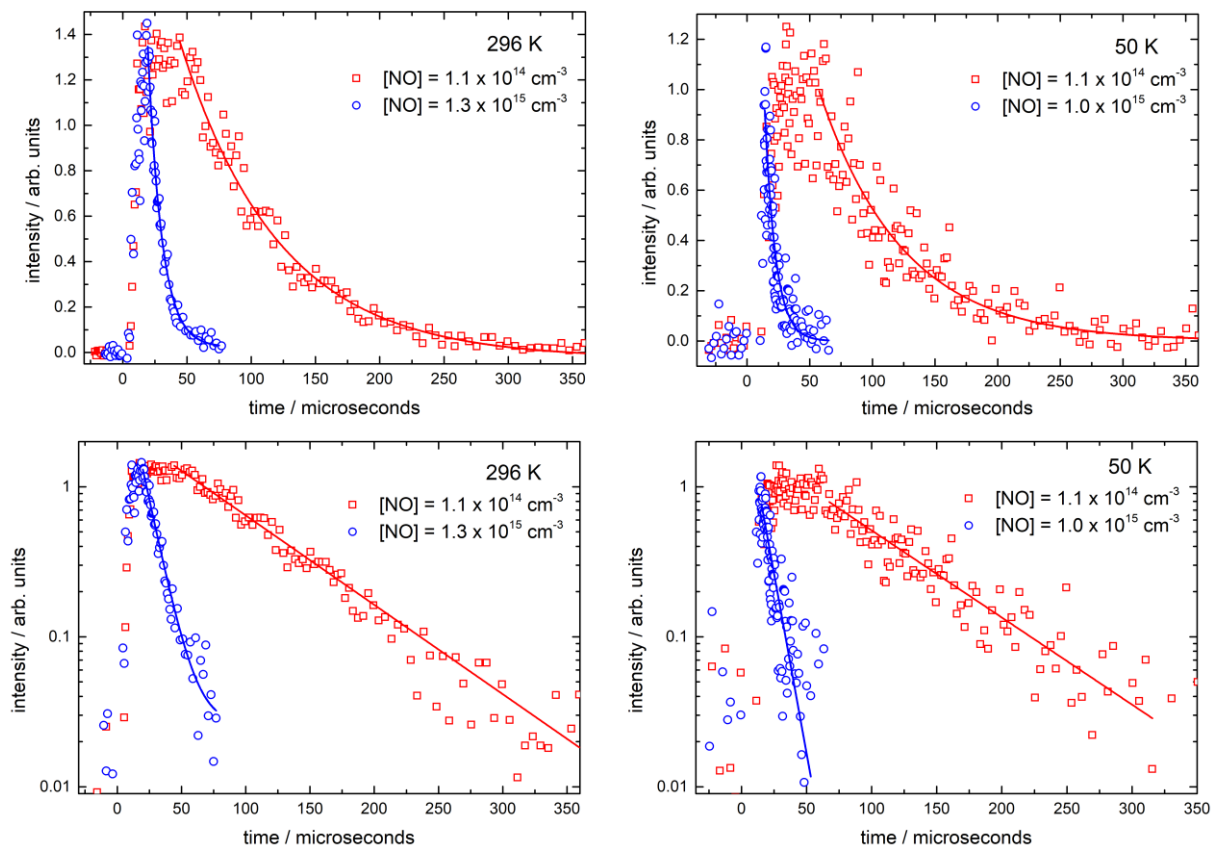


Figure 5.1 $N(^2D)$ VUV LIF signal as a function of time. Left panel recorded at 296 K (red open squares) $[NO] = 1.1 \times 10^{14} \text{ cm}^{-3}$, (blue open circles) $[NO] = 1.3 \times 10^{15} \text{ cm}^{-3}$. Right panel recorded at 50 K, (red open squares) $[NO] = 1.1 \times 10^{14} \text{ cm}^{-3}$, (blue open circles) $[NO] = 1.0 \times 10^{15} \text{ cm}^{-3}$. Bottom panels are the logarithmic representation of the $N(^2D)$ VUV LIF signals as a function of time. Solid red and blue lines represent exponential fits to the data using expression 2.5.

Pseudo-first-order decays were recorded for several NO concentrations and the second-order rate constants were extracted from the slopes through a weighted linear least-squares fit of the datapoints as shown in *Figure 5.2* for 50 K, 75 K and 296 K.

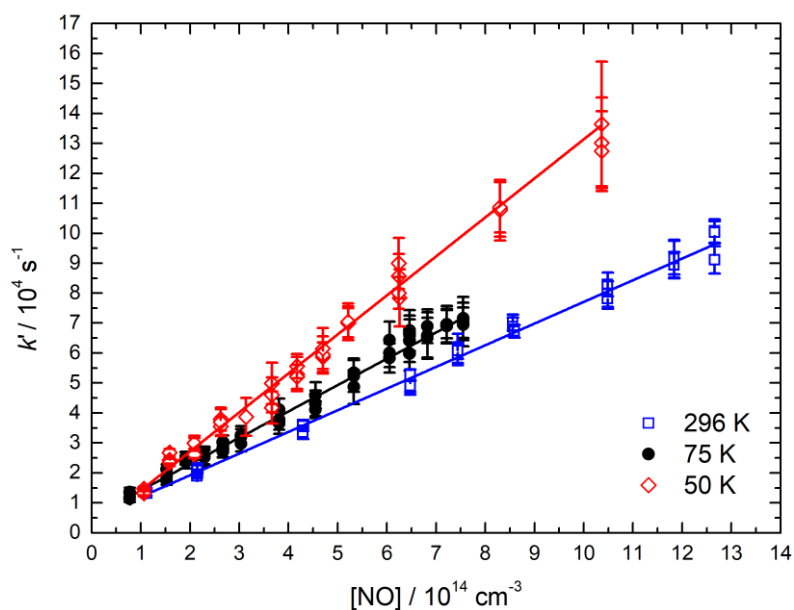


Figure 5.2 Second order plots for the $N(^2D) + NO$ reaction (red open diamonds) data recorded at 50 K, (black solid circles) data recorded at 75 K, (blue open squares) data recorded at 296 K. The solid lines represent linear least-squares fits to the data, weighted by the statistical uncertainties of the individual data points obtained through pseudo-first-order fits.

The second order rate constants obtained as a function of temperature are displayed in Figure 5.3 together with other experimental and theoretical determinations.

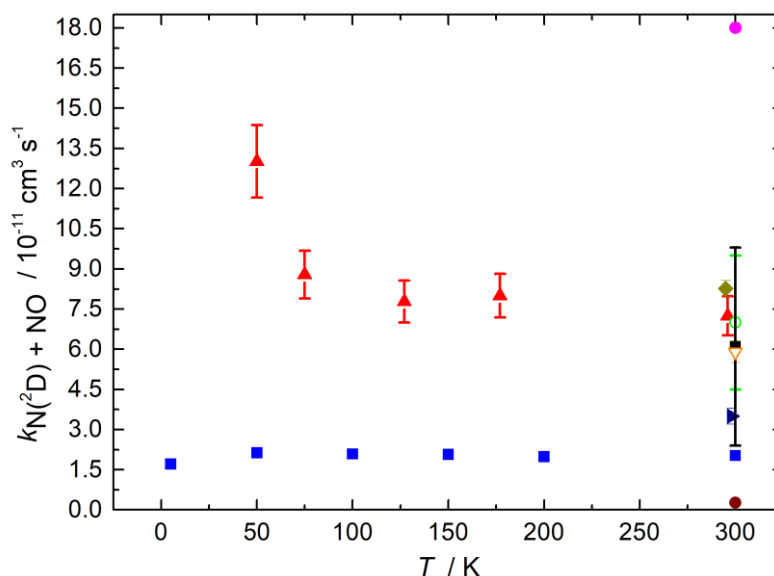


Figure 5.3 Rate constants for the $N(^2D) + NO$ reaction as a function of temperature. Experimental studies (solid red triangles) this work; (solid dark yellow diamond) Umemoto et al.;¹⁶ (open green circle) Lin and Kaufman;¹² (solid black square) Husain et al.;¹³ (open orange triangle) Husain et al.;¹⁴ (solid dark blue triangle) Sugawara et al.;¹⁵ (solid magenta circle) Black et al.¹¹ Theoretical studies (solid dark red circle) Gonzalez et al.;²⁸ (solid blue squares) Li et al.²⁹ Error bars in the present result represent the combined statistical (1σ) and systematic uncertainties (10%).

The second-order rate constants, the concentration ranges and the number of experiments performed in each case are summarized in *Table 5.1*.

Table 5.1 Temperature dependent rate constants for the N(²D) + NO reaction.

T(K)	N ^b	[NO](10 ¹⁴ cm ⁻³)	$k_{N(^2D)+NO}$ (10 ⁻¹¹ cm ³ s ⁻¹)
296	29	1.1 - 12.7	(7.3 ± 0.7) ^c
177 ± 2 ^a	36	0.7 - 8.1	(8.0 ± 0.8)
127 ± 2	28	0.8 - 9.2	(7.8 ± 0.8)
75 ± 2	43	0.8 - 7.6	(8.8 ± 0.9)
50 ± 1	35	1.1 - 10.4	(13.0 ± 1.4)

^aUncertainties in the calculated temperatures represent the statistical (1σ) errors obtained from Pitot tube measurements of the impact pressure. ^bNumber of individual measurements. ^cUncertainties in the measured rate constants represent the combined statistical (1σ) and estimated systematic (10%) errors.

5.3.2. Discussion

The N(²D) + NO reaction has been extensively studied at room temperature with a recommended value of 6.0 x 10⁻¹¹ cm³ s⁻¹.¹ As can be seen from *Figure 5.3* our experimental determination at room temperature is in good agreement with all but two of the previous determinations of the rate constants. The measurements of Black et al.¹¹ (1.8 x 10⁻¹⁰ cm³ s⁻¹) and Sugawara et al.¹⁵ (3.5 x 10⁻¹¹ cm³ s⁻¹) are considerably higher and lower than the rest of the determinations at room temperature. The good agreement between our data and the other measurements validates our new production method for N(²D) atoms.

Regarding the theoretical investigations, it can be seen from (*Figure 5.3*) that the rate constants in the study of Gonzalez et al.²⁸ and Li et al.²⁹ are lower compared with the experimental values. As was stated before, these two calculations were performed for only one exit channel of the reaction R 5.5 (b). Gonzalez et al.²⁸ performed a QCT study on the ground singlet 1 ¹A' potential energy of N₂O. These authors distinguished three different reactive mechanisms. The first one involved an attack of the N(²D) atom on the nitrogen end of the NO molecule with the system evolving through an NNO well yielding products without another intermediate structure. The second one involved N(²D) atom attack on the oxygen end of the NO molecule with the system evolving through several minima and transition states to products. The first and second mechanism share a common transition state in their pathways, the interchange between these two mechanisms through that transition state represents the third mechanism. They obtained a rate constant for channel R 5.5 (b) of (2.6 ± 0.4) x 10⁻¹² cm³ s⁻¹, which is

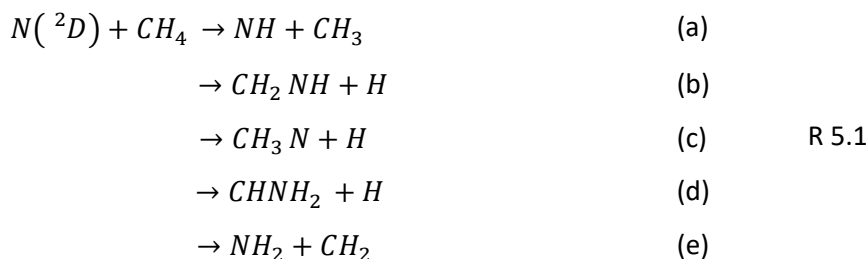
more than an order of magnitude lower than the lowest experimental value for the total rate constant at room temperature. However, as there are in fact five potential energy surfaces which adiabatically correlate with $O(^1D) + N_2$ products, they tried to take into account the reactivity due to the other four excited PESs connecting with products. Gonzalez et al.²⁸ concluded that the $2\ ^1A'$ and the $1\ ^1A''$ surfaces might also contribute to the reactivity estimating a total rate constant of $7.9 \times 10^{-12} \text{ cm}^3 \text{ s}^{-1}$ at room temperature. As the latter value is still lower compared to the experimental result, these authors suggest that the inclusion of the other exit channels R 5.5 (a) and R 5.5 (c) could lead to a better agreement between the theoretical and experimental rate constants. On the other hand, the more recent calculations of Li et al.²⁹ are in better agreement with the experimental values. These authors used a ground state $1\ ^1A'$ potential energy surface calculated with a higher level of theory along with a proper description of the long-range forces,³⁰ which are critical for a quantitative description of the $N(^2D) + NO$ reaction as the N_2O intermediate formation follows a capture type mechanism. These authors²⁹ obtained a rate constant of $(2.0 \pm 0.2) \times 10^{-11} \text{ cm}^3 \text{ s}^{-1}$ at room temperature which is one third of the recommended experimental value and four times smaller compared to our value, a discrepancy that almost certainly indicates the role of other exit channels leading to R 5.5 (a), R 5.5 (b) and R 5.5 (c).

When the temperature is lowered to values of astrochemical interest, our measured rate constants display a slight negative temperature dependence down to 75 K and a more pronounced increase at even lower temperatures (*Figure 5.3*). This large measured increase in reactivity below 75 K could be indicative of the increasing contribution of another reaction mechanism at low temperature. Indeed Gonzalez et al.²⁸ explain the possible existence of a crossing seam between the lowest singlet and triplet adiabatic potential energy surface. This crossing might become more important as the temperature falls and the intermediate N_2O lifetime increases.

5.4. The $N(^2D)$ + alkanes (C_nH_{2n+2}) reactions

The reactions of $N(^2D)$ atoms with alkanes lead to the formation of N-bearing organic molecules which might represent the basis for the formation of larger prebiotic molecules in planetary atmospheres.³¹ In Titan's atmosphere, as the deactivation of $N(^2D)$ atoms in collision with N_2 is a slow process, the reaction between $N(^2D)$ and CH_4 (the second most abundant constituent) has been recognized as an important process and has caught the attention of both theoreticians and experimentalists. The kinetics of this reaction has been studied at room temperature^{11,16,32,33} with a recommended value^{1,4} of $4.0 \times 10^{-12} \text{ cm}^3 \text{ s}^{-1}$. In addition, Takayanagi et al.³³ studied the temperature dependence of the $N(^2D) + CH_4$ reaction over the 223 – 292 K temperature range reporting rate constants according to the Arrhenius expression $k = 7.1 \times 10^{-11} \times \exp(-750/T) \text{ cm}^3 \text{ s}^{-1}$. Concerning the dynamics of the $N(^2D) + CH_4$

reaction, there are some discrepancies between theoreticians and experimentalists. Kurosaki et al.³⁴ performed a study of the reaction mechanism and primary products for this reaction using ab initio calculations. These authors identified the following exothermic channels



In addition, Kurosaki et al.³⁴ performed IRC calculations to elucidate the reaction mechanism showing that N(²D) inserts into one of the C-H bonds of CH₄ through a small barrier (~4.2 kJ/mol) forming a CH₃NH intermediate which later dissociates to products. Umemoto et al.^{35,36} identified NH from channel (a) and H from channels (b) and (c) as primary reaction products with absolute yields of 0.3 ± 0.1 and 0.8 ± 0.2 respectively. These authors state that the NH product is formed by an insertion mechanism rather than abstraction and suggested that the CH₃N + H channel was minor in comparison with the CH₂NH + H channel at room temperature. In contrast, Balucani et al.³⁷ combined CMB experiments at five different collision energies (22.2 – 65.1 kJ/mol) and ab initio structure calculations to shed light on the various forms of CH₃N isomers formed (channels b, c and d). However, these authors found that the insertion mechanism was barrierless in contrast with the previous studies and reported the CH₃N and CH₂NH isomers as primary products with production yields that vary significantly with the total available energy. More recently, Ouk et al.^{38,39} performed accurate ab initio calculations confirming the presence of a small barrier (~3.86 kJ/mol) in the entrance channel of the N(²D) + CH₄ reaction.

Ethane is the second most abundant hydrocarbon in Titan's atmosphere and although it is present in trace amounts, photochemical models^{6,10} highlight the need for low temperature rate constants for the N(²D) + C₂H₆ reaction to improve the accuracy of current models. While there are two experimental kinetics determinations^{16,32} of this reaction at room temperature with a recommended rate constant value⁴ of $1.9 \times 10^{-11} \text{ cm}^3 \text{ s}^{-1}$, to the best of our knowledge there are no determinations at low temperature. Regarding the dynamics of this reaction, Balucani et al.⁴⁰ have performed both a CMB study at two collision energies (18.0 and 31.4 kJ/mol) and ab-initio electronic structure calculations. These authors identified 22 exothermic exit channels from their theoretical calculations showing the complexity of the N(²D) + C₂H₆ reaction. This complexity arises from the versatility of carbon and nitrogen in forming bonds and the numbers of atoms involved.

The kinetics of the next larger alkane C_3H_8 in reaction with $N(^2D)$ atoms has also been investigated at room temperature^{16,32} with a recommended value^{1,4} of $2.9 \times 10^{-11} \text{ cm}^3 \text{ s}^{-1}$. As far as we know there are no dynamics studies for this reaction, thus conclusions on the preferred exit channels can only be extracted by analogy with the two previous $N(^2D)$ + alkanes reactions.

Currently, atmospheric models of Titan's atmosphere^{41,42} consider temperature independent rate constants (equal to the recommended values at room temperature) for the reactions of $N(^2D)$ atoms with C_2H_6 and C_3H_8 due to the lack of data at low temperatures. To solve this issue, in this chapter we determine the temperature dependence of the rate constants for the $N(^2D)$ + CH_4 , C_2H_6 and C_3H_8 reactions over a wide temperature range providing the necessary information for these reactions.

5.4.1. Results

To study the kinetics of $N(^2D)$ atoms in reaction with C_nH_{2n+2} , $[C_nH_{2n+2}]$ and $[NO]$ were maintained in a large and known excess with respect to the concentration of $N(^2D)$ and $C(^3P)$ atoms. NO was added to the flow in a fixed excess quantity to produce $N(^2D)$ atoms as explained in section 5.2.2. Under these conditions, the pseudo-first-order curves (*Figure 5.4*) are described by a coupled process in which $N(^2D)$ atoms are formed through R 5.4 and consumed by reaction with the alkanes and with NO. As explained in section 5.3.1, scattered light from the photolysis laser leads to a saturation of the signal for the first 15 μs and consequently the rise of the curve corresponding to $N(^2D)$ formation could not be recorded close to zero. Finally, to obtain the pseudo-first-order rate constants, the $N(^2D)$ signal was fitted with a single exponential function (expression 2.5) as described for the study of the $N(^2D)$ + NO reaction. The pseudo-first-order curves recorded at high $[C_nH_{2n+2}]$ were always considerably more scattered than the data recorded at low $[C_nH_{2n+2}]$ due to absorption of the $N(^2D)$ VUV LIF emission by residual C_nH_{2n+2} present in the reactor.

Here, several secondary reactions involving CBr_4 photolysis products ($C(^3P)$ and $C(^1D)$) or reactions R 5.4 and R 5.5 products (CN , $N(^4S)$ and $O(^1D)$) with the alkanes reagents could occur in the reactor. As both $C(^3P)$ and $N(^4S)$ are unreactive with CH_4 , C_2H_6 and C_3H_8 at room temperature and below, these reactions do not need further consideration. On the other hand, $C(^1D)$ atoms are going to react with CH_4 , C_2H_6 and C_3H_8 leading to products⁴³ such as atomic hydrogen and hydrocarbon radicals (CH and CH_3) but these species are present in very low concentrations and none of them will yield $N(^2D)$ as a product in reaction with NO. Furthermore, although CN and $O(^1D)$ will react readily with saturated hydrocarbon molecules⁴⁴⁻⁴⁶ none of these products are thought to lead to the formation of $N(^2D)$ atoms. Then as we are following directly $N(^2D)$ atoms, these secondary reactions are not expected to interfere with our determinations of the rate constants for the primary $N(^2D)$ + C_nH_{2n+2} reactions.

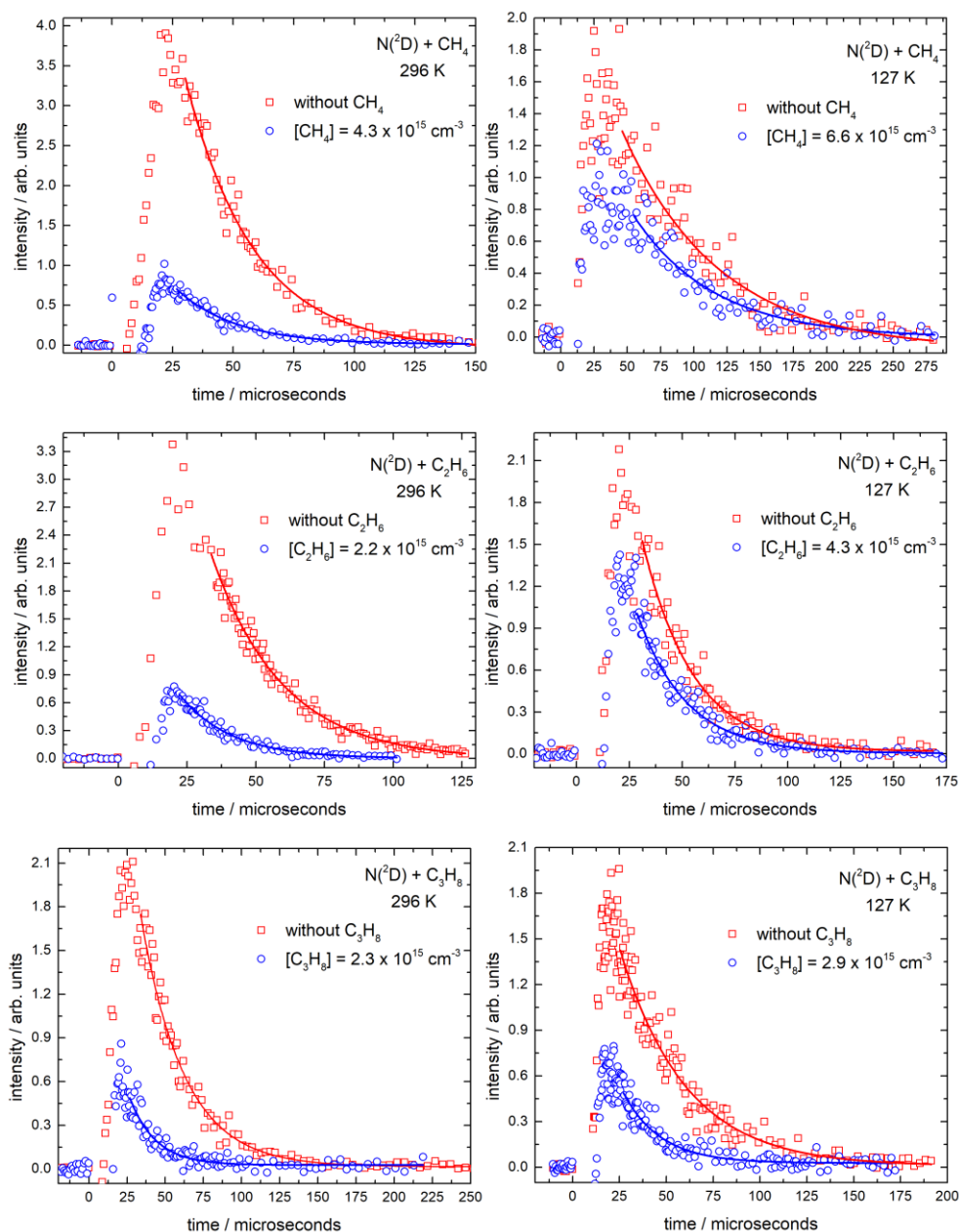


Figure 5.4 $N(^2D)$ VUV LIF signal as a function of time. Left panel recorded at 296 K; right panel recorded at 127. (Red open squares) without C_nH_{2n+2} added, (blue open circles) maximum concentration of alkane added. The NO concentration was fixed to $\sim 4.5 \times 10^{14} \text{ cm}^{-3}$ at 296 K and $\sim 3.1 \times 10^{14} \text{ cm}^{-3}$ at 127 K. Solid red and blue lines represent exponential fits to the data using expression 2.5.

The second-order rate constants were extracted from the slope in a plot of the pseudo-first-order rate constants against $[C_nH_{2n+2}]$. It is important to notice that the intercept of these plots represent the loss of $N(^2D)$ in reaction with NO assuming that diffusional losses are small in comparison.

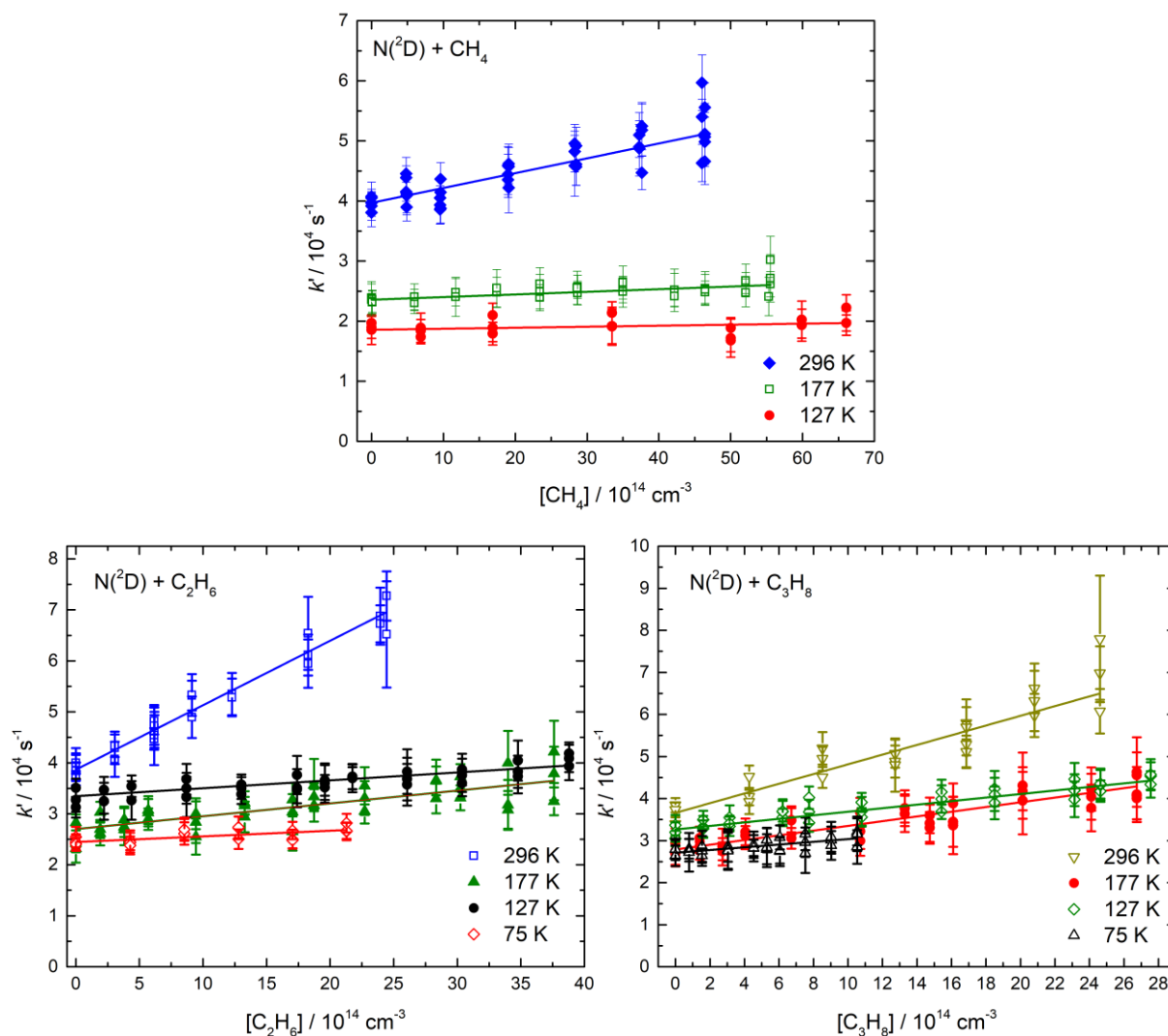


Figure 5.5 Second-order plots for the $N(^2D) + C_nH_{2n+2}$ reactions. The solid lines represent linear least-squares fits to the data, weighted by the statistical uncertainties of the individual data points obtained through pseudo-first-order fits.

To study the kinetics of $N(^2D)$ atoms with C_nH_{2n+2} , it is necessary to add NO in the system to produce $N(^2D)$ atoms. Then the chosen NO concentration plays an important role in the pseudo-first-order decays producing $N(^2D)$ atoms at a variable rate. In addition, as can be seen in Figure 5.5 the range of pseudo-first order rate constants is quite small due to a combination of both the initial NO concentration chosen and the slow second-order rate constants for the processes. Thus, it is necessary to test the influence of the initial NO concentration in the determination of the second-order rate constants for the target reactions. To perform these test experiments, pseudo-first order curves were recorded for a range of alkane concentrations using different initial NO concentrations at the same temperature. The resulting pseudo-first-order rate constants were plotted against the corresponding alkane concentration as shown in Figure 5.6. In these plots, the intercept value increases with increasing NO concentration as expected due to the increasing rate of $N(^2D)$ loss.

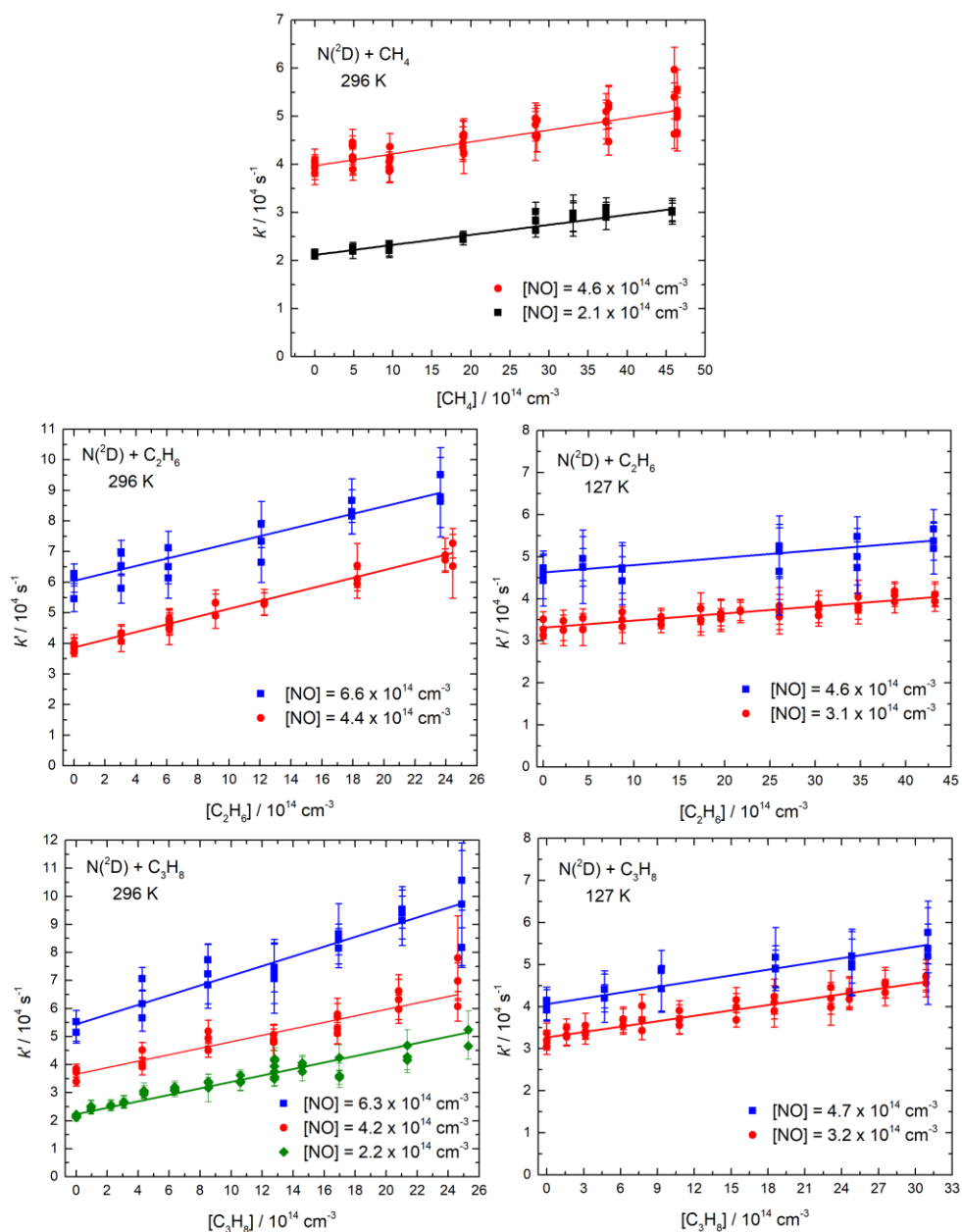


Figure 5.6 Second-order plots for the $N(^2D) + C_nH_{2n+2}$ reactions using different concentrations of NO at the same temperature. The solid lines represent linear least-squares fits to the data, weighted by the statistical uncertainties of the individual data points obtained through pseudo-first-order fits.

Finally, the second-order rate constants as a function of temperature for the $N(^2D) + C_nH_{2n+2}$ reactions are shown in Figure 5.7 and summarized in Table 5.2 along with the NO concentration used, the number of experiments performed in each case and the range of $[C_nH_{2n+2}]$.

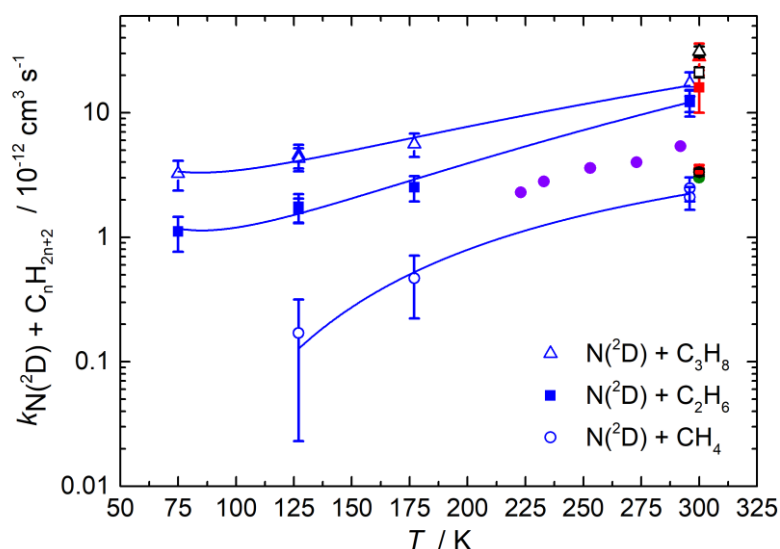


Figure 5.7 Rate constants for the $N(^2D) + C_nH_{2n+2}$ reactions as a function of temperature. The $N(^2D) + C_3H_8$ reaction: (open blue triangles) this work; (black open triangle) Umemoto et al.,¹⁶ (red solid triangle) Fell et al.³² The $N(^2D) + C_2H_6$ reaction: (solid blue squares) this work; (black open square) Umemoto et al.,¹⁶ (red solid square) Fell et al.³² The $N(^2D) + CH_4$ reaction: (open blue circles) this work; (black open circle) Umemoto et al.,¹⁶ (red solid circle) Fell et al.,³² (green solid circle) Black et al.,¹¹ (purple solid circles) Takayanagi et al.³³ The solid blue lines represent simple Arrhenius or Kooij type fits to the present experimental data. Error bars in the present results represent the combined statistical (1σ) and systematic uncertainties (estimated to be 20% of the nominal value of the rate constant except for measurements of the $N(^2D) + CH_4$ reaction at 177 K and 127 K where it was estimated to be 50%).

In this case, we report the second-order rate constants with a systematic error of 20% (50% in the case of $N(^2D) + CH_4$ reaction at 177 K and 127 K; see details in the discussion) because our procedure to obtain $N(^2D)$ atoms is complex, combining two processes (formation of the $N(^2D)$ atoms through chemical reaction and $N(^2D)$ decay through reaction with the target molecules and with NO). Furthermore, instead of fitting the pseudo-first order curves to a biexponential function (which describe the whole process) we were required to fit to a single exponential curve; a procedure in which the choice of the starting point should be made carefully. These issues combined generate a larger uncertainty in the determined second-order rate constant.

Table 5.2 Temperature dependent rate constants for the N(²D) + C_nH_{2n+2} reactions.

T(K)	N ^b	[NO](10 ¹⁴ cm ⁻³)	[CH ₄](10 ¹⁴ cm ⁻³)	$k_{N(^2D)+CH_4}$ (10 ⁻¹² cm ³ s ⁻¹)
296	44	4.6	0 - 46.4	(2.5 ± 0.5) ^c
296	24	2.1	0 - 45.8	(2.1 ± 0.4)
177 ± 2 ^a	38	2.6	0 - 55.5	(0.5 ± 0.2)
127 ± 2	20	1.5	0 - 66.1	(0.2 ± 0.1)
T(K)	N	[NO](10 ¹⁴ cm ⁻³)	[C ₂ H ₆](10 ¹⁴ cm ⁻³)	$k_{N(^2D)+C_2H_6}$ (10 ⁻¹² cm ³ s ⁻¹)
296	28	4.4	0 - 24.4	(12.6 ± 2.6)
296	18	6.6	0 - 23.6	(12.2 ± 2.9)
177 ± 2	39	2.7	0 - 37.6	(2.5 ± 0.6)
127 ± 2	38	3.1	0 - 43.2	(1.7 ± 0.4)
127 ± 2	18	4.6	0 - 43.1	(1.8 ± 0.5)
75 ± 2	19	2.7	0 - 21.3	(1.1 ± 0.4)
T(K)	N	[NO](10 ¹⁴ cm ⁻³)	[C ₃ H ₈](10 ¹⁴ cm ⁻³)	$k_{N(^2D)+C_3H_8}$ (10 ⁻¹² cm ³ s ⁻¹)
296	22	4.2	0 - 22.9	(11.5 ± 2.5)
296	21	6.3	0 - 23.1	(17.3 ± 3.8)
296	40	2.2	0 - 25.3	(11.6 ± 2.4)
177 ± 2	38	2.7	0 - 26.7	(5.6 ± 1.2)
127 ± 2	36	3.2	0 - 30.9	(4.6 ± 1.0)
127 ± 2	18	4.7	0 - 31.0	(4.3 ± 0.9)
75 ± 2	30	2.7	0 - 10.5	(3.3 ± 0.9)

^aUncertainties in the calculated temperatures represent the statistical (1σ) errors obtained from Pitot tube measurements of the impact pressure. ^bNumber of individual measurements. ^cUncertainties in the measured rate constants represent the combined statistical (1σ) and estimated systematic (20 and 50%) errors.

5.4.2. Discussion

For the N(²D) + CH₄ reaction, the previously reported rate constants at room temperature vary in the range of (3.0 – 5.4) × 10⁻¹² cm³ s⁻¹. These values were obtained employing a variety of experimental techniques such as photolysis-chemical tracer,¹¹ microwave discharge-electron spin resonance absorption,³² PLP-fluorescence, etc.¹⁶ Our measured rate constants at room temperature using two different concentrations of NO yield very similar values (see Table 5.2) but they are slightly lower than the literature values. The temperature dependence of this reaction was studied by Takayanagi et al.³³ using pulsed radiolysis-resonance absorption over the 223 – 292 K temperature range. Although the

values reported by these authors are almost twice as large as our determined values, we find a similar positive temperature dependence. Our measured rate constants below room temperature are smaller than $10^{-12} \text{ cm}^3 \text{ s}^{-1}$, a value that is normally considered as the lower limit for the rate constants that can be measured in a CRESU apparatus (assuming that the minor reagent decay can be followed over at least two half-lives). In the case of the rate constants determined at 177 K and 127 K, the losses of $\text{N}(\text{}^2\text{D})$ atoms were followed for approximately one half-life due to a combination of the slow rate constant for the process and the corresponding maximum hydrodynamic time for each Laval nozzle. Consequently, the derived second order rate constants at these temperatures are characterized by uncertainties substantially larger than those usually associated with this type of measurement. In this respect, we have increased our estimate of the systematic errors on these two measurements to 50% of the nominal value. An Arrhenius fit to our data yields the following Arrhenius parameters; $A = 1.93 \times 10^{-11} \text{ cm}^3 \text{ s}^{-1}$ and $(E_a/R) = 638$.

The kinetics of the $\text{N}(\text{}^2\text{D}) + \text{C}_2\text{H}_6$ and C_3H_8 reactions have been investigated at room temperature by Fell et al.³² and Umemoto et al.¹⁶ In the case of the $\text{N}(\text{}^2\text{D}) + \text{C}_2\text{H}_6$ reaction, they obtained very similar rate constants, $(2.7 \pm 1.0) \times 10^{-11} \text{ cm}^3 \text{ s}^{-1}$ and $(2.1 \pm 0.2) \times 10^{-11} \text{ cm}^3 \text{ s}^{-1}$ respectively, however the critical review of Herron et al.¹ estimated that the rate constants determined by Fell et al.³² should be adjusted downwards by a factor of 0.6 yielding $(1.6 \pm 0.6) \times 10^{-11} \text{ cm}^3 \text{ s}^{-1}$. The rate constants determined by us using two different NO concentrations are very similar (see *Table 5.2*) but slightly lower than the previous work of Fell et al.³² and Umemoto et al.¹⁶ Our rate constants decrease as the temperature falls reaching a value of $(1.1 \pm 0.3) \times 10^{-12} \text{ cm}^3 \text{ s}^{-1}$ at 75 K. An Arrhenius fit to the present data does not yield a good fit over the entire temperature range, so we choose instead to use a modified Arrhenius type expression $k = A * \left(\frac{T}{300}\right)^n * \exp\left(-\frac{E_a}{RT}\right)$ where $A = 3.58 \times 10^{-12} \text{ cm}^3 \text{ s}^{-1}$, $n = 4.45$ and $\frac{E_a}{R} = -379$. The deviation from Arrhenius behaviour at low temperature might be an indication that H-atom tunnelling plays a small but non-negligible role in the $\text{N}(\text{}^2\text{D}) + \text{C}_2\text{H}_6$ reaction.

For the $\text{N}(\text{}^2\text{D}) + \text{C}_3\text{H}_8$ reaction, Fell et al.³² and Umemoto et al.¹⁶ found rate constants with the values $(4.6 \pm 1.4) \times 10^{-11} \text{ cm}^3 \text{ s}^{-1}$ and $(3.1 \pm 0.3) \times 10^{-11} \text{ cm}^3 \text{ s}^{-1}$ respectively, however after the correction suggested by Herron et al.¹ to the data of Fell et al.³² the rate constant at room temperature is $(2.8 \pm 0.8) \times 10^{-11} \text{ cm}^3 \text{ s}^{-1}$. As these values are higher than our determined rate constants at room temperature we performed further tests to check for potential errors in the current work. In particular, as $\text{N}(\text{}^2\text{D})$ atoms are formed through reaction R 5.4 rather than prompt formation through direct photolysis, it is possible that $\text{N}(\text{}^2\text{D})$ formation and $\text{N}(\text{}^2\text{D})$ loss through the $\text{N}(\text{}^2\text{D}) + \text{C}_3\text{H}_8$ reaction were occurring over the same time period. Indeed, such an effect is expected to lead to slower pseudo-first-order rate constants for the target reaction. Then the second-order rate constants for the $\text{N}(\text{}^2\text{D}) + \text{C}_3\text{H}_8$ reaction

were measured at room temperature using three different fixed NO concentrations (2.2, 4.2 and $6.3 \times 10^{14} \text{ cm}^{-3}$). Assuming a rate constant of $1.5 \times 10^{-10} \text{ cm}^3 \text{ s}^{-1}$ for reaction R 5.4,⁴⁷ we obtain pseudo-first-order rate constants of 3.3, 6.3, $9.5 \times 10^4 \text{ s}^{-1}$ respectively thus allowing us to calculate the half-life times for N(²D) formation under these conditions. The delay times when only 13% of the initial C(³P) remains to be converted to N(²D) (corresponding to three half-lives) are 64, 33 and 22 μs , indicating that data acquired at delays shorter than these values may not accurately reflect the kinetics of the N(²D) + C₃H₈ reaction. For the lowest NO concentration, the data acquired after 64 μs was difficult to analyse given the weak signal levels, with a measured rate constant of $(1.2 \pm 0.2) \times 10^{-11} \text{ cm}^3 \text{ s}^{-1}$. With the intermediate NO concentration, a similar measured rate constant of $(1.2 \pm 0.2) \times 10^{-11} \text{ cm}^3 \text{ s}^{-1}$ was obtained. Only the rate constant value obtained for the N(²D) + C₃H₈ reaction with [NO] = $6.3 \times 10^{14} \text{ cm}^{-3}$ (yielding (296 K) = $(1.7 \pm 0.4) \times 10^{-11} \text{ cm}^3 \text{ s}^{-1}$ respectively) was retained to derive the temperature dependent fitting parameters. Our determined rate constant decreases as the temperature falls reaching a value of $(3.2 \pm 0.9) \times 10^{-12} \text{ cm}^3 \text{ s}^{-1}$ at 75 K. As the Arrhenius expression does not yield a good fit to the data over the entire temperature range, the modified Arrhenius type expression described above is used instead where $A = 7.36 \times 10^{-12} \text{ cm}^3 \text{ s}^{-1}$, $n = 2.99$ and $\frac{E_a}{RT} = -252$.

Taking into account our determined rate constants for the N(²D) + C_nH_{2n+2} reactions and including the results at room temperature from previous determinations, we can state that the rate constants for C₂H₆ and C₃H₈ are considerably larger than those for CH₄. Furthermore, the small rate constants measured for these systems suggest an activation barrier in the entrance channel implying that the rate constants are going to be significantly smaller than currently predicted at temperatures of interest to Titan's atmosphere.

Regarding the dynamics of the N(²D) atoms + C_nH_{2n+2} reactions, it is thought that N(²D) atoms insert into one of the C-H bonds leading to the formation of an intermediate which later fragments into products. In the case of the N(²D) + CH₄ reaction, Umemoto et al.³⁵ suggested that the CH₃NH intermediate is short lived and explained the preferential formation of CH₂NH + H over the CH₃N + H due to the tri-radical character of N(²D) atoms. After insertion of N(²D) into the C-H bond there is still one unpaired electron which might interact with the electron of the carbon atom to form a C=N double bond and consequently a H-atom must be ejected promptly. On the other hand, Balucani et al.³⁷ identified a large yield for the CH₃N isomer, which increases with the collision energy (22.2 – 65.1 kJ/mol). These authors suggested that the C-N and N-H bonds will break easier than the C-H bond (even though the latter is weaker) because the excess of energy in the newly formed intermediate CH₃NH is going to be concentrated in the C-N and N-H bonds. In addition, the short lifetime of the CH₃NH complex does not allow an efficient intramolecular energy distribution, thereby favouring the rupture

of the more stable bonds. These authors conclude that while at high collision energies the reaction is dominated by dynamical effects with the formation of the products $\text{CH}_3\text{N} + \text{H}$ and $\text{CH}_3 + \text{NH}$, at low collision energies it behaves statistically with a redistribution of the available energy to form the more stable products $\text{CH}_2\text{NH} + \text{H}$. As our experiments are performed at much lower equivalent energies, the lifetime of the CH_3NH intermediate will increase, favouring the preferential formation of the more stable $\text{CH}_2\text{NH} + \text{H}$ channel in agreement with the results of Umemoto et al.³⁵ performed at room temperature.

In the case of the $\text{N}(^2\text{D}) + \text{C}_2\text{H}_6$ reaction, the CMB result of Balucani et al.⁴⁰ shows that the reaction proceeds through the formation of one or more bound intermediates, results that were supported by their electronic structure calculations of the $\text{C}_2\text{H}_6\text{N}$ PES. As the $\text{CH}_3\text{CH}_2\text{NH}$ complex has an increased capability to randomize the internal energy (due to an increased number of degrees of freedom with respect to the CH_3NH complex), the $\text{N}(^2\text{D}) + \text{C}_2\text{H}_6$ reaction behaves mostly statistically. From the 22 different exit channels that were identified in their calculations the major reaction channel at the characteristic temperatures of Titan's atmosphere involves C-C bond breaking leading to $\text{CH}_3 + \text{CH}_2\text{NH}$ (78.8%) followed by the $\text{H} + \text{CH}_3\text{CHNH}$ (12.4%) and minor contributions from the channels $\text{NH} + \text{C}_2\text{H}_5$ (5.5%), $\text{H} + \text{CH}_2\text{CHNH}_2$ (1.9%) and $^3\text{CH}_2\text{NH} + \text{CH}_3$ (1.4%).

In the case of the $\text{N}(^2\text{D}) + \text{C}_3\text{H}_8$ reaction, there is no information on the nature of the products. However, the behaviour of this reaction is expected to be similar to the methane and ethane reactions. Making analogies with the $\text{N}(^2\text{D})$ insertion into C_2H_6 , Dutuit et al.⁴ propose that the products $\text{CH}_2\text{NH} + \text{C}_2\text{H}_5$ or $\text{CH}_3\text{CHNH} + \text{CH}_3$ might be formed. They also propose the formation of $\text{NH} + \text{C}_3\text{H}_7$ and $\text{C}_2\text{H}_5\text{CHNH} + \text{H}$. Further dynamical and kinetic studies are required for this reaction with the aim to clarify the nature of the products at low temperature.

5.5. Astrochemical implications

As stated in the introduction, several reactions involving N(²D) atoms are a major source of uncertainty in photochemical models of planetary atmospheres. Kinetic studies of these key reactions are necessary to characterize the complex chemistry of these atmospheres, but the experimental production of N(²D) atoms has represented a significant challenge to experimentalists. This work provides a solution to this problem reporting a new method to obtain metastable N(²D) atoms. The method presented in this chapter allows us to study the kinetics of several gas-phase reactions at low temperatures if the losses of C(³P) atoms (our source of N(²D))) in reaction with the reagent in excess are not too significant.

To date, we have employed this method to study the reactions of N(²D) with methane, ethane and propane down to 50 K. Current photochemical models of Titan's atmosphere use the recommended room temperature rate constants for the N(²D) + C₂H₆, C₃H₈ reactions as temperature independent values to describe the reactivity of these reactions at lower temperature. However, if we take 150 K as a representative temperature for Titan's atmosphere, in the case of the N(²D) + C₂H₆ reaction we will obtain using our best fit parameters a rate constant of $2.1 \times 10^{-12} \text{ cm}^3 \text{ s}^{-1}$, which is almost an order of magnitude lower than the currently recommended value ($1.9 \times 10^{-11} \text{ cm}^3 \text{ s}^{-1}$). In the case of N(²D) + C₃H₈ reaction, the fit to our data yields a rate constant of $5.0 \times 10^{-12} \text{ cm}^3 \text{ s}^{-1}$ at 150 K; a value that is six times smaller than the currently recommended value ($2.9 \times 10^{-11} \text{ cm}^3 \text{ s}^{-1}$). Consequently, the results presented here represent an improvement to future predictions of these photochemical models.

5.6. References

- (1) Herron, J. Evaluated Chemical Kinetics Data for Reactions of $N(^2D)$, $N(^2P)$, and $N(A^3\Sigma^+_u)$ in the Gas Phase. *J. Phys. Chem. Ref. Data* **1999**, *28*, 1453–1483.
- (2) Gerard, J.-C. Thermospheric Odd Nitrogen. *Planet Sp. Sci* **1992**, *40*, 337–353.
- (3) Rusch, D. W.; Gerard, J.-C.; Sharp, W. E. The Reaction of $N(^2D)$ with O_2 as a Source of $O(^1D)$ Atoms in Aurorae. *Geophys. Res. Lett.* **1978**, *5*, 1043–1046.
- (4) Dutuit, O.; Carrasco, N.; Thissen, R.; Vuitton, V.; Alcaraz, C.; Pernot, P.; Balucani, N.; Casavecchia, P.; Canosa, A.; Picard, S. le; et al. Critical Review of N , N^+ , N_2^+ , N^{++} , And N_2^{++} Main Production Processes and Reactions of Relevance to Titan's Atmosphere. *Astrophys. J. Suppl. Ser.* **2013**, *204*, 1–45.
- (5) Krasnopolsky, V. A. Photochemistry of the Martian Atmosphere : Seasonal , Latitudinal , and Diurnal Variations. *Icarus* **2006**, *185*, 153–170.
- (6) Loison, J. C.; Hébrard, E.; Dobrijevic, M.; Hickson, K. M.; Caralp, F.; Hue, V.; Gronoff, G. The Neutral Photochemistry of Nitriles , Amines and Imines in the Atmosphere of Titan. *Icarus* **2015**, *247*, 218–247.
- (7) Krasnopolski, V. A. Photochemistry of the Martian Atmosphere (Mean Conditions). *Icarus* **1993**, *101*, 313–332.
- (8) Fox, J. L. The Production and Escape of Nitrogen Atoms on Mars. *J. Geophys. Res.* **1993**, *98*, 3297–3310.
- (9) Hébrard, E.; Dobrijevic, M.; Loison, J. C.; Bergeat, A.; Hickson, K. M. Neutral Production of Hydrogen Isocyanide (HNC) and Hydrogen Cyanide (HCN) in Titan's upper Atmosphere. *Astron. Astrophys.* **2012**, *541*, A21.
- (10) Dobrijevic, M.; Hébrard, E.; Hickson, K. M. Coupling of Oxygen, Nitrogen, and Hydrocarbon Species in the Photochemistry of Titan's Atmosphere. *Icarus* **2014**, *228*, 324–346.
- (11) Black, G.; Slinger, T. G.; John, G. A. S. T.; Youngt, R. A. Vacuum-Ultraviolet Photolysis of N_2O . IV. Deactivation of $N(^2D)$. *J. Chem. Phys.* **1969**, *51*, 116–121.

- (12) Lin, C.-L.; Kaufman, F. Reactions of Metastable Nitrogen Atoms. *J. Chem. Phys.* **1971**, *55*, 3760–3770.
- (13) Husain, D.; Kirsch, L. J.; Wiesenfeld, J. R. Collisional Quenching of Electronically Excited Nitrogen Atoms, N(²D,²P) by Time-Resolved Atomic Absorption Spectroscopy. *Faraday Discuss. Chem. Soc.* **1972**, 201–210.
- (14) Husain, D.; Mitra, S. K.; Young, A. N. Kinetic Study of Electronically Excited Nitrogen Atoms, N(²D_J, ²P_J), by Attenuation of Atomic Resonance Radiation in the Vacuum Ultra-violet. *J. Chem. Soc., Faraday Trans. 2* **1974**, *70*, 1721–1731.
- (15) Sugawara, K.; Ishikawa, Y.; Sato, S. The Rate Constants of the Reactions of the Metastable Nitrogen Atoms, ²D and ²P, and the Reactions of N(⁴S)+NO→N₂ + O(³P) and O(³P)+NO + M→NO₂ +M. *Bull. Chem. Soc. Jpn.* **1980**, *53*, 3159–3164.
- (16) Umemoto, H.; Hachiya, N.; Matsunaga, E.; Suda, A.; Kawasaki, M. Rate constants for the deactivation of N(²D) by simple hydride and deuteride molecules. *Chem. Phys. Lett.* **1998**, *296*, 203–207.
- (17) Chastaing, D.; Le Picard, S. D.; Sims, I. R. Direct Kinetic Measurements on Reactions of Atomic Carbon, C(³P), with O₂ and NO at Temperatures down to 15 K. *J. Chem. Phys.* **2000**, *112*, 8466–8469.
- (18) Bergeat, A.; Calvo, T.; Dorthe, G.; Loison, J.-C. Fast-Flow Study of the C + NO and C + O₂ Reactions. *Chem. Phys. Lett.* **1999**, *308*, 7–12.
- (19) Andersson, S.; Marković, N.; Nyman, G. Computational Studies of the Kinetics of the C + NO and O + CN Reactions. *J. Phys. Chem. A* **2003**, *107*, 5439–5447.
- (20) Sam, C. L.; Yardley, J. T. Excimer Laser Photolysis in CBr₄ and CF₂Br₂: Luminescence from Br₂, Br, CF₂ and C₂. *Chem. Phys. Lett.* **1979**, *61*, 509–512.
- (21) Greene, J. R.; Francisco, J. S.; Xu, D.; Huang, J.; Jackson, W. M. Photodissociation Dynamics of CBr₄ at 267 nm by Means of Ion Velocity Imaging. *J. Chem. Phys.* **2006**, *125*, 133311.
- (22) Shannon, R. J.; Cossou, C.; Loison, J.-C.; Caubet, P.; Balucani, N.; Seakins, P. W.; Wakelam, V.; Hickson, K. M. The Fast C(³P) + CH₃OH Reaction as an Efficient Loss Process for Gas-Phase Interstellar Methanol. *RSC Adv* **2014**, *4*, 26342–26353.

- (23) Nuñez-Reyes, D.; Hickson, K. M. The Reactivity of C(¹D) with Oxygen Bearing Molecules NO and O₂ at Low Temperature. *Chem. Phys. Lett.* **2017**, *687*, 330–335.
- (24) Donovan, R. J.; Husain, D. Recent Advances in the Chemistry of Electronically Excited Atoms. *Chem. Rev.* **1970**, *70*, 489–516.
- (25) Sims, I. R.; Smith, I. W. M. Pulsed Laser Photolysis-Laser-Induced Fluorescence Measurements on the Kinetics of CN(*v* = 0) and CN(*v* = 1) with O₂, NH, and NO between 294 and 761 K. *J. Chem. Soc., Faraday Trans. 2* **1988**, *84*, 527–539.
- (26) Sander, S. P.; Friedl, R. R.; Barker, J. R.; Golden, D. M.; Kurylo, M. J.; Sciences, G. E.; Wine, P. H.; Abbatt, J. P. D.; Burkholder, J. B.; Kolb, C. E.; et al. Chemical Kinetics and Photochemical Data for Use in Atmospheric Studies Evaluation Number 17. *JPL Publ. 10-6* **2011**.
- (27) Bergeat, A.; Hickson, K. M.; Daugey, N.; Caubet, P.; Costes, M. A Low Temperature Investigation of the N(⁴S) + NO Reaction. *Phys. Chem. Chem. Phys.* **2009**, *11*, 8149–8155.
- (28) González, M.; Valero, R.; Sayós, R. Ab initio and Quasiclassical Trajectory Study of the N(²D)+NO(X ²Π)→O(¹D)+N₂(X ¹Σ_g⁺) Reaction on the Lowest ¹A' Potential Energy Surface. *J. Chem. Phys.* **2000**, *113*, 10983–10998.
- (29) Li, J.; Caridade, P. J. S. B.; Varandas, A. J. C. Quasiclassical Trajectory Study of the Atmospheric Reaction N(²D)+ NO(X ²Π) → O(¹D)+N₂(X ¹Σ_g⁺). *J. Phys. Chem A* **2014**, *118*, 1277–1286.
- (30) Li, J.; Varandas, A. J. C. Accurate Ab-initio-Based Single-Sheeted DMBE Potential-Energy Surface for Ground-State N₂O. *J. Phys. Chem. A* **2012**, *116*, 4646–4656.
- (31) Balucani, N. Elementary Reactions of N atoms with Hydrocarbons: First Steps Towards the Formation of Prebiotic N-Containing Molecules in Planetary Atmospheres. *Chem. Soc. Rev* **2012**, *41*, 5473–5483.
- (32) Fell, B.; Rivas, I. V.; McFadden, D. L. Kinetic Study of Electronically Metastable Nitrogen Atoms, N(²D_J), by Electron Spin Resonance Absorption. *J. Phys. Chem.* **1981**, *85*, 224–228.
- (33) Takayanagi, T.; Kurosaki, Y. Kinetic Studies on the N(²D, ²P) + CH₄ and CD₄ Reactions: The Role of Nonadiabatic Transitions on Thermal Rate Constants. *J. Phys. Chem. A* **1999**, *103*, 250–255.
- (34) Kurosaki, Y.; Takayanagi, T.; Sato, K.; Tsunashima, S. Ab initio Molecular Orbital Calculations of

- the Potential Energy Surfaces for the N(²D)+ CH₄ reaction. *J. Phys. Chem. A* **1998**, *102*, 254–259.
- (35) Umemoto, H.; Nakae, T.; Hashimoto, H.; Kongo, K.; Kawasaki, M. Reactions of N(²D) with Methane and Deuterated Methanes. *J. Chem. Phys.* **1998**, *109*, 5844–5848.
- (36) Umemoto, H.; Kimura, Y.; Asai, T. Production of NH Radicals in the Reaction of N(²D) with CH₄: Nascent Rotational and Vibrational Distributions of NH. *Chem. Phys. Lett.* **1997**, *264*, 215–219.
- (37) Balucani, N.; Bergeat, A.; Cartechini, L.; Volpi, G. G.; Casavecchia, P. Combined Crossed Molecular Beam and Theoretical Studies of the N(²D) + CH₄ Reaction and Implications for Atmospheric Models of Titan. *J. Phys. Chem. A* **2009**, *113*, 11138–11152.
- (38) Ouk, C. M.; Zvereva-Loëte, N.; Bussery-Honvault, B. Towards a Converged Barrier Height for the Entrance Channel Transition State of the N(²D) + CH₄ Reaction and its Implication for the Chemistry in Titan's Atmosphere. *Chem. Phys. Lett.* **2011**, *515*, 13–18.
- (39) Ouk, C. M.; Zvereva-Loëte, N.; Scribano, Y.; Bussery-Honvault, B. Transition State Theory Thermal Rate Constants and RRKM-based Branching Ratios for the N(²D) + CH₄ Reaction Based on Multi-State and Multi-Reference Ab Initio Calculations of Interest for the Titan's Chemistry. *J. Comput. Chem.* **2012**, *33*, 2211–2224.
- (40) Balucani, N.; Leonori, F.; Petrucci, R.; Stazi, M.; Skouteris, D.; Rosi, M.; Casavecchia, P. Formation of Nitriles and Imines in the Atmosphere of Titan : Combined Crossed-Beam and Theoretical Studies on the Reaction Dynamics of Excited Nitrogen Atoms N(²D) with Ethane. *Faraday Discuss.* **2010**, *147*, 189–216.
- (41) Dobrijevic, M.; Loison, J. C.; Hickson, K. M.; Gronoff, G. 1D-coupled Photochemical Model of Neutrals, Cations and Anions in the Atmosphere of Titan. *Icarus* **2016**, *268*, 313–339.
- (42) Vuitton, V.; Yelle, R. V.; Klippenstein, S. J.; Hörst, S. M.; Lavvas, P. Simulating the Density of Organic Species in the Atmosphere of Titan with a coupled Ion-Neutral Photochemical Model. *Icarus* **2018**.
- (43) Nunez-Reyes, D.; Hickson, K. M. A Kinetic and Product Study of the Reactions of C(¹D) with CH₄ and C₂H₆ at Low Temperature. *J. Phys. Chem. A* **2017**, *121*, 3851–3857.
- (44) Meng, Q.; Hickson, K. M.; Shao, K.; Loison, J.-C.; Zhang, D. H. Theoretical and Experimental Investigations of Rate Coefficients of O(¹D) + CH₄ at Low Temperature. *Phys. Chem. Chem. Phys.*

2016, *18*, 29286–29292.

- (45) Nunez-Reyes, D.; Hickson, K. M. Rate Constants and H-Atom Product Yields for the Reactions of O(¹D) Atoms with Ethane and Acetylene from 50 to 296 K. *J. Phys. Chem. A* **2018**, *122*, 4696–4703.
- (46) Sims, I. R.; Queffelec, J. L.; Travers, D.; Rowe, B. R.; Herbert, L. B.; Karthäuser, J.; Smith, I. W. M. Rate Constants for the Reactions of CN with Hydrocarbons at Low and Ultra-Low Temperatures. *Chem. Phys. Lett.* **1993**, No. 4–5, 461–468.
- (47) Geppert, W. D.; Reignier, D.; Stoecklin, T.; Naulin, C.; Costes, M.; Chastaing, D.; Le Picard, S. D.; Sims, I. R.; Smith, I. W. M. Comparison of the Cross-Sections and Thermal Rate Constants for the Reactions of C(³P_j) Atoms with O₂ and NO. *Phys. Chem. Chem. Phys.* **2000**, *2*, 2873–2881.

Conclusions and perspectives

This thesis presents the results of my three years of doctoral work in experimental astrochemistry. We have studied nineteen gas-phase reactions employing the mini-CRESU (Cinétique de Réaction en Ecoulement Supersonique Uniforme) apparatus located at the ISM (Institute des Sciences Moléculaires). Using this apparatus, temperatures in the range of 50 - 296 K can be achieved allowing us to study reactions that are important in the chemistry of the interstellar medium and in planetary atmospheres.

Here, the neutral-neutral reactions of atomic carbon, oxygen and nitrogen in their first excited electronic states (1D , 1D and 2D respectively) with several molecules of relevance to the atmospheres of Titan and Mars have been investigated, providing rate constants for these processes. The excited electronic states of carbon and oxygen were generated by PLP of a suitable precursor and the rate constants for these processes were determined using the isolation method where the concentration of the molecular reagent was placed in a large and known excess with respect to the atomic species. The changes in the concentration of the target species were followed by on-resonance VUV LIF. For some multichannel exit reactions leading to H-atom production, we have determined the H-atom yields by comparing with a reference reaction that is known to produce H-atoms with a yield of 100%. The fast rate constant determined for the reaction of $C(^1D)$ with CH_4 combined with the abundance of methane in Titan's atmosphere suggests that this reaction could be a significant source of larger hydrocarbons. As the rate constants for $O(^1D) + CO_2$ are quite fast, this quenching process is likely to be efficient in the atmosphere of Mars. Isotopic studies ($C(^1D) + HD$ and $O(^1D) + D_2/HD$) have been performed with the aim to clarify the reaction mechanism of the primary reaction ($C(^1D)/O(^1D) + H_2$) and to benchmark theoretical methods. Rate constants for several reactions of fundamental interests ($C(^1D) + NO/O_2$ and $O(^1D) + C_2H_6/C_2H_2$) have been reported down to 50 K and their mechanisms have been discussed through comparisons with other reported studies performed at higher temperatures or on the electronic ground state equivalent reactions.

We have proposed a new method to obtain $N(^2D)$ atoms based on the chemical reaction between $C(^3P)$ and NO facilitating the study of several $N(^2D)$ atom reactions at the low temperature that characterize planetary atmospheres. Using this method, the rate constants for the reactions of $N(^2D) +$ methane, ethane and propane have been measured and are seen to decrease as the temperature is lowered. This result, once included in photochemical models of Titan's atmosphere will contribute to the improvement of their accuracy because current models use temperature independent rate constants for some of these processes by extrapolating the measured room temperature values to the low

temperature region. This approximation overestimates the importance of these processes at low temperatures.

The reaction between the electronic ground state carbon (3P) and water has also been studied experimentally and theoretically with the aim to shed some light on the disagreement between the observed and predicted abundances of water in the ISM. Rate constants and branching ratios for $C(^3P) + \text{water}$ and deuterated water have been investigated experimentally down to 50 K demonstrating the role of tunnelling in these reactions as the temperature is lowered. MESMER calculations have also been performed to help us understand the reaction mechanism and to extrapolate the rate constants to the low temperatures and densities of the interstellar medium. We estimate a fast rate constant at 10 K, which combined with the water abundances make this reaction the main sink of interstellar gas-phase water. Then if this reaction is included in models of the ISM, the current discrepancies between the observed and predicted water abundances (where the predicted water abundance is too large by an order of magnitude) are likely to be reduced.

The kinetic studies performed in this thesis contribute to a better understanding of the complex chemistry at work in the interstellar medium and in planetary atmospheres, providing important data for the models to explain the observed abundances of several molecules. The rate constants for most of the processes studied here including excited state atoms are seen to remain fast below room temperature and consequently their influence should be tested on photochemical models by including the formation and loss channels of these excited states atoms. The $N(^2D)$ atom production method developed in this work sets the basis for future studies of other key reactions identified in photochemical models such as $N(^2D) + \text{acetylene}$ and ethylene . With the aim of identifying and quantifying the product channels for these reactions studied it would be interesting to couple the CRESU apparatus with a mass spectrometric detection method or with broadband rotational spectroscopy to detect polar molecular products. This latter spectroscopic method is currently being implemented in our laboratory under the project OSCAR (Original Submillimeter Chirped pulsed instrumentation for Astrochemical Reactivity) which will combine the existing CRESU apparatus with a novel broadband rotational spectrometer in the submillimeter range. Furthermore, the VUV generation scheme used in this thesis to detect H-atoms opens the possibility to study for the first time at low temperature several reactions between H or D-atoms and radicals such as NO_2 , OH, CH, NH, NH_2 , and CH_3 . Indeed, with this method it is also possible to determine the rate constants for several reactions that could be important mechanisms for deuterium enrichment in planetary atmospheres and the interstellar medium.

Publications

1. Hickson, K. M.; Loison, J.-C.; Núñez-Reyes, D.; Mereau, R. Quantum Tunneling Enhancement of the C + H₂O and C + D₂O Reactions at Low Temperature. *J. Phys. Chem. Lett.* 2016, 3641 - 3646.
2. Núñez-Reyes, D.; Hickson, K. M. A Kinetic and Product Study of the Reactions of C(¹D) with CH₄ and C₂H₆ at Low Temperature. *J. Phys. Chem. A.* 2017, 121, 3851 - 3857.
3. Núñez-Reyes, D.; Hickson, K. M. The Reactivity of C(¹D) with Oxygen Bearing Molecules NO and O₂ at Low Temperature. *Chem. Phys. Lett.* 2017, 687, 330 - 335.
4. Loison J.-C.; Agúndez M.; Wakelam V.; Roueff E.; Gratier P.; Marcelino N.; Núñez-Reyes, D.; Cernicharo J.; Gerin M. The interstellar chemistry of C₃H and C₃H₂ isomers. *Monthly Notices of the Royal Astronomical Society.* 2017, 470, 4075 - 4088.
5. Núñez-Reyes, D.; Hickson, K. M.; Larrégaray, P.; Bonnet, L.; González-Lezana, T.; Suleimanov, Y. V. A Combined Theoretical and Experimental Investigation of the Kinetics and Dynamics of the O(¹D) + D₂ Reaction at Low Temperature. *Phys. Chem. Chem. Phys.* 2018, 20, 4404 - 4414.
6. Núñez-Reyes, D.; Kłos, J.; Millard, A.; Dagdigian, P.J.; Hickson, K. M. Experimental and Theoretical Investigation of the Temperature Dependent Electronic Quenching of O(¹D) atoms in Collision with Kr. *J. Chem. Phys.* 2018, 148, 124311.
7. Núñez-Reyes, D.; Hickson, K. M. Kinetics of the Gas-Phase O(¹D) + CO₂ and C(¹D) + CO₂ Reactions over the 50 - 296 K Range. *J. Phys. Chem. A* 2018, 122, 4002 - 4008.
8. Núñez-Reyes, D.; Hickson, K. M. Rate Constants and H-Atom Product Yields for the Reactions of O(¹D) Atoms with Ethane and Acetylene from 50 to 296 K. *J. Phys. Chem. A* 2018, 122, 4696 - 4703.
9. Núñez-Reyes, D.; Hickson, K. M. A Low Temperature Investigation of the Gas-Phase N(²D) + NO Reaction. Towards a Viable Source of N(²D) Atoms for Kinetic Studies in Astrochemistry. *Phys. Chem. Chem. Phys.*, 2018, 20, 17442 - 174.
10. Schleier, D.; Humeniuk, A.; Reusch, E.; Holzmeier, F.; Núñez-Reyes, D.; Alcaraz, C.; Garcia G.; Loison, J.-C.; Fischer, I.; Mitric R. Diborene: Generation and Photoelectron Spectroscopy of an Inorganic Biradical. *J. Phys. Chem. Lett.*, 2018, 9, 5921 - 5925.
11. Núñez-Reyes, D.; Loison J.-C.; Hickson, K. M.; Dobrijevic, M. A low temperature investigation of the N(²D) + CH₄, C₂H₆, C₃H₈ reactions. *Phys. Chem. Chem. Phys.*, 2019, 21, 6574 - 6581.
12. Wu, Y.; Cao, J.; Ma, H.; Zhang, C.; Bian, W.; Núñez-Reyes, D.; Hickson, K. M. Conical intersection-regulated intermediates in bimolecular reactions: Insights from C(¹D) + HD dynamics. Accepted in *Science Advances*.

Acknowledgements

I would like to thank my supervisors Kevin M. Hickson, Jean Christophe Loison and Michel Dobrijevic for their support and encouragement throughout my PhD research studies. It was a real privilege and an honour to work with them and learn from their scientific knowledge.

Special thanks to Kevin M. Hickson for his availability, constant advice and constructive suggestions, which were determinant for the accomplishment of this manuscript and my three years of formation in experimental Astrochemistry.

I would like to express my gratitude to Sebastien Le Picard, Frédérique Battin-Leclerc and Séverine Boyé-Péronne for accepting to be members of the jury of this thesis. Special thanks to the referees for their precise and efficient reviewing of the manuscript.

I would like to express my sincere gratitude to the members of COMEX group: Astrid Bergeat, Sebastien Morales and Christian Naulin for their encouraging words and always be ready to help me.

To my friends at the ISM Cesar, Alberto, Laurie and Bruno for their support and unconditional friendship during these three years. I am very thankful for their help whenever I needed it.

Finally, I would like to thank to my family especially to my husband Miguel for his unconditional support and love.

“Experimental Astrochemistry: The kinetics of neutral-neutral reactions at low temperature and their relevance to the chemistry of planetary atmospheres and interstellar clouds”

The last 50 years have been characterized by the fast development of astrochemistry as a science. To date, more than 150 gas-phase neutral-neutral reactions have been investigated at low temperatures relevant to planetary atmospheres and in cold regions of the interstellar medium. However, the rate constants and nature of the products for many potentially important gas-phase processes remain unknown. We performed kinetic studies of reactive and non-reactive removal processes between electronically excited atoms [$C(^1D)$, $O(^1D)$ and $N(^2D)$] with several molecules in order to quantify their importance in the chemistry of planetary atmospheres. Furthermore, we also investigated the reaction between carbon atoms in their ground electronic state (3P) with water, providing new evidence of a quantum mechanical tunnelling mechanism at low temperatures, which could play an important role in the chemistry of interstellar clouds. Rate constants and branching ratios for these processes were determined over the 50 - 296 K temperature range using a CRESU (Cinétique de Réaction en Ecoulement Supersonique Uniforme) apparatus coupled with pulsed laser photolysis (PLP) and vacuum ultraviolet laser induced fluorescence (VUV LIF).

Keywords: astrochemistry, chemical kinetics, gas-phase reactions, excited state atoms, CRESU

“Astrochimie expérimentale: Cinétique des réactions neutre-neutre à basse température et pertinence pour la chimie des atmosphères planétaires et des nuages interstellaires ”

Les 50 dernières années ont été caractérisées par le développement rapide de l'astrochimie. Plus de 150 réactions entre espèces neutres ont déjà été étudiées aux basses températures qui sont celles du milieu interstellaire et des atmosphères planétaires. Néanmoins, les constantes de vitesse et la nature des produits restent inconnues pour de nombreuses réactions potentiellement importantes pour caractériser ces milieux. Nous avons effectué des études cinétiques pour des processus réactifs, et non réactifs entre des atomes dans un état électronique excité [$C(^1D)$, $O(^1D)$ et $N(^2D)$] et plusieurs molécules stables afin de quantifier leur importance dans la chimie des atmosphères planétaires. Nous avons aussi étudié la réaction entre les atomes de carbone dans leur état électronique fondamental (3P) et l'eau, confirmant l'importance, pour certaines réactions avec barrière, de l'effet tunnel pour la réactivité à basse température. Les constantes de vitesse et les rapports de branchement pour ces processus ont été déterminés dans la gamme de température entre 50 et 296 K en utilisant un appareil CRESU, les atomes étudiés ont été produits par photolyse à l'aide d'un laser pulsé (PLP) et détectés par fluorescence induite par laser dans l'ultraviolet du vide (VUV LIF).

Mots-clés: astrochimie, cinétique chimique, réactions en phase gazeuse, atomes à l'état excité, CRESU